



HAL
open science

Virtual Prototyping of Electro-Hydrostatic Modules Equipped with Vane Pumps - Application to Injection Moulding Machines

Emanuele Gnesi

► **To cite this version:**

Emanuele Gnesi. Virtual Prototyping of Electro-Hydrostatic Modules Equipped with Vane Pumps - Application to Injection Moulding Machines. Mechanical engineering [physics.class-ph]. INSA de Toulouse, 2015. English. NNT : 2015ISAT0051 . tel-02059681

HAL Id: tel-02059681

<https://theses.hal.science/tel-02059681>

Submitted on 6 Mar 2019

HAL is a multi-disciplinary open access archive for the deposit and dissemination of scientific research documents, whether they are published or not. The documents may come from teaching and research institutions in France or abroad, or from public or private research centers.

L'archive ouverte pluridisciplinaire **HAL**, est destinée au dépôt et à la diffusion de documents scientifiques de niveau recherche, publiés ou non, émanant des établissements d'enseignement et de recherche français ou étrangers, des laboratoires publics ou privés.

Université Fédérale



Toulouse Midi-Pyrénées

THÈSE

En vue de l'obtention du

DOCTORAT DE L'UNIVERSITÉ DE TOULOUSE

Délivré par :

Institut National des Sciences Appliquées de Toulouse (INSA de Toulouse)

Présentée et soutenue par :

EMANUELE GNESI

Le lundi 21 Septembre 2015

Titre :

Prototypage Virtuel des Modules Electro-Hydrostatiques Equipés de
Pompe à Palettes – Application Presses à Injecter

École doctorale et discipline :

ED MEGEP: Génie mécanique, mécanique des matériaux

Unité de recherche :

Institut Clément Ader

Directeur de Thèse :

Prof. Jean-Charles Maré

Jury :

Prof. Grigore Gogu

Prof. Gianpietro Di Rito

Résumé

Dans les dernières années la politique des entreprises s'est concentrée sur la recherche de solutions industrielles plus écologiques pour réduire l'impact sur l'environnement et l'énergie consommée. La tendance s'est élargie aux machines stationnaires dans l'automatisation industrielle. Il inclut la technologie d'entraînement pour contrôler le mouvement séquentiel de plusieurs axes dans les presses à injecter. La conception des systèmes se focalise sur une approche conduisant à l'amélioration du rendement énergétique aussi bien que l'augmentation de la pression de service, la réduction de cycle de la machine et l'amélioration de sa répétabilité. Toutes ces exigences ont poussé la technologie d'entraînement à se développer en augmentant l'intérêt pour les modules électromécaniques et électro-hydrostatiques (EHM). Dans cette thèse, une solution innovatrice d'EHM est proposée qui associe un convertisseur, un servomoteur AC brushless et la pompe à palettes Parker. En détail, l'intérêt de recherche concerne le développement d'un modèle à niveau système de la pompe à palette. L'objectif principal est de permettre l'évaluation des pertes d'énergie de la pompe et la performance de module pendant des phases spécifiques du cycle de la machine : accélération, dépressurisation et phase de maintien de la pression. Premièrement analysée au moyen de l'approche analytique, la dynamique est alors évaluée par des modèles plus avancés basés sur le prototypage virtuel construit dans l'environnement LMS-AMESim. Les avantages concernant la prévision des performances du module EHM et sur l'évaluation des paramètres fondamentaux inconnus (comme la compressibilité du fluide et le contenu d'air dans le fluide) sont montrés par comparaison avec des résultats expérimentaux obtenus dans le laboratoire. Les phénomènes de la cavitation et d'aération sont aussi pris en compte pendant les phases d'accélération et des modèles sont ainsi développés pour prévoir les conditions de fonctionnement qui promeuvent ces phénomènes. La consommation d'énergie de l'EHM est alors analysée au moyen des modèles thermo-hydrauliques capables de déterminer les échanges de chaleur entre les composants de module et l'environnement.

Université de Toulouse
Institut Clément Ader

-
Parker Hannifin Manufacturing France S.A.S.

Virtual Prototyping of Electro-Hydrostatic Modules Equipped with Vane Pumps

- Application to Injection Moulding Machines

Doctoral Thesis

Prepared by: Emanuele Gnesi

Supervisor: Prof. Jean-Charles Maré

Reviewers: Prof. Grigore Gogu

Prof. Gianpietro Di Rito

Toulouse
September 2015

Summary

In last years companies' policy has been focusing on research of more eco-friendly solutions in order to reduce the environmental impact and the consumed energy. The trend has been affecting the stationary machinery in the industrial automation too. It includes the drive technology for motion control in the injection moulding machines. The design studies concern energy efficiency improvement, as well as increased service pressure, shorter cycle time and repeatability over a long period of time. All these requirements have led the drive technology to evolve by increasing the interest for the electro-mechanical and electro-hydrostatic modules (EHM). In this thesis an innovative solution of EHM is proposed that associates industrial inverter, AC brushless servo motor and fixed-displacement low-noise Parker vane pump. In detail, the research interest concerns the development of a system level model of the vane pump. The main objective is to enable assessing the pump energy losses and full module performance in specific phase of machine's cycle: acceleration, depressurisation and holding pressure phases. Firstly analysed by means of analytical approach, dynamics are then evaluated through more advanced models based on virtual prototyping built in LMS-AMESim environment. The advantages on predicting the EHM performance and on estimating the unknown fundamental parameters (e.g. Bulk Modulus and fluid air content) are showed through comparison with experimental results obtained in laboratory. The cavitation/aeration phenomena are also taken into account during acceleration transients and models are thus developed in order to predict the operating conditions which promote these phenomena. Energy behaviour of the EHM is then analysed by means of thermal hydraulic models able to determine the heat exchanges between module components and environment.

Mots Clés

Electro-hydrostatique

Presses à injecter

Pompe à palettes

Economie d'énergie

Cavitation

Injection statique

Thermo-hydraulique

AMESim

Key Words

Electro-hydrostatic

Injection moulding machines

Vane pump

Energy saving

Cavitation

Static injection

Thermo-hydraulic

AMESim

To my family

Remerciements

Je voudrais tout d'abord remercier mon professeur, Jean-Charles Maré, pour avoir eu confiance en moi depuis le début, pour avoir partagé tout son savoir et m'avoir enseigné sa rigueur scientifique.

Je tiens également à remercier le Directeur Général, Blaise Goupy, et le responsable Business Unit, Sylvain Roncari, pour leur accueil excellent et pour m'avoir donné l'opportunité de travailler au sein de l'industrie Parker, à Vierzon.

Je voudrais par ailleurs remercier sincèrement le Directeur R&D, Jean Luc Bordet, et l'ingénieur, Christophe Dubois, pour leur grande disponibilité et compréhension, pour m'avoir enseigné théorie et pratique des pompes à palettes et pour m'avoir aidé à m'intégrer à l'industrie Parker.

Un merci de tout cœur à toute ma famille, en particulier à ma mère, mon père et Elisa pour m'avoir encouragé à entreprendre cette aventure il y a trois ans, avoir cru en moi et avoir été toujours près de moi malgré la distance.

Un merci tout spécial à Amélie, qui m'a soutenu chaque jour sans jamais démordre, qui m'a encouragé dans les moments les plus difficiles et qui a toujours été là comme une présence solide.

Je remercie tous mes amis, les nouveaux comme ceux de longue date. Ils ont su montrer leur proximité et leur affection.

Je remercie tout le bureau R&D et Méthodes qui m'a aidé à m'intégrer rapidement dans l'équipe et qui m'a enseigné le « français berrichon ».

Je voudrais enfin remercier tous les doctorants et étudiants que j'ai pu connaître pendant la période passée à l'ICA de Toulouse et avec lesquels j'ai pu vivre de beaux moments.

Desidero ringraziare il professore Jean-Charles Maré per aver avuto fiducia in me fin dal primo momento, per aver condiviso tutto il suo sapere ed avermi insegnato il suo rigore scientifico.

Ringrazio poi il direttore generale Blaise Goupy et il responsabile operativo Sylvain Roncari per l'ottima accoglienza e per avermi dato l'opportunità di lavorare nel seno dell'industria Parker a Vierzon.

Desidero ringraziare il direttore R&D Jean Luc Bordet e l'ingegnere Christophe Dubois per la loro grande disponibilità, per avermi insegnato teoria e pratica delle pompe a palette e per avermi fatto sentire come a casa.

Un grazie di cuore a tutta la mia famiglia, in particolare a mia madre, mio padre ed Elisa per avermi incoraggiato ad intraprendere questa avventura tre anni fa, aver creduto in me ed essermi stati sempre accanto nonostante la distanza.

Un grazie speciale ad Amélie che mi ha supportato ogni giorno senza mai demordere, per avermi compreso e supportato soprattutto nei momenti più difficili e per essere stata sempre là come una solida presenza.

Voglio ringraziare anche tutti i miei amici di nuova e vecchia data che hanno saputo dimostrare la loro vicinanza ed il loro affetto.

Ringrazio tutto l'ufficio R&D e Metodi per l'aiuto dato ad integrarmi rapidamente nel gruppo e per avermi insegnato il francese berrichone.

Desidero ringraziare infine tutti i dottorandi e studenti che ho potuto conoscere durante il periodo trascorso all'ICA di Tolosa e con i quali ho potuto vivere dei bei momenti insieme.

Contents

Figures.....	v
Tables.....	viii
Nomenclature.....	ix
Introduction.....	1
1	Injection Moulding Machines and Drives 10
1.1	INJECTION MOULDING MACHINES..... 11
1.1.1	<i>Units Composing Machine..... 13</i>
1.1.2	<i>IMM Functional Process 16</i>
1.2	EVOLUTION OF DRIVE TECHNOLOGIES..... 18
1.2.1	<i>Advantages of Electro-Hydrostatic Modules..... 23</i>
1.2.2	<i>Control Techniques in EHMs..... 27</i>
1.3	REQUIREMENTS AND LIMITATIONS..... 32
1.4	TEST BENCH 35
1.5	CONCLUSION..... 41
REFERENCES	42
2	Vane Pump 45
2.1	STATE OF ART OF VANE PUMP 46
2.1.1	<i>Product Evolution and Competitors 46</i>
2.1.2	<i>Design and Modelling 52</i>
2.1.3	<i>Parker Vane Pump: Denison Technology 55</i>
2.1.3.1	<i>Operation Principle.....56</i>
2.1.3.2	<i>T7 Series Vane Pump for Electro-Hydrostatic Modules.....59</i>
2.2	DEVELOPING A MODEL OF ENERGY LOSSES 61
2.2.1	<i>Structure of Pump Losses Model 63</i>
2.2.2	<i>Parametric Model of Pump Leakages and Frictions..... 64</i>
2.2.3	<i>Detail Model: Hydraulic Virtual Prototype 69</i>
2.2.3.1	<i>Frictional Torques.....70</i>
2.2.3.2	<i>Internal Leakages.....72</i>
2.3	CONCLUSION..... 74
REFERENCES	76

3	Acceleration and Depressurisation Phases	78
3.1	REFERENCE ARCHITECTURE.....	81
3.2	ACCELERATION TRANSIENT: PARAMETERS LIMITING PERFORMANCE....	84
3.2.1	<i>Current Loop Dynamics</i>	<i>85</i>
3.2.2	<i>Effect of Max Torque and Inertia</i>	<i>85</i>
3.2.3	<i>Hydrostatic Torque.....</i>	<i>87</i>
3.2.4	<i>Contribution of Motor and Pump Energy Losses.....</i>	<i>88</i>
3.2.5	<i>Contribution of Fluid Compressibility</i>	<i>89</i>
3.2.6	<i>Conclusions</i>	<i>90</i>
3.3	VELOCITY CLOSED LOOP SYNTHESIS	94
3.3.1	<i>Closed Loop System Dynamics: ω/ω^* Transfer Function</i>	<i>94</i>
3.3.2	<i>Proportional Controller.....</i>	<i>95</i>
3.3.3	<i>Parallel Feedforward Compensator.....</i>	<i>97</i>
3.3.4	<i>Advantages and Limitations of Feedforward Compensator</i>	<i>99</i>
3.4	DETAIL MODEL THROUGH A FULL VIRTUAL PROTOTYPE	102
3.4.1	<i>Velocity Closed-Loop Control and Inverter.....</i>	<i>102</i>
3.4.2	<i>Electric Motor and Motor/Pump Coupling.....</i>	<i>104</i>
3.4.3	<i>Vane Pump_02 Prototype.....</i>	<i>104</i>
3.4.4	<i>Hydraulic Circuit_01.....</i>	<i>105</i>
3.4.5	<i>Advantages of Virtual Prototyping: Energy Losses and Bulk Modulus.....</i>	<i>107</i>
3.5	LABORATORY TESTS FOR ACCELERATION	108
3.5.1	<i>Simulation Procedure of Prototype</i>	<i>109</i>
3.6	COMPARISON BETWEEN ANALYTICAL MODEL, REAL AND VIRTUAL TESTS	111
3.6.1	<i>Validation of Full Virtual Prototype.....</i>	<i>112</i>
3.7	DEPRESSURISATION TRANSIENT	115
3.8	LABORATORY TESTS FOR DEPRESSURISATION	115
3.8.1	<i>Simulation Procedure for Virtual Prototype: Determination of Optimum Young's Modulus of the Flexible Hose</i>	<i>117</i>
3.9	COMPARISON BETWEEN EXPERIMENTAL AND SIMULATED RESULTS....	118
3.10	CONCLUSION.....	120
	REFERENCES	121

4	Identification of Operating Conditions Favourable for Cavitation Development	122
4.1	INTRODUCTION	123
4.2	CAVITATION	124

4.2.1	<i>Effects on Vane Pump</i>	126
4.2.2	<i>Methods to Detect and Prevent Cavitation</i>	129
4.3	AERATION	130
4.4	ANALYTICAL MODEL FOR INLET PIPE AND PUMP	132
4.4.1	<i>Pipe and Tube Fitting: Inertial and Resistive Effects</i>	133
4.4.2	<i>Pump and Inlet Pipe: Hydraulic Capacity</i>	136
4.4.3	<i>Resolution of Model</i>	137
4.5	VIRTUAL PROTOTYPES: INLET LINE AND PUMP MODELLING	140
4.5.1	<i>Basic Prototype: Characterisation of Inlet Line</i>	141
4.5.2	<i>Advanced Prototype: Characterisation of Pump Interiors</i>	144
4.5.3	<i>Comparison between Prototypes</i>	148
4.6	COMPARISON BETWEEN ANALYTICAL AND VIRTUAL MODEL	150
4.7	LABORATORY TESTS	153
4.7.1	<i>Simulation Procedure</i>	155
4.7.1.1	<i>Determination of Optimum Fluid and Friction Factors Characteristics</i>	156
4.7.1.2	<i>Free Air Propagation inside Model: Limitations of AMESim</i>	158
4.8	COMPARISON BETWEEN MEASURED AND SIMULATED PRESSURE	161
4.9	CONCLUSIONS	165
	REFERENCES	166
5	Thermal Divergence	167
5.1	PHENOMENON DESCRIPTION	168
5.2	PROPOSED SOLUTIONS	170
5.3	FUNCTIONAL THERMAL MODEL OF PUMP	172
5.3.1	<i>Fluid Properties versus Temperature: Viscosity Model</i>	173
5.3.2	<i>Work Rate Equilibrium</i>	174
5.3.3	<i>Energy Conservation Balance</i>	174
5.3.4	<i>Heat Transfer Equations</i>	177
5.3.5	<i>Resolution of Functional Model</i>	180
5.4	LABORATORY TESTS	184
5.4.1	<i>Experimental Results</i>	185
5.4.2	<i>Comparison between Measured and Analytically Simulated Results</i>	186
5.5	ADVANCED MODEL: VIRTUAL PROTOTYPING	190
5.5.1	<i>Vane Pump Thermal Virtual Prototype</i>	190
5.5.2	<i>Full Thermal Model</i>	193
5.5.3	<i>Heat Transfer Parameters Identification</i>	196
5.5.3.1	<i>Internal Forced Convection</i>	196
5.5.3.2	<i>Natural Convection and Radiation</i>	197
5.5.3.3	<i>Thermal Conduction</i>	199

5.6	COMPARISON BETWEEN ANALYTICAL MODEL, REAL AND VIRTUAL TESTS	
	199
5.7	CONCLUSIONS	204
	REFERENCES	206
Conclusion		208
	Appendix A-Characteristics of Components constituting the Test Bench	216
	Appendix B - Preliminary Calculation of Effective Bulk Modulus through the Evaluation of Parasitic Contributions	220
	Appendix C - Thermal Supercomponent for Calculation of Released Powers associated to Pump Internal Leakages	227

Figures

Figure 0.1	Injection moulding machine's requirements	4
Figure 0.2	Electric and hydraulic drives in actuation systems for stationary applications, from [5].....	5
Figure 0.3	Parker EHM: NX Series servo motor and T7 Series vane pump	6
Figure 0.4	Research organization of dissertation	7
Figure 1.1	Typical custom plastic parts domains, from [1].....	11
Figure 1.2	Injection Moulding Machines: Ferromatik Milacon on left-side, from [6], REP - Rubber in Motion on right-side, from [7]	13
Figure 1.3	Schematic of injection unit: direct driven screw by an electric or hydraulic motor (top), unit with plasticisation screw and injection ram (bottom), from [8].....	14
Figure 1.4	Schematic of clamping unit with Direct Hydraulic Lock, from [8]	15
Figure 1.5	Example of IMM cycle's phases for plastic and power consumptions, from [8]	17
Figure 1.6	Technology shift driven by market forces in IMMs, from [15].....	18
Figure 1.7	Conventional IMM drives using valves as signal-to-power interfaces: manually operated valve a), on-off valves in parallel b), valves operated by proportional solenoid c) and servo valve d) 19	
Figure 1.8	SHM, EHM and EMM concepts	20
Figure 1.9	EHM concept with variable-displacement pump for IMM, from [17].....	21
Figure 1.10	Electro-mechanical modules (left) and control loop architecture schematic (right), [17].....	21
Figure 1.11	Examples of some EHM available on market: asynchronous motor with variable-displacement axial piston or fixed-displacement vane pump, Parker, from [21], a), asynchronous motor with fixed-displacement internal gear pump, Voith, from [22], b) synchronous servo motor with fixed-displacement radial piston pump, Moog, from [23], c)	23
Figure 1.12	Efficiency comparison of three EHMs, from [16].....	24
Figure 1.13	Normalised energy consumption of two moulded parts: switch and gear. Comparison between several drive technology in a IMM, from [13].....	25
Figure 1.14	Relationships among: machine and process variables, final part quality and material properties, from [28]	27
Figure 1.15	Time evolution of cavity and hydraulic pressure during dynamic and static injection, from [8].	28
Figure 1.16	Schematic of a typical closed-loop controller of EHM.....	29
Figure 1.17	Block diagram of ILC algorithm, from [35]	30
Figure 1.18	Injection Moulding Machine's cycle	32
Figure 1.19	Schematic of the test bench built in laboratory	35
Figure 1.20	Example of command in Simulink environment.....	38
Figure 1.21	Test Bench: module and hydraulic circuit.....	39
Figure 1.22	Test Bench: Measurements of temperature and pressure	39
Figure 1.23	Test Bench: measurements of temperatures on motor and pump body and pressure in pump inlet.....	40
Figure 1.24	Test Bench: Control Station.....	40
Figure 2.1	Patent N.2677330: Vane Pump, 04/05/1954, United States Patent Office, [1].....	46
Figure 2.2	Evolution of power density (left side) and reduction of average price (right side) of vane pumps in 1940-1964, from [4]	47
Figure 2.3	Qualitative comparison of principal advantages and drawbacks of fixed and variable displacement pump technologies: internal gear, vane, axial pistons, and variable axial pistons.	50

Figure 2.4	Variation of internal leakages in a vane pump versus viscosity and fluid contamination level, from [15].....	53
Figure 2.5	Evolution of Denison vane pump technology from 1952 to 2010	55
Figure 2.6	Functional quadrants of operation of the vane pump selected in this work	56
Figure 2.7	Vane Pump general design.....	57
Figure 2.8	Cartridge components and cross-sectional view	58
Figure 2.9	Sections of the T7 Series vane pump inserted in the EHM	60
Figure 2.10	Placement of thermocouples for measuring fluid temperature inside pump	61
Figure 2.11	Energy losses of Parker T7 vane pump (22,5 cc/rev) at 3 temperatures vs. line pressure drop and pump speed (left: internal leakage, right: frictional torque).....	62
Figure 2.12	Simplified causal Bond-graph of the vane pump with energy losses	63
Figure 2.13	Internal pump leakages: experimental data (marks) and curves obtained by parametric model (dashed lines) at three temperatures	67
Figure 2.14	Frictional pump torques: experimental data (marks) and curves obtained by parametric model (dashed lines) at three temperatures	68
Figure 2.15	Hydraulic virtual prototype of vane pump	70
Figure 2.16	Component for pump frictions simulation, FR1RK000, from [29]	71
Figure 2.17	Frictional pump torques: extrapolation in the pump range: [-3500, 3500] rev/min provided by component FR1RK000.....	72
Figure 2.18	Component for pump leakages simulation, VOR001, from [29]	73
Figure 2.19	Internal pump leakages: extrapolation in the pump range: [-3500, 3500] rev/min provided by component VOR001.....	74
Figure 3.1	Reference architecture of the test bench	82
Figure 3.2	Control Volume	83
Figure 3.3	Percentage of contribution on EHM acceleration given by each parameter (or effect) with reference to case N.°1) characterised by: max peak motor torque, total inertia and hydrostatic torque.....	93
Figure 3.4	Proportional Motor Speed Controller.....	95
Figure 3.5	Two degrees of freedom controller: closed-loop controller and feedforward compensator	98
Figure 3.6	Simulation of the speed time response $\omega(t)$ obtained by analytical model for three different cases. The torque limit is fixed to C_{max}	100
Figure 3.7	Full Virtual Prototype.....	102
Figure 3.8	Virtual prototype of velocity closed-loop control and inverter	103
Figure 3.9	Virtual prototype of electric motor	104
Figure 3.10	Vane pump_02 virtual prototype	105
Figure 3.11	Virtual prototype of the hydraulic circuit	106
Figure 3.12	Characteristics of the measured speed time response	109
Figure 3.13	Scheme of simulation steps sequence.....	110
Figure 3.14	Comparison between measured, analytical and simulated speeds (top) and pressures.....	111
Figure 3.15	Characteristics of speed and pressure time response	116
Figure 3.16	Iterations of the optimization process for the E determination.....	117
Figure 3.17	Experimental and simulated speed and pressure in Test01.....	119
Figure 4.1	Variation of the fluid pressure versus time: aeration and cavitation processes	124
Figure 4.2	Plots of the conditions for static equilibrium of cavitation nuclei. Variation of pressure adjacent to cavity as function of cavities radius and gas content, from [4]	125

Figure 4.3	Cavitation erosion: symmetrical collapse (a) and asymmetrical collapse (b), from [8].....	126
Figure 4.4	Cavitation erosion: craters on port plate, from [2].....	127
Figure 4.5	Cavitation erosion: craters on pins, from [2].....	127
Figure 4.6	Saturation of the flow rate through an orifice produced by cavitation, from [1].....	128
Figure 4.7	Aeration damage: grooves on port plate (up) and vane break (down), from [2].....	131
Figure 4.8	Aeration damage: black mark on cam ring due to air bubble implosion, from [2].....	131
Figure 4.9	Schematic of the complete analytical model.....	132
Figure 4.10	Schematic of the Pipe and of the inside contained fluid.....	133
Figure 4.11	Equivalence between pump and linear hydraulic cylinder.....	136
Figure 4.12	Virtual prototypes of vane pump and hydraulic circuit for cavitation evaluation.....	141
Figure 4.13	Vane Pump virtual prototype: Vane_Pump_03.....	142
Figure 4.14	Hydraulic circuit virtual prototype with inlet line modelling: Hydraulic_Circuit_02.....	143
Figure 4.15	Representation of total volume at low pressure inside pump.....	144
Figure 4.16	Representation of total volume section: a) longitudinal section, b) transversal section.....	145
Figure 4.17	Advanced Prototype: Pump interior and inlet pipe.....	147
Figure 4.18	Inlet Pressure and inside pump with the two different prototypes.....	148
Figure 4.19	Comparison between analytical model and virtual basic level prototype results: temporal evolution of pressure in pump inlet.....	151
Figure 4.20	Comparison of inlet pressure between measured and simulated results for command step of 2000 rpm imposed for 10 ms.....	154
Figure 4.21	Scheme of simulation steps sequence.....	156
Figure 4.22	Henry's law in AMESim: fraction of undissolved air/gas versus fluid pressure in high and low pressure hydraulic circuit.....	160
Figure 4.23	Comparison of inlet pressure between measured and simulated results for command step of 2400 rpm imposed for 10 ms and 0bar.....	162
Figure 5.1	Schematic of the thermal cycle at the origin of the thermal divergence phenomenon.....	168
Figure 5.2	External hydraulic bypass linked to high pressure pump volume for maintaining constant the line pressure and for fluid recirculation.....	171
Figure 5.3	External drain linked to drain pump volume of low pressure to evacuate the internal leakages and to reduce the temperature inside pump.....	171
Figure 5.4	Sketch map of the Control Volumes of the full analysed system and thermal exchanges between: hydraulic fluid, pump body, motor body and environment air.....	175
Figure 5.5	Schematic of the input ports to differential equations in T_f and T_p	181
Figure 5.6	Comparison between measured and simulated temperatures: Test-01 (top), Test-02.....	187
Figure 5.7	Vane pump thermal-hydraulic virtual prototype.....	191
Figure 5.8	"Supercomponent" for internal forced convection evaluation.....	193
Figure 5.9	Sketch map of full system modelled in the advanced analysis through virtual prototyping.....	194
Figure 5.10	Complete thermal virtual prototype of EHM (top: hydraulic load and test bench, bottom; electrohydrostatic module).....	195
Figure 5.11	Comparison between measured, analytically and virtually simulated temperatures: Test-01 (top) and Test-02 (bottom).....	201
Figure 5.12	Contributions of absorbed and released powers at the end simulation time (top of each figure) and absorbed and released energies (bottom of each figure) for pump body, motor body and fluid. Data of Test-01 in left column and data of Test-02 in right column.....	203

Tables

Table 0.1	Injection unit specifications of a 2000 kN injection moulding machine, from [3]	5
Table 1.1	Basic rubber and plastic parts	12
Table 1.2	Comparison between: SHMs, EHMs and EMMs	26
Table 1.3	Reference cycle of a rubber/plastic IMM	33
Table 2.1	Differences in pump cartridge for mobile and industrial applications.....	59
Table 2.2	Values of parameters obtained by means of LSM	65
Table 3.1	Evaluation of inertial contributions	87
Table 3.2	Numerical results of the maximum delta speed $\Delta\omega$ reached after 10 ms and obtained by means of the equations described in last sections.....	92
Table 3.3	Characteristics of the transfer function H_ω of ω/ω^*	96
Table 3.4	Numerical values of H_ω transfer function characteristics	96
Table 3.5	Comparison between measured data and simulated data by virtual prototype when the following controller is implemented: P controller, P controller + feedforward compensator of inertial contributions and P controller + complete feedforward compensator	113
Table 3.6	Value of the parameters influencing β_e selected by means of comparison between experiments and virtual results	114
Table 3.7	Tests performed for depressurisation.....	116
Table 3.8	Comparison between experimental and simulated data.....	118
Table 4.1	Vapour pressure of a typical hydraulic oil as function of temperature, from [6]	125
Table 4.2	Summary of System's Equations	137
Table 4.3	Characteristics of the transfer function in p1	139
Table 4.4	Comparison between advanced and basic prototype in terms of integration option and CPU time	149
Table 4.5	Operating conditions for laboratory tests.....	153
Table 4.6	Final values of the system parameters obtained by means of optimisation process	158
Table 4.7	Comparison between measured and simulated data	163
Table 5.1	System of equations of the thermal hydraulic model of pump at functional level	180
Table 5.2	Differential equations in T_f and T_p	181
Table 5.3	Expression of transfer functions of T_f and properties of H_{f0}	184
Table 5.4	Value of heat transfer coefficients selected in the functional model	188
Table 5.5	Values of characteristics of H_f for Test-01	190
Table 5.6	Nusselt numbers calculation for natural convection over the surface of: pump and motor body and base support	198
Table 5.7	Values of heat transfer coefficients selected for EHM virtual simulations	200

Nomenclature

A_{cont}^{pm}	Pump/motor contact area	[m ²]
A_e	Emitting surface	[m ²]
A_{ext}	External pump surface	[m ²]
A_{ext}^p	External pump area	[m ²]
A_{fcv}	valve coefficient	[m ³]
A_{in}^p	Internal pump area in contact with fluid	[m ²]
A_{int}	Internal surface	[m ²]
$Area$	Section surface	[m ²]
a_{fcv}	valve coefficient	[m ³ /Pa/s]
C_{com}	Command torque	[Nm]
C_{est}	Estimated torque	[Nm]
C_f	Thermal fluid capacity	[J/K]
C_{fm}	Motor fricitons	[Nm]
C_{fp}	Frictional pump torque	[Nm]
C_h	Hydraulic capacity	[m ³ /Pa]
C_{hyd}	Hydrostatic torque	[Nm]
C_L	Load torque	[Nm]
C_m	Motor torque	[Nm]
\bar{C}_m	Continuous motor torque	[Nm]
C_{max}	Motor max peak torque	[Nm]
C_{m0}	Torque constant coefficient	[Nm]
C_p	Thermal pump capacity	[J/K]
C_q	Discharge coefficient	[-]
C_0	Constant coefficient	[Nm]
c_p	Specific heat at constant pressure	[(J/kg)/K]
c_{pf}	Fluid specific heat at constant pressure	[(J/kg)/K]
c_{pp}	Pump material specific heat at constant pressure	[(J/kg)/K]
D	Diameter	[m ³]
D_f	Transfer function denominator	[1/s ²]
D_{f0}	Transfer function denominator coefficient	[1/s ²]
D_{f1}	Transfer function denominator coefficient	[1/s]
E	Young's modulus of material	[Pa]
E_{cin}	Kinetic Energy	[J]
E_p	Potential Energy	[J]
E_{tot}	Total Energy	[J]
\dot{E}_{cin}	Kinetic Energy	[W]
\dot{E}_p	Potential Energy	[W]
\dot{E}_{tot}	Total Energy	[W]
f	Friction factor	[-]

f_c	Frequency	[Hz]
G_r	Grashof number	[-]
g	Gravitational acceleration	[m/s ²]
$HAha$	Coefficient	[J ² /K ²]
H_f	Transfer function of fluid	[s]
H	Specific enthalpy	[J/kg]
h_{cond}	contact conductance	[J/m ² /K]
h_{cond}^{pm}	Pump/motor thermal contact conductance	[J/m ² /K]
h_{conv}	convection coefficient	[J/m ² /K]
h_{conv}^p	Pump natural convection coefficient	[J/m ² /K]
h_i	Specific input enthalpy	[J/kg]
h_{int_conv}	Internal forced convection coefficient	[J/m ² /K]
h_o	Specific output enthalpy	[J/kg]
J_f	Inertia of the Fluid	[kg m ²]
J_m	Motor Inertia	[kg m ²]
J_p	Pump Inertia	[kg m ²]
J_{tot}	Total Inertia	[kg m ²]
K_f	Gain of transfer fluid function	[-]
K_ω	Gain of velocity closed-loop	[Nm/rad/s]
k_f	Thermal fluid conductivity	[W/m/K]
k_m	Motor electromagnetic coefficient	[Nm/A]
I_h	Hydraulic inertia	[kg/m ⁴]
L	Length	[m]
L_c	Characteristic length	[m]
M_p	Pump mass	[kg]
m_f	Fluid mass	[kg]
\dot{m}	Mass flow rate	[kg/s]
\dot{m}_i	Input mass flow rate	[kg/s]
\dot{m}_o	Output mass flow rate	[kg/s]
N_f	Fluid transfer function numerator	[1/s]
N_u	Nusselt number	[-]
n_o	Zero of the transfer function numerator	[1/s]
Pr	Prandtl number	[-]
P_{copper}	Joule losses	[W]
p	Pressure	[Pa]
p_i	Input pressure	[Pa]
p_o	Output pressure	[Pa]
p_1	Pole of transfer function	[1/s]
p_2	Pole of transfer function	[1/s]
Q	Flow rate	[m ³ /s]
Q_i	Input flow rate	[m ³ /s]
\dot{Q}_{fp}	Heat transfer between fluid/pump	[W]
Q_{lp}	Internal pump leakage	[m ³ /s]

\dot{Q}_{me}	Motor/environment natural convection	[W]
\dot{Q}_{ms}	Motor/support thermal contact conductance	[W]
Q_o	Output flow rate	[m ³ /s]
Q_{out}	Output flow rate signal	[m ³ /s]
\dot{Q}_{pe}	Pump/environment natural convection	[W]
\dot{Q}_{pm}	Pump/motor thermal contact conductance	[W]
\dot{Q}_r	Radiation	[W]
\dot{Q}_{se}	Support/environment natural convection	[W]
Q_{th}	Theoretical flow rate	[m ³ /s]
\dot{Q}_{tot}^{heat}	Total heat flow rate	[W]
Ra	Rayleigh number	[-]
Re	Reynolds number	[-]
R_m	Motor windings resistance	[Ohm]
S	Surface	[m ²]
s	Complex variable	[1/s]
T	Temperature	[°C]
T_{asp}	Pump aspiration temperature	[°C]
T_e	Environment temperature	[°C]
T_f	Fluid temperature	[°C]
T_{f-in-p}	Fluid temperature inside pump	[°C]
T_i	Initial temperature	[°C]
T_i^f	Initial temperature of fluid	[°C]
T_i^m	Initial temperature of motor body	[°C]
T_i^p	Initial temperature of pump body	[°C]
T_m	Motor temperature	[°C]
T_{max}	Max temperature	[°C]
T_{m-body}	Motor body temperature	[°C]
T_{mean}	Mean temperature	[°C]
T_o	Output temperature	[°C]
T_o^f	Output temperature of fluid	[°C]
T_o^m	Output temperature of motor body	[°C]
T_o^p	Output temperature of pump body	[°C]
T_{out}	Fluid temperature in pump outlet	[°C]
T_p	Pump temperature	[°C]
T_{plate}	Pump plate temperature	[°C]
T_{p-body}	Pump body temperature	[°C]
T_{pp}	Fluid temperature into the pump plate	[°C]
T_{s-body}	Base support temperature	[°C]
T_{tank}	Fluid temperature in tank	[°C]
T_∞	Fluid temperature away from surface	[°C]
t	Thickness	[m]
U	Internal energy	[J]
\dot{U}	Internal energy rate	[W]

V	Volume	[m ³]
\dot{V}	Volume time rate	[m ³ /s]
V_0	Pump displacement	[m ³ /rad]
\dot{W}_i	Input work rate	[W]
\dot{W}_{loss}	Work loss rate	[W]
\dot{W}_o	Output work rate	[W]
\dot{W}_{tot}	Total work rate	[W]
α_p	Thermal expansion coefficient	[1/K]
α_{fm}	Static friction of motor	[Nm]
α_{fp}	Static friction of pump	[Nm]
α_{pc}	Coulomb friction	[Nm]
α_{ps}	Stiction friction	[Nm]
β	Volume expansion coefficient	[1/K]
β_c	Container Bulk Modulus	[Pa]
β_e	Effective Bulk Modulus	[Pa]
β_f	Fluid Bulk Modulus	[Pa]
β_{fp}	Viscous friction coefficient of pump	[ISU]
β_{lp}	Speed dependent leakage coefficient	[ISU]
β_g	Gas Bulk Modulus	[Pa]
Δp	Pressure drop	[Pa]
ε_ω	Speed error signal	[rad/s]
ε_s	Surface emissivity coefficient	[-]
Γ	Gas/vapor polytropic index	[-]
γ_{fp}	Pressure dependent friction coefficient of pump	[ISU]
γ_{lp}	Pressure dependent leakage coefficient of pump	[ISU]
η_{vol}	Volumetric efficiency	[-]
λ	Flow number	[-]
λ_t	Thermal conductivity	[W/(m K)]
μ	Dynamic viscosity	[Pa s]
μ_i	Initial dynamic viscosity	[Pa s]
μ_o	Output dynamic viscosity	[Pa s]
ν	Kinematic viscosity	[m ² /s]
θ	Angle	[rad]
ρ	Density	[kg/m ³]
ρ_i	Input density	[kg/m ³]
ρ_o	Output density	[kg/m ³]
$\dot{\rho}$	Density rate	[kg/m ³ /s]
ΣHA	Coefficient	[J/K]
σ	Coefficient of dynamic viscosity	[1/K]
σ_s	Stefan-Boltzmann constant	[W/m ² /K ⁴]
$\tau_{1,2,3,p,\omega}$	Time constants	[s]

ω	Pump speed	[rad/s]
$\dot{\omega}$	Pump rotational acceleration	[rad/s ²]
$\omega_{c,f,n,m,p,\omega}$	Undamped natural pulsations	[1/s]
$\xi_{c,f,n,m,p,\omega}$	Damping ratios	[-]

<i>CFD</i>	Computational Fluid Dynamics
<i>CPU</i>	Central Processing Unit
<i>DHL</i>	Direct Hydraulic Lock
<i>DSE</i>	Deep Sea Electronics
<i>EBHA</i>	Electro-Backup Hydrostatic Actuator
<i>EHA</i>	Electro-Hydrostatic Actuator
<i>EHM</i>	Electro-Hydrostatic Module
<i>EMA</i>	Electro-Mechanical Actuator
<i>EMM</i>	Electro-Mechanical Module
<i>EUROMAP</i>	Europe's Association for Plastics and Rubber Machinery Manufacturers
<i>FF</i>	Feedforward
<i>HP</i>	High Pressure
<i>ILC</i>	Iterative Learning Control
<i>IMM</i>	Injection Moulding Machine
<i>LP</i>	Low Pressure
<i>LSM</i>	Least Square Method
<i>SHA</i>	Servo-Hydraulic Actuator
<i>SHM</i>	Servo-Hydraulic Module
<i>TL</i>	Toggle Lock

* = Command signal

' = Simulated Signal

~ = Measured Signal

^ = Estimated Signal

Introduction

Dans le Chapitre 1, la machine à injecter est décrite en termes d'unités et de processus fonctionnel. L'état de l'art des drives est présenté en soulignant les avancements récents sur le marché. Les modules électro-hydrostatiques sont comparés aux solutions conventionnelles et modules électromécaniques afin de présenter les avantages et les potentialités. Un regard est aussi porté sur les techniques d'asservissement plus utilisées. Le cahier de charge est décrit à travers deux cycles typiques d'injection en caoutchouc et en plastique, en mettant en évidence les limitations des modules qui pourraient gêner les accomplissements de performance exigée.

Dans le Chapitre 2, l'état de l'art de la pompe à palette est présenté et une comparaison avec les concurrents principaux est exposée. Sa conception et sa modélisation passées et actuelles sont brièvement abordées. La technologie à palette Parker est décrite à travers ses composants et son principe de fonctionnement. Dans la deuxième partie, les pertes d'énergie de la pompe, déterminées par les essais en laboratoire, qui font partie de ce travail de thèse, sont représentées en fonction de conditions de fonctionnement. Premièrement, un modèle paramétrique et ensuite un prototype virtuel sont développés pour prévoir ou reproduire les pertes d'énergie de la pompe.

Dans le Chapitre 3, l'accélération et les phases de décompression d'un cycle typique de machine à injecter sont analysées. Les paramètres fondamentaux de système, qui peuvent limiter la performance, sont identifiés et un modèle analytique est créé. Une synthèse sur l'asservissement de vitesse en boucle fermée est développée, en montrant les avantages et les limitations de la compensation feedforward. Dans la deuxième partie de chapitre, un modèle détaillé de banc d'essai est réalisé par prototypage virtuel. La comparaison est effectuée entre des mesures expérimentales, des résultats analytiques et simulés. Le prototype virtuel complet, qui est capable de prévoir l'accélération et les phases de décompression, est finalement validé.

Dans le Chapitre 4, les phénomènes de cavitation et d'aération sont pris en compte. Les effets principaux sur la pompe à palettes sont montrés et des méthodes pour les détecter sont proposées. Un modèle analytique est développé qui évalue les effets inertiels, résistifs et capacitifs de la pompe et du tuyau d'aspiration entre pompe et réservoir. Deux prototypes virtuels sont aussi construits, aux niveaux différents de détail, afin de simuler

l'évolution de la pression à l'entrée de la pompe. Cette pression représente un paramètre susceptible aux réductions causées par le développement de cavitation/aération. Le prototype virtuel est finalement validé par comparaison avec résultats expérimentaux.

Dans le Chapitre 5, l'accouplement thermo-hydraulique de la pompe à palettes est analytiquement étudié. Un modèle thermique de la pompe est ainsi développé pour évaluer les échanges de chaleur avec l'ambiance externe et le moteur électrique. L'analyse est alors améliorée en créant un prototype virtuel thermique de banc d'essais. Ce prototype simule l'évolution de la température de chaque composant du module pendant la phase d'injection statique d'une machine à injecter. Les paramètres fondamentaux de transfert thermique sont identifiés à travers la validation du prototype.

Introduction

In last 20 years the growing interest to environmental issues has turned companies policy's attention to research of more eco-friendly solutions with lower environmental impact and energy saving. Thus the energy consumption, the CO₂ and acoustic emissions have become essential requirements, in addition to functionality and productivity demands, that the industrial engineering has to take into account during conceptual and preliminary phases.

The Injection Moulding Machine (IMM) sector of is one of the industrial automation highest energy consumers and so design studies focus more and more on energy efficiency improvement.

The IMM is a cyclical machine producing manufactured articles by means a versatile process based on the ability of plastic materials to be melted, shaped and subsequently cooled. These plastics are principally made with thermoplastic and thermosetting polymers but also metals, elastomers and glasses can be used. A wide range of moulded parts can be produced, from simpler to more complex geometry, by varying dimensions and application domains (automotive, electronics, consumables, transportation, etc.).

Just to have an idea of global IMM production, a study released in 2008 estimated the annual number of IMM built around the world: just less than 20.000 in Europe while more than 30.000 in Asia, in particular in South Korea, even if the European manufacturers are considered the leaders in advanced technology. The US market is a little smaller in machinery production volume but however important [1].

A recent report published in 2011 by EUROMAP [2], showed that in last 20 years the energy consumption of IMMs has been cut by around 40 % whereas the production efficiency has been almost doubled. This is thanks to development in manufacturing technology, the greater use of electro-mechanical and electro-hydrostatic modules and energy recovery solutions. Advances in screw technology have also improved the melt quality and reduced the cycle time by shortening the injection unit size too.

The energy efficiency is not the only criterion that is taken into account to improve the machine performance. Figure 0.1 lists the principal requirements to be fulfilled for an IMM. The increase of productivity and part quality represent very important goals to be pursued by keeping low production costs. The part production cost depends on several

factors as: material utilization, machine requirements, energy consumption, cycle time, labour charge and production yields. Modularity and integration of peripheral devices into the machine promotes easy-to-use configurations and improve the machine/operator interface. In order to meet the machine's requirements, the improvements have to be made at machine unit level: injection, clamping and motion/control unit including the drive system. Also increase of material recycling, mould design optimisation in preliminary design stage (by means of rapid prototyping) and deal of ancillary equipments (for material transporting, moulded parts removal and post-machining), are others improvements which have to be taken in place [3].

The drive system plays a fundamental role in this context because it enables reducing the energy consumption, reducing the machine's cycle time for higher productivity and lowering costs while improving the part quality. The machine's cycle time has thus to be optimised through the improvement of dynamic performance, reliability and reduction of the mould changeover time [3].

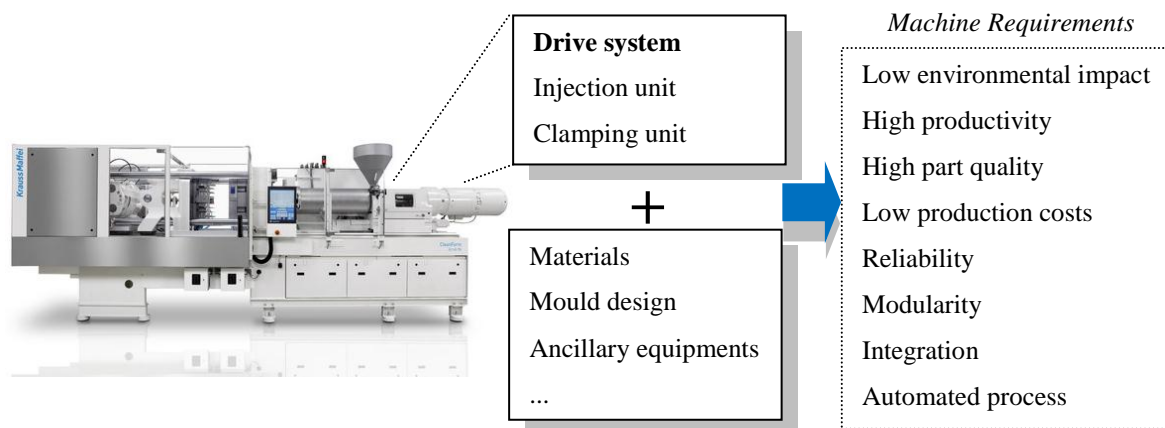


Figure 0.1 Injection moulding machine's requirements

Within the framework of environment respect and energy saving a significant improvement has been put concerning the actuation technology. Initially hydraulically-powered and valve-controlled, the actuators have been or are being replaced by electrically supplied, power-on-demand solutions, thanks to the increasing maturity of high power electronics and the progress of rare earth electric motors and their controls.

The aerospace industry is an example. In last decade it has dedicated itself to development of greener aircrafts: in the commercial transport the recent A380 and the Boeing 787 are considered the first “more electric aircrafts”. This is due to adoption of power-by-wire

actuators such as electro-hydrostatic actuators (EHAs), electro-backup hydrostatic actuators (EBHAs) and electromechanical actuators (EMAs) principally in backup mode for primary and secondary flight controls, in place of the conventional servohydraulic actuators (SHAs) [4].

The evolution trend has also affected the actuators for stationery applications, like the IMMs. In an injection moulding machine the movement of all machine axles is actuated by means of hydraulic or electric drives or combination of them (fig. 0.2). The electrical network is fed by an external power plant operated by an electricity provider.

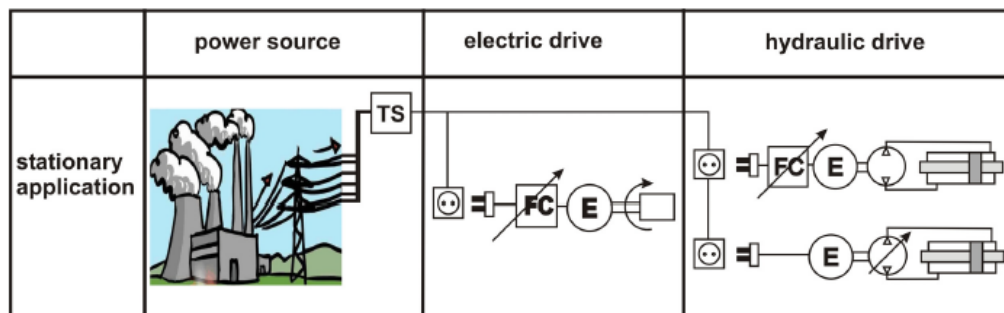


Figure 0.2 Electric and hydraulic drives in actuation systems for stationary applications, from [5]

Today the demands on IMM drive systems and control are pressing to:

- high energy efficiency,
- noise reduction,
- increase of service pressure,
- increase of velocities,
- great control precision.

This enables saving energy and lowering environmental impact, reducing cycle time, increasing the productivity, improving the parts quality and increasing the repeatability over a long period of time. Table 0.1 shows the evolution in forty years of the drive requirements for a typical 2000 kN injection moulding machine. This confirms the evolution in the drives specifications through the years.

Specification by Year	1970	1990	2010
Maximum Melt Pressure (MPa)	100	200	300
Maximum Injection Velocity (mm/sec)	80	150	400
Shot Size (cm ³)	100	100	80
Typical Power Consumption (kW)	40	25	20
Closed Loop Control	Analog	Digital PID	Digital Adaptive
Response Time (ms)	40	20	10

Table 0.1 Injection unit specifications of a 2000 kN injection moulding machine, from [3]

Recently the demand for drive solutions with higher force density has fostered the development of new electro-hydrostatic solutions (EHAs). By combining the advantages of power-by-wire (energy saving) of EMAs and the low maintenance cost of SHAs, the EHAs makes the injection molding machines more competitive than before [6]. In particular the interest concerns EHAs equipped with electro-hydrostatic modules consisting of centralized, fixed-displacement pump driven by variable-speed electric motor. End-user power transformation is made by hydraulic cylinders where mechanical motion is required on the machine. This concept can be implemented technologically by use of gear pumps, pistons pumps or vane pumps.

This dissertation aims at providing accurate virtual prototyping to quickly determine and predict the performance limits of an existing electro-hydrostatic module (EHM) for energy requirements and dynamical behaviour. Specific issues, which can occur during severe phases of an injection moulding machine's cycle, are thus dealt. They concern:

- Dynamic performance of the EHM during acceleration and depressurisation phases to reduce moulding cycle and to increase productivity,
- Cavitation/aeration phenomena in transient phases that may significantly reduce the pump lifetime,
- Rapid temperature increase during low speed / high pressure that may rapidly lead to pump jamming.

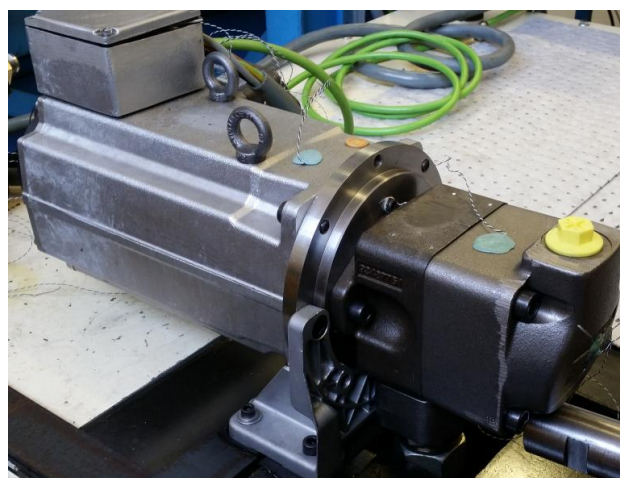


Figure 0.3 Parker EHM: NX Series servo motor and T7 Series vane pump

The integrated electro-hydrostatic module showed in figure 0.3, that associates a Parvex NX860 series AC brushless servo motor and a Parker T7 series vane pump, is thus selected and studied in this research work. Vane pump have been preferred for their good high efficiency, extremely low pressure ripple and low noise emission.

The research approach followed in the thesis is shown in figure 0.4.

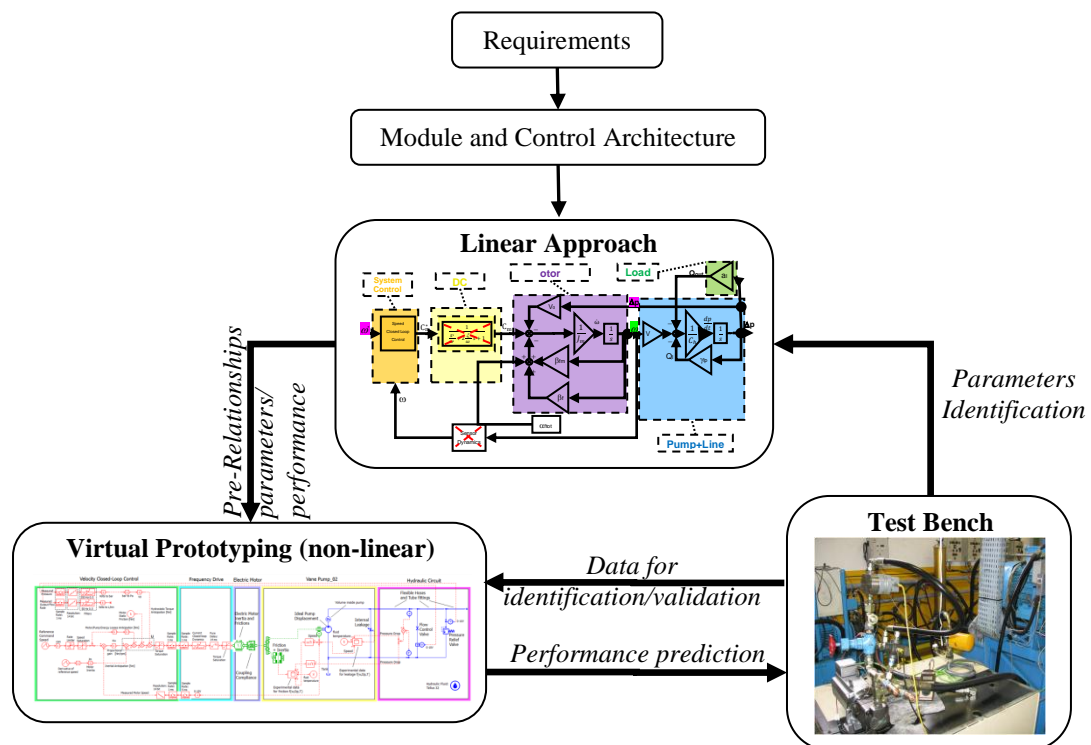


Figure 0.4 Research organization of dissertation

In **Chapter 1**, the injection moulding machine is described in terms of machine units and functional process for producing moulded articles. The state of the art in machine drives is introduced by underlying the recent market advances. The electro-hydrostatic modules are compared to conventional and electro-mechanical solutions in order to present the advantages and the potentialities. A look is also taken at the used control techniques. The drive requirements to be satisfied are listed through the description of two typical cycles of rubber and plastic injection moulding machines, by highlighting the drive limitations that could hinder the achievements of required performance.

In **Chapter 2**, the state of art of vane pump is introduced and a comparison with the principal competitors is exposed. Past and recent design and modelling studies are briefly described. The Parker vane pump technology is characterised through its components and operation principle. In second part the pump energy losses, determined by laboratory tests that are part of this thesis work, are represented as function of operating conditions. Firstly a parametric model and then a virtual prototype are developed to predict or reproduce the energy losses.

In **Chapter 3**, the acceleration and depressurisation phases of injection moulding machine's cycle are analysed. The fundamental system parameters, which can limit the performance, are identified and an analytical model is created. Synthesis of the velocity closed-loop is made by showing the advantages and limitations of feedforward compensation. In second part of chapter, a detailed model of full test bench, built in laboratory, is achieved through virtual prototyping. Comparison is carried out between experimental measurements, analytical and simulated results. The full virtual prototype is finally validated that predicts the acceleration and depressurisation phases of the moulding machines.

In **Chapter 4**, the phenomena of cavitation and aeration are taken into account. The principal effects on vane pump are showed and methods to detect them are proposed. An analytical model is developed that evaluates the inertial, resistive and capacitive effects of pump and of the inlet pipe between pump and tank. Two virtual prototypes are also built, at different accuracy levels, to simulate the time evolution of the pressure in pump inlet, being this a parameter susceptible to reductions caused by cavitation/aeration development. Finally the virtual prototype is validated by means of comparison with experimental results.

In **Chapter 5**, the thermal hydraulic coupling of the vane pump is analytically studied. A thermal model of pump is thus developed in order to evaluate the heat exchanges with the external ambiance and the electric motor. The analysis is then improved by creating a thermal virtual prototype of test bench that enables simulating the temperatures rise of each components during a typical machine's static injection phase. The fundamental heat transfer parameters are identified by validating the prototype.

In the **Conclusion**, the present work is concluded by underling the important obtained results and the future perspectives.

References

- [1] S Helduser. Development trends in electrohydraulic drives and controls. *6th International Fluid Power Conference, March 31-April 2, 2008, Dresden, Germany. Pp. 29-64.*
- [2] O. Urbanek. The “Energy Efficiency: European Plastics and Rubber Machines Well Placed” Study. *Euromap, December 1 2011. Frankfurt, Germany.*
- [3] D. O. Kazmer, R. G. Speight. Polymer Injection Molding Technology for the Next Millenium. *Journal of Injection Molding Technology, 1997. Vol. 1, pp. 81-90.*
- [4] J-C Maré. Towards more electric drives for embedded applications: (re)discovering the advantages of hydraulics. *7th International Fluid Power Conference, March 22-24, 2010, Aachen, Germany.*
- [5] H. Murrenhoff. Hydraulic Drives in Stationary Applications. *5th International Fluid Power Conference, March 20-22, 2006, Aachen, Germany. Pp 11-36.*
- [6] A Feuser. Modern electrohydraulic drive technology for stationary machinery in industrial automation. *7th International Fluid Power Conference, March 22-24, 2010, Aachen, Germany.*

Presses à Injecter et Modules

Dans ce chapitre, les machines à injecter sont caractérisées en termes d'unité d'injection, de serrage et de commande en détaillant leurs composants principaux. Le processus fonctionnel est décrit à travers la séquence des phases qui constituent le cycle typique de la machine. L'état de l'art des modules est présenté en mettant en évidence l'évolution de cette technologie depuis les années quatre-vingt jusqu'à aujourd'hui, incluant une tendance future du marché dans les cinq ans suivants. Les modules électro-hydrostatiques sont décrits et une comparaison avec les modules servo-hydrauliques et électromécaniques est effectuée en termes d'avantages contre limitations. Les techniques principales d'asservissement, mises en place dans les machines à injecter, sont adressées, y compris l'implémentation de contrôleurs feedforward. Les cahiers de charge de la machine, qui imposent les prestations aux modules, sont représentés à travers deux cycles typiques en caoutchouc et en plastique. Les limites de performance des composants, constituant le module, sont listés et le banc d'essais, qui a été conçu et assemblé dans le laboratoire Parker, est montré.

1 Injection Moulding Machines and Drives

In this chapter a general description of the injection moulding machines is addressed with focus on units composing machines and the functional process. A look on past and present drive technologies is proposed by underling the principal advantages and drawbacks of electro-hydrostatic and electro-mechanical drives. The principal control techniques used for module are overviewed and the machine's requirements are dealt with reference to two typical rubber and plastic cycles. The design limitations of the module selected for this thesis are listed. The test bench, designed in the frame of this work, assembled in Parker laboratory and used to perform the electro-hydrostatic module, is also described.

1.1 Injection Moulding Machines

The injection moulding is one the most used and developed technologies for converting thermoplastic and thermosetting materials from raw form to ready-to-use parts. It permits to produce a huge variety of articles for several application domains, from automotive products to food packaging. The versatility of process allows obtaining a lot of dimensions and geometries, from very simple to more complex ones with narrow tolerance. Figure 1.1 shows some typical custom plastic domains like bed frame hardware, drive assembly components and pharmaceutical/medical products.



Figure 1.1 Typical custom plastic parts domains, from [1]

Table 1.1 shows the basic products which can be today injection moulded by using rubber and plastic materials, even if more and more other parts can be created. Concerning the rubbers, more than 50 % of products are used for manufacture of tyres.

<i>Rubber parts¹</i>	<i>Plastic parts</i>
Manufacture of tyres	Power-tool housing
Seals, gaskets and membranes	Telephone handsets and DVDs
Tubing and hoses	Television cabinets
Shoes and shoe soles	Electrical switches
Flooring	Automotive bumpers and dash boards
Gloves, containers and protectors	Battery casings
Conveyor belting, pulleys and belts	Drug inhalation units
Bollards, bumpers and blocks	Disposable razors and syringes
Boats and equipment	Washing-up bowls
Aerospace/automotive applications	Recycling boxes
Clothing/protective/sports equipment	Bottle lids/closures

Table 1.1 Basic rubber and plastic parts

This fully automated process is seen as the foundation of highly developed manufacturing technology over the last fifty years. The first injection moulding machines occurred in the 1870's. They were used for celluloid process and were based on pressure die casting technology. In the 1920's, IMMs were produced in Germany thanks to industrial developments. Being hand operated, they were again very rudimentary. In fact, simple lever arrangement was used to clamp two-pieces moulds together. Low pressure process limited the production of thermoplastic parts. In 1930's IMMs were for first time driven by hydraulic systems which made them more efficient. The great development in large-scale occurred in 1950's especially in Germany. IMMs were based on plunger arrangements to push the material into the mould. Drawbacks were relative to lack of melt homogenisation and poor transfer properties, subsequently resolved through the introduction of injection barrel [2].

Modern IMMs have reached high maturity level thanks to development in manufacturing technology, drives evolution and control electronics. In order to better understand the

¹ Rubber products refer to information provided by [3] while plastic products refer to [4]

development through the years, a brief description of the machine units and process is proposed in next section.

1.1.1 Units Composing Machine

Typical injection moulding machines are represented in figure 1.2. The essential components consist of injection unit, clamping unit and motion and control unit. The majority of machines are horizontal built (on left-side of fig. 1.2) but other configurations with vertical clamping or injection unit are also proposed for space-saving (on right-side of figure 1.2). Machines are classified on the basis of clamping force, unit disposal and injection material volume, in accordance to technical recommendations provided by the Europe's Association for plastics and rubber machinery manufactures (Euromap) [5]. They can generate clamping forces from a few hundred kN up to 88000 kN , depending on parts size to be produced.

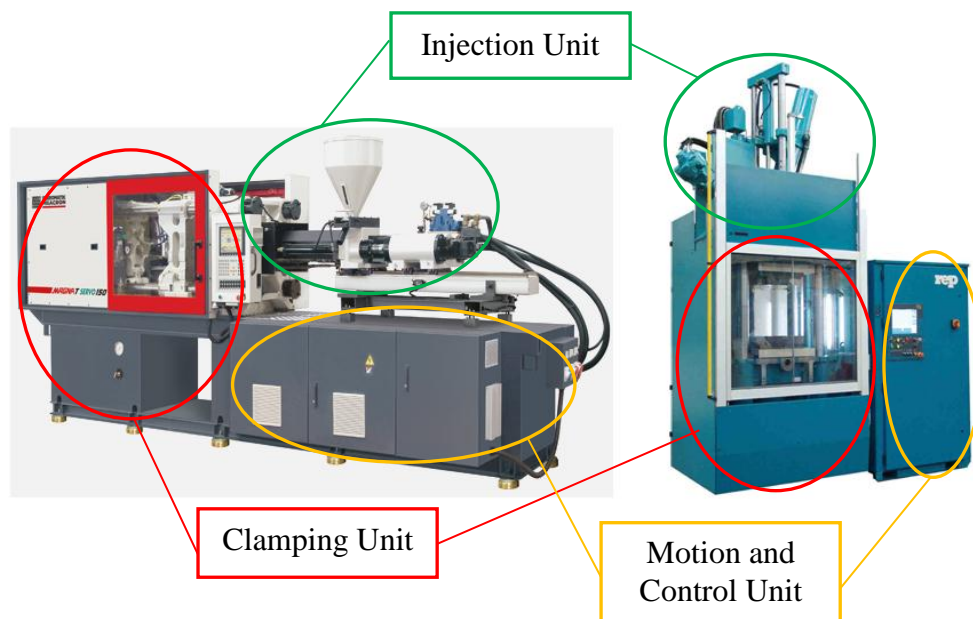


Figure 1.2 Injection Moulding Machines: Ferromatik Milacon on left-side, from [6], REP - Rubber in Motion on right-side, from [7]

The **injection unit** contains hopper, barrel, injection screw and motor (fig. 1.3). The main functions of the injection unit are to melt the moulding material and force it into the mould.

The raw material is firstly supplied through the feed hopper. Thermoplastics are usually fed in pellets form while rubbers are fed in powder or ribbon form. Then material falls into the barrel containing the helical form injection screw. The screw is directly driven by

means of an electric or hydraulic motor (fig. 1.3). The rotation of screw and its helical nature permits to draw the material towards the screw tip. Along the barrel, the material is progressively molten and homogenised thanks to heat developed by internal shears and heats transferred by ceramic resistance heaters, fitted around the barrel wall. This deals with **plasticisation** or **vulcanisation**. In the traditional configuration with reciprocating screw (schematic on the top of figure 1.3), the screw (without rotation) is also driven forward through pressure produced inside the hydraulic cylinder, acting just like a plunger [8]. The molten material is so pushed into the mould through the barrel nozzle. Other configuration known as two-stage screw (schematic on bottom of figure 1.3), is constituted by a parallel injection ram that has the function to receive the material extruded by the screw and then to inject it in the mould. The accuracy and the regularity are so improved, in this second solution, thanks to a better control of injection process temperature [9]. The temperature of the melt is generally closed-loop controlled and measured by thermocouples installed in the barrel wall. The material temperature is in fact a fundamental parameter to be controlled during the entire machine's cycle in order to guarantee the optimal thermal conditions for the final product achievement [10].

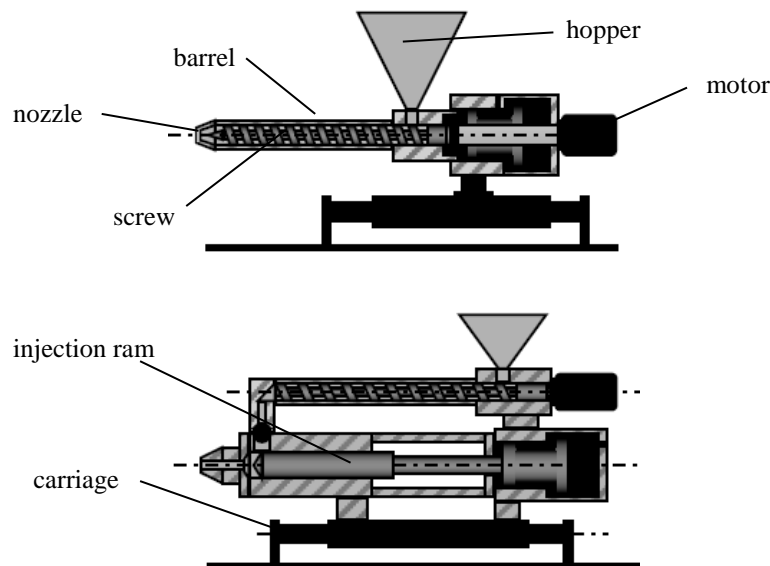


Figure 1.3 Schematic of injection unit: direct driven screw by an electric or hydraulic motor (top), unit with plasticisation screw and injection ram (bottom), from [8]

The **clamping unit** mainly consists of (fig. 1.4) mould, tie bars, movable and fixed plates, carriage arrangement, hydraulic cylinders and ejectors. The functions of the clamping unit are to keep the mould closed during the material injection, plasticisation and cooling time

and finally to eject the moulded parts. The mould determines the shape of the articles to be produced. Its design hardly influences the part quality and the manufacturing cost. It so results extremely important to use development tools, preliminary prototyping and structural analysis in order to predict and optimise the mould design in conceptual stage [11].

Several configurations of clamping unit exist which differ with regard to clamping force generating system, movable and fixed parts, ejector types and horizontal/vertical configuration. Figure 1.4 proposes a commune horizontal solution characterised by detached clamping unit with movable tie-bars and direct hydraulic actuation system for clamping force.

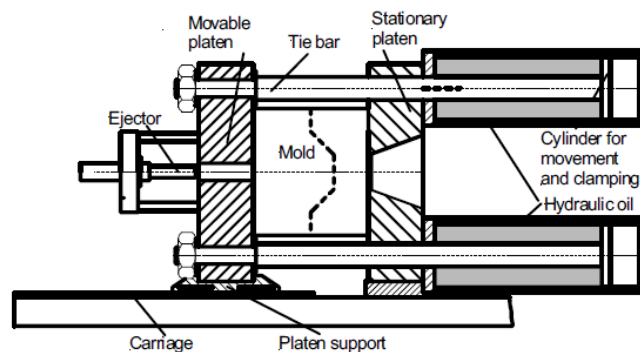


Figure 1.4 Schematic of clamping unit with Direct Hydraulic Lock, from [8]

The mould is closed within the platen arrangement and a clamping force is applied to hold the mould shut, during the melt injection through the barrel nozzle. This prevents external leakages of material over the mould. The clamping force has to be greater of the injection pressure to keep the two plates, constituting the mould, in permanent contact [2]. Several systems are available to opening/closing and locking the mould but they can be generally reunited into two types: Direct Hydraulic Lock (DHL) and Toggle Lock (TL). The DHL uses hydraulic cylinders to both move the platen and to lock the mould. In TL hydraulic pistons carry out the platen movement and a mechanical blocking arrangement, hydraulically actuated, permits to lock the mould, i.e. through pressure pads that surround the tie-bars. In both cases the functions of platen movement and mould locking are performed by different hydraulic cylinders: in fact cylinders with small surface are used for platen moving, being high speed required, while cylinders with large surface are used for generating high clamping force [12].

The **motion and control unit** represents the heart of machine. The movement of all

machine axles is actuated by means of hydraulic or electric modules or by combination of them. The module is generally constituted by an electric motor driving a hydraulic pump, or simply an electric motor with gear box when “all electric” solutions are used. The module, combined with hydraulic cylinders or linear jacks, composes the actuator which can be electro-hydrostatic or electro-mechanical. It represents the machine motion unit that operates sequentially the movement of all cylinders installed in the injection and clamping unit. Most of machines have at least five or six cylinders to be moved. The control unit consists of power electronics, sensors and controls. It receives the position, speed, torque, pressure, force and temperature signals from the machine through local transducers. It then controls them in closed-loop and it sends command signals to machine modules to operate the several machine cycle’s phases. More details of motion and control unit are provided in next sections.

The historical evolution of the IMMs has also been involved the drive and control technology that has had to develop in order to meet the new requirements imposed by market. Next paragraph describes the typical IMM functional process, useful to understand the sequencing phases to obtain moulded part.

1.1.2 IMM Functional Process

The injection moulding process is mainly constituted by seven sequential and recurrent process phases [12]:

- 1) Closing of the mould and clamping
- 2) Dynamic injection
- 3) Holding pressure phase (or static injection)
- 4) Dosing of the feedstock
- 5) Plasticisation for plastic or vulcanisation for rubber
- 6) Cooling time
- 7) Reopening of the mould and parts ejection

The cycle starts with the **mould closure**. At this stage, the nozzle is pushed against the sprue bushing of mould that represents the connection between barrel nozzle and mould.

In the barrel of injection unit the melt is already collected in front of screw tip. The **dynamic injection** is the following phase in which the melt is injected into the mould cavity thanks to the hydraulic pressure that pushes the injection ram forward. Once the mould is filled with material, the screw and the injection ram are held under pressure in forward position and a quantity of melt is collected in front of screw tip. In this way, it permits the melt in front of screw tip to enter into the mould in the case of volume contraction of the solidifying material in the mould. This phase is known as **holding pressure** or commonly **static injection**.

The solidification continues and, when the material is solidified in the connection point between mould and nozzle, the hydraulic pressure (case of hydraulic IMM) is gradually reduced up to zero in order to minimise the residual stresses in the mould. Once the solidification is terminated, the mould must be held closed for a certain period of **cooling time**. This time permits to dissipate the heat of the moulded part towards mould such that its temperature falls to a level and the part can be finally ejected without excessive distortion (**parts ejection**). Mould temperature is also controlled by means of channels for pressurised water flow. During the cooling phase, the barrel of the screw is recharged with material for the next moulding cycle (**feedstock dosage**) and the **plasticisation** occurs through screw rotation and material heating [2].

Figure 1.5 shows a typical IMM cycle for plastic parts with total time duration of 17 s and the consumed power related to each phase.

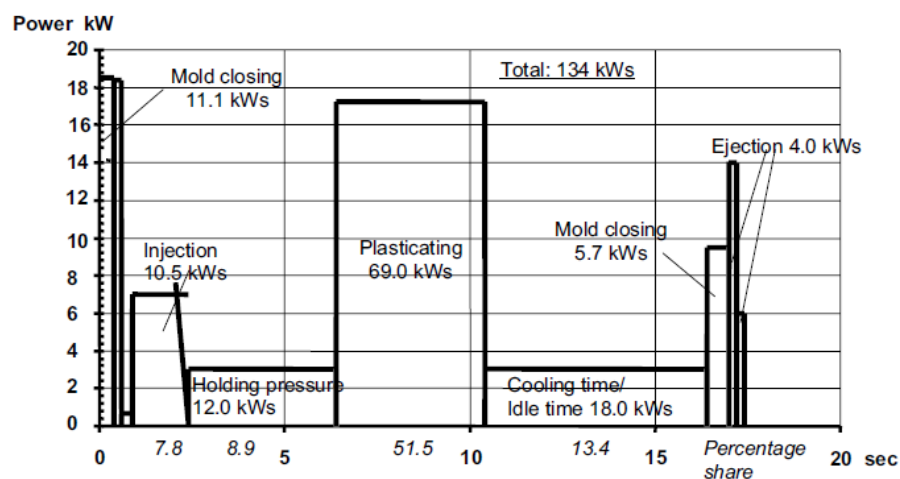


Figure 1.5 Example of IMM cycle's phases for plastic and power consumptions, from [8]

1.2 Evolution of Drive Technologies

Today there are several IMM drive concepts available on market. The demands on drive systems and control are pressing to increase service pressure, velocities and repeatability over a long period of time. This enables increasing IMM productivity while saving energy and reducing noise and maintenance costs [13]. The principal concurrent technologies are the electro-hydrostatic module (EHM) (ARP6154 SAE Standards for definition of EHM, [14]) and the electro-mechanical module (EMM). It is possible to distinguish between IMMs driven by an EHM, by some EMMs in parallel or by combination of EHM and EMM. The EHM normally represents the only drive installed in the machine. Indeed, just a power pack is sufficient to move sequentially all the cylinders. Sometimes parallel movements are permitted by means of the addition of hydraulic accumulator, as the case of ejection phase. When the EMMs are implemented in the machine, each one is responsible of the movement of a single axis, due to its specific configuration.

The graph in figure 1.6 shows the drive technology, equipping European IMMs from 1990, and the expected technologies which will be used in near future.

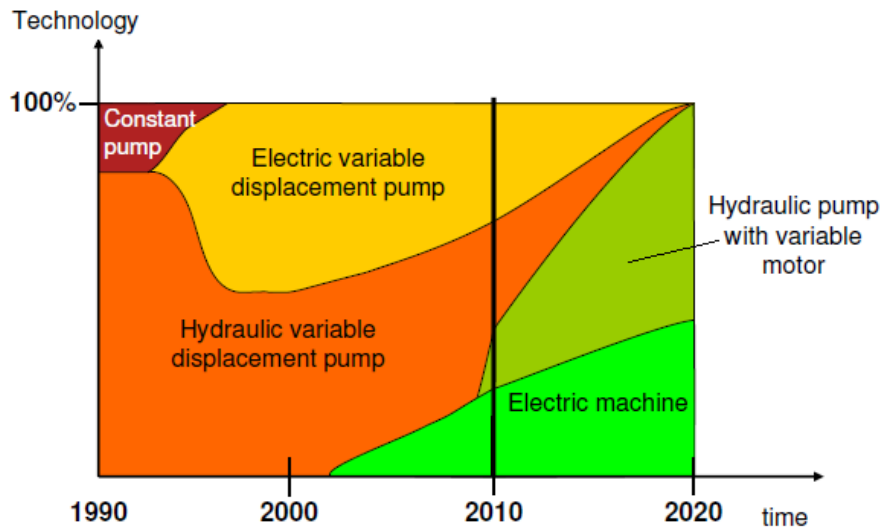


Figure 1.6 Technology shift driven by market forces in IMMs, from [15]

The estimation for 2020 predicts a balanced partition of market between electro-mechanical modules (electric machines in figure) and electro-hydrostatic modules (hydraulic pump with variable motor in figure) for little and medium IMMs (clamping forces below 4000 kN). The market of big IMMs (over 4000 kN), about the 15 % of entire population, will yet belong to electro-hydrostatic modules thanks to their higher power density [15].

In order to understand the recent competition between EHM and EMMs, it is useful to describe the evolution that has led to development of these technologies.

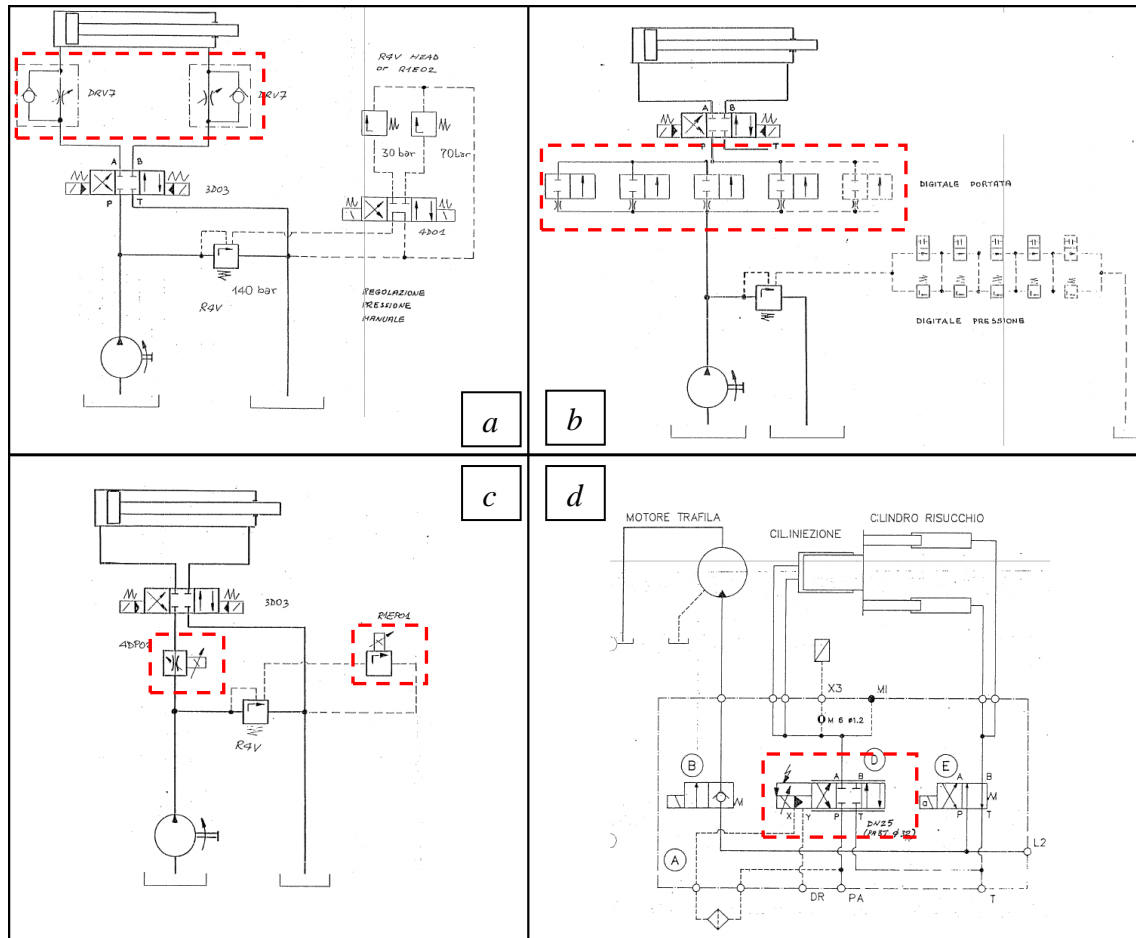


Figure 1.7 Conventional IMM drives using valves as signal-to-power interfaces: manually operated valve a), on-off valves in parallel b), valves operated by proportional solenoid c) and servo valve d)

Practice in the past was the employment of hydraulically driven IMM where the axes' control was achieved through manually operated valves, supplied at a constant pressure from a centralised hydraulic power generation (fig. 1.7a). Drives were composed by a constant-speed motor, a fixed-displacement pump and flow/throttle control valves, together with pressure control valves, which were used for open loop control's functions. These valves played the role of signal-to-power interfaces. They were soon substituted by on-off valves which were used in parallel (fig. 1.7b): the operator initially set the valves' closure positions, in a central board, to produce specific values of output flow and pressure. Load-sensitive circuits began very popular in 1980s thanks to the use of valves directly operated by solenoid for flow and pressure control (fig. 1.7c). The most important novelty however concerned innovative proportionally operated directional valves, with

load-sensing features which conferred improved dynamic response. In 1990s the servo-hydraulic modules (SHM) made their appearance by reducing the response times compared to proportional valves (fig. 1.7d). SHMs consisted of electrically signaled valves (servo valves) characterised by better accuracy but more expensive than previous. The SHMs were especially used to position or pressure closed-loop control in injection unit by means of variation of valve hydraulic resistance. Although this last solution offers real advantages, it mainly suffers from the bad efficiency of valve control over a full mission (energy was consumed for full force, pressure in excess was wasted as pressure drop at valves orifices).

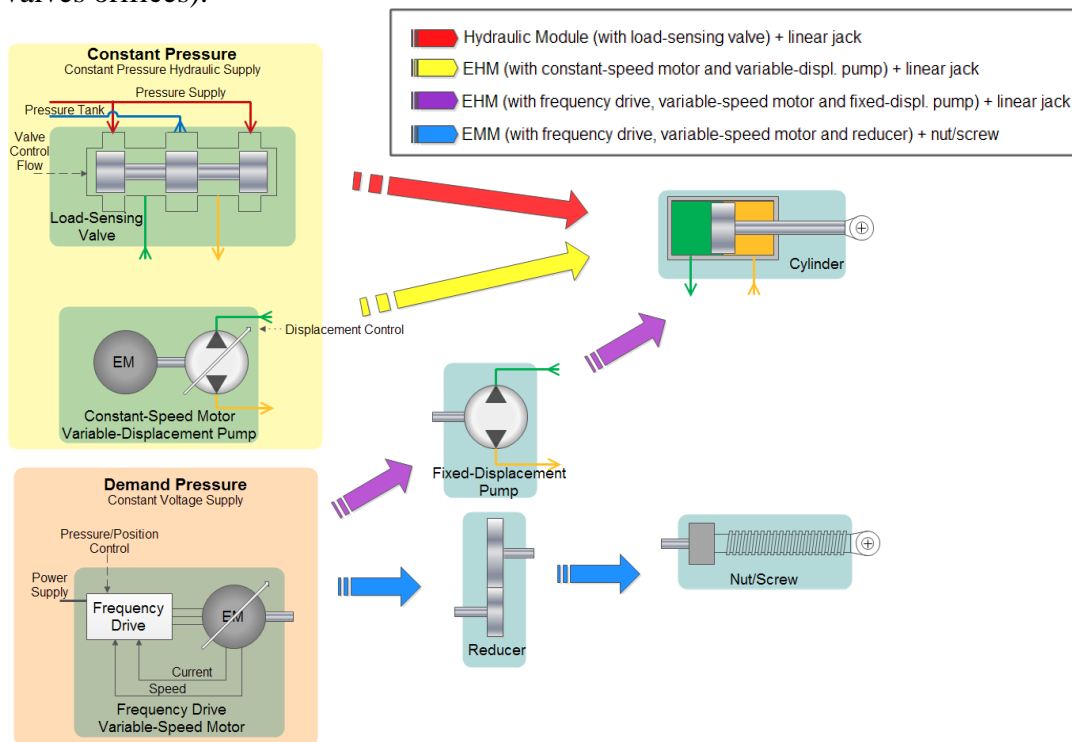


Figure 1.8 SHM, EHM and EMM concepts

The electrohydraulic drives and controls manufacturers picked up development trends in those years, already in the 1990s and during all the 2000's decade. The increasing maturity of high power electronics and the progress of rare earth electric motors and their controls permitted to replace the SHMs with new power-on-demand solutions. They were based on a constant-speed electric motor driving a variable-displacement pump which represented a favorable alternative to valve controlled drives towards reduction of energy losses, fig. 1.8 [16]. The use of pressure/flow variable displacement pump controls in fact achieved good energy efficiency, especially in utilizations with high pressure and moderate to high volume flow rates [13]. There, the variable-displacement pumps,

originally hydraulically controlled, were hence electrically controlled in closed-loop thanks to integration of digital electronics directly in a high-response valve. Figure 1.9 shows an example of variable displacement axial piston pump driven by an asynchronous electric motor. The pump swivel angle and position control loop of the valve spool and the pressure control loop are integrated in the high-response valve. It communicates with the machine control unit through field bus interface.

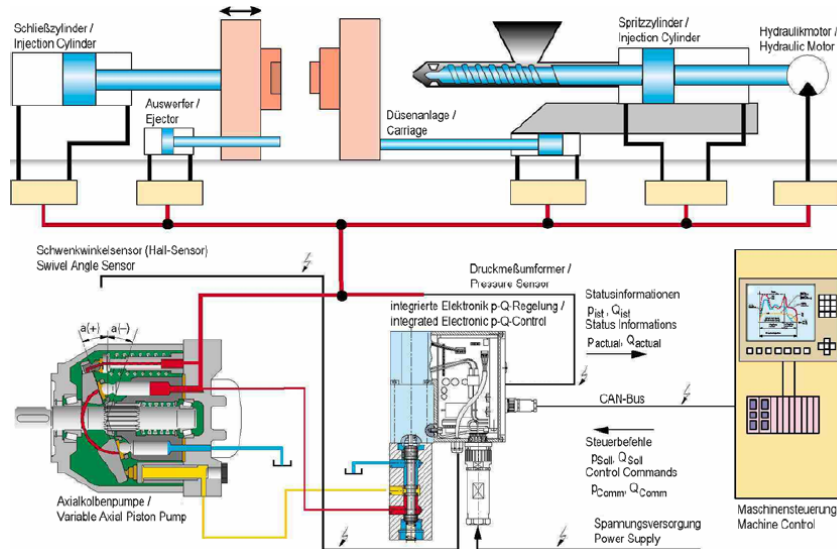


Figure 1.9 EHM concept with variable-displacement pump for IMM, from [17]

In the same years in Japan, some machine manufactures started to propose IMM driven by all-electric solutions, thanks to significant progress of EMMs in terms of availability, cost, power density, power management and energy saving. The electromechanical module EMM is typically constituted by a DC servo motor controlled by a frequency converter and driving the translating load through a mechanical power transmission device composed by gear and ball-screw (fig. 1.8).

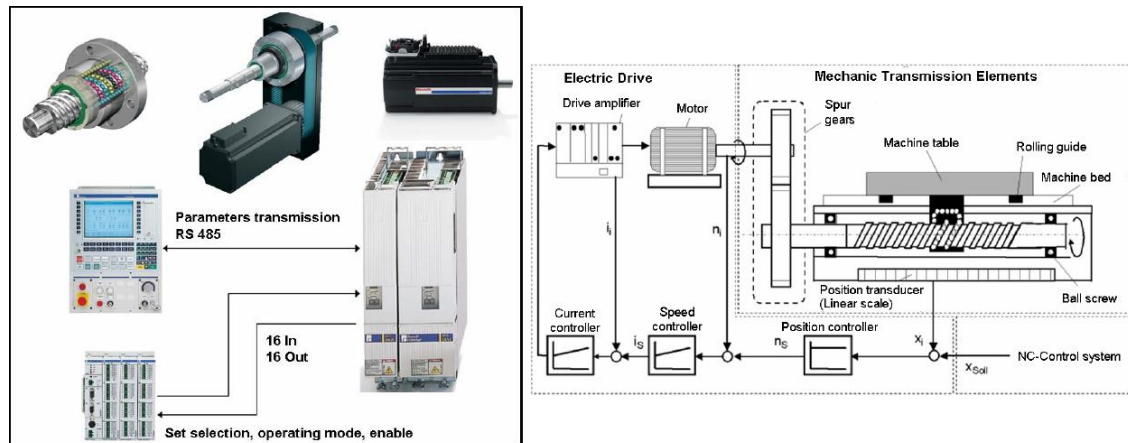


Figure 1.10 Electro-mechanical modules (left) and control loop architecture schematic (right), [17]

A simple controller in cascade is used and composed by three closed-loop control respectively on: load linear position, motor speed and motor currents (fig. 1.10). In a typical all-electric IMM, it is necessary to implement an EMM per axis.

For an average production cycle, this design could potentially save around 30% energy compared with the most efficient hydraulically driven IMM due to improved efficiency of EMMs. Shorter cycle time and higher accuracy are obtained with simpler control [18]. The drawbacks of this technology mainly concerns cost (about 20-30% higher than comparable hydraulically driven IMMs, [16]), low capability to dispose the heat generated by the energy losses, high kinetic energy of rotating parts and low tolerance to jamming of mechanical components. This last fault involves a frequent need of maintenance and further cost increase: replacing rolling elements (nut-screws, bearings, etc.) in heavy duty machines is much more expensive than replacing hydraulic seals [19].

Recently the demand for drive solutions with higher force density has again pushed to the fore the electro-hydrostatic solution. In particular the interest concerns the EHMs concept of speed-controlled fixed-displacement pump driven by a variable-speed synchronous servo motor with its inverter (fig. 1.8). The motor works in closed-loop speed control and the line pressure (or cylinder piston position or load force) is also closed-loop controlled. The motor currents are also controlled through an inner closed-loop. By combining the advantages of electric-mechanical (energy saving) and hydraulics (fluid as a heat conveyor) without requiring a motor power drive per axis, this design makes the IMM more competitive than before [20]. Compared with variable-displacement pump driven by constant-speed motor, it reveals its advantages of drastic reduction of energy consumption, especially in processes characterized by long phases with no or little oil flow [18]. Therefore, it appears as the principal competitor of EMMs when accuracy, reliability, flexibility and noise are considered. In particular, maintenance costs are significantly cut as it is cheaper to replace hydraulic seals than ball-screws and bearings.

Several other configurations of EHMs exists today: combination of an asynchronous motor or synchronous servo motor driving fixed-displacement pump (vane, internal gear, external gear, radial piston pump etc.) or variable-displacement pump (i.e. axial piston pump) (fig. 1.11). In this context an EHM constituted by a permanent magnet synchronous motor driving a fixed-displacement vane pump is analysed and performed.

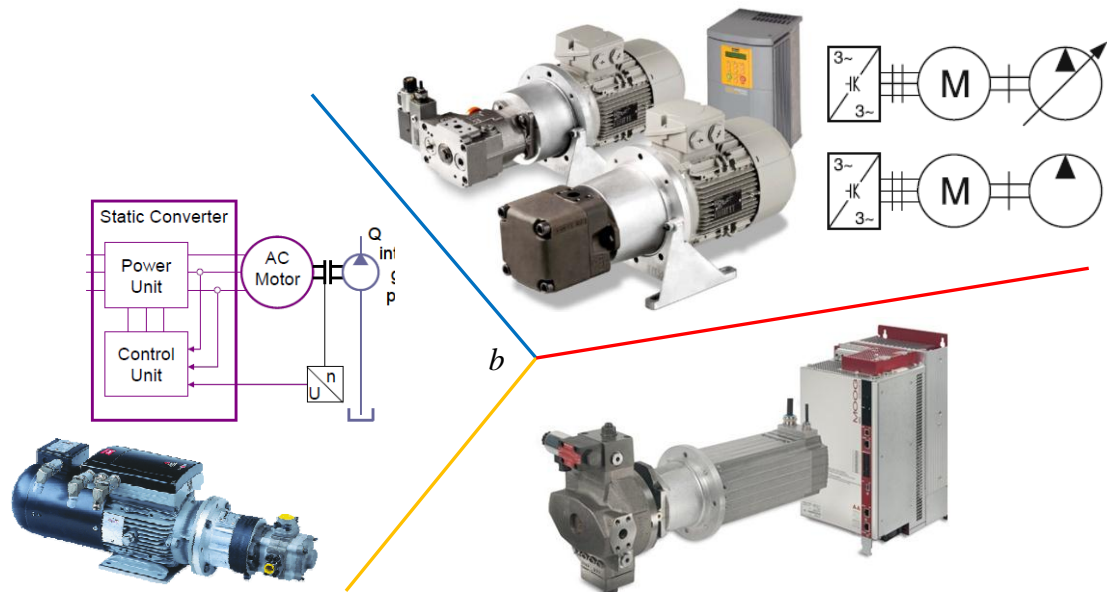


Figure 1.11 Examples of some EHM available on market: asynchronous motor with variable-displacement axial piston or fixed-displacement vane pump, Parker, from [21], a) asynchronous motor with fixed-displacement internal gear pump, Voith, from [22], b) synchronous servo motor with fixed-displacement radial piston pump, Moog, from [23], c)

1.2.1 Advantages of Electro-Hydrostatic Modules

Several experimental comparisons were carried out, in the recent past, between some EHM concepts in typical stationery machinery. In particular EHM with speed-controlled fixed-displacement pump was compared to other existing solutions: conventional SHM, EMM and EHM with variable-displacement pumps driven by constant-speed motor. [24] investigated the efficiency and the noise level of two EHMs configurations: speed-controlled fixed-displacement pumps and variable-displacement pumps. It was demonstrated the superiority of first one for both partial (50 bar) and full load (200 bar) of clamping force. The lower noise emission was also observed, included the total noise elimination, during the breaks of machine, due to switch off option of the variable-speed motor driving the fixed-displacement pumps. [25] compared the total efficiency of three EHMs (fig. 1.12): variable-displacement pump with constant-speed motor (asynchronous motor), variable-displacement pump combined with a variable-speed motor (asynchronous motor) and a speed-controlled fixed-displacement pump (AC servo motor). The pumps tested were variable- and fixed-displacement radial piston pumps.

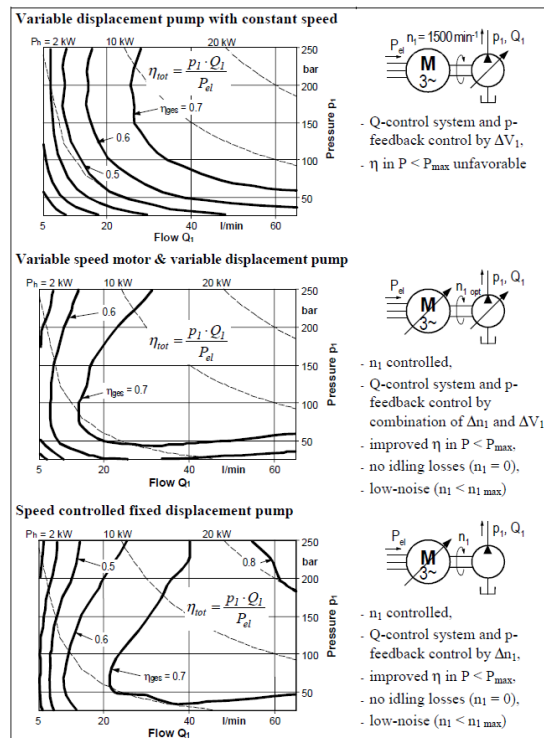


Figure 1.12 Efficiency comparison of three EHMs, from [16]

It was proved that, when there is no requested pressure and flow, the variable-displacement pump with constant-speed (up in fig. 1.12) consumes more energy than the others. The speed-controlled fixed-displacement pump (bottom in fig. 1.12) is especially suitable for drive tasks in partial and full load conditions with medium/high flow rate. The advantage of this solution is also the high dynamic performance that it can produce thanks to the AC servo motor. The variable-displacement pump combined with variable-speed motor shows good energy efficiency in the whole extent but it hardly achieves high dynamic requirements [13].

Another test performed in 2008 investigated the energy consumption of drives installed in a typical IMM. Two different plastic parts were selected which differed in volume and geometry: a switch (16 mould cavities) and a small gear (one mould cavity). Five drives were performed: three all hydraulic (2 SHM or 1 EHM), one hybrid and one EMM. Figure 1.13 shows the comparison of normalized energy consumption during IMM’s cycle. The machine 4, driven by an EHM, demonstrates the competitiveness of EHM when compared to EMMs (machine 5 in fig. 1.13). The machine 2 and 3 driven by conventional SHM need major energy to run. The hybrid machine 1 is the worst for energetic consumption but it offers high speed capability, by means of the accumulator, especially useful for

producing thin-walled parts. The drawback of heat generation of EMMs is also observed compared to hydraulic modules.

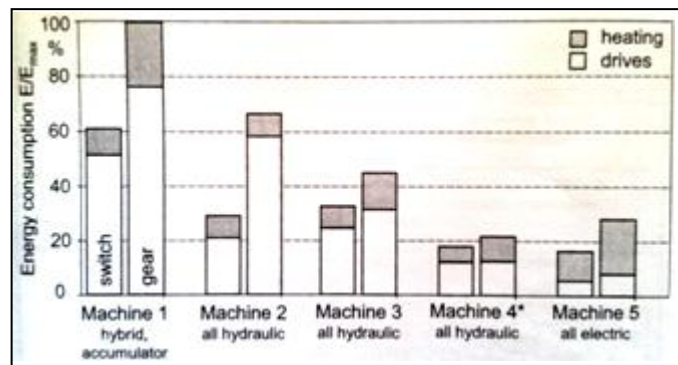


Figure 1.13 Normalised energy consumption of two moulded parts: switch and gear. Comparison between several drive technology in a IMM, from [13]

The superiority of the more recent EHM on conventional SHMs has thus been confirmed in terms of: energy efficiency, noise level, and dynamical response capability. In the last years other efforts have been making which promote the installation of EHMs. It concerns the: drive decentralisation, function integration and modular design. The integration of the digital electronic control assemblies and digital interfaces into hydraulic components takes benefits by creating a decentralised control structure: the machine controller communicates via fieldbus network with the drive electronics with typical delivery times less than 10 ms. It so permits user-friendly integration of EHMs in the control structure of machine. It makes the system more flexible as regards modifications and extensions. It also facilitates the combination of EHMs and EMMs in the same machine for a “hybrid” solution. As the EMMs, also the EHMs have to fulfil safety requirements, like to prevent unexpected start-ups, to bring dangerous motion to a halt in time and reliable setting of defined maximum speeds. Safety-integrated solutions are so proposed by using subordinate equipments like switching valves with closed-loop control.

Special recent customer’s needs for EHMs concern minimised installation space and costs, low noise level and reduction of external leakages. These requirements have been increasing the development of “ease of use” and compact solutions. Compact power units with function integration are provided which reduce the tank size and the pipes length, minimise the tube fittings, seals and the interfacing issues [13]. Some drawbacks make these solutions again to be investigated and tested. Just thinking to the thermal issues due to heat generation during operation: the heat transfer by the hydraulic oil is hardly reduced

due to small tank [26]. The objective is to compete with the EMMs in applications demanding powers lower than 10 kW thanks to their drive cost reduction.

Table 1.2 summarises the principal advantages and disadvantages of SHM, EHM and EMM.

<i>Aspects</i>	SHM	EHM	EMM
<i>Power modulation principle</i>	Full force demand and speed on demand (valve control)	Power-on-demand (for speed control)	Power-on-demand
<i>Power density (module)</i>	High	High	Medium due to power electronics
<i>Energy efficiency</i>	Low	Medium/High	High
<i>Dynamics</i>	High (good servo valve response, lower reflected inertia)	Medium (huge rotary inertia reflected from motor to cylinder)	Medium (huge rotary inertia reflected from motor to jack)
<i>Stiffness</i>	Medium (fluid compressibility)	Medium (fluid compressibility)	Medium (backlash and lost motion)
<i>Easiness of control</i>	Medium (non-linear)	Medium (non-linear)	Easy (control in cascade)
<i>Heat rejection</i>	Easy through the fluid	Easy through the fluid	Hard
<i>Compactness</i>	Medium	Medium	High
<i>Maintenance time</i>	High (bleeding, filtration)	Medium (some hydraulic components involved)	Low (more easily for electrics)
<i>Cost</i>	Low	Medium	High
<i>Noise level</i>	Medium	Low	Low
<i>Environment friendless</i>	Bad (pollution due to hydraulic leakages)	Medium	Good
<i>N^o necessary for IMM motion</i>	At least one power pack	At least one power pack	More than one power pack (1 EMM per axis)

Table 1.2 Comparison between: SHMs, EHMs and EMMs

The comparison especially concerns modules installed in stationery machineries (IMMs, presses, die casting, etc.) but the results can be rapidly generalised to mobile applications, like in aircrafts (flight control system, landing gears) [19], oil & gas equipments (turbines) [27], wind turbines (pitch control system), refuse trucks and construction equipment machines (excavator, loaders, etc.). It is remarkable the advances of the EHM's compared

to conventional SHMs when energy consumption, maintenance facility and environmental impact (contamination and noise level) are analysed. The advantages of noise reduction are mainly notable when little or no flow is requested because the motor speed is adapted to required flow [18].

The EMMs are slightly better than EHM's thanks to energy saving, shorter maintenance time, compactness and environmental cleanliness. The fluid maintenance is thus not necessary but the fluid-cooled high performance machines increases the investment and operating cost. They unfortunately appear more expensive, more sensitive to thermal issues and incapable to generate the same forces than the EHM's.

1.2.2 Control Techniques in EHM's

The quality of the moulded parts, and also the productivity, depend hardly on process variables which are the melt pressure and temperature inside nozzle and in the mould cavity (fig. 1.14). It is thus fundamental to control these variables during each cycle's phases to guarantee final accuracy and precision.

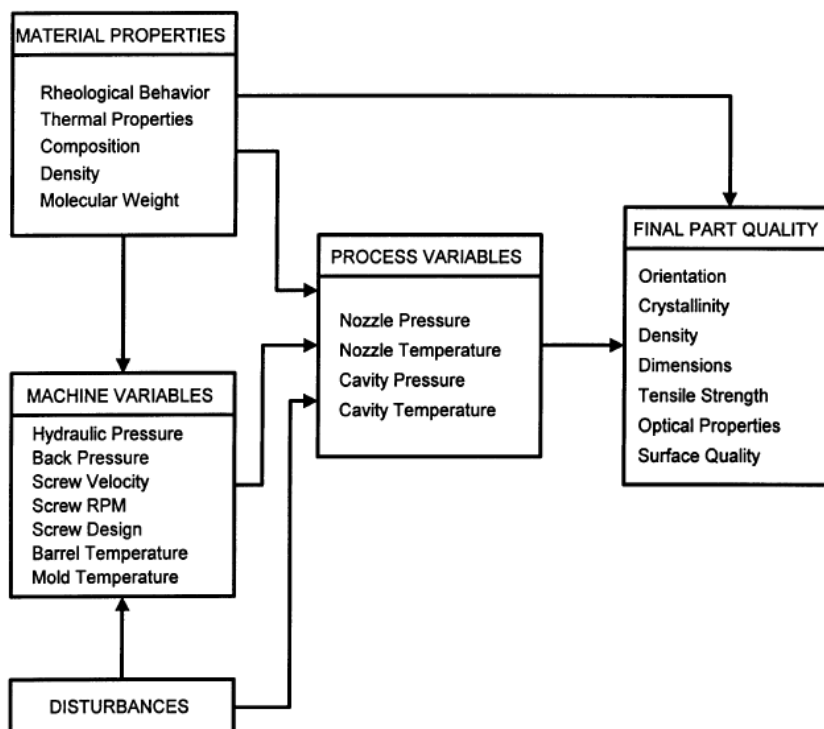


Figure 1.14 Relationships among: machine and process variables, final part quality and material properties, from [28]

The majority of IMMs traditionally uses to control other variables, defined as “machine variables”. The machine variables are principally (fig. 1.14):

- Hydraulic pressure that pushes forward the injection ram and all the other hydraulic cylinders composing the machine’s axles
- Velocity (or position) of cylinder rods
- Temperature of the barrel and outside the mould

The explanation of controlling machine variables lies in the fact that it results simpler (easier sensor installation), cheaper, safer (for possible damage that moulded parts could undergone caused by sensors installation) and more direct. It is important to remark that the machine variables control is effectively more direct that the process variables control. In fact the hydraulic pressure can be controlled in closed-loop by action on pump speed and motor torque. The time evolution of melt pressure in mould cavity is instead a consequence of the time evolution of the hydraulic pressure pushing the injection ram. For controlling the melt pressure is so necessary to know the existing correspondence between it and the hydraulic pressure. Unfortunately the pressure, produced in mould cavity, rarely corresponds to hydraulic pressure in the injection ram (fig. 1.15) and it also depends on several other factors.

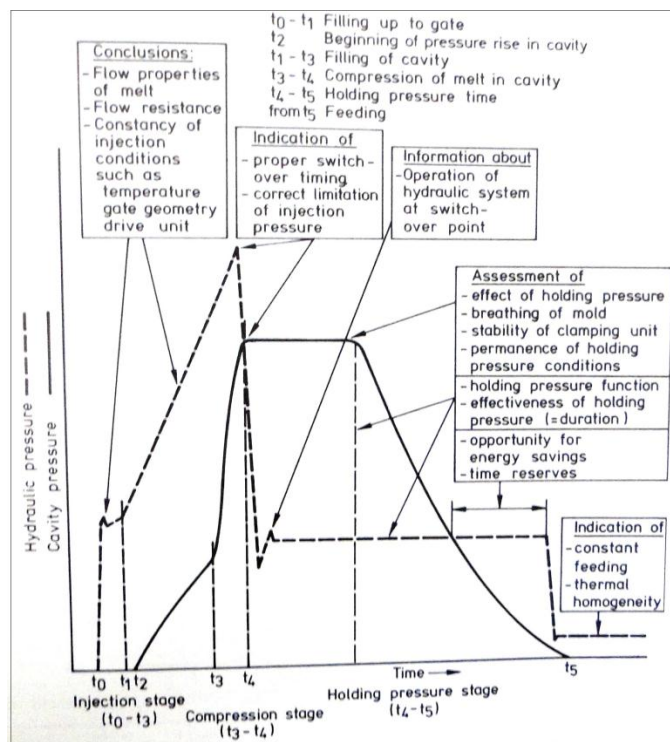


Figure 1.15 Time evolution of cavity and hydraulic pressure during dynamic and static injection, from [8]

For example, process variables, and also the machine variables, are influenced by the material properties (density, molecular weight, etc.) and “disturbances” dependent on machine like pump/valve leakages, voltage fluctuation and electrical noise [29]. The size of the parts to be moulded also plays a role on time evolution of pressure and temperature in mould cavity. In addition, the hydraulic fluid represents another very influencing factor. When it is exposed to forces, it acts like a spring with limited stiffness, due to compressibility, and makes the behaviour strongly non-linear. These are the reasons because it is finally difficult to control the process and to obtain products which meet the customer’s needs.

Experimental tests and process variables recordings permit to gain experience on the relationships between process and machine variables. In this way, sets of reference drive commands are identified for producing several types of moulded articles. Recently new sensors technologies have been installing which promote the measurements of temperature and pressure directly into the nozzle and in the mould. These are “non-invasive” and consist of optical, ultrasonic and infrared typologies which enable to characterise in real time the process variables [11].

The machine variables are conventionally closed-loop controlled since the 1970’s. A typical control electronic unit performs three closed-loops in cascade (fig. 1.16). The more external loop concerns either the cylinder rod position (or velocity) or the hydraulic pressure. The motor power unit operates in closed-loop on motor shaft speed and an inner closed-loop motor torque control. The external position/pressure controller with P, PI or PID components provides the command for the motor speed control loop generally characterized by PI components. The last one forms then the input for the motor torque PID type loop [20], [22]. Special function manages the switch over from rod position to hydraulic pressure depending on working point of machine’s cycle [18].

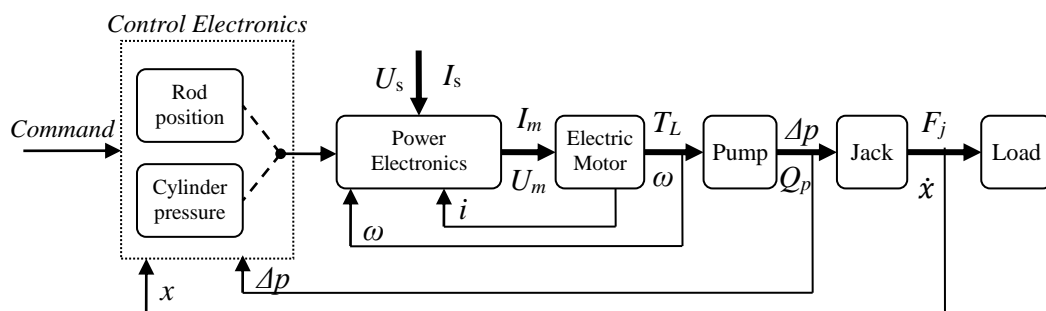


Figure 1.16 Schematic of a typical closed-loop controller of EHM

In order to improve the dynamic performance of the feedback controllers, in 1980's decade more detailed feedback control algorithms were developed. Adaptive controllers were then investigated, i.e. for the control of ram velocity during the dynamic injection [30]. Adaptive and self-tuning controllers have the advantage of on-line identification of system parameters and they accommodate changing process dynamics in order to follow the set command profiles [11]. Early in 1990's the use of feedforward algorithms was investigated [31]. Thanks to highly repeating sequences featuring the typical machine process, the IMMs are suitable to be controlled by using feedforward compensations. Position control loops are often supported by dynamic feedforward control, acting in parallel to feedback controller. It permits to enhance the tracking control performance by means of compensation of load disturbance in accordance to load size and direction. Finally reduction of cycle time can be achieved thanks to dynamic machine performance optimisation, like described for the opening/closing times of a clamping unit in [32] and [33]. The feedforward structure is faster and more effective than a closed-loop structure because it is not limited by stability issues. It doesn't affect the closed-loop system stability because the action of anticipation is robust as far as the anticipated effect is well modelled [34].

Iterative learning control (ILC) is today very common in the IMMs. Initially developed and implemented in robotics, this control is very suitable for all the repetitive processes, especially when non-linear and time-variant characteristics influence the machine dynamics. It represents an offline control which stores in memory the past control information. It uses the error between the desired trajectory and the measured signal of the previous cycle to calculate a feedforward signal for next cycle. It is updated in a point-to-point fashion and it constitutes a closed-loop control over the cycles (fig. 1.17).

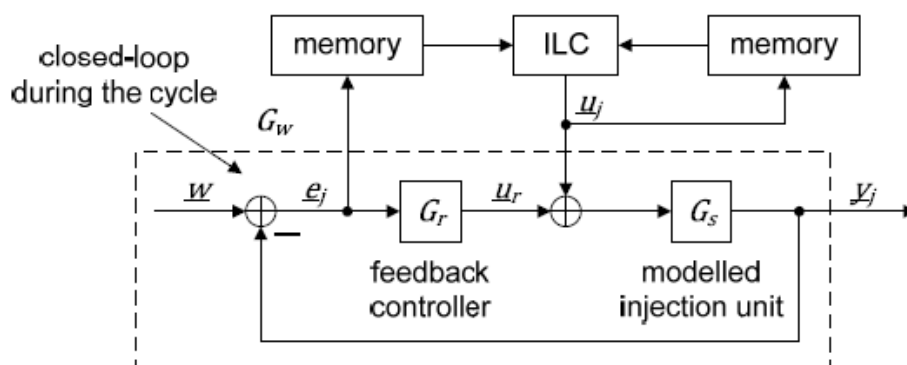


Figure 1.17 Block diagram of ILC algorithm, from [35]

Improvements of typical dynamic and static injection phases are obtained by ILC implementation [31]. By using ILC strategy, minimal pressure overshoot is also achieved by smooth switching between the two phases for guaranteeing high product quality [35].

All the entire cycle of machine is important for obtaining final good part quality but the phases, which more importantly influence part characteristics and have to be perfectly controlled, are the dynamic and static injection.

During dynamic injection, the melt is sent into the mould through the boost coming from the injection ram under hydraulic pressure. In this phase, it is fundamental to control the ram motion versus its linear velocity or position. This phase primarily affects the appearance of moulded parts. Recent habit is to increase the pressure of melt filling the barrel, by regulating the ram motion trajectory or velocity. The increase of pressure causes an increase of the melt temperature that earlier reaches the final temperature. The goal is so to reduce the total cycle duration by reducing material heating time. The drawback is the excessive surface degradation, due to too high material internal shears generated during the under pressure, and consequence reduction of part lifetime [10].

The static injection is more important to be controlled because it affects the part dimensions and weights caused by flaws like shrinkages and voids. The hydraulic pressure has to be hold for a certain time duration depending from article dimensions and material types. The plastics need rapid static injection phases which last some seconds. The parts in rubber need longer static injection phases, generally of some minutes, due to temperature requirements of the vulcanisation process.

1.3 Requirements and Limitations

In order to design the Parker electro-hydrostatic module and to verify its capability in fulfilling the machine's requirements, two typical cycles of rubber and plastic IMM are considered. Figure 1.18 shows a general sequence of all phases composing the IMM's cycle. Table 1.3 summarises the required performance respectively for a rubber and a plastic IMM, with reference to phases numeration of fig. 1.18.

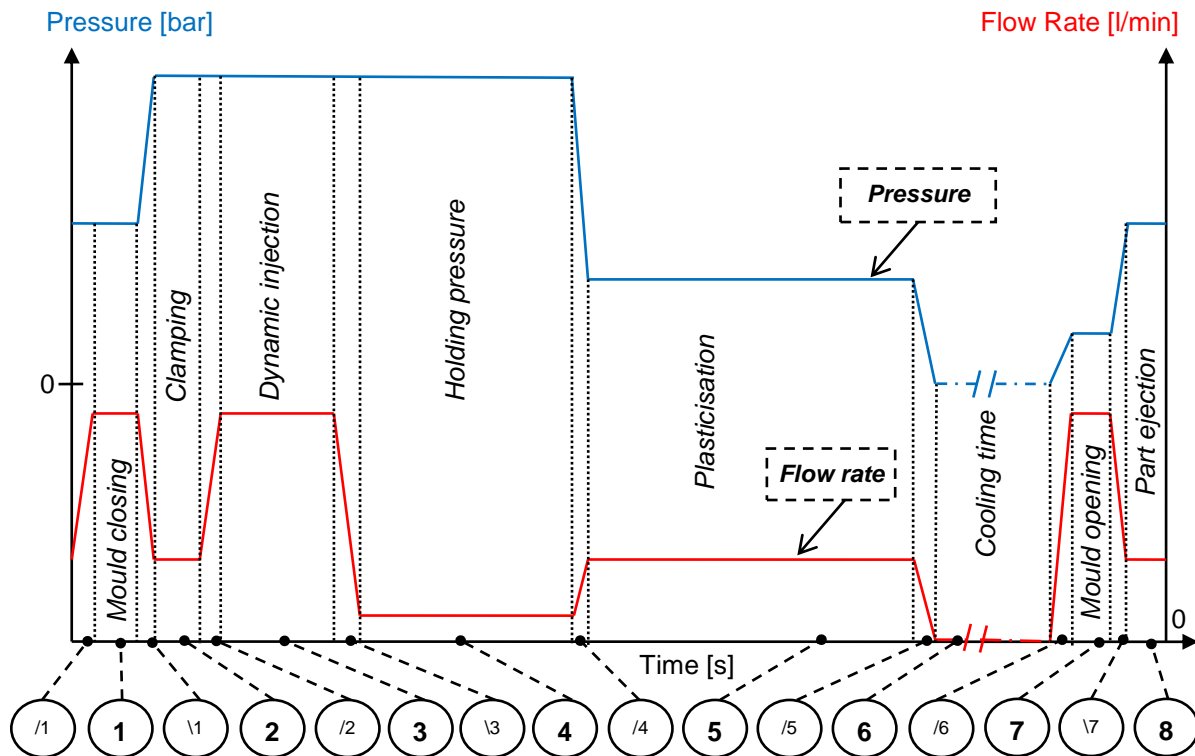


Figure 1.18 Injection Moulding Machine's cycle

It is remarkable that the rubber cycle is much longer than the plastic cycle, principally due to duration of: dynamic, static injection and cooling time phases. In detail, the rubber cycle lasts 211 s while the plastic cycle lasts only 30,5 s.

Other difference concerns the maximum cylinder pressure required during the process: 250 bar for rubber and only 155 bar for plastic. The output flow rate reaches the maximum value of 67,5 l/min for: mould closing, opening and dynamic injection in the rubber cycle. The maximum required for plastic corresponds to 63 l/min during the dynamic injection.

The holding pressure has to be performed at the minimum value of output flow rate for energy saving requirements. The minimum output flow rate depends on EHM capability

of generating the required line pressure by reducing its rotational speed as far as possible. Possible limitations are both mechanical and thermal which could damage the components and reduce their lifetime (more details are provided in the chapter 5).

The cooling time is a phase of variable time duration that hardly depends on geometry and dimension of the moulded parts. It greatly influences the total cycle time. Possible reduction of this phase is the increase of the melt temperature before filling the mould cavity in order to reach earlier the final value, like described in the last paragraph.

Concerning all the transient phases of acceleration and deceleration, customers do not require specific performance to be satisfied. In general these transients must last less than 50 ms to reduce the total cycle time. Cavitation and aeration phenomena influence the dynamic performance of EHM.

Cycle's Phases		Cylinder Pressure [bar]	Output Flow Rate [l/min]	Motor Speed [rpm]	Time Duration [s]	Pressure Variation [bar]	Speed Variation [rpm]
/1	Acceleration	-	-	-	< 0,05	210/110	3000/2100
1	Mould Closing	210/110	67,5/47,25	3000/2100	3/0,6	-	-
\1	Deceleration	-	-	-	< 0,05	40/30	1500/600
2	Clamping	250/140	33,75	1500	4/0,3	-	-
/2	Acceleration	-	-	-	< 0,05	0/15	1500/1300
3	Dynamic Injection	250/155	67,5/63	3000/2800	35/1,5	-	-
\3	Deceleration	-	-	-	< 0,05	0/20	> 2500/2300
4	Holding pressure	250/125	min	min	60/20	-	-
/4	Acceleration	-	-	-	< 0,05	120/20	> 1000/2200
5	Vulcanisation	130/105	33,75/60,75	1500/2700	105/6,5	-	-
\5	Deceleration	-	-	-	< 0,05	130/105	1500/2700
6	Cooling Time	0	0	0	?	-	-
/6	Acceleration	-	-	-	< 0,05	105/110	3000/1500
7	Mould Opening	105/110	67,5/33,75	3000/1500	2/0,6	-	-
\7	Deceleration	-	-	-	< 0,05	105/60	1500/300
8	Part Ejection	210/50	33,75/20,25	1500/1200	2/1	-	-

Table 1.3 Reference cycle of a rubber/plastic IMM

The energy losses of electric motor and pump play a fundamental role in the determination of EHM performance. In particular the internal leakages and the frictional torques of the vane pump have to be taken into account both in the transients and in the steady-state

phases. EHM performance limitations are thus affected by pump energy losses and an accurate analysis has to be carried out to define these dependences.

In addition to energy losses, it is useful to list the principal design limits of the EHM. A bottom-up approach is chosen for this purpose by identifying the performance limits of each individual component, that constitutes the EHM, and by determining the limitations of the complete EHM. On the basis of this procedure, the performance limits of electric motor, pump and inverter are as follows:

- Maximum transient electric motor torque @ 3000 rpm = 137 Nm
- Maximum output transient pressure produced by the vane pump = 300 bar
- Sampler time in the inverter input ports = 1 and 5 ms (one port at 1 ms and all the rests at 5 ms)
- Sampler time in the inverter output ports = 5 ms
- Inverter internal pure delay \cong 14 ms

The maximum transient electric motor torque mainly influences the dynamic performance, in particular the acceleration transient. The maximum output transient pressure produced by the vane pump normally does not represent a limitation for the IMM's cycles which are considered in this context. The inverter ports sampler times and the pure delay slowdowns the transfer of the command and feedback signals to test bench and to external control system.

1.4 Test Bench

In the frame of this thesis we conceived, designed and assembled, in Parker laboratory, a test bench for performing the EHM. The figure 1.19 shows a schematic of the complete test bench. It is possible to observe the module connected to hydraulic circuit on the right and a control system on the left. The components are:

- Servo motor NX860WAF
- Vane pump T7ASW E22
- Flow control valve
- Pressure relief valve
- Flexible hose
- Heat exchange
- Tank
- Flow meter, pressure sensors and thermocouples
- Control station
- Inverter SSD AC890SD

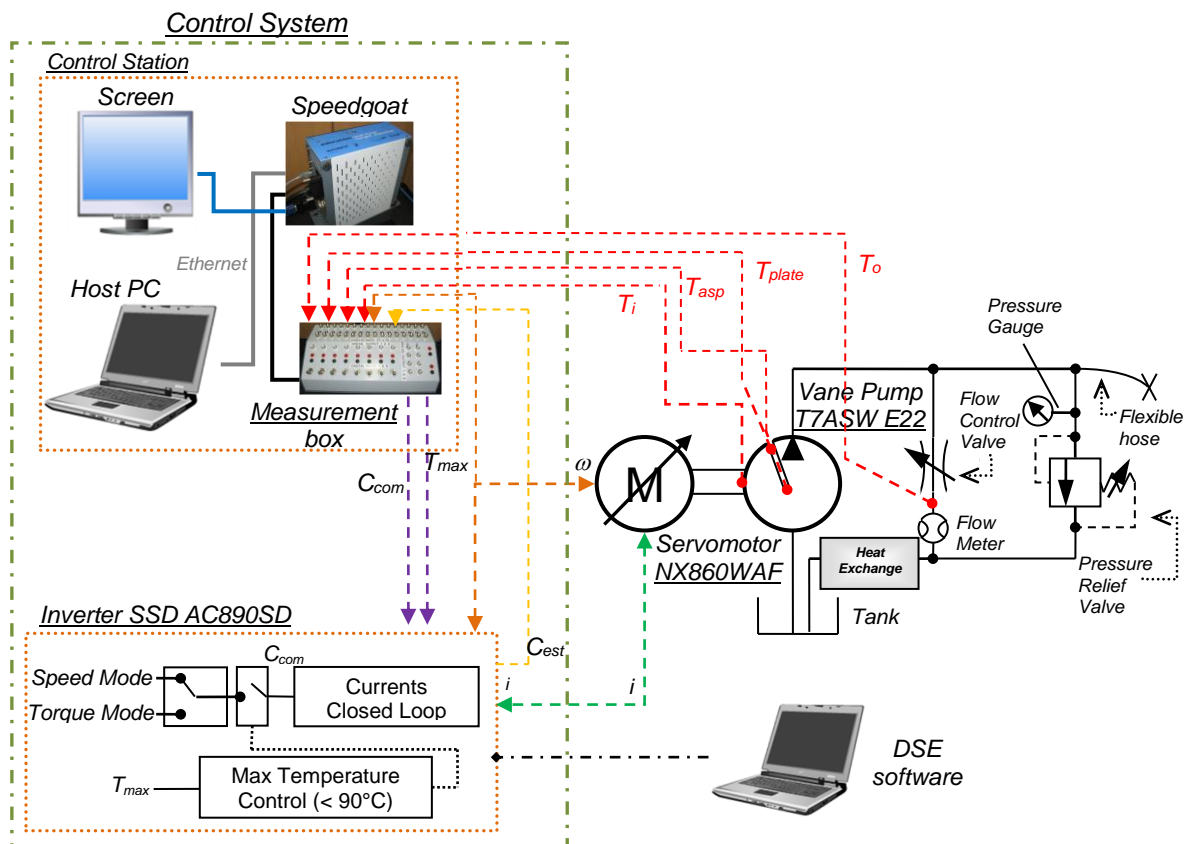


Figure 1.19 Schematic of the test bench built in laboratory

The characteristics of the components are provided in Appendix A.

The flow control valve has the function of generating the hydraulic load while the pressure relief valve limits the maximum line pressure. The flexible hose increases the full hydraulic capacity of the circuit and reproduces similar characteristics of long hydraulic lines occurring in typical IMMs.

The complete control system of test bench is constituted by the control station and the inverter. The control station is used to achieve outer closed-loop controls which suit to specific needs of simulation in the frame of this work. The command signals are thus generated in the control station and then sent to inverter that just operates the currents inner closed-loop control, in accordance with the schematic of figure 1.16. This type of approach so makes easy and quick the control prototyping thanks to its versatility in testing several control solutions without modification of the inverter's software. Next step should concern the direct implementation of the best control solution in the inverter but it does not form part of this research work.

In detail, the control station is constituted by: measurement box, host PC, Speedgoat target machine and a screen.

- **Measurement box**

The measurement box receives and sends analogical signals from/to the test bench communicating with inverter and control station. The inputs are:

- T_i , pump inlet temperature
- T_{asp} , pump suction temperature
- T_{plate} , pump plate temperature
- T_o , pump output temperature
- T_{p-body} , pump body temperature
- T_{m-body} , motor body temperature
- p , hydraulic line pressure
- p_{in} , pressure in pump inlet
- Q_{out} , output flow rate
- C_{est} , estimated torque
- ω , motor speed

The outputs are:

- C_{com} , command torque
- T_{max} , maximum temperature

T_{max} represents the highest reached temperature between all the recorded ones, excluded T_{m-body} that is controlled by inverter. The temperatures, pressures and flow rate are sent by sensors installed in the test bench while C_{est} and ω are measured by the inverter that then sends them to measurement box. C_{com} and T_{max} are sent to inverter after processing by control station.

As mentioned above, a specific limited use of inverter is made in this work by preferring the control station for module control prototyping. Nevertheless, the inverter can work in two different modes: *speed mode* and *torque mode*. In *speed mode* a command speed signal is generated manually in the DSE software and it is controlled in closed-loop through a PI controller implemented in the inverter. A torque signal C_{com} is produced by starting from speed error signal between command and effective value, and it is then transformed in current signals which are then sent to electric motor. Saturations are carried out on current signals in order to guarantee the system safety. A closed-loop control on currents works too.

In *torque mode* the inverter takes the C_{com} signal sent directly by the measurement box and generated in the Simulink model, and applies currents to electric motor accordingly. The saturations and the closed-loop on currents work. The motor speed closed control loop inside inverter is not active in this case and so it is necessary to control speed externally through the Simulink model. In order to test pressure or pump speed commands generated by the Simulink model, the *torque mode* is thus selected. The C_{com} is sampled, in the inverter port, through a simple time equal to 1 *ms* while the T_{max} through a simple time of 5 *ms*. The inverter also operates a control on T_{max} to avoid the overcoming of 90 °C (fig. 1.19) and a control on motor winding temperature to remain lower than 145 °C. When one of these temperatures exceeds the limit, the inverter switches off the torque signal C_{com} for stopping the motor operation.

The inverter receives the feedback signal of motor speed ω and it also calculates the estimated torque C_{est} by starting from the feedback signals of motor currents. It sends them to measurement box by means of two output analogical ports with simple time of 5 *ms*. During tests in *torque mode*, a pure delay of about 14 *ms* is observed that is produced inside the currents closed-loop of inverter. The origin of this delay is not quite clear. In each case it has to be taken into account during simulations.

- **Host PC** (with Simulink software)

In the Host PC, several Simulink models are built in order to command the total test bench. Pressure in the hydraulic line or pump velocity is closed-loop controlled, in accordance with schematic of figure 1.16. Command signals are created, by repeating sequence and pulse generator, and compared to measured feedback signals in order to produce error signals. The feedback controller then provides the torque command C_{com} (fig. 1.20) for the motor torque control loop, being the latter implemented in the inverter. The Simulink model also deals with calculation of T_{max} .

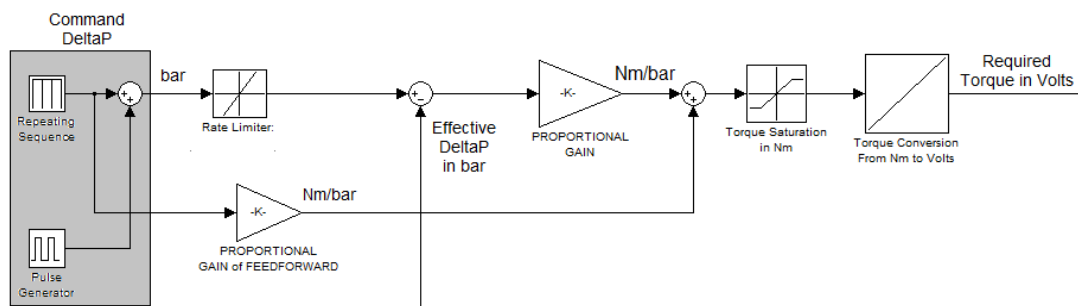


Figure 1.20 Example of command in Simulink environment

- **Speedgoat target machine**

It represents the target PC that is fully optimized for the use with Simulink and *xPC Target* that represents a tool of Simulink software. It permits to test and prototype real-time systems. By means of Simulink blocks and *xPC Target* library, it is so possible to create models in the Simulink environment which provide the input signals to run simulations of the test bench depending on needs. In addition the models can run in non-real time too. To enable host-target communication, a network connection (Ethernet adapter card) is used.

Figures 1.21-1.22 show respectively the test bench assembled in the laboratory, including module and hydraulic circuit, and the placement of thermocouples and pressure sensors. Figure 1.23 shows the placement of two added thermocouples and a sensor of pressure in pump inlet, later installed for simulation needs. Figure 1.24 shows the control station.

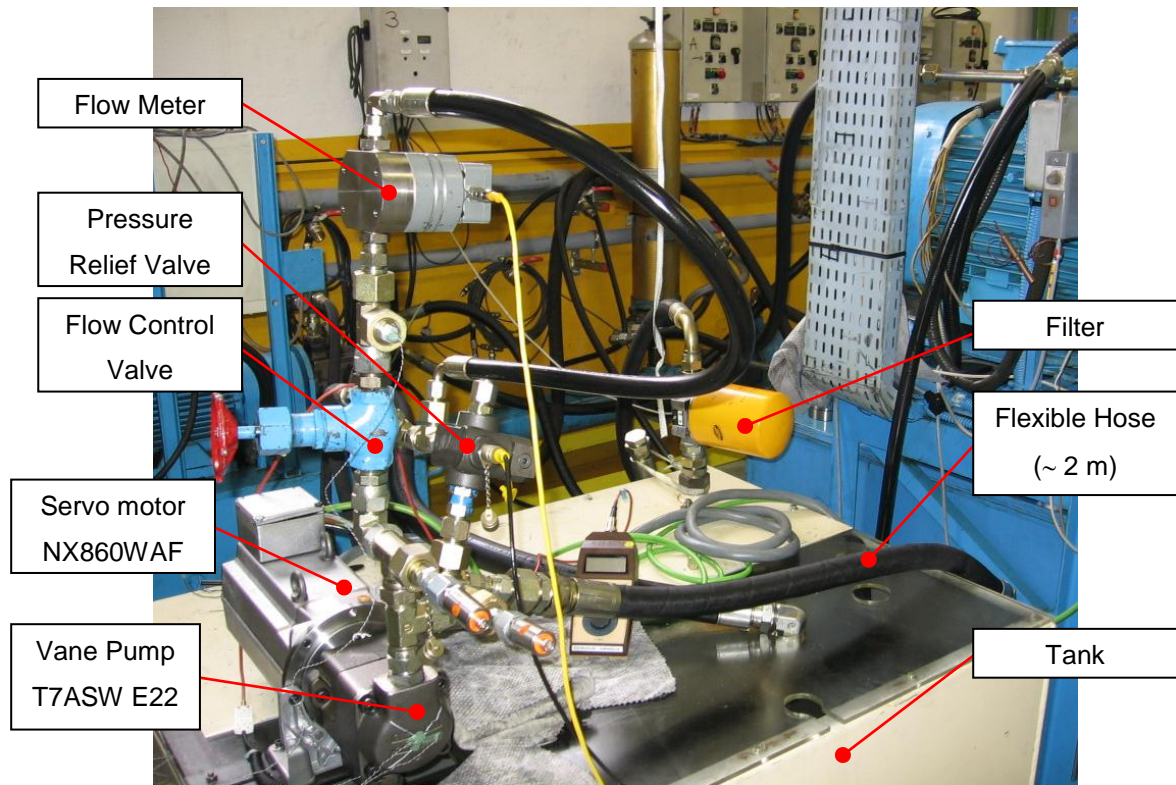


Figure 1.21 Test Bench: module and hydraulic circuit

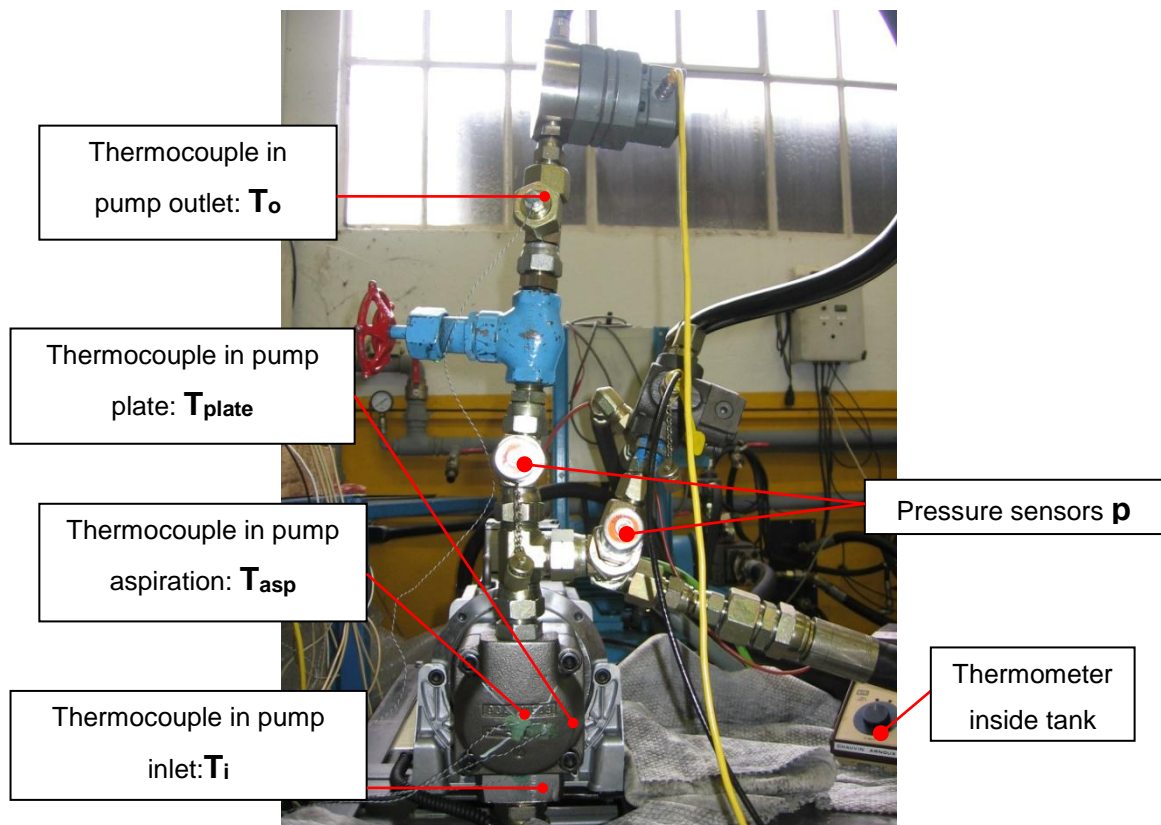


Figure 1.22 Test Bench: Measurements of temperature and pressure

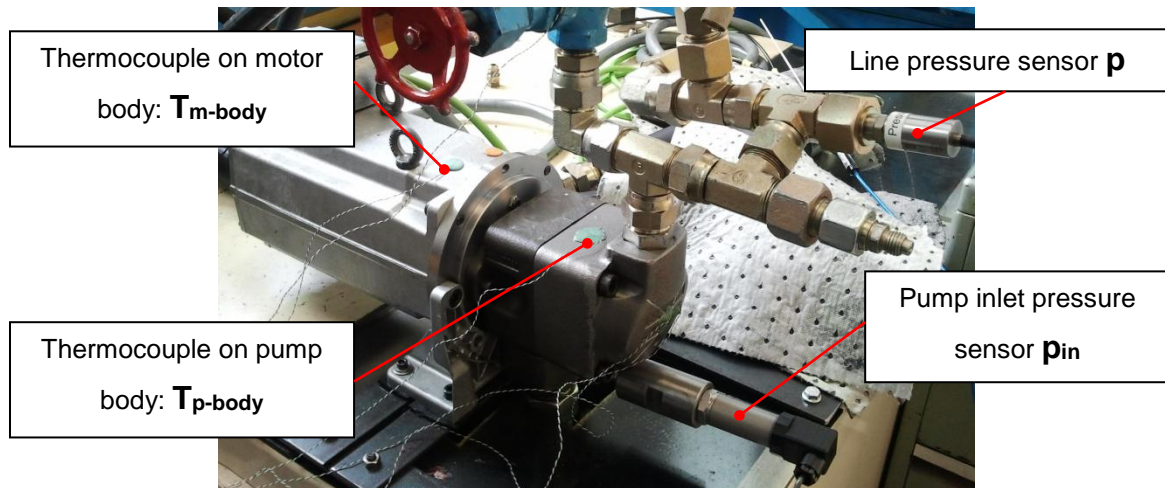


Figure 1.23 Test Bench: measurements of temperatures on motor and pump body and pressure in pump inlet

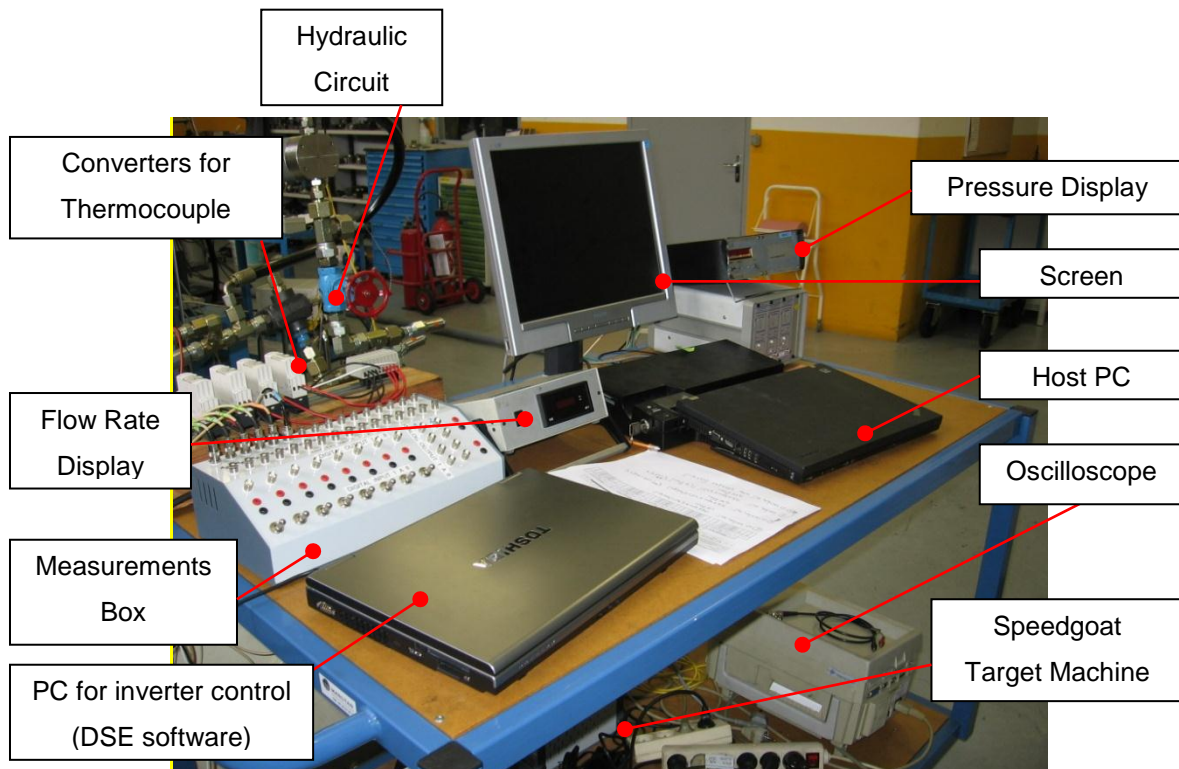


Figure 1.24 Test Bench: Control Station

1.5 Conclusion

In this chapter the injection moulding machines have been described in terms of injection, clamping and motion and control units by detailing about their principal components. The machine functional process has been addressed through the sequence of phases composing a typical machine's cycle. The state of the art of drive technology has been dealt through an overview on evolution since the eighties up to today, included an estimation of future market trend in next five years. The interest on electro-hydrostatic modules has been described by comparing them to servo-hydraulic and electro-mechanical modules, in terms of advantages versus drawbacks. The principal control techniques, implemented in injection moulding machines, have been addressed consisting of feedback controllers with addition of feedforward compensations. The machine's requirements, which impose performance to be satisfied by drives, have then been listed through two typical cycles for rubber and plastic parts. The design limits of the individual components of module analysed in this work, have been enumerated and the test bench, conceived and assembled in Parker laboratory, has been showed.

References

- [1] <http://www.rodongroup.com/services-products/product-gallery>
- [2] A. Morris. Plastic Injection Moulding – An Introduction. *Materials Information Service* edited by Justin Furness. 3 April 2001.
- [3] http://www.repdevulc.com/index.php?option=com_content&view=article&id=18
- [4] G. P. Thomas. Recent Innovations in Injection Moulding. 20 April 2013.
- [5] Euromap 1, January 1983. <http://www.euromap.org/technical-issues/technical-recommendations>
- [6] <http://www.ferromatik.com/en/index.php>
- [7] <http://www.repinjection.com/>
- [8] F. Johannaber. Injection Molding Machines – A User’s Guide. 4th Edition. *Hanser Gardner Publications*. 1 November 2007.
- [9] http://www.repinjection.fr/index.php?option=com_content&view=article&id=90
- [10] Rep – rubber in motion. Turbo-cure.
http://www.repinjection.fr/index.php?option=com_content&view=article&id=35
- [11] D. O. Kazmer, R. G. Speight. Polymer Injection Molding Technology for the Next Millenium. *Journal of Injection Molding Technology*, 1997. Vol. 1, pp. 81-90.
- [12] G. P. Holzinger, R. Schiffers. Achievements and Potentials of Hydraulic Drive Technology Demonstrated on Plastic Injection Moulding Machinery. 8th *International Fluid Power Conference, March 26-28 2012, Dresden, Germany*.
- [13] S Helduser. Development trends in electrohydraulic drives and controls. 6th *International Fluid Power Conference, March 31-April 2, 2008, Dresden, Germany*. Pp. 29-64.
- [14] ARP6154 SAE Standards. EHM General Specifications.
- [15] O. Urbanek. The “Energy Efficiency: European Plastics and Rubber Machines Well Placed” Study. *Euromap, December 01, 2011. Frankfurt, Germany*.
- [16] S Helduser. Improved energy efficiency in plastic injection moulding machines. 8th *Scandinavian International Conference of Fluid Power, May 7-9, 2003. Tampere, Finland*.
- [17] A. Feuser. New Developments in the Field of Electrohydraulic Drive Technology. 10th *Scandinavian International Conference on Fluid Power, May 21-23, 2007. Tampere, Finland 2007*.
- [18] K Muller, and U Dorn. Variable speed drives – customer benefits in injection molding machines and presses. 7th *International Fluid Power Conference, March*

- 22-24, 2010. Aachen, Germany.
- [19] J-C. Maré. Combining Hydraulics and Electrics for Innovation and Performance Improvement in Aerospace Actuation. 12th Scandinavian *International Conference on Fluid Power*, May 18-20 2011, Tampere, Finland. Pp. 255-270.
- [20] A. Feuser. Modern electrohydraulic drive technology for stationary machinery in industrial automation. 7th *International Fluid Power Conference*, March 22-24, 2010. Aachen, Germany.
- [21] Parker Catalogue HY11-3352UK. Drive Controlled Pump. Energy-Efficient Hydraulic System Solutions, 2013.
- [22] H. Murrenhoff. Hydraulic Drives in Stationary Applications. 5th *International Fluid Power Conference*, March 20-22, 2006. Aachen, Germany. Vol. 2, pp. 11-36.
- [23] <http://www.moog.com/news/operating-group-news/2010/new-moog-speed-controlled-pump-system-cuts-energy-use-in-hydraulic-industrial-machines/>
- [24] S. Heduser, I. Ruhlicke. Elektro-hydraulische Antriebssysteme mit drehzahlveränderbaren Pumpen. 1996, N. 071070.
- [25] T. Neubert. Untersuchungen von drehzahlveränderbaren Pumpen, Dissertation. *TU Dresden 2002*.
- [26] S. Michel, T. Schulze, J. Weber. Energy-Efficiency and Thermo Energetic Behaviour of Electrohydraulic Compact Drives. *The 9th International Fluid Power Conference*, March 24-26, 2014. Aachen, Germany, 2014. Pp. 163-177.
- [27] A. Helbig, A. Noll, C. Boes. Electro Hydrostatic Actuation for Gas and Steam Turbine Process Valves. *Power-Gen Europe, Keeping Europe's Power Flowing*, June 4-6 2013, Messe Wien, Vienna, Austria.
- [28] Y. Yang. Adaptive Control of Injection Molding Process. *Hong Kong University of Science and Technology. Degree of Master in Philosophy in Chemical Engineering. December 1998*.
- [29] M. Rafizadeh. Physically-Based Dynamic Model for the Control of the Cavity Pressure in Thermoplastics Injection Molding. *Degree of Doctor in Philosophy. Department of Chemical Engineering, McGill University, Montreal, Canada. December 1996*.
- [30] C. Y. Zhang, J. Leonard, R. G. Speight. Adaptive Controller Performance used for Ram Velocity Control during Filling Phase. *Proceeding ANTEC*, 1996, vol. 1. Pp. 593-597.
- [31] H. Havlicsek, A. Alleyne. Nonlinear Control of an Electrohydraulic Injection Molding Machine via Iterative Adaptive Learning. *IEEE/ASME Transactions on*

Mechatronics. Vol. 4, N. 3, September 1999.

- [32] H. Zhang, L. Quan. The Kinetic Characteristics of a Clamping Unit in Injection Molding Machine driven by New Pump Control System. *Advances in Information Sciences and Service Sciences (AISS). Vol. 4, N. 21, November 2012. Pp. 468-475.*
- [33] S. Racklebe, J. Weber. Reduction of Cycle Time for Injection Moulding Machines with Electric Hydrostatic Drives. 12th Scandinavian *International Conference on Fluid Power, May 18-20 2011, Tampere, Finland.*
- [34] Raven F. H. Automatic Control Engineering. *5th edition, McGraw Hill, 1995.*
- [35] B. Wagner, J. Weber. Iterative Learning Control for an Injection Unit of a Plastic Injection Moulding Machine. *The 8th International Fluid Power Conference, March 26-28, 2012. Dresden, Germany. Pp. 67-82.*

Pompe à Palettes

Ce chapitre est consacré à l'exposition de l'état de l'art de la pompe à palettes et son évolution dans les soixante-dix dernières années. Une comparaison qualitative est effectuée avec les concurrents principaux, notamment avec les pompes à engrenages internes et les pompes à pistons axiaux, en soulignant les avantages et les limitations. La spécificité de la pompe à palettes Parker, technologie Denison, est décrite avec caractérisation de ses composants, de son principe de fonctionnement et des différentes applications industrielles et mobiles. En particulier le fonctionnement de la pompe, typiquement dans deux quadrants, l'absence de drain externe et le concept de cartouche, sont mis en évidence. La modélisation de la pompe à palettes est alors développée en évaluant ses pertes d'énergie venant de fuites internes et de pertes du couple. Des tests de laboratoire sont exécutés, dans le cadre de ce travail, pour acquérir des données sur les pertes d'énergie en fonction de pression de service, vitesse de la pompe et de température du fluide hydraulique. Après cela, un modèle paramétrique est créé pour la conception d'asservissement et comme support au développement des modèles fonctionnels préliminaires. Un prototype virtuel hydraulique de la pompe est finalement réalisé dans l'environnement AMESim afin de simuler les pertes d'énergie. Il est basé sur des look-up tables, constitués par toutes les données expérimentales, et il permet aussi la reproduction des fuites internes et des pertes du couple hors de la plage de fonctionnement utilisée en laboratoire. Il représente ainsi un outil très utile pour simuler les pertes d'énergie de pompes opérantes dans les quatre quadrants de fonctionnement.

2 Vane Pump

In this chapter the vane pump state of art is described by highlighting the evolution of the product through the years and the comparison with other pump technologies. After an overview on existing modelling and analysis provided by literature and on Denison vane pump technology, the context focuses on a parametric model proposed to describe the energy losses based on theoretical approach and on fitting the measurement data. The fundamental dependence on operating conditions is underlined that modifies largely the pump performance. An advanced virtual model provides a key instrument to simulate the energy losses inside the range of experimental data and to predict them out of that range.

2.1 State of Art of Vane Pump

2.1.1 Product Evolution and Competitors

The development of vane pumps is more than seventy years old and the interest in this technology increased in the two decades 1940-1960, as confirmed by several patents published concerning designs of balanced and unbalanced vane pumps [1,2,3] (Fig. 2.1).

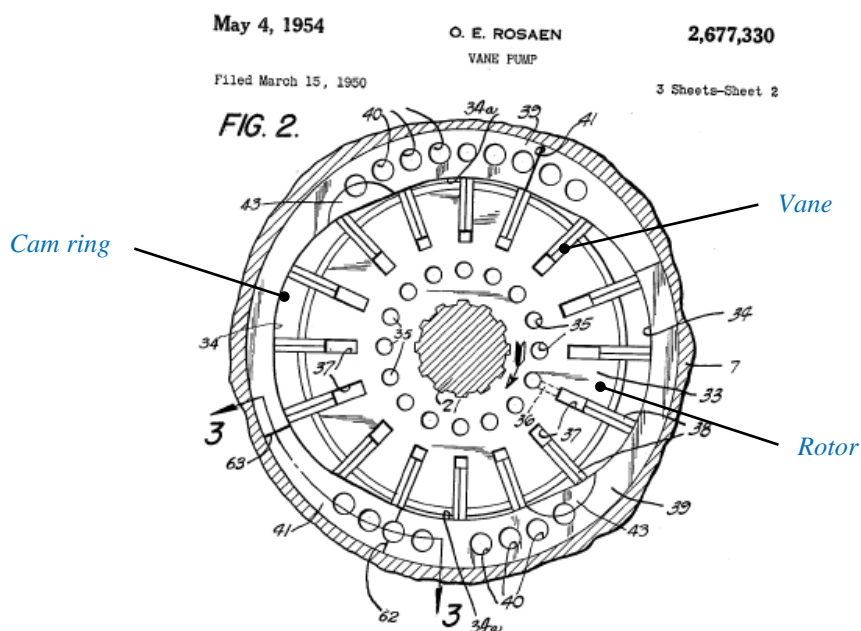


Figure 2.1 Patent N.2677330: Vane Pump, 04/05/1954, United States Patent Office, [1]

Figure 2.1 shows the concept of balanced vane pump. The rotor is the rotating part that is eccentrically located within the cam ring. The cam ring has an inner elliptic profile that determines the pump fixed displacement. Two inlet and two outlet ports are diametrically opposed in such a way a complete radial forces balance is achieved. Two strokes per revolution are fulfilled. The rotor has radial grooves where the vanes are arranged. When the rotor turns, the centrifugal forces and the hydraulic pressure push the vanes tips against the internal cam contour. Chambers are so created by two consecutive vanes, the cam internal profile and the external surface of rotor. The hydraulic fluid, suctioned by the inlet port, fills the pump chambers and, during rotation, is compressed due to the specific profile of cam that reduces the chambers volume. The fluid finally exits the delivery ports. In unbalanced vane pumps the rotor is offset from the centre of cam and fixed or variable displacement can be realised.

In Sixties, designers of construction equipment machinery began to turn to balanced vane pumps in mobile applications for medium and large rate of flow, thanks to relatively high overall efficiency maintained throughout the life of vehicle [4]. In these years the gear pumps had established themselves firmly in machines where a small flow rate was required and where the attractive purchase price was of primary importance. Nevertheless the vane pumps advanced on market by showing a better capability of power density and reduction of costs.

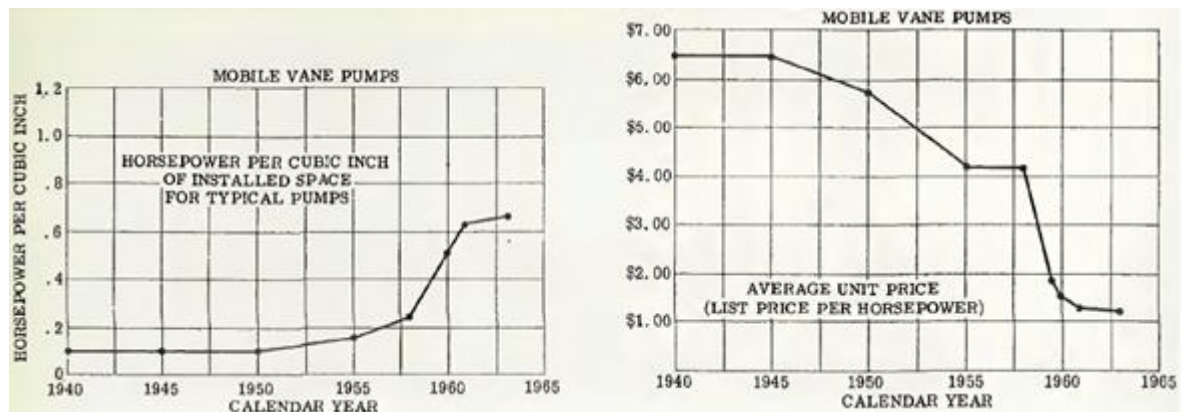


Figure 2.2 Evolution of power density (left side) and reduction of average price (right side) of vane pumps in 1940-1964, from [4]

Figure 2.2 shows: on left-hand side, the increase of vane pump power density evaluated in horsepower-per-cubic-inch of installed space (package size) from 1940 to 1964, while on right-hand side the reduction of vane pump average price per power unit. In about 24

years the price was reduced of 80 %, thanks to improvements in design and manufacturing, by enabling to purchase vane pump power capability for \$1.30 (it corresponds to about \$9.80 in 2015). Pistons pumps also increased their popularity in these years thanks to evolution in designs, materials and in manufacturing techniques, even if the economic aspects made them again less attractive than vane pumps. Variable displacement piston pumps were sold for a price more five times higher than vane pumps price. Typical applications of hydraulic pumps were about power steering systems and arms actuation in front-end loader, wheel scraper, soil stabilizer, high-lift loader and more. Substantial progress was also made in improving the performance of hydraulic motors, in terms of increased pressure and speed, longer life and efficiency. It was the case of high-speed vane motors which were preferable to large low-speed high-torque hydraulic motors severely limited in their speed range [4].

In last fifty years the increased maturity of hydraulic technology and the resolution of controls complexity problems which appeared insurmountable in Sixties, thanks to evolution of controls technology and power electronics, have been permitted to continue the upward trend of hydraulic pumps in terms of performance, size and ability to handle progressively more tasks required by customers.

The global crisis of 2008 drastically reduced the sale of construction equipments for machinery given that the infrastructures undergone a general building slowdown. In this generalized situation the only choice to withstand harsh times was to reduce the components costs by safeguarding the product quality. It was a favorable moment for privileging plastics materials to cast iron and steel, cheaper and with comparable performance level, e.g. the production of plastic filters for construction machinery. For the pump bodies the cast iron was now preferred to aluminum to guarantee a longer life in extreme condition environments, like high temperature variations, adverse weathers and mud projection.

The *energy saving* concept become of primary importance in selecting pumps and components to face the fuel price increase and to reduce CO₂ emissions. The development of energy recovery solutions increased, e.g. in refuse trucks characterised by energy absorption in braking phase and energy release in acceleration phase [5]. The new requirements for pumps and motors became to concern efficiency optimization and cost reduction, by enhancing the compactness and the low noise level. Improved solutions were developed for vane pumps based on advanced manufacturing processes to reduce the

pressure ripple, in comparison with in gear pumps, and to reduce noise level to same level as axial piston pumps. Specific pump components were produced suitable to resist to corrosive environments, for compatibility with special fluids (skydroll, fluid at high viscosity, etc.) or to extreme environments (high contamination level, high temperature variations, etc.) like in mines and offshore [6].

The *components integration* assumed considerable importance: in order to reduce the overall energy consumption, a fully integrated module had to be developed by consisting of electric motor, pump and frequency drive. No more the only performance of pump taken individually count, but the ability to integrate itself in a full module. It was demonstrated for example high reduction of consumed energy by replacing a variable displacement axial piston pump with a fixed-displacement vane pump and by using a variable-speed electric motor for industrial applications where the machine's cycle is well-known in advance. Compact modules which reduce the encumbrance and which suppress flexible hoses with the further advantages of vibration reduction, are now the favorite. The energy saving requirements become part of new pumps design and of the existing pump re-design [7].

Today, the world competition between the several pump technology types is far from being finished. The increasing demand of customer for pumps having high performance in terms of operative pressure, low energy consumption, good reliability, versatility and low noise level makes a great challenge for the designers in developing continuously new competitive products. The major fixed-displacement pump competitors of the balanced vane pump are today: the external gear, internal gear, axial pistons (in-line or bent axis). The variable axial pistons pumps otherwise represent another competitor in the variable-displacement pump domain.

We propose a qualitative comparison between these pump types, based on experiences and benchmarking, in terms of advantages and drawbacks and of cost product versus performance, figure 2.3. The information inserted in fig. 2.3 are general and they refer to some pump model that was taken as reference between the more important brands. Concerning the performance level, by neglecting the external gear pumps which represent a low-performing technology compared to all the others, the internal gear pumps are principally known for: their compactness, low enough pressure ripple, high suction capability and low purchase price. In this type of bi-directional pump, two gears mesh each other (the inner is connected to drive) and chamber constant volumes are created

between the gears profile and housing. The fluid is then forced out at the delivery port by the contact force generated on gears teeth. The internal gear pumps suffer from sensitivity to fluid contamination, have a low mechanical efficiency (< 90%) and operative pressure level not very high (up to 250 bar).

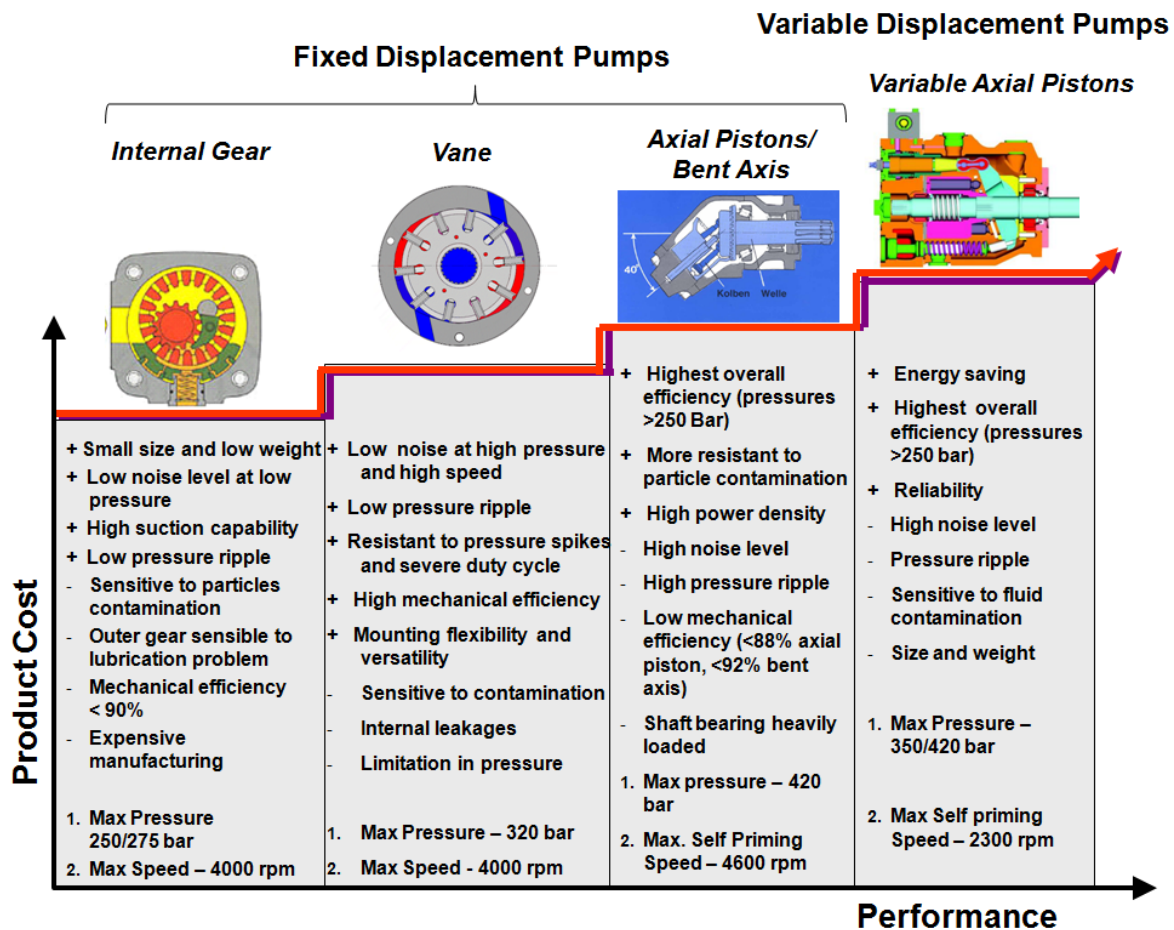


Figure 2.3 Qualitative comparison of principal advantages and drawbacks of fixed and variable displacement pump technologies: internal gear, vane, axial pistons and variable axial pistons.

The vane pump represents a more advanced technology notoriously well-known to be quietest in all operating conditions, included at high pressure and speed, having extremely low pressure ripple and mechanical efficiencies higher than 90%. This is obtained by optimization of cam shape and surface state, as well as by design improvement of the plates containing the suction and discharge ports. Its main drawbacks concern the relatively low volumetric efficiency due to internal leakages and the contamination sensitivity. More expensive than the internal gear pump but with higher performance level being able to reach the 320 bar in transient and the 280 bar in continuous.

The axial pistons pumps include bent and in-line configurations. In bent axis piston

pumps, the drive shaft is connected to a moving cylinder block through a universal joint and an offset angle is set between shaft and block. The moving cylinder block contains a number of pistons whose rods are connected with the flange of drive shaft. The rotation of shaft forces the pistons in and out of their bores and the inclination of the shaft flange produce a piston stroke that compresses the fluid inside. The pump displacement is controlled by modifying the offset angle. In the in-line piston pumps the drive shaft is aligned to cylinder block axis. A swash plate is fixed to shaft and the reciprocal angle defines the pump displacement. The pistons are coaxially aligned with the shaft and connected to swash plate. The axial piston pumps are located a step above the vane pump in terms of performance thanks their higher power density, higher overall efficiency and lower contamination sensitivity. They however generate higher noise and higher pressure ripple levels.

The variable displacement axial pistons pumps increased their performance with respect to past, thanks to controls technology evolution that makes them easily save energy. Reliable and efficient, they are put at disadvantages when the product costs, sizes and noise level are taken into account as selection parameters.

In short, the vane pump places itself between the internal gear pump, cheaper but lower performing, and the fixed/variable displacement axial pistons pumps which are more expensive but having superior performance.

In literature, articles are rarely published concerning the comparison between the existing pump technologies because considered proprietary material. They underline more the qualities of a specific pump type and they generally describe studies to improve the drawbacks related to that technology. About the vane pump, next paragraph mentions some studies conducted by several authors through the years.

2.1.2 Design and Modelling

Performance criteria and studies on theoretical operation were proposed since 1946 on the basis of simple mathematical models. They were initially conceptual models to determine flow and torque characteristics in hydraulic pumps and motors. A first model for internal leakage flow was proposed by assuming their proportional dependence to pressure differential [8]. A more complete model for frictional torque was instead proposed by consisting of three components: a component dependent on pressure, a component dependent on viscous friction and a constant component independent on pump operating conditions.

These models quickly revealed insufficient to fully represent the real characteristics. In particular the same author pointed out ten years after the importance of the thermal effects by showing that the clearance optimisation, based on isothermal theory, was not sufficient to design pumps [9].

Successfully other authors proposed improved models to characterize the pump efficiency, in particular for friction torque to better model the mechanical efficiency, considered a key factor as well as the volumetric efficiency, in evaluating pump performance [10]. The friction torque, caused by the friction between cam contour and vane tips, were experimentally and theoretically investigated to identify the geometrical parameters which essentially determined the mechanical efficiency of a balanced vane pump having small displacement (8 to 13 *cc/rev*) for power steering systems. By testing a pump operated for 500 hours under constant conditions, running-in positive effects were also studied by showing the reduction of friction coefficient due to smooth of the surface at sliding parts. The same authors then revealed that the fine surface roughness of the cam contour greatly affected the mechanical efficiency at high pressure conditions [11].

The study carried out by the authors in [12], touched on the importance of reproducing by simulation the internal leakages and frictional torques of vane pumps when the EHM's power sizing and temperature management are taken into account. These parasitic effects, initially assumed as linear in the analytical preliminary models, were then simulated through look-up tables composed by experimental data. The frictional torques and the internal leakages were, at that modelling level, considered to depend on hydraulic line pressure drop and on the pump speed only. In practice, they also depend on dynamic fluid viscosity that is highly impacted by the fluid temperature. Such effects were also modelled

in [13] from measurements performed on vane pumps and of internal gear pumps where the oil temperature was measured at pump outlet. However these measurements are considered not sufficient for the present need. In fact it was shown in Parker laboratory that the oil temperature inside pump can be far different from temperature measured at the pump outlet. This is also confirmed in [14], in particular through the temperature measurements taken from eight thermocouples placed in the cam-ring and in the side-plate of the pump.

The importance of the viscosity variation associated to temperature rise on pump characteristics were also investigated in [15]. In that work, the internal leakage flow was evaluated by changing the viscosity for a vane (Fig. 2.4), an external gear and an axial pistons pumps. The sensitivity to fluid contamination was also analysed by showing the performance variation when pollution particles of different dimensions (from 5 to 40 μm) were added in the fluid. It was noticed that the internal leakages of vane pump reduced from the 55% to 7% of delivery flow rate for viscosity increase from 13 to 38 mm^2/s , at constant level of fluid contamination (correspondent to particles with dimension up to 40 μm) (Fig. 2.4). The better resistance to contamination of the axial piston pumps were finally confirmed in comparison with vane pumps and external gear pumps.

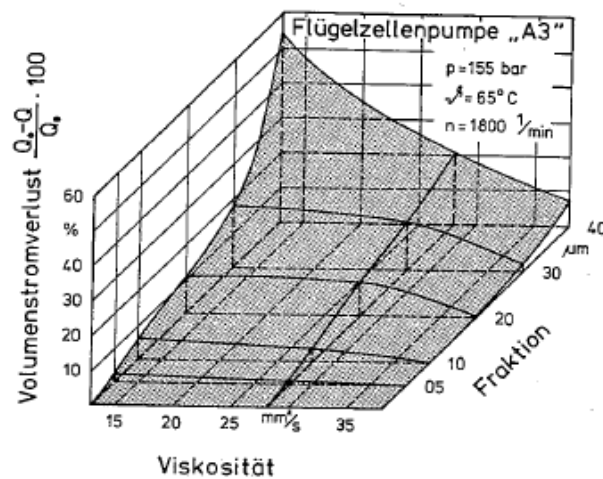


Figure 2.4 Variation of internal leakages in a vane pump versus viscosity and fluid contamination level, from [15]

It is worth mentioning works regarding methods for determining the theoretical flow rate through the calculation of the volume derivatives of all pumping chambers and guidelines for the design of the inner contour of cam ring [16]. Other communications address solutions to reduce the flow ripple amplitude generated by the pump in power steering

systems: it is transmitted along the hydraulic circuit and it generates structural vibration and sound emission due to interaction with the hoses impedance [17], [18]. Ports geometry designs and metering grooves are also the objectives of some study to reduce the pressure fluctuations and to reduce noise level by means of virtual tools, Computational Fluid Dynamics (CFD) [19] and algorithms of cam shape optimisation [20].

Today vane pumps have reached a great level of maturity that makes them very competitive compared to the other existing pump models, in terms of performance, efficiency, noise levels and compactness. Although they possess good performance, again and again it can be made to improve them, in particular to answer to new recent applications of variable-speed drives in automation. The characterisation of pump operation through the analysis of constant speed steady-state condition is not more sufficient. The evaluation of pump dynamics in transient phases, like acceleration and depressurisation, as well as in constant pressure phase at low speed, is now mandatory. Certain versatility is requested to vane pump in order to adapt itself to different stationary machinery applications but also mobile applications as construction and forestry machines, refuse trucks etc. To improve the pump operation, it is so firstly necessary to develop an excellent knowledge of its energy losses and their dependence from operating conditions. In this context, the energy losses are analysed and reproduced by means of a parametric model and virtual prototype that enables extrapolating the results out of range of experimental data.

2.1.3 Parker Vane Pump: Denison Technology

In 1952 Denison Company launched its first vane pumps which found application in power steering and in automatic transmissions [21]. Denison Company was bought by Parker in 2004. The vane pumps and motors concept, design and production have been developing in the site of Vierzon, France, for more than sixty years. Through the years, the product has evolved by increasing the operative pressure from the initial 148 *bar* up to the actual 320 *bar* while reducing noise level and internal leakage. This evolution is related to release of several pump families from T1 to T7 series (Fig. 2.5).

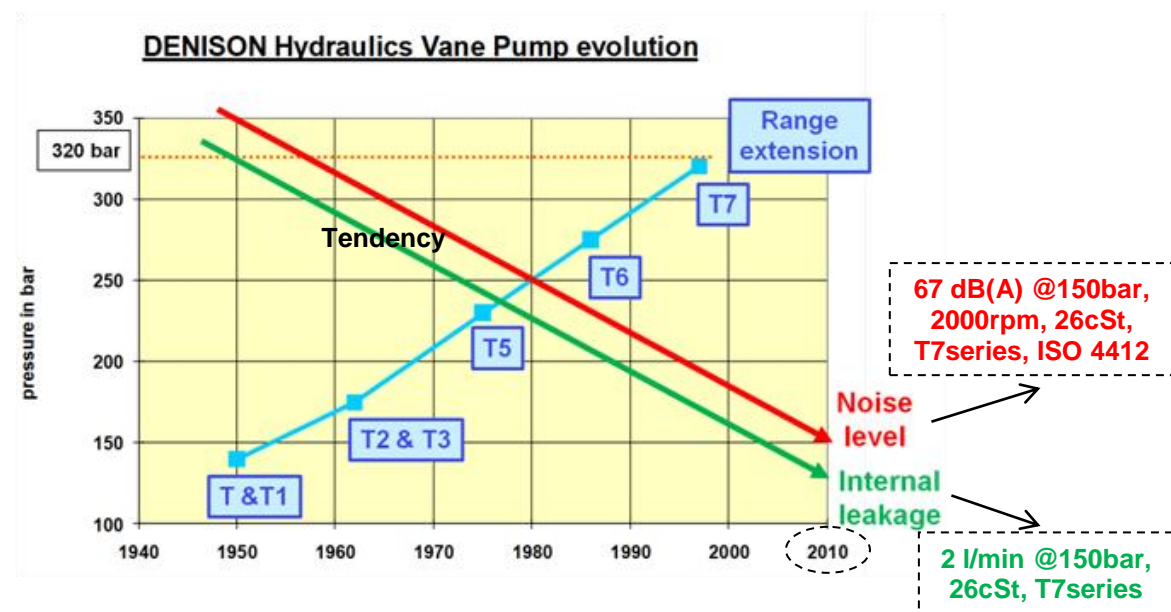


Figure 2.5 Evolution of Denison vane pump technology from 1952 to 2010

Recent fixed-displacement Parker vane pumps are well-known for their high performances (operating pressure up to 320 *bar* up to 3600 *rpm*), high overall efficiency, low noise levels (e.g. 71 *db(A)* @ 250*bar*, 3000*rpm*, 26*cSt*, T7B Series), low pressure ripple, good compactness, mounting flexibility and good reliability. The plenty of possible configuration makes pump versatile and adapted to market requirements. In fact the product catalogue is based on five cartridge families with displacement included in the range 5.8 ÷ 268.7 *ml/rev* and maximum pressure in the range 240 ÷ 320 *bar*. In addition double and triple pumps versions exist. The combination of different cartridges in double and triple pumps allows low flow at high pressure (300 *bar* max.) and high flow at lower pressure. Lasts pumps feature also enables a very fast pressure cycle change with very precise flow repeatability [22]. Another developed solution is the *hybrid* pump

characterized by combination of fixed-displacement vane pump with a variable-displacement axial piston pump [22]. Parker refers to normative NAS 1638 class 8 or better (or ISO 18/14 or better) for guaranteeing that the level of contamination of the hydraulic fluid remains under the admissible limits for the vane pump. In detail, the NAS 1638 class 8 corresponds to a contamination of: up to 64000 particles per 100 ml of dimensions between 5 and 15 μm , up to 11400 particles per 100 ml of dimensions between 15 and 25 μm , up to 2025 particles per 100 ml of dimensions between 25 and 50 μm , up to 360 particles per 100 ml of dimensions between 50 and 100 μm and up to 64 particles per 100 ml of dimensions $> 100 \mu\text{m}$.

Vanes market is shared in two parts: mobile and industrial applications. Concerning the mobile, typical applications are: dumpers, wheel loaders, excavators, refuse trucks, off highway, defence and more. Typical industrial applications are: presses, injection machines, die casting, lubrication, etc.

2.1.3.1 Operation Principle

Vane pump has not external drains to take away the internal leakages (and the generated heat) and it has two allowed functional quadrants of operation, fig. 2.6: positive pressure difference producible at positive and negative speed. The performance values inserted in fig. 2.6 refer to the pump model selected in this work. It is important to remark that the extent of acceptable negative speeds is not precisely defined, due to lack of experience feedback, and excessive negative speeds could seriously impact the pump service life. The determination of the negative speed limit is not part of this research work.

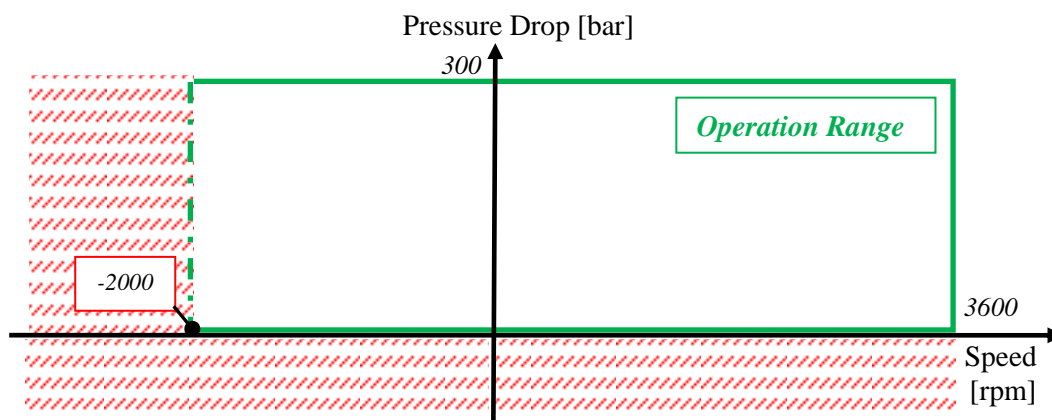


Figure 2.6 Functional quadrants of operation of the vane pump selected in this work

The principal components constituting a vane pump are (figure 2.7):

- housing: pump body with aspiration orifice
- transmission shaft with ball bearing
- cap: component with discharge orifice, shaft seal and anchorage system
- cartridge: components assembly

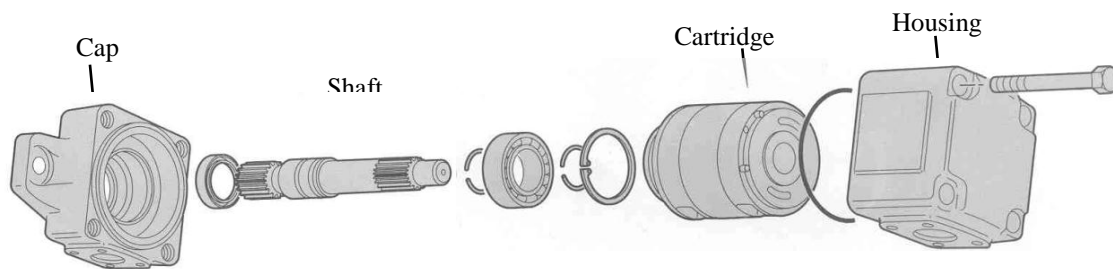


Figure 2.7 Vane Pump general design

The versatility of vane pump is thanks to “cartridge concept”. Cartridge represents the pump heart and it is located inside housing (fig. 2.8). It includes:

- cam ring: its internal profile defines pump displacement
- rotor: component with radial cavities containing the vanes
- vanes (10 or 12 depending on models)
- pins: they press the vanes against cam ring profile
- side plates: they integrate aspiration and discharge orifices, they keep cartridge in position

The cam ring has an elliptic inner profile that determines the pump constant displacement (Fig. 2.8). By substituting only the cam ring, it is possible to change the pump displacement without modifying the other components. Two delivery and two suction ports diametrically opposite each other provide hydraulic balance of all internal radial force and two strokes per revolution are thus realised. Thanks to radial balance, the bearing loads are so greatly reduced. Each vane has two radial holes which equilibrate the pressure drop between upper and bottom (fig. 2.8). The wear between vane tip and cam profile are limited by designing the vane with two lips (fig. 2.8). The vanes are always pushed against the cam ring profile by centrifugal forces and oil hydrostatic forces. The hydrostatic force is produced by the oil pressure acting on the base of the pins (fig. 2.8) and it pushes them against the vanes. This oil under pressure enters the rotor by means of

side feed holes, located on rotor surfaces, and flows through it by means of internal cavities (fig. 2.8). The pins so assure the vane placement and the steady contact between vane tip and cam contour. Two side plates, located at both sides of rotor, provide axial cartridge positioning. The side plates integrate aspiration and discharge orifices with back pressure grooves which permit to reduce the pressure ripple. The pump chambers are achieved by two adjacent vanes, the external surface of rotor and the cam inner contour, in conjunction with the side plates. When the primer rotates the rotor, a pressure difference is created between tank and inside of pump, thanks to expansion of the sealed chambers volume. The oil is so suctioned through pump inlet port and fills the chambers. During rotation, the chamber volumes are then reduced, due to the elliptic profile of cam ring, and the oil is thus compressed. After 90° of rotation, the oil under pressure is finally forced out at the delivery port.

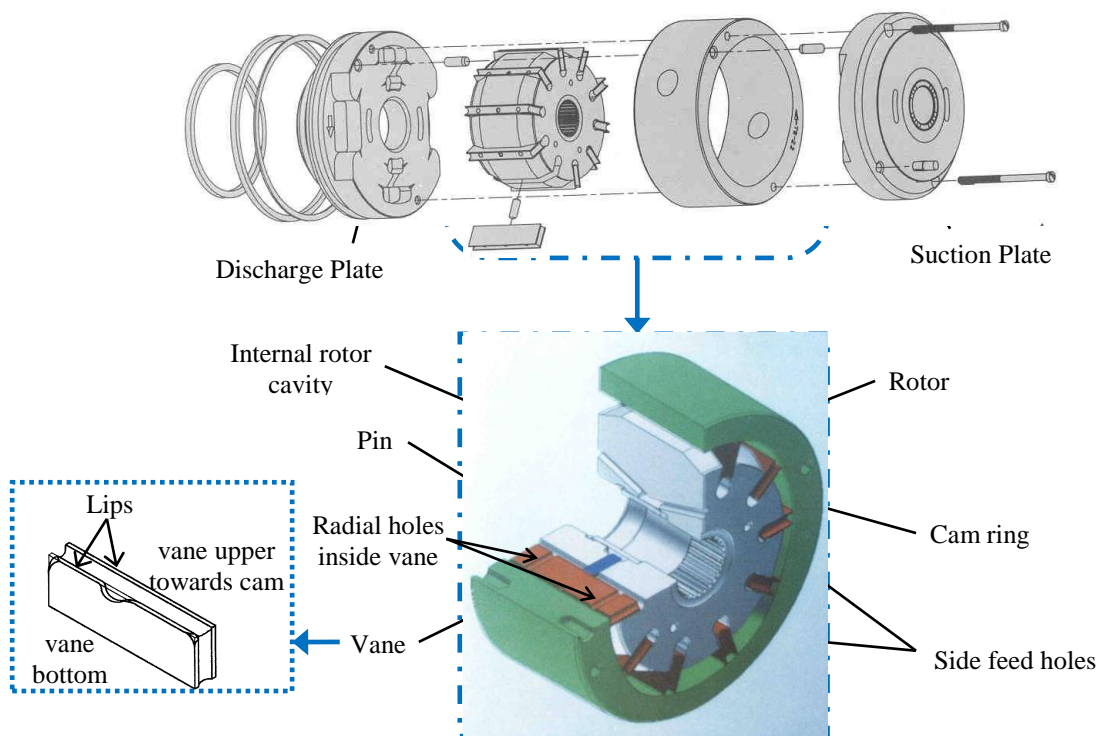


Figure 2.8 Cartridge components and cross-sectional view

2.1.3.2 T7 Series Vane Pump for Electro-Hydrostatic Modules

Several technologies exist in order to adapt the vane pump to each different application, depending on operating conditions: mobile and industrial. Various cartridges are so conceived whose differences mainly reside in the rotor and in the way to press the vane against the cam. All the other components remain the same.

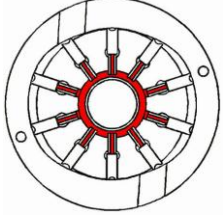
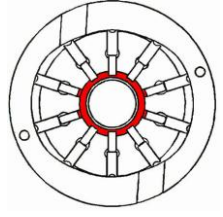
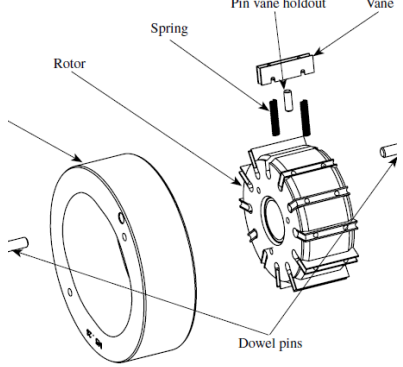
<p>Mobile Applications:</p> <ul style="list-style-type: none"> – Rotor: 5/6 side feed holes/face – Pins: hollow type 	
<p>Traditional Industrial Applications:</p> <ul style="list-style-type: none"> – Rotor: 3 side feed holes/face – Pins: solid type 	
<p>Recent Industrial Applications:</p> <ul style="list-style-type: none"> – Rotor: 3 side feed holes/face – Pins: solid type – Spring: 2 for each vane 	

Table 2.1 Differences in pump cartridge for mobile and industrial applications

Table 2.1 summarises the difference in the cartridge concept. The mobile applications are typically characterised by high viscosity conditions due to low environment temperatures in outside operations and low speed motions. It is consequently necessary to increase the forces acting at the bottom of vanes in order to maintain the vanes in steady contact with the cam contour. This is achieved by hollowing the pins. In this case the feed holes, placed on the face of rotor, are less deep and are not linked to the base of pins. Their function is just to facilitate the lubrication of pump internal parts while the internal leakages guarantee the filling of volume under and inside the pins. The traditional industrial applications are characterised by higher operative temperatures which reduce the fluid viscosity and higher speeds. Consequently, just using three side feed holes, it is sufficient for pressurising each cavity. Solid pins are used in this case. Recently, some industrial

applications require improved dynamic performance and low energy consumption, as described in Chapter 1. In these applications, new concept of cartridge is developed to reduce the rotational speed up to very low values. For maintaining the vanes in contact with cam ring profile, springs are thus inserted which generate an additional radial force at the bottom of vanes. Figure 2.9 shows two sections of the T7 Series vane pump composing the EHM analysed and performed in this context. In this pump model, the suction plate is absent and the suction orifices are directly integrated in the housing.

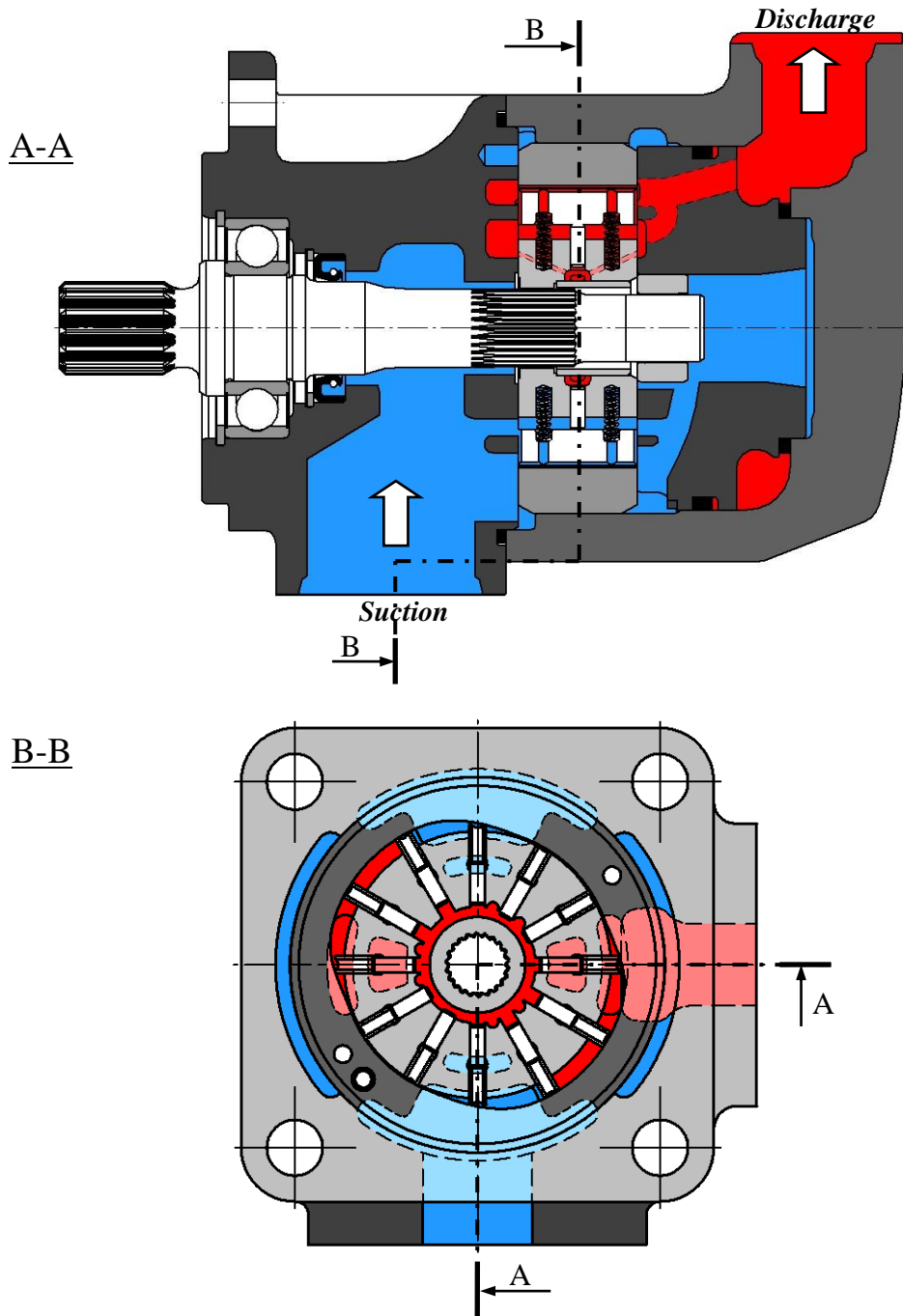


Figure 2.9 Sections of the T7 Series vane pump inserted in the EHM

2.2 Developing a Model of Energy Losses

The linear approach, proposed in the past for modelling the pump energy losses, provides results that are not sufficiently realistic for virtual prototyping. In particular the coupled non-linear parasitic effects are not reproduced. Concerning for example the internal leakages, the model based only on linear dependence to pressure drop, proposed in [8], has to be substituted by a new model that takes into account also the dependence from the other operating conditions like rotational speed and temperature.

Concerning the pump friction C_{fp} , the viscous model, involving the coefficient β_{fp} , represents the simplest model to reproduce the speed influence on friction. For getting higher accuracy, a more detailed friction model is proposed in [23]:

$$C_{fp}(\omega) = \left[\alpha_{fpc} + (\alpha_{fps} - \alpha_{fpc})e^{-\frac{|\omega|}{\alpha_k}} + \beta_{fp}|\omega| \right] \text{sign}(\omega) \quad (2.1)$$

where

α_{fpc} = Coulomb friction

α_{fps} = stiction friction

α_k = Stribeck constant

β_{fp} = motor viscous coefficient

$(\alpha_{fps} - \alpha_{fpc})e^{-\frac{|\omega|}{\alpha_k}}$ is the Stribeck friction and $\beta_{fp}|\omega|$ the viscous friction [23].

The sensitivity of viscosity, due to temperature variation, also plays an important role in the determination of frictional torques, as just exposed in section 2.1.2. The friction contribution due to pressure drop results to be relevant too.

Figure 2.11 displays the internal leakages and frictional torques obtained by means of laboratory tests realised in the frame of this research work. It concerns a T7 Series Parker vane pump. The internal leakages and frictional torques are dependent on: line pressure drop, pump speed and fluid temperature inside the pump.

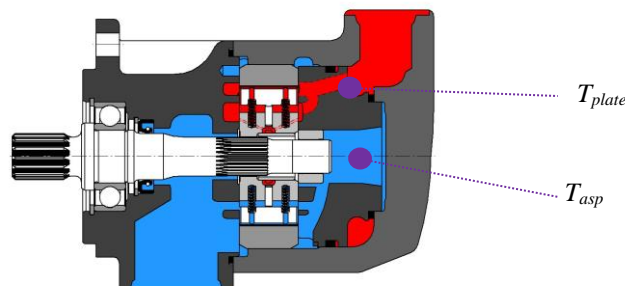


Figure 2.10 Placement of thermocouples for measuring fluid temperature inside pump

Two thermocouples are used and placed respectively in the drain pump volume and into the pressure plate (high pressure side), fig. 2.10. They reveal a temperature gap lower than 1°C between these two locations.

It is clearly observed that the internal leakage is nearly independent from the pump speed while it varies linearly with the line pressure drop, at a given fluid temperature. At constant pressure and velocity, it is confirmed that the internal leakage varies in the same direction as the fluid temperature.

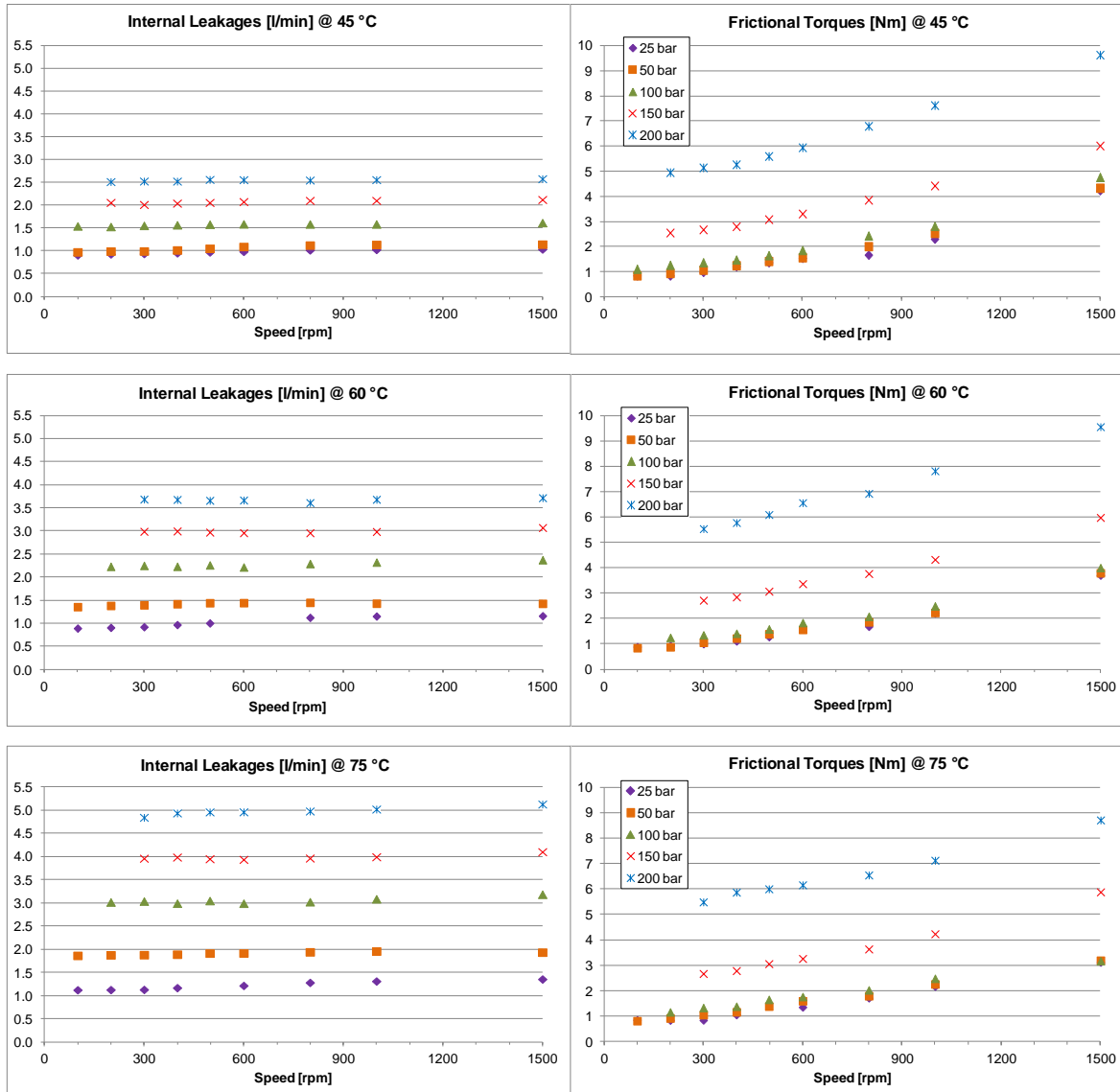


Figure 2.11 Energy losses of Parker T7 vane pump (22,5 cc/rev) at 3 temperatures vs. line pressure drop and pump speed (left: internal leakage, right: frictional torque)

On its side, the frictional torque characteristic is more complex. It is necessary to distinguish two different regions of influence from the operating conditions. In the first region characterized by line pressure drops up to 100 bar, the frictional torques appear

approximately independent from pressure with a low dependency from fluid temperature and exhibit a nearly monotonous increase with speed. At higher pressures, friction becomes more sensitive to pressure. When the fluid temperature increases, the frictional torque reduces as a consequence of lower viscosity. However this effect is not observable at higher pressures where normal load at contacts is increased.

2.2.1 Structure of Pump Losses Model

In this context the structure of the system-level model of the vane pump with energy losses model is firstly addressed with support of a causal Bond Graph, figure 2.12, following the approach proposed in [24].

The pump is interfaced with the electric motor and shaft (mechanical port) through the shaft speed and with the hydraulic circuit (hydraulic ports) through the input/output pressures and flow rates. In addition, the pump exchanges the heat produced by its energy losses through the absorbed/released powers and temperature at the thermal port.

The functional power flow is pointed out using bold power bonds. Friction is modelled as R dissipative effect dependent on speed. Introducing the RS field enables friction to be made sensitive to temperature and power loss to be output as a power source for the thermal model. Then, pressure influence is introduced using the modulated RS field (MRS) and is taken from an effort detector.

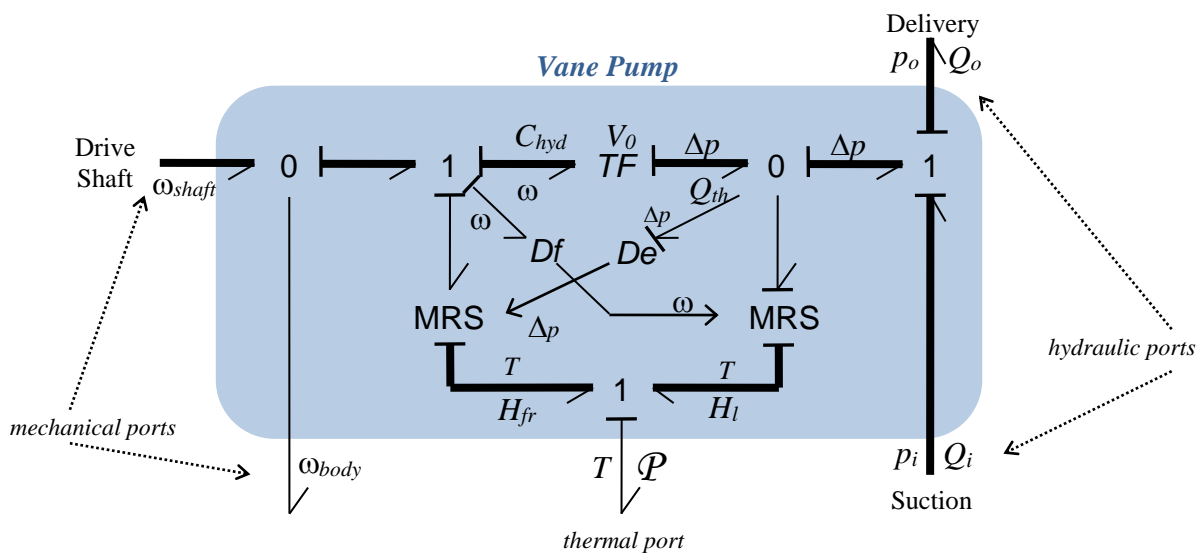


Figure 2.12 Simplified causal Bond-graph of the vane pump with energy losses

The same approach is applied to leakage where the R dissipative effect structurally indicates the algebraic dependence of leakage on pressure while influence of temperature and velocity is introduced by changing the R element into a modulated RS field. A flux detector enables getting the shaft to body relative velocity. Causalities are forced for the MRS elements in order to meet numerical requirements and are propagated to facilitate the introduction of shaft inertia.

Thermal model and dynamic parasitic effects such as shaft inertia and fluid compliance are not explicitly displayed on the figure that focuses on energy losses. It is important to keep in mind that, when it is intended to address air release and cavitation, considering the outlet/inlet pressure difference is not acceptable because absolute pressure directly impacts these effects (inlet and outlet pressures are to be entered separately as modulating signals in the MRS elements).

When experiments are available, the MRS characteristic of friction and leakage can be simply defined as 3-D look-up tables. Each of them depends on velocity, pressure and temperature.

However, developing a parametric model can be of interest for understanding the contribution of each variable defining the operation point. At this modelling level, it is not planned to identify the relation between principal geometrical dimensions of pump and energy losses, as made in [10], but the idea is so to construct theoretically a mathematical model for energy losses that fits the measured data obtained in laboratory. Such a model is developed in the next section.

2.2.2 Parametric Model of Pump Leakages and Frictions

This section intends to develop a parametric model based on the radial gap theory [25] where the effect of temperature is introduced by expressing the fluid viscosity as a function of temperature, according to the Reynolds equation [26]. In this approach, influence of pressure on viscosity is neglected in comparison with influence of temperature, although the influence of working pressure could lead to significant mistakes especially when the Δp is higher than 300 bar [27]. Just thinking that the dynamic viscosity of ISO VG 32 oil increases of about 16 times from 20 to 100 °C whereas only of 1,8 times from 0 to 250 bar. In this context the range of operating pressure variation is

between 25 and 200 *bar*.

A one-degree polynomial type model is taken as a starting point [12]. In this model the dependence from temperature is not taken into account and the relationships between variables are linearly expressed. Then the model is improved as follows.

The internal pump leakage Q_{lp} is given as a function of shaft to body angular velocity ω , pump pressure difference Δp and temperature T :

$$Q_{lp} = \beta_{lp}\omega^A + \gamma_{lp}\frac{\Delta p^B}{\mu_i e^{-\sigma(T_0-T_i)}} \quad (2.2)$$

where the parameters β_{lp} , γ_{lp} , A and B are identified from experiments using the Least Square Method (LSM) [28]. The reference absolute viscosity $\mu_i = 6,74 \cdot 10^{-2} \text{ Pa}\cdot\text{s}$ is taken from data sheets at reference temperature T_i equal to 20 °C and $\sigma = 0.037 \text{ 1}/^\circ\text{C}$.

In the same manner, the model of frictional torque C_{fp} originally proposed in [12] is modified to introduce the dependence of viscosity on temperature:

$$C_{fp} = \alpha_{fp} + \beta_{fp}\mu_i e^{-\sigma(T_0-T_i)}\omega^C + \gamma_{fp}\Delta p^D \quad (2.3)$$

where the parameters α_{fp} , β_{fp} , γ_{fp} , C and D are again identified from experiments using the LSM.

The table below shows the values of the obtained parameters.

Parameters	Unit	Value
β_{lp}	ISU	$4.94 \cdot 10^{-5}$
γ_{lp}	ISU	$3.14 \cdot 10^{-14}$
A	-	0.19
B	-	0.94
α_{fp}	Nm	0.92
β_{fp}	ISU	$8.33 \cdot 10^{-6}$
γ_{fp}	ISU	$2.79 \cdot 10^{-12}$
C	-	2.64
D	-	3.17

Table 2.2 Values of parameters obtained by means of LSM

It is important to remark that all the previous parameters are physical quantities

experimentally determined and that the final expressions of eq.s (2.2)-(2.3) are the result of a preliminary analysis in which double-terms (as $\Delta p \cdot \omega \dots$) were considered too. A comparison between the terms has finally permitted to neglect the higher-order terms and to reduce the parametric model up to the form described above.

Figures 2.13 and 2.14 compare the measured internal leakages and frictional torques with the calculated ones by means of the parametric model (eq.s 2.2 and 2.3).

The relative error in percentage of internal leakages is computed as:

$$e_{rel}^Q \% = \frac{(Q_{lp}^{experimental} - Q_{lp}^{model})}{Q_{lp}^{experimental}} 100 \quad (2.4)$$

The e_{rel}^Q between parametric leakage model and measured leakage is globally lower than 10% and never exceeds 25% for the whole tested domain of figure 2.13.

The relative error in percentage of frictional torques is computed as:

$$e_{rel}^C \% = \frac{(C_{fp}^{experimental} - C_{fp}^{model})}{C_{fp}^{experimental}} 100 \quad (2.5)$$

The e_{rel}^C between parametric friction model and measured friction is globally lower than 15% and never exceeds 28% for the whole tested domain of figure 2.14.

In conclusion, the parametric model of pump energy losses involves 9 parameters. It can be used with profit for control design (the control loops admit modelling errors). However, as it introduces a non-negligible modelling error, it is not consistent with accurate simulation of thermal-hydraulic coupling in open loop model operation. This is certainly due to the presence of numerous and coupled effects (e.g. dilatation, centrifuge effects, local cavitation, etc.) that make energy losses difficult to be accurately modelled in practice for the whole operation domain of a vane pump. For this reason, look-up tables are preferred for the development of the thermal-hydraulic pump model. They enable frictions and leakages to be reproduced within the range of experimental data acquired in laboratory. Unfortunately, the rapid temperature increase does not allow taking measurements at extremely low shaft velocities. It is important to note that out of the experimental range, data have to be extrapolated that introduces modelling uncertainties. In next paragraph the modelling through look-up tables implemented in a virtual prototype is described.

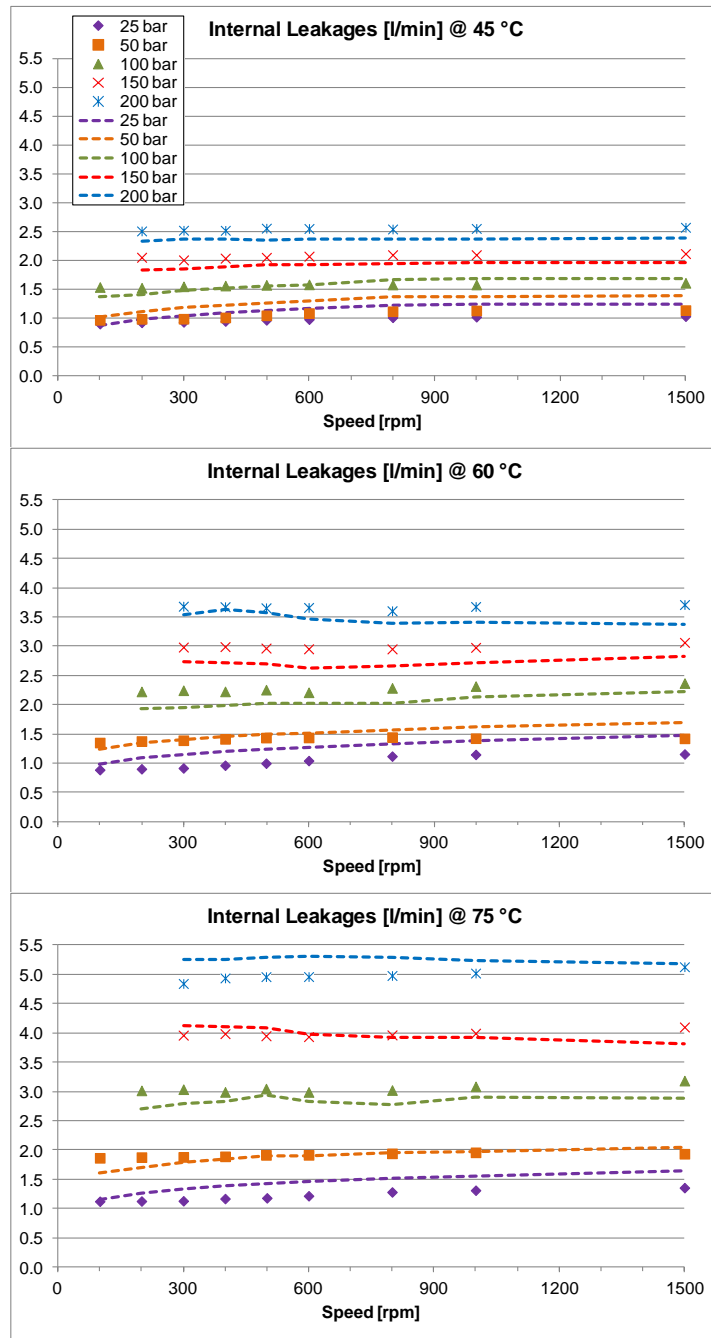


Figure 2.13 Internal pump leakages: experimental data (marks) and curves obtained by parametric model (dashed lines) at three temperatures

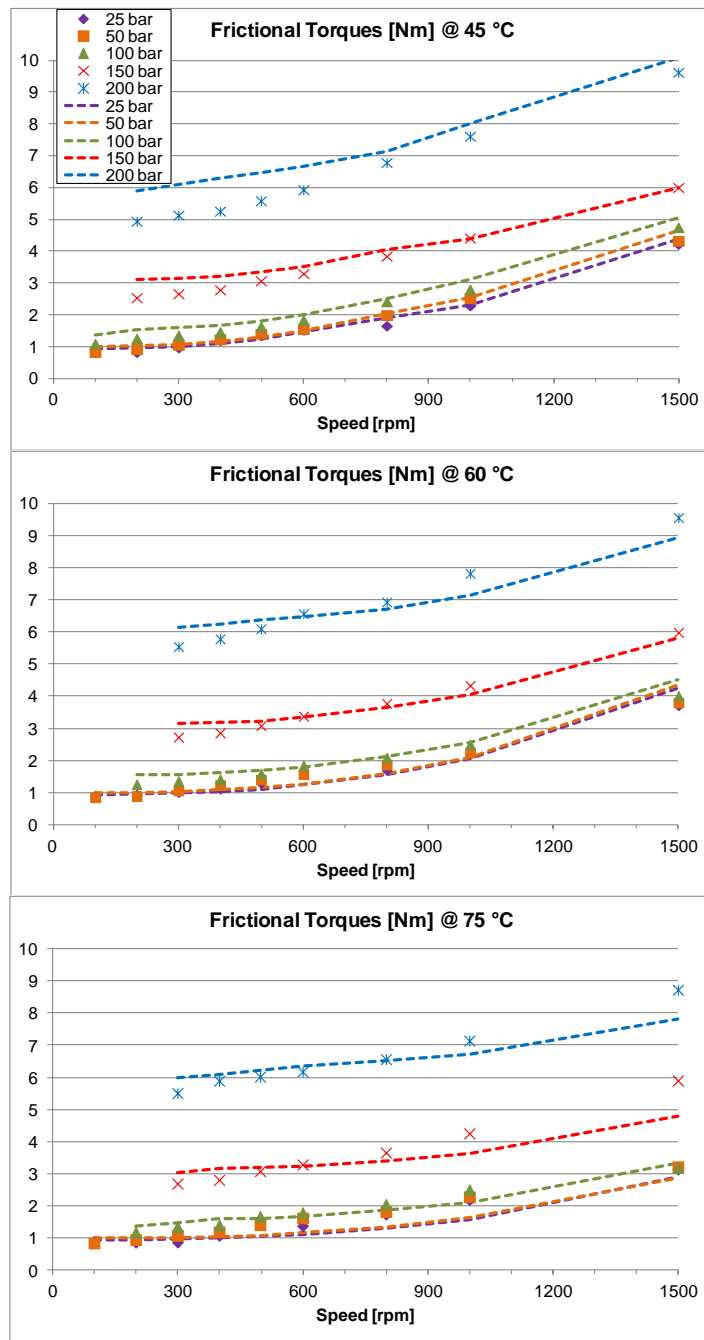


Figure 2.14 Frictional pump torques: experimental data (marks) and curves obtained by parametric model (dashed lines) at three temperatures

2.2.3 Detail Model: Hydraulic Virtual Prototype

The development of the parametric model in 2.2.2 has demonstrated the drawbacks due to modelling errors that make the parameterisation only useful for control design. The progressive improvement of the vane pump modeling concerns the evaluation of major non-linearities effects in a more realistic way through virtual prototyping.

The vane pump dynamics are now analyzed through the development of an AMESim virtual test bench which aims at simulating the frictional torques and the leakage flow rates in accordance to experimental data. The purpose is to insert the experimental curves directly in the AMESim model through lookup tables. Specific mechanical and hydraulic sub-models of the AMESim libraries are identified and simulation tests are performed in order to select the more adapted ones to reproduce the friction and leakage effects. At this modelling level, two models for pump energy losses are possible to be constructed:

- a hydraulic model that considers the dependence only from pressure and speed
- a thermal-hydraulic model that also evaluates the dependence from temperature

The thermal-hydraulic prototype represents a more complete model very useful when the variations of temperature have to be considered. It is developed in Chapter 5. For evaluation of all the other pump performance, e.g. acceleration and depressurisation phases, the hydraulic model represents a sufficient solution because the operative temperature can be assumed constant during all phases running and equal to tank temperature. AMESim Rev11 software enables to realise and simulate three different types of virtual prototypes which meet our needs:

- 1) hydraulic prototype with constant fluid temperature
- 2) hydraulic prototype with variable temperature affecting fluid properties
- 3) thermal-hydraulic prototype with variable temperature affecting fluid properties and pump energy losses

First solution, concerning the hydraulic prototype with fluid temperature maintained constant for all simulation time, is suitable to reproduce the pump energy losses as function of only pressure and speed. It is thus selected in this work section and described later. The third AMESim solution results useful for simulating the thermal-hydraulic effects which involve the module and so it is described in Chapter 5. The second solution

represents an intermediary between the others that permits to analyse the influence of fluid properties on pump performance when the temperature is varied.

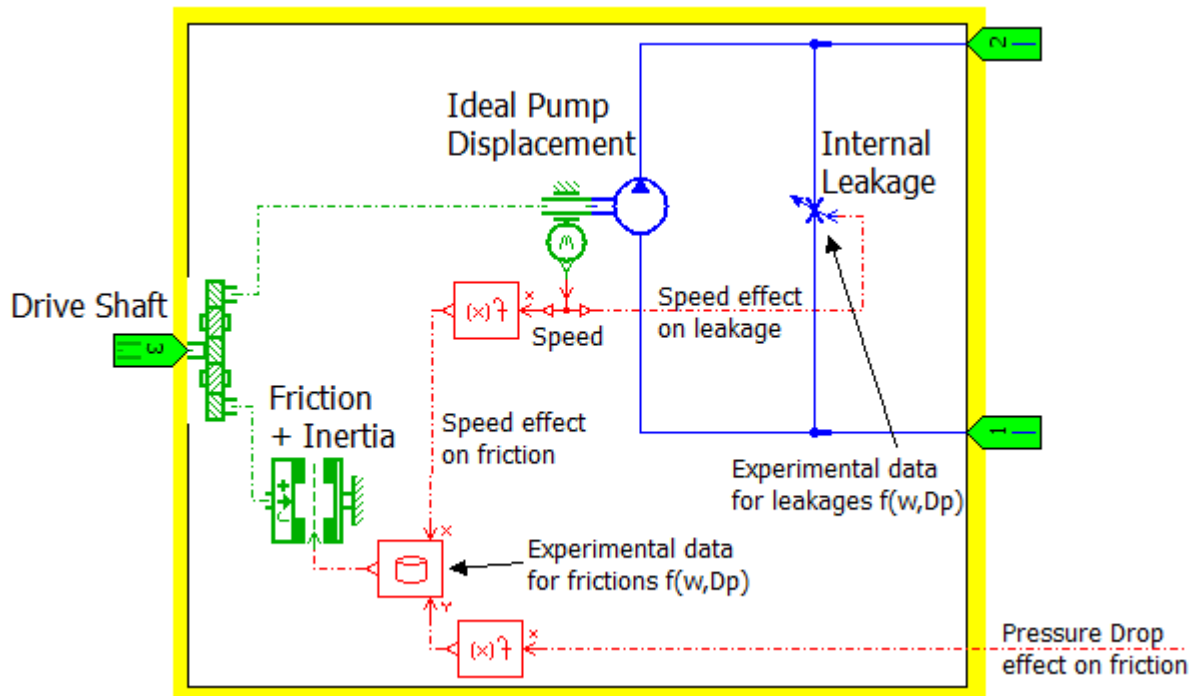


Figure 2.15 Hydraulic virtual prototype of vane pump

Figure 2.15 shows the hydraulic virtual prototype which simulates the vane pump performance using a generic implementation of its energy losses. At hydraulic ports 1 and 2, the line pressure is the input signal while at port 3 the input signal is represented by motor torque. The pressure drop represents another input signal necessary to evaluate the frictional torques (in the bottom of figure on right-hand side).

Therefore the frictional torques and leakages are considered dependent only on hydraulic lines pressure drop and on the pump speed while the temperature was fixed to 45 °C, value correspondent to typical fluid temperature inside tank.

2.2.3.1 Frictional Torques

In order to simulate the frictional torques, the component *FRIRK000* in the mechanical library of AMESim is selected (fig. 2.16) for its ability to vary friction versus operating conditions [29]. It is a rotary friction torque generator based on Karnopp model [30] that

deals and solves efficiently the numerical implementation of transition between sticking and sliding conditions. As required by the Karnopp model, the pump inertia is included in the friction component.

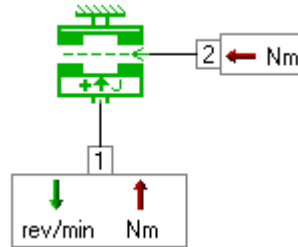


Figure 2.16 Component for pump frictions simulation, *FRIRK000*, from [29]

The experimental data of frictions torques can be implemented in AMESim by means of an ASCII file in the format multi 1-D tables [29]. It represents the input signal at port 2 of the component in fig. 2.16. This signal can be made dependent on pressure, velocity and temperature, either using a parameterised function or through a 3-D look-up table. A comparison between results provided by simulated and experimental curves is carried out in order to verify the quality of the simulation. The simulation results obviously agree well with experimental data inside the range of operating conditions performed in laboratory.

In order to extend the range of operating conditions where the AMESim model is capable to provide values of frictional torques, data have to be extrapolated. A linear extrapolation is carried out by the component *FRIRK000* in the range of pump speed from -3500 to 3500 *rev/min* and for positive pressure drop values. It is important to remark that the limit negative speed of -3500 *rpm* is just selected for simulation, even if it is not again demonstrated that the pump could really operate in this condition.

Figure 2.17 shows both the experimental curves in the range of laboratory tests and the extrapolated curves. It is interesting to mention that at zero speed the simulated frictional torques are not null but they correspond to stiction effect. This would not have been possible if *tanh* models were used. However, the Karnopp model requires defining a region around the exact null speed, where a threshold speed value is provided by user for transition between sticking and sliding conditions. In this context the value entered is of 0,36 *rev/min*, that corresponds to 1/10000 of the rated velocity.

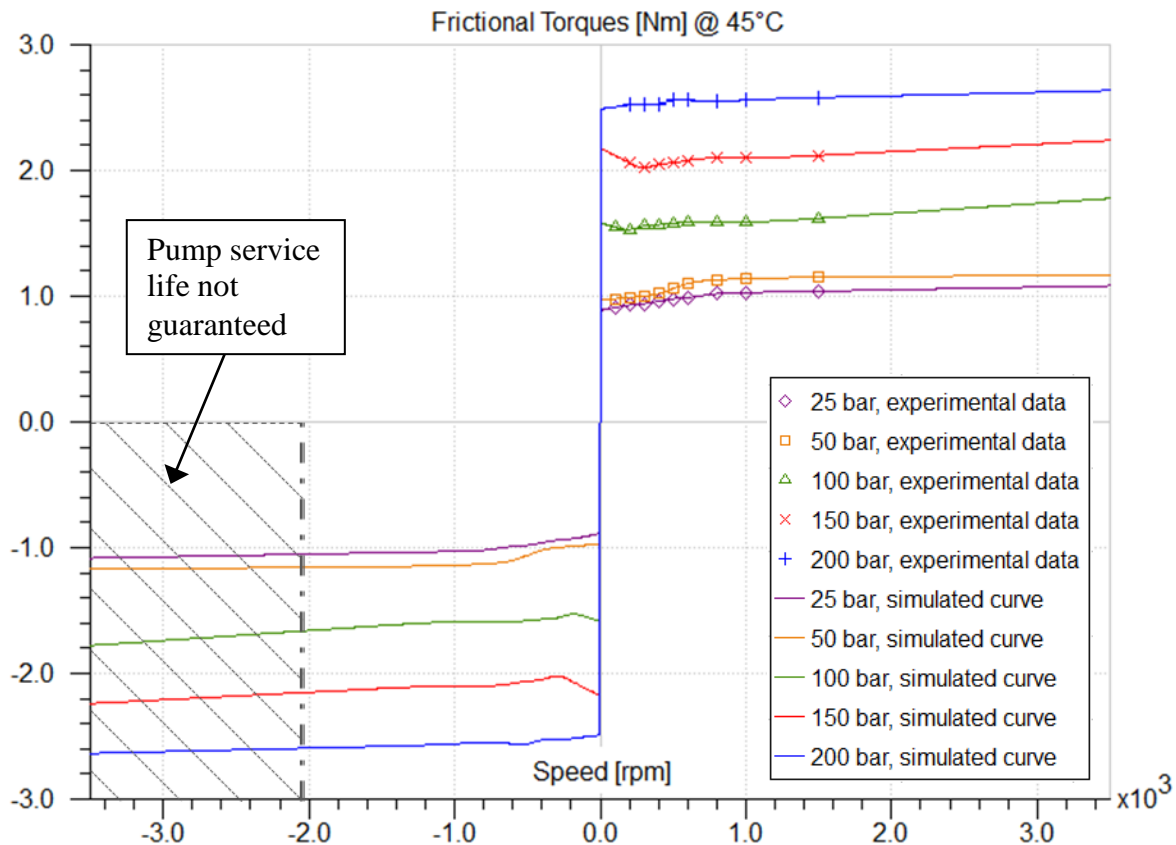


Figure 2.17 Frictional pump torques: extrapolation in the pump range: [-3500, 3500] rev/min provided by component FR1RK000

It is not easy to validate the extrapolated results provided at low speed near to zero through laboratory tests under constant operating temperature. Indeed, in condition of low speed, the volumetric flow coming into pump is not sufficient to produce an adequate recirculation of fluid that guarantees constant temperature inside pump. The AMESim model of frictional torques can be then improved by adding the dependence of friction to fluid temperature and by allowing testing the pump in those processes in which the evolution of temperature plays a fundamental role on performance degradations (thermo-hydraulic virtual prototype).

2.2.3.2 Internal Leakages

Concerning the leakages flow rates, the component *VOR001* is selected in the hydraulic AMESim library in order to simulate them by non-linear functions of pressure drop, pump speed (fig. 2.18) and later fluid temperature.

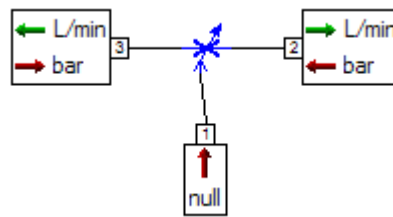


Figure 2.18 Component for pump leakages simulation, VOR001, from [29]

It represents a variable hydraulic orifice which provides, as outputs (ports 2 and 3), the leakage flow rate. In the component parameters table it is possible to insert directly the experimental data file as a $Q-\Delta p-\omega$ look-up table. The signal at port 1 is the pump speed. Like for the frictional torques, the experimental data have been implemented in AMESim model. A comparison between results provided by simulated and experimental curves is carried out in order to verify the quality of the simulation. Once again the simulation results obviously agree well with experimental data inside the range of operating conditions performed in laboratory.

For extending the range of operating conditions where the AMESim model provides values of leakage flow rates, an extrapolation of data is carried out. The intention is to make a generic model that can be used for pumps able to operate in all four quadrants. As just mentioned in section 2.1.3.1, the vane pumps do not accept negative values of pressure drop because they are designed to operate in two functional quadrants only, and they do not guarantee too severe negative speeds. Nevertheless the AMESim model also enables reaching these conditions through data cubic extrapolation for the speed range from -3500 to 3500 *rev/min* and for negative/positive pressure drops. Figure 2.19 shows both the experimental curves in the range of laboratory tests and the extrapolated curves. Ideally, it should be interesting to generate warnings during simulation when the model operates out of the pump acceptable domain.

Due to difficulty to maintain constant the operating temperature during laboratory tests, as already described for frictional torques, it is not an easy task to validate the extrapolated results provided at low speed near to zero. The AMESim model of internal pump leakages can be then improved by adding the dependence to the fluid temperature.

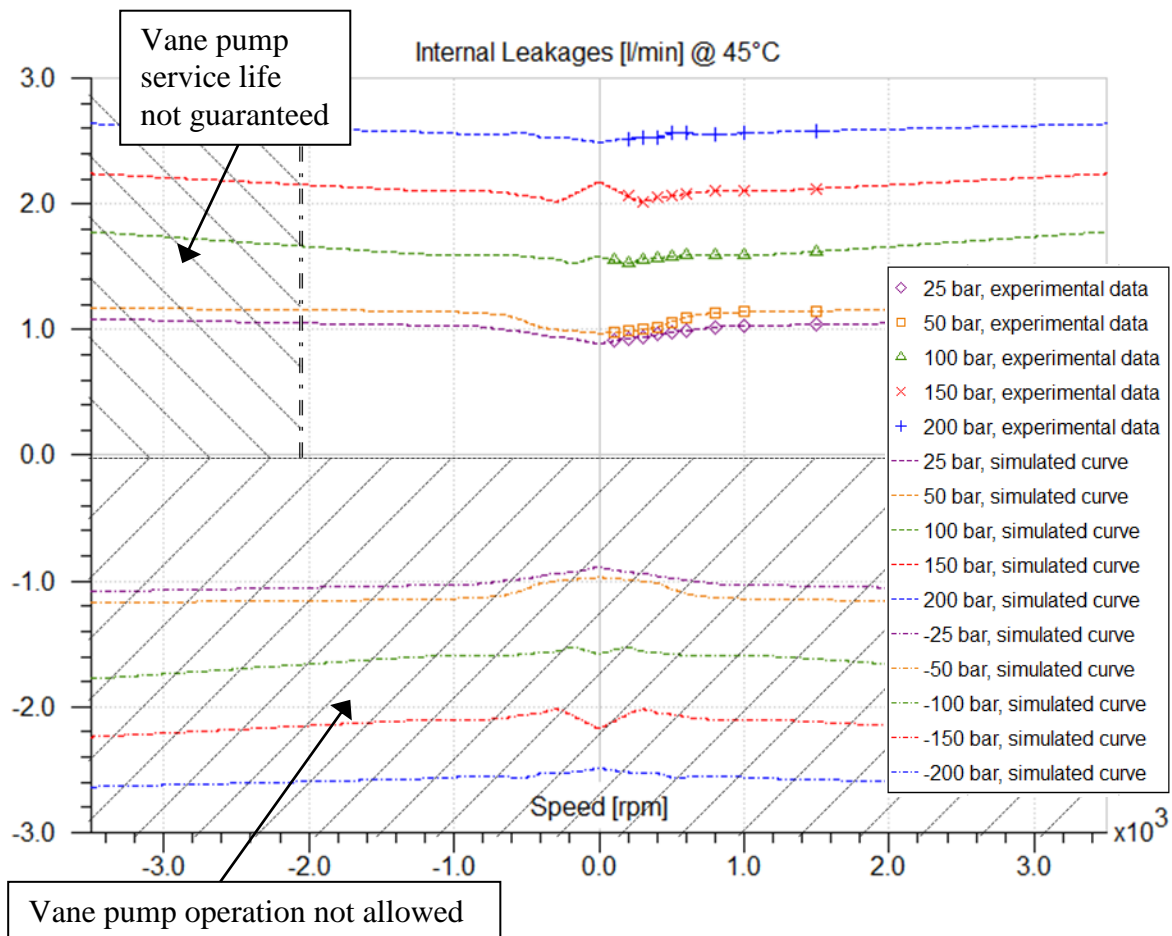


Figure 2.19 Internal pump leakages: extrapolation in the pump range: [-3500, 3500] rev/min provided by component VOR001

2.3 Conclusion

This chapter is dedicated to state of art of vane pump and its evolution in last seventy years. A qualitative comparison has been carried out with the principal competitors, especially the internal gears and axial pistons pumps, in order to underline advantages and limitations. The specificity of Parker vane pump Denison technology has been described with focus on pump components, operation principle and configurations for mobile and industrial applications. In particular the pump features of no-drained, two functional power quadrants and of cartridge concept have been addressed. The modelling at vane pump level has then been developed by evaluating its energy losses coming from internal leakages and frictional torques. Laboratory experiments were performed, in the frame of this work, in order to collect data for energy losses by varying the operating conditions in

terms of output pressure, pump speed and temperature of the fluid. After that a parametric model has been developed and found suitable for control design and preliminary functional models. A hydraulic virtual prototype of vane pump has finally been created in AMESim environment in order to simulate the energy losses. It is based on look-up tables, constituted by all the experimental data, and it also enables reproducing the internal leakages and the frictional torques out of the laboratory operating range. It thus results a very useful tool for simulating energy losses of general pumps operating in four quadrants too.

References

- [1] O. E. Rosaen. Vane Pump. *Patent N.2677330, May 04 1954, United States Patent Office.*
- [2] W. R. Tucker. Balanced Vane Pump. *Patent N.2368789, February 06 1945, United States Patent Office.*
- [3] C. S. Prendergast. Vane Displacement Pumps and Motors. *Patent N. 2928350, Mars 15 1960, United States Patent Office.*
- [4] P. C. Mortenson. Trends in Hydraulic Equipment for Mobile Construction Machinery. *Automotive Industries, June 15 1964.*
- [5] G. Hermann. Innover Face à la Crise. *Fluides & Transmissions N. 124, May 2009.*
- [6] G. Hermann. A la Recherche de l'Éfficacité Énergétique. *Fluides & Transmissions, February/Mars 2011.*
- [7] G. Hermann. Integration de Fonctions et Développement d'Ensembles Complets. *Fluides & Transmissions May/June 2013.*
- [8] W. E. Wilson. Rotary-Pump Theory. *Trans. ASME, 1946. vol. 68, n. 4, pp. 371-383.*
- [9] W. E. Wilson. Design of Optimum Clearances in Positive-Displacement Pumps and Motors. *Trans. ASME, 1956. pp. 117-122.*
- [10] Y. Inaguma, A. Hibi. Vane Pump Theory for Mechanical Efficiency. *Proc. IMechE, 2005. Vol. 219 part C. pp. 1269-1278.*
- [11] Y. Inaguma, A. Hibi. Reduction of Friction Torque in Vane Pump by Smoothing Cam Ring Surface. *Proc. IMechE, 2007. Vol. 221 part C. pp. 527-534.*
- [12] E. Gnesi, J-C. Maré, J. L. Bordet. Modelling of EHA Module Equipped with Fixed-Displacement Vane Pump. *The Thirteenth Scandinavian International Conference on Fluid Power, June 3-5, 2013. Linkoping, Sweden, pp. 141-152.*
- [13] N. Yoshida, Y. Inaguma. Mathematical Analysis of Efficiencies in Hydraulic Pumps for Automatic Transmissions. *Jtekt Engineering Journal, English Edition No. 1011E. pp. 64-73.*
- [14] T. Kazama, Y. Narita. Temperature Measurement of a Cam-Ring and Side-Plates in a Vane Pump. *Proceedings of the eighth JFPS International Symposium on Fluid Power, October 25-28, 2011. Okinawa, Japan, pp. 122-127.*
- [15] D. P. Winner. *Untersuchung der Verschmutzungsempfindlichkeit von Hydraulischen Verdrängereinheiten. Aachen, Germany, Mars 1987.*
- [16] A. Giuffrida, R. Lanzafame. Cam Shape and Theoretical Flow Rate in Balanced Vane Pumps. *Mechanism and Machine Theory 40, 2005. pp. 354-369.*

- [17] L. Z. Rocha, D. N. Johnston, S. N. Y. Gerges. Flow Ripple Reduction in Power Steering Hydraulic Pumps. University of Bath, 2010.
- [18] B. L. Jones, D. N. Johnston, D. K. Longmore. Simulation of Suction Flow Ripple in Power Steering Pumps. SAE, paper 982023.
- [19] S. Rancic. Reduction of Pressure Pulsations on Automotive Transmission Oil Vane Pump. Department of Mechanical Engineering, McMaster University, Hamilton, May 2014.
- [20] S. Yakabe, K. Nagata. Reduction of Pressure Fluctuation in a Vane Pump Using Genetic Algorithm. Proceedings of the 5th JFPS International Symposium on Fluid Power, Nara, Japan, November 13-15 2002.
- [21] <http://www.referenceforbusiness.com/history2/35/Denison-International-plc.html>
- [22] Parker Catalogue HY29-0008/US. Hydraulic Pump T7AS/T7ASW Series Vane Pumps, December 2005.
- [23] E G Papadopoulos, and G C Chasparis. Analysis and model-based control of servomechanisms with friction. *Proceedings of the IEEE/RSJ International Conference on Intelligent Robots and System, Lausanne, Switzerland, 2002.*
- [24] G. Velazquez, J-C. Maré. Bottom-up design of a variable displacement vane pump for automotive gear box, CD Rom Proceedings, 9th Scandinavian International Conference on Fluid Power, Linköping, Sweden, June 1-3, 2005, 11 pages.
- [25] P Krus. *Formula Book For Hydraulics and Pneumatics*. Fluid and Mechanical Engineering Systems, Department of Management and Engineering, Linköping University, Sweden. Revised 2008-10-27.
- [26] H. Rahnejat. Tribology and Dynamics of Engine and Powertrain: Fundamentals, Applications and Future Trends, 2010. Woodhead Publishing Limited
- [27] D. Knezevic, V. Savic. Mathematical Modeling of Changing of Dynamic Viscosity, as a Function of Temperature and Pressure, of Mineral Oils for Hydraulic Systems. *Facta Universitatis, Series: Mechanical Engineering*, vol. 4, n.1, 2006. pp. 27-34.
- [28] H. Abdi. The Method of Least Squares. Neil Salkind, 2007, Encyclopedia of Measurement and Statistics.
- [29] LMS-AMESim. *AMEHelp*
- [30] D Karnopp. Computer simulation of stick-slip friction in mechanical dynamic systems. *Journal of Dynamic Systems, Measurement and Control*. Vol. 7, March 1985.

Phases d'Accélération et Décompression

Dans ce chapitre les phases d'accélération et de décompression d'un cycle typique d'une machine à injecter sont analysées. L'architecture de référence du banc d'essais est tout d'abord définie et les équations principales décrivant sa dynamique sont développées. Puis, les contributions des paramètres de système, qui peuvent limiter la performance du module pendant l'accélération, sont évaluées séparément à travers une approche progressive basée sur l'analyse de boucle ouverte. Des valeurs numériques sont aussi fournies.

L'importance d'ajouter un contrôle en boucle fermée sur la vitesse de la pompe, pour l'asservissement du module dans la phase d'accélération, est montrée à travers un modèle linéarisé. L'étude est basée sur des hypothèses obtenues grâce aux conclusions dans la première partie de chapitre. Une amélioration d'architecture d'asservissement est alors réalisée par la mise en œuvre d'un compensateur feedforward. Les avantages du système complet contrôlé en boucle fermée, concernant la meilleure capacité d'accélération et l'erreur statique nulle, sont analytiquement simulés.

Un modèle de détail de banc d'essais est créé dans AMESim et constitué par l'asservissement en boucle fermée de vitesse, le variateur, le moteur électrique, l'accouplement moteur/pompe, la pompe à palettes et le circuit hydraulique.

Le prototype de la pompe à palettes représente une version améliorée du modèle décrit dans le Chapitre 2, grâce à la modélisation du volume HP de la pompe. Les avantages du prototype virtuel complet concernent la simulation des effets non-linéaires comme les pertes d'énergie de la pompe et la compressibilité du fluide. En particulier la compressibilité du fluide est rendue plus réaliste en évaluant les dépendances de l'effective Bulk Modulus de la pression de service, de la température du fluide, de la pression de saturation du liquide, de l'indice polytropique du gaz, du contenu d'air/vapeur et la déformabilité des tuyaux hydrauliques. Les essais en laboratoire sont alors exécutés et le prototype virtuel complet est finalement validé dans l'accélération la condition du régime établi.

La phase de décompression est ensuite simulée à travers le même prototype virtuel complet. Des essais du laboratoire ont permis de valider ce prototype. La pression de service ou la vitesse de la pompe sont contrôlés en boucle fermée, pendant les essais en

laboratoire, par l'utilisation d'un compensateur feedforward. La procédure de validation de prototype a également permis de déterminer un optimum du module d'Young qui est approprié pour simuler les dépendances entre la déformabilité des tuyaux hydrauliques et le delta pression pendant la décompression.

3 Acceleration and Depressurisation Phases

In this chapter the phases of acceleration and depressurisation are described in terms of requirements. Then preliminary analysis by means of analytical approach, and later by virtual prototyping for a more advanced estimation and reproduction, are addressed. The speed control synthesis is studied by underlining the advantages that the feedforward compensation adds in these phases where the speed is the controlled fundamental variable. The full virtual prototype is finally validated that permits to simulate: acceleration and depressurisation transient as well as steady-state conditions.

The acceleration transients represent a little percentage of the total cycle time duration of typical stationery machinery. Nevertheless customers impose requirements to minimise these transients because the final objective is to reduce the cycle time and to demonstrate high capability of productivity of own machine. Being apparently negligible, the transient times are usually not on total cycle time duration. Just thinking that the productivity of a plastic injection moulding machine, typically working 24 hours per day, can be increased up to 10-15 % monthly, by reducing the transients to minimum.

During acceleration transient, the motor speed has to be controlled in closed loop in order to meet specific machine cycle's requirements (table 1.3 in Chap. 1). The speed controlled acceleration represents the transition between the following moulding machine's phases (refers to fig. 1.18):

- Starting point/Mould closing
- Clamping/Dynamic injection
- Static injection/Vulcanisation (Plasticisation)
- Cooling time/Mould opening

It is observable from tab. 1.3 that, for example, the mould closing/opening and the dynamic injection for rubber need the maximum flow rate to be delivered. This flow has to be produced by the pump at the maximum speed of 3000 *rpm*. Therefore, the acceleration transients are characterized by a velocity max variation of $\Delta\omega = 3000 \text{ rpm}$ to be performed in lower than 50 *ms* (correspondent to 6283 *rad/s*²). On its side, the

acceleration transient, prior the vulcanisation, is lower: the $\Delta\omega$ is only of 1200 *rpm*, by considering a typical speed of 300 *rpm* during the static injection.

The depressurisation is a transition phase whose requirements to be satisfied are not generally defined a priori by customer. During this transient, the line pressure has to be reduced from a steady-state value to null. There are depressurisations in which the velocity also has to be reduced to zero while others in which just a speed reduction occurs (Tab. 1.3 in Chap. 1).

During depressurisation, the motor speed (or the line pressure) has to be controlled in order to meet specific machine cycle's requirements. By observing the table 1.3, it is possible to note that the depressurisation represents the transition between the following moulding machine's phases:

- Dynamic injection/ Static injection (for plastic)
- Vulcanisation /Cooling time (for rubber/plastic)
- Mould opening/Part ejection (for plastic)

The pressure drop, in the cycles described in tab. 1.3, is equal to 130 *bar* for rubber and to 105 *bar* for plastics between Vulcanisation and Cooling phases with reduction of velocity respectively of 1500 and 2700 *rpm*.

The study of acceleration and depressurisation phase is performed using a progressive approach to point out the main contributions to performance limitations. Then speed closed-loop controller is proposed to support the preliminary design of control architecture and to show the potential advantages of solutions involving feedforward.

3.1 Reference Architecture

In order to develop analytical models of the EHM, a reference architecture is firstly identified and showed in fig. 3.1. It refers to test bench built in Parker laboratory and described in section 1.4. The control system performs three closed-loops in cascade as it typically occurs in the control electronics unit implemented in machines (see fig. 1.16 in Chap. 1). The hydraulic pressure command Δp^* represents the input of the more external

loop concerning the actual pressure Δp . This pressure closed-loop then provides the speed command ω^* for the motor speed control loop. The output of torque C_m^* finally forms the input for the motor torque closed-loop that acts on motor currents. As just mentioned in section 1.4, the pressure and speed controls are implemented in the Host PC while the inner motor torque closed-loop is operated by the inverter. The dynamics of the motor rotor, vane pump, hydraulic line and load are then introduced by making the following assumptions for simplifying the treatise:

- 1) The mechanical transmission between electric motor and vane pump is considered perfectly rigid: the inertia of motor and pump are thus merged as single inertia J_{tot}
- 2) The pressure drops in the hydraulic line between pump and load are neglected. In this way the output pump flow rate corresponds to input hydraulic load flow rate
- 3) A separation in frequency domain is carried out by reproducing only the lowest frequencies, lower than 900 Hz. So the dynamics of torque, speed, flow rate and pressure sensors are neglected.

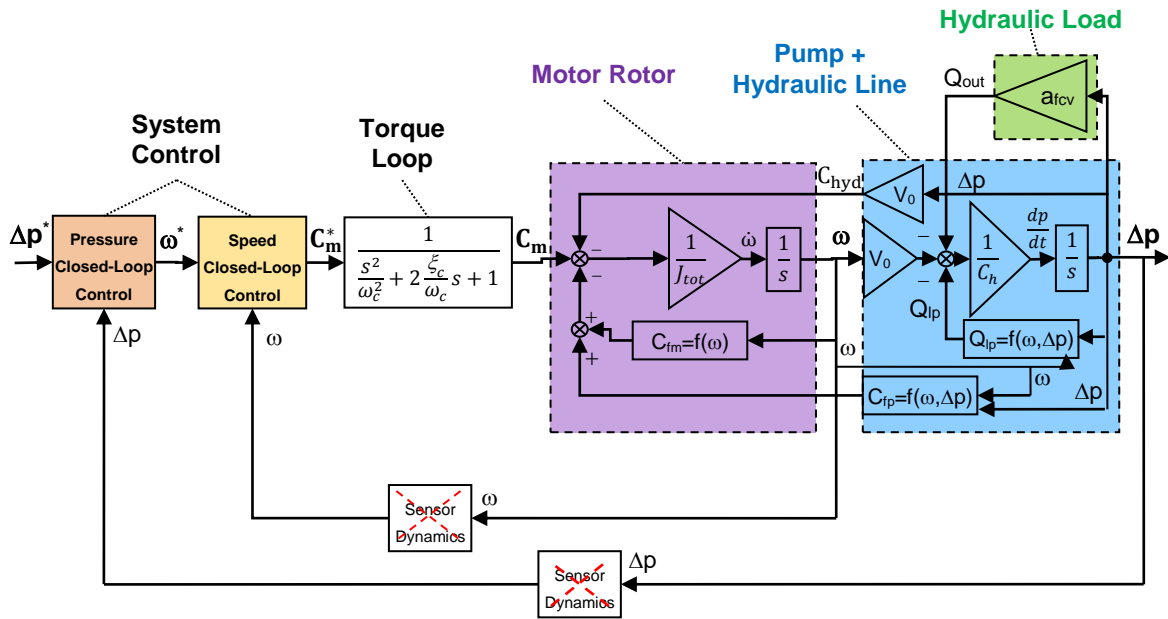


Figure 3.1 Reference architecture of the test bench

On the basis of these assumptions the functional model for analysis of EHM and test bench dynamics consists of the five following equations (3.1) to (3.5).

The **Momentum Balance** equation permits to correlate the torques applied on motor/pump shaft. Referred to shaft, the equation is given by:

$$J_{tot}\dot{\omega} = C_m - C_{hyd} - C_{fp} - C_{fm} \quad (3.1)$$

where

J_{tot} = total inertia of motor and pump

$\dot{\omega}$ = motor acceleration

C_m = motor torque

C_{hyd} = hydrostatic torque

C_{fp} = pump frictions

C_{fm} = motor frictions

The hydrostatic torque C_{hyd} is defined as:

$$C_{hyd} = V_0 \Delta p \quad (3.2)$$

where

V_0 = pump displacement

The pump dynamics is described by means of the **Flow Conservation Equation** written in reference to Control Volume of figure 3.2.

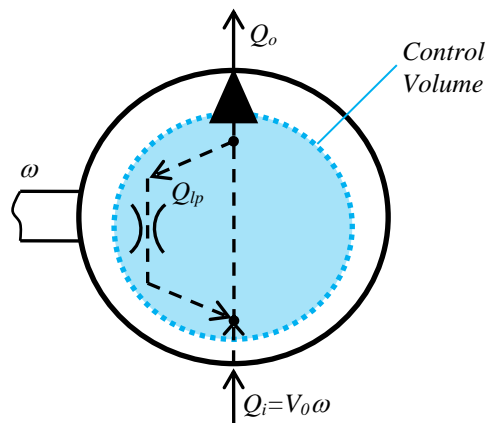


Figure 3.2 Control Volume

The balance of fluid flow rate, for the fluid contained in the control volume and under the assumption of no deformation of pump body, can be written in this way:

$$Q_o = V_0 \omega - Q_{lp} - C_h \dot{p} \quad (3.3)$$

where

Q_o = pump output flow rate

Q_{lp} = pump internal leakages

C_h = hydraulic capacity of the fluid

\dot{p} = time derivative of the pressure

$V_0 \omega = Q_i$ = pump input flow rate

The terms of hydraulic capacity C_h includes the fluid filling the pump and the hydraulic

line between pump and load.

A simplified model of the **hydraulic load** is also added. In this context, it is assumed that the load, represented by the flow control valve in test bench, acts as a hydraulic resistance under laminar flow:

$$Q_o = a_{fcv} \Delta p \quad (3.4)$$

where

a_{fcv} = characteristic of the flow control valve installed in the test bench

Appendix A shows the characteristics of the flow control valve in term of pair of pressure/flow rate values (Δp , Q_{out}). It is possible to assert that the valve almost behaves like a laminar orifice when “slow” variation of speed are applied. When acceleration/deceleration phases are indeed considered, we have decided to carry out a linearization by selecting the tangent to this curve at the specific operative point.

The torque (or current) control provides the command torque C_m to electric motor. It thus correlates the input signal C_m^* to C_m by means a relation that is function of the closed-loop dynamics:

$$C_m = f(C_m^*, t) \quad (3.5)$$

The motor power unit conventionally operates an inner closed-loop control on motor currents (or motor torque). This closed-loop is magnetically coupled because of the presence of the induced electromotive force, but it is not physically visible. The motor currents are generally not accessible by the user that so commands the drive by sending demand signals to motor currents closed-loop (as carried out in this thesis). The inverter’s manufacturer generally provides a model of the currents (or torque) dynamics characterised by a second order in which the dependence from the electromotive force is almost totally removed.

3.2 Acceleration Transient: Parameters Limiting Performance

The implementation of the motor speed control, as illustrated in fig. 3.1, improves the pressure control of EHM by operating an inner closed-loop. The advantages obtained through the speed control are particularly evident during the acceleration transients.

Indeed, requirements of time duration have to be satisfied for reducing as far as possible the transient and finally reducing all the cycle time.

In this context, a progressive analytical approach is thus proposed to point out the contribution of functional and parasitic parameters to EHM performance. The analysed system is composed by the dynamics of EHM and hydraulic circuit plus the speed and torque closed-loops while the pressure control is not considered at this modelling level (fig. 3.1). The following parameters or effects are taken into account:

- Motor current closed loop dynamics: natural frequency (f_c) and damping ratio (ξ_c)
- Electric motor: inertia (J_m), maximum peak torque (C_{max}) and frictions (α_{fm} and β_{fm})
- Vane pump: inertia (J_p), displacement (V_0), internal leakages (γ_{lp} and β_{lp}) and frictions (α_{fp} , β_{fp} and γ_{fp})
- Hydraulic circuit: fluid inertia (J_f) and hydrostatic torque ($\propto \Delta p$)

In next paragraph they are considered separately in order to evaluate each contribution.

3.2.1 Current Loop Dynamics

The current loop dynamics impacts the motor acceleration response time. According to the drive supplier, this dynamics can be represented by a second order transfer function with a natural frequency $f_c = 700 \text{ Hz}$ and damping ratio $\xi_c = 0.7$. In these conditions, the torque response C_m to torque demand C_m^* shows a response time t_c given by [1]:

$$t_c = \frac{2,9}{2\pi f_c} = 0.00066 \text{ s} \quad (3.6)$$

It only corresponds to 6.6 % of the targeted response time (10 ms) of the Parker EHM and so the equality $C_m = C_m^*$ is hereinafter assumed.

3.2.2 Effect of Max Torque and Inertia

In order to evaluate the contribution of motor peak maximum torque C_{max} , the open loop dynamics of the test bench is analysed through the motor speed time response $\omega(t)$

generated by a motor torque step demand $C_m(t)$. The equations described in section 3.1 are thus considered under the following simplifying hypotheses:

- 1) motor and pump frictions are neglected in (3.1)
- 2) pump internal leakages are neglected in (3.3)
- 3) the fluid is assumed to be incompressible in (3.3).

By inserting the expression of Q_o (3.4) in the (3.3), then by inserting the expression of Δp so obtained in the (3.2) and finally the expression of C_{hyd} in (3.1), it results:

$$J_{tot}\dot{\omega} + \frac{V_0^2}{a_{fcv}}\omega = C_m \quad (3.7)$$

The (3.7) represents a first order differential equation with constant coefficients and variable $\omega(t)$. The solution for a torque step of $C_m(t) = C_{m0} \cdot u(t)$ (where $u(t) = 0$ for $t < 0$ and $u(t) = 1$ for $t \geq 0$), is given by:

$$\omega = k_{\omega c1}(1 - e^{-t/\tau_1})C_{m0} \quad (3.8)$$

where

$$\tau_1 = \frac{J_{tot}a_{fcv}}{V_0^2} \text{ time constant}$$

$$k_{\omega c1} = \frac{a_{fcv}}{V_0^2} = \frac{\tau_1}{J_{tot}}$$

The (3.8) permits to analyse the motor speed time response $\omega(t)$ of the system in open loop conditions, when a torque step $C_m(t)$ is applied.

It clearly appears that the speed increase is directly proportional to the electromagnetic torque C_m . For this reason, it is interesting to parameterize the drive in order to allow the transient torque to be as great as possible in order to obtain the maximum acceleration.

The total inertia J_{tot} of the system influences the performance by means of the time constant τ_1 in the eq. (3.8). J_{tot} consists of three terms:

$$J_{tot} = J_m + J_p + J_f \quad (3.9)$$

where

J_m = motor inertia

J_p = pump inertia

J_f = inertia of the fluid

The inertia J_f represents the contribution of hydraulic inertia I_h of the fluid in the hydraulic lines linking the pump to machine. It reflects into the mechanical domain, at level of motor shaft. J_f is given by:

$$\begin{aligned} J_f &= I_h V_0^2 \\ I_h &= \frac{\rho L}{S} \end{aligned} \quad (3.10)$$

where

ρ = density of the fluid

L = length of the hydraulic line

S = cross-sectional area of hydraulic line

The table below compares each term of the (3.9) with reference to laboratory test bench characteristics and a hydraulic line of $L = 3 \text{ m}$ and inner pipe diameter = 26 mm .

Inertia	Value in [kgm^2]	% of J_{tot}
J_m	0,0092	96
J_p	0,00032	3,3
J_f	0,000062	0,7

Table 3.1 Evaluation of inertial contributions

On the basis of results inserted in tab. 3.1, it's possible to assert that:

- J_p and J_f can be neglected when compared to J_m
- J_p and J_f do not limit acceleration significantly

In the calculation of J_f , the assumption of hydraulic circuit length of 3 m is made. In the hypothesis of length up to 10 m , like it could occur in moulding machines, the contribution to J_{tot} in any case remains lower than 2.5 %.

3.2.3 Hydrostatic Torque

When the contribution of the hydrostatic torque C_{hyd} is also not considered in the eq. (3.1), the speed response $\omega(t)$ to step torque $C_m(t) = C_{m0} \cdot u(t)$ (where $u(t) = 0$ for $t < 0$ and $u(t) = 1$ for $t \geq 0$) degenerates into:

$$\omega = \frac{C_{m0}}{J_{tot}} t \quad (3.11)$$

A calculation is carried out for evaluating the contribution of hydrostatic torque in the acceleration and inserted in section 3.2.6.

3.2.4 Contribution of Motor and Pump Energy Losses

The contribution of motor frictions C_{fm} and pump leakages Q_{lp} and frictions C_{fp} is now considered in equations (3.1) and (3.3). The pump energy losses are described by means of parametric relations introduced in Cap. 2 where the dependence on temperature is here neglected by introducing a constant output viscosity μ_0 . For analysis, they are here linearized via Taylor series expansion to first order and around the reference point given by $\bar{\omega}=1154 \text{ rpm}$ and $\bar{\Delta p}=100 \text{ bar}$. Assuming that the energy losses do not appreciably modify the final value of ω compared to $\bar{\omega}$, The pump internal leakages (eq. 3.12) and frictional torques (eq. 3.13) are so expressed by:

$$\left\{ \begin{array}{l} Q_{lp} = B \frac{\gamma_{lp}}{\mu_0} \Delta p \\ C_{fp} = \alpha_{fp} + \beta_{fp} \mu_0 [\bar{\omega}^C + C \bar{\omega}^{C-1} (\omega - \bar{\omega})] + \gamma_{fp} [\bar{\Delta p}^D + D \bar{\Delta p}^{D-1} (\Delta p - \bar{\Delta p})] \end{array} \right. \quad (3.12)$$

The dependence of leakages on pressure is simplified in (3.12) because the coefficient $B=0.94$ is nearly to unit. The dependence on speed is indeed not considered because it is fully negligible when compared to pressure contribution.

The motor frictions C_{fm} are expressed, according to the supplier data, by considering Coulomb torque α_{fm} and viscous effect of parameter β_{fm} :

$$C_{fm} = \alpha_{fm} + \beta_{fm} \omega \quad (3.14)$$

By inserting the eq. (3.12) in (3.3) and (3.13-3.14) in (3.1) the speed response $\omega(t)$ to torque demand $C_m(t) = C_{m0} \cdot u(t)$ (where $u(t) = 0$ for $t < 0$ and $u(t) = 1$ for $t \geq 0$) is given by:

$$\omega = k_{\omega c2} \left(1 - e^{-\frac{t}{\tau_2}} \right) (C_{m0} - C_0) \quad (3.15)$$

where

$$\tau_2 = \frac{J_{tot} \left(\alpha_{fcv} + B \frac{\gamma_{lp}}{\mu_0} \right)}{V_0^2 + \gamma_{fp} D \bar{\Delta p}^{D-1} V_0 + (\beta_{fm} + \beta_{fp} \mu_0 C \bar{\omega}^{C-1}) \left(\alpha_{fcv} + B \frac{\gamma_{lp}}{\mu_0} \right)}$$

$$k_{\omega c2} = \frac{\tau_2}{J_{tot}}$$

$$C_0 = \alpha_{fm} + \alpha_{fp} + \beta_{fp} \mu_0 \bar{\omega}^C (1 - C) + \gamma_{fp} \bar{\Delta p}^D (1 - D)$$

3.2.5 Contribution of Fluid Compressibility

The former calculations are carried out by assuming that the fluid to be infinitely rigid. It is now intended to assess the effect of fluid compliance. For this purpose, the equivalent fluid Bulk Modulus β_f has to be evaluated. In practice β_f varies as function of several parasitic effects (major details are provided in Appendix B). In the present context the contribution of β_f is analysed by fixing its value and by considering that the hydraulic capacity C_h in the eq. (3.3) is given by:

$$C_h = \frac{V_{tot}}{\beta_f} \quad (3.16)$$

where

V_{tot} = total volume of pump + hydraulic line between pump and flow control valve

By neglecting the motor and pump energy losses, the speed response $\omega(t)$ to step torque $C_m(t) = C_{m0} \cdot u(t)$ (where $u(t) = 0$ for $t < 0$ and $u(t) = 1$ for $t \geq 0$) is given by the following expression dependent on actual value of β_f . $\omega(t)$ results:

$$\omega = k_{\omega c1} \left(1 - k_{\omega c3} e^{-\xi_n \omega_n t} \sin \left(\omega_n \sqrt{1 - \xi_n^2} t + \varphi \right) \right) C_{m0} \quad (3.17)$$

where

$$k_{\omega c1} = \frac{a_{fcv}}{V_0^2}$$

$$k_{\omega c3} = \sqrt{\frac{1 - 2\xi_n \omega_n \tau_3 + \omega_n^2 \tau_3^2}{1 - \xi_n^2}}$$

$$\omega_n = V_0 \sqrt{\frac{1}{J_{tot} C_h}}$$

$$\xi_n = \frac{a_{fcv} C_h \sqrt{J_{tot}}}{2V_0}$$

$$\tau_3 = \frac{C_h}{a_{fcv}}$$

$$\varphi = \text{atan} \left(\omega_n \tau_3 \sqrt{1 - \xi_n^2} / (1 - \xi_n \omega_n \tau_3) \right) + \text{atan} \left(\sqrt{1 - \xi_n^2} / \xi_n \right)$$

3.2.6 Conclusions

Numerical results are obtained by applying the equations of former sections which analytically determine the motor speed time response $\omega(t)$ to a motor torque step demand $C_m(t) = C_{m0} \cdot u(t)$ where $u(t) = 0$ for $t < 0$ and $u(t) = 1$ for $t \geq 0$. The maximum delta speed $\Delta\omega$ that can be reached after $t = \bar{t} = 10 \text{ ms}$ is thus calculated for the given parameters. Table 3.2 shows the parameters (or effects) taken into account, the analytical expression of $\omega(t)$ and the final results of $\Delta\omega$ after 10 ms. The case defined as 1) in the table, represents the reference condition when C_{m0} is assumed equal to the maximum peak motor torque C_{max} and the total inertia and the hydrostatic torque are also considered in the calculation. Next cases are instead obtained by modifying, adding or subtracting one parameter or more with reference to case 1). The numerical values of the motor torques and frictions are taken by catalogue [2] and the inertias are inserted in table 3.1. It is supposed to be produced a line pressure difference of $\Delta p = 100 \text{ bar}$ that determines the value of the coefficient a_{fcv} of the flow control valve acting as a hydraulic load in the test bench. The fluid hydraulic capacity C_h is calculated by fixing the fluid Bulk Modulus to $\beta_f = 6000 \text{ bar}$ and the total volume of fluid V_{tot} to 1,8 l. The pump energy losses are evaluated by means of the parametric model described in Chap. 2. The calculations inserted in the table 3.2 aim to show an example of the contribution of each functional and parasitic parameter on the acceleration performance. The idea is so to demonstrate as to neglect some contributions can hardly influence the final solution. It is also important to underline that the dynamic behavior is influenced by the equilibrium condition. Table 1.3 page 30 shows in fact that the acceleration transients can occur at different initial speeds and both at null or not pressure drop. In order to simulate the contributions with just a study case, we have finally decided to select an operative point at 100 bar and to show the effects of hydraulic torque and energy losses too.

The results listed in table 3.2 are revised in figure 3.3 by showing the contribution on delta speed $\Delta\omega$ that each parameter (or effect) can add or subtract to/from the reference case described by 1). In particular it is remarkable that:

- when the torque input is reduced by C_{max} to \bar{C}_m = continuous motor torque, $\Delta\omega$ reduces of about 60 %. Here clearly it appears that the speed is directly proportional to electromagnetic torque C_m
- if the hydrostatic torque C_{hyd} is not considered, $\Delta\omega$ increases over the 18 %

- if the pump J_p and line J_f inertia are not taken into account in the total inertia J_{tot} the committed error is of little consequence, lower than 3,5 %
- the motor and pump energy losses contribute to reducing $\Delta\omega$ of only 2 %
- Considering the fluid compliance permits to increase the maximum speed $\Delta\omega$ up to 19 %. However it is important to highlight that in this case the line pressure after 10 *ms* only corresponds to 16 *bar* (the 100 *bar* are reached after about 25 *ms*).

It is finally possible to conclude that:

- 1) The motor current closed loop dynamics does not limit the acceleration
- 2) The motor peak maximum torque directly limits the acceleration. Therefore the C_{max} of the upper bound of demand torque saturation in the inverter has to be set to the motor maximum acceptable value, without risk of demagnetisation or excessive temperature at windings
- 3) The line pressure in the hydraulic circuit produces a hydrostatic torque that cannot be neglected because it significantly limits acceleration
- 4) The pump J_p and fluid J_f inertia are negligible compared with motor inertia J_m
- 5) The motor frictions and the pump internal leakages and frictional torques do not limit the acceleration
- 6) The fluid compliance has to be taken into account because it significantly limits acceleration

Case	Parameters	Expression of $\omega(t)$, Hp: $C_m = C_m^*$	$\Delta\omega(t)$ after 10 ms
Torque loop dynamics only	f_c, ξ_c	Response time t_c of torque command C_m to torque demand C_m^* $t_c = \frac{2,9}{2\pi f_c} = 0,00066 \text{ s}$	
I) = max peak motor torque + total inertia + hydrostatic torque	$C_{m0} = C_{max}$ J_{tot} $C_{hyd}@100bar$	$\omega = k_{\omega c1} (1 - e^{-t/\tau_1}) C_{m0}$	1148 rpm
I) with max peak motor torque = continuous m. torque	$C_{m0} = \bar{C}_m$ J_{tot} $C_{hyd}@100bar$	$\omega = k_{\omega c1} (1 - e^{-t/\tau_1}) C_{m0}$	696 rpm
I) - hydrostatic torque	$C_{m0} = C_{max}$ J_{tot}	$\omega = \frac{C_{m0}}{J_{tot}} t$	1365 rpm
I) - pump inertia - line inertia	$C_{m0} = C_{max}$ J_m $C_{hyd}@100bar$	$\omega = k_{\omega c1} (1 - e^{-t/\tau_1}) C_{m0}$	1188 rpm
I) - line inertia	$C_{m0} = C_{max}$ $J_m + J_p$ $C_{hyd}@100bar$	$\omega = k_{\omega c1} (1 - e^{-t/\tau_1}) C_{m0}$	1154 rpm
I) + motor/pump energy losses	$C_{m0} = C_{max}$ J_{tot} $C_{hyd}@100bar$ C_{fm}, C_{fp}, Q_{lp}	$\omega = k_{\omega c2} \left(1 - e^{-\frac{t}{\tau_2}}\right) (C_{m0} - C_0)$	1122 rpm
I) + fluid compliance	$C_{m0} = C_{max}$ J_{tot} $C_{hyd}@100bar$ $\beta_f=6000bar$	$\omega = k_{\omega c1} \left(1 - k_{\omega c3} e^{-\xi_n \omega_n t} \sin\left(\omega_n \sqrt{1 - \xi_n^2} t + \varphi\right)\right) C_{m0}$	1364 rpm
I) + fluid compliance + motor/pump energy losses	$C_{m0} = C_{max}$ J_{tot} $C_{hyd}@100bar$ $\beta_f=6000bar$ C_{fm}, C_{fp}, Q_{lp}	eq.(3.21) developed in section 3.3.2	1340 rpm

Table 3.2 Numerical results of the maximum delta speed $\Delta\omega$ reached after 10 ms and obtained by means of the equations described in last sections

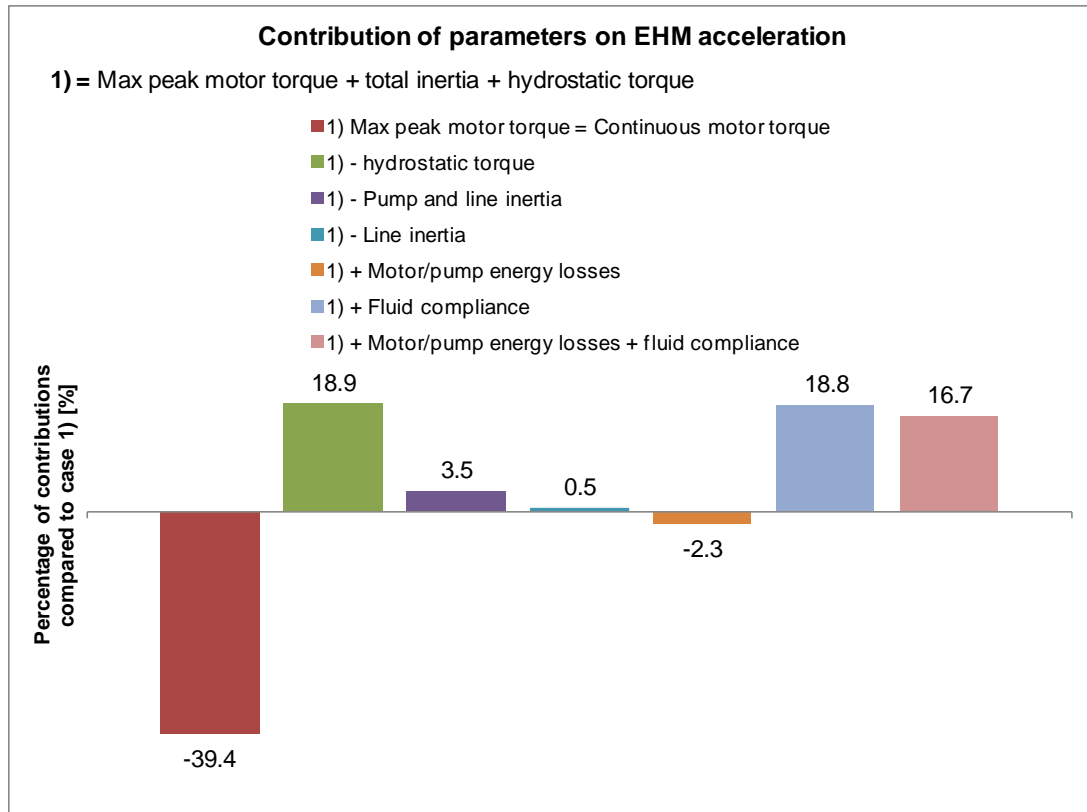


Figure 3.3 Percentage of contribution on EHM acceleration given by each parameter (or effect) with reference to case N.º1) characterised by: max peak motor torque, total inertia and hydrostatic torque

3.3 Velocity Closed Loop Synthesis

In this paragraph the closed loop dynamics of the speed loop is analysed in a linear form through system transfer function. Then various controller types are proposed and compared: firstly a conventional controller with simple pure gain is described, after that it is improved by adding parallel feed-forward compensators on the basis of an S-R-T controller scheme.

3.3.1 Closed Loop System Dynamics: ω/ω^* Transfer Function

The system dynamics in closed loop is analyzed through the transfer function ω/ω^* obtained by the schematic of test bench in fig. 3.1. The dynamics of: rotor, pump, hydraulic line and load are taken into account. The ω can be expressed by means of relation:

$$\omega = f(\omega^*, \Delta p, \alpha_{ftot}) \quad (3.18)$$

where ω^* represents the input command signal, Δp is the disturbance signal related to line pressure and α_{ftot} is the disturbance signal given by sum of motor α_{fm} and pump α_{fp} static frictions.

On the basis of conclusions obtained in 3.2.6 concerning the parameters limiting performance and on general considerations, the following hypotheses are made to get a low-order linear model:

- 1) A separation in frequency domain is carried out by reproducing only the frequencies lower than 700 Hz. So the motor current closed loop dynamics is neglected: $C_m = C_m^*$
- 2) The total inertia corresponds to motor inertia: $J_{tot} = J_m$
- 3) The motor enables to generate the max peak torque C_{max}
- 4) The fluid is assumed compressible, so the hydraulic capacity C_h is used
- 5) The motor and pump energy losses are linearly considered.

The motor and pump energy losses are taken into account even if they do not play a fundamental role in the acceleration while they significantly influence the steady-state performance.

By starting from these hypotheses, the speed control synthesis is so fulfilled in order to design the best solution able to satisfy the requirements of accuracy, rapidity and stability in acceleration and in steady-state condition.

3.3.2 Proportional Controller

The speed controller is initially considered proportional with pure gain K_ω (fig. 3.4). It provides a reference performance and points out the effort to be done for meeting the performance requirements.

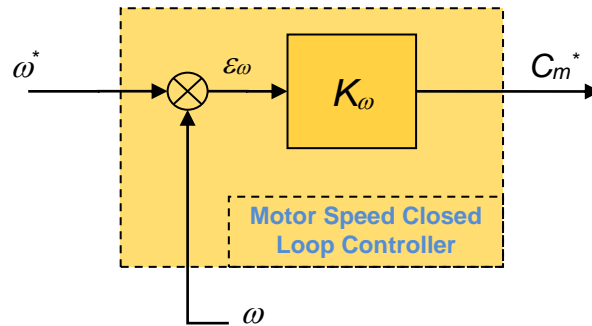


Figure 3.4 Proportional Motor Speed Controller

The proportional controller is defined by:

$$C_m^* = K_\omega \varepsilon_\omega \quad (3.19)$$

where

K_ω = proportional gain

ε_ω = velocity error

ε_ω is given by the following relation:

$$\varepsilon_\omega = \omega^* - \omega \quad (3.20)$$

Consequently the closed-loop transfer function ω/ω^* is obtained by means of the eq.s (3.1) to (3.5) and (3.19) and (3.20). It results:

$$\omega(s) = H_\omega(s) K_\omega \omega^*(s) \quad (3.21)$$

where H_ω is the transfer function of the system. Table 3.3 contains the expression of

numerator N_ω , denominator D_ω and gain k_ω of H_ω . In the same table the expression of the damping ratio ξ_ω and of the undamped natural frequency ω_ω , characterizing the denominator D_ω , and of the τ_ω relative to zero of the numerator N_ω , are also inserted.

$H_\omega = k_\omega \frac{N_\omega}{D_\omega}$	
$k_\omega =$	$1/(J_m \tau_\omega \omega_\omega^2)$
$N_\omega =$	$1 + \tau_\omega s$
$D_\omega =$	$\frac{s^2}{\omega_\omega^2} + 2 \frac{\xi_\omega}{\omega_\omega} s + 1$
$\tau_\omega =$	$\frac{C_h}{\left(a_{fcv} + B \frac{\gamma_{lp}}{\mu_0}\right)}$
$\xi_\omega =$	$\frac{\left[\left(a_{fcv} + B \frac{\gamma_{lp}}{\mu_0}\right) J_m + C_h (\beta_{fm} + \beta_{fp} \mu_0 C \bar{\omega} + K_\omega)\right]}{2 \sqrt{C_h J_m} \sqrt{\left(a_{fcv} + B \frac{\gamma_{lp}}{\mu_0}\right) (\beta_{fm} + \beta_{fp} \mu_0 C \bar{\omega} + K_\omega) + \gamma_{fp} D \Delta \bar{p} V_0 + V_0^2}}$
$\omega_\omega =$	$\frac{\sqrt{\left(a_{fcv} + B \frac{\gamma_{lp}}{\mu_0}\right) (\beta_{fm} + \beta_{fp} \mu_0 C \bar{\omega} + K_\omega) + \gamma_{fp} D \Delta \bar{p} V_0 + V_0^2}}{\sqrt{C_h J_m}}$

Table 3.3 Characteristics of the transfer function H_ω of ω/ω^*

The transfer function H_ω is constituted by a pair of complex conjugate poles and a zero, both placed in the half-plane of Real negative axis in the (Re, Imm) domain. Table 3.4 shows the numerical values obtained by selecting the fluid Bulk Modulus $\beta_f = 6000 \text{ bar}$, $\mu_0 = 2.77 \cdot 10^{-2} \text{ Pa}\cdot\text{s}$ at 45°C and the control gain $K_\omega = 0.382 \text{ Nm/rad/s}$.

A study is then conducted on the major requirements of accuracy, rapidity and stability that the controlled dynamical system has to satisfy when a speed step $\omega^*(t) = \omega_0 \cdot u(t)$, with $u(t) = 0$ for $t < 0$ and $u(t) = 1$ for $t \geq 0$, is applied. The constant value of ω_0 is fixed to 1000 rpm . The speed response is traced in figure 3.6.

k_ω	$[1/(\text{Nm}\cdot\text{s})]$	1.395
τ_ω	$[\text{s}]$	0.078
ξ_ω	-	0.855
ω_ω	$[1/\text{s}]$	31.11

Table 3.4 Numerical values of H_ω transfer function characteristics

In practice, the proportional controller is not sufficient to make system dynamics enough quick by producing a low rise time, even if the presence of the zero ($-1/\tau\omega$) improves the rapidity of the system dynamics by moving the poles pair toward the negative direction of Real axis in the Complex plane (Re,Imm). In addition, the steady-state value is equal to 493 rpm and the $\pm 5\%$ response time is not acceptable (about 23 ms). Moreover the steady-state value of velocity also depends on the constant disturbance α_{frot} (eq. 3.21) that comes from the motor and pump static frictions. Being about 1.5 Nm, its impact on the control gain is not negligible.

In next paragraph an advanced solution is proposed to improve the performance of velocity closed loop obtained with a simple proportional controller.

3.3.3 Parallel Feedforward Compensator

In order to improve the performance of the velocity closed-loop control in both transient and steady-state conditions, a solution is proposed making use of a *two degrees of freedom controller*. It combines the closed-loop proportional controller and a feedforward compensator.

The feedforward control is often used in parallel to PID controller to optimise its behaviour as, for example, in the case of clamp mechanism motion control in injection moulding machines described in [3]: there the knowledge beforehand of the force required to move the crosshead and based on reference velocity signal, permits to obtain the position of the proportional valve in advance, and so to provide the right anticipation signal through a feedforward action. Another typical application is the compensation of load disturbance. In this case a dynamic feedforward control is implemented to enhance the tracking control performance, as described in [4]. Iterative Learning Controls also develop feedforward actions generated by the error signals formed during the previous control cycle and updated in a point-to-point fashion [5]: processes with repetitive nature are controlled in this way as the injection moulding processes and in robotics domain.

In this specific application case, the closed-loop proportional controller is maintained invariant with respect to description in 3.3.2. The feedforward contribution consists of adding a feedforward control signal u_f to control the signal u_p in order to minimise the velocity error (fig. 3.5). In this way an anticipation effects is produced that improves the

acceleration transient capability and, in the same time, that reduces the static error for better system accuracy.

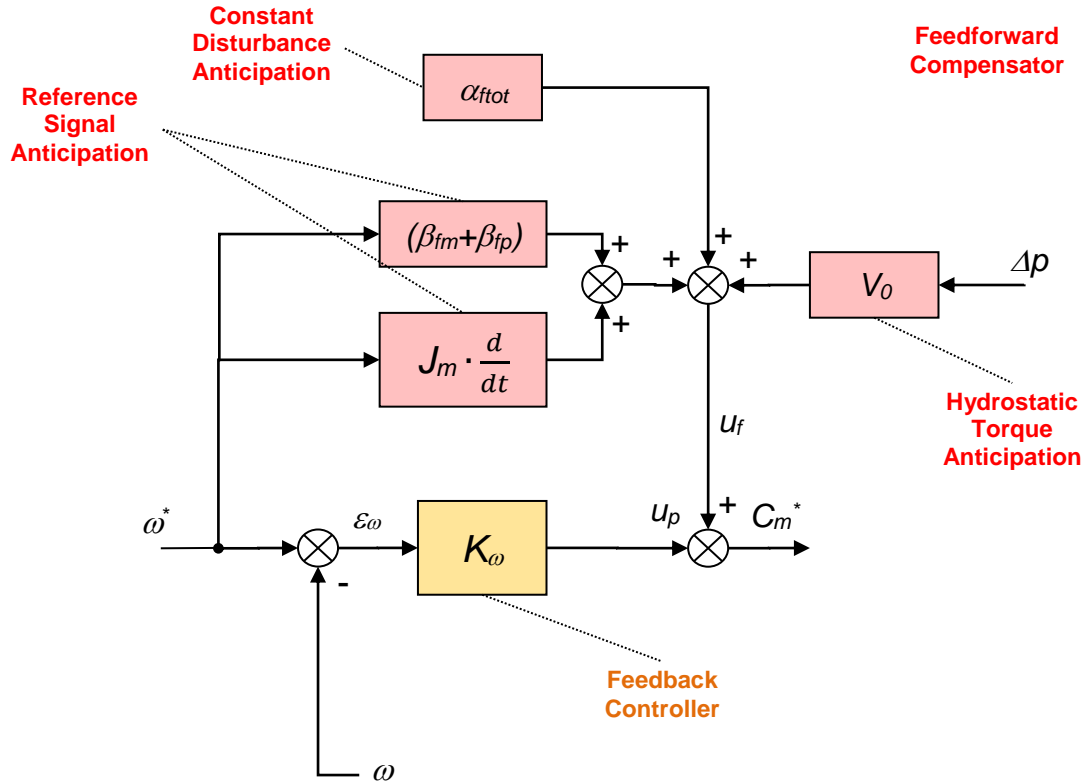


Figure 3.5 Two degrees of freedom controller: closed-loop controller and feedforward compensator

With reference to fig. 3.5, the equation (3.19) relative to controller dynamics can be rewritten as follows:

$$C_m^* = u_p + u_f \quad (3.22)$$

By assuming $\omega = \omega^*$ at any time and by using the eq. (3.1) for express C_m^* , the (3.22) can be re-elaborated as follows:

$$\omega^*(J_m s + \beta_{fm} + \beta_{fp}) + V_0 \Delta p + \alpha_{ftot} = K_\omega \varepsilon_\omega + u_f \quad (3.23)$$

Being the objective to eliminate the static error ε_ω , u_f is finally given by:

$$u_f = \omega^*(J_m s + \beta_{fm} + \beta_{fp}) + \alpha_{ftot} + V_0 \Delta p \quad (3.24)$$

The signal u_f is so constituted by four terms:

- 1) Derivative contribution of command speed input ω^* due to inertial motor torque
- 2) Viscous friction contributions of motor and pump
- 3) Static friction of motor and pump
- 4) Hydrostatic torque related to line pressure

In particular, the derivative contribution enables to improve the acceleration transient being equal to zero in steady-state condition, the pump/motor frictions especially contribute in steady-state condition while the hydrostatic torque in both of them. At this modeling level, the internal pump leakages are not taken into account even if they principally play a role on system accuracy.

It is worth mentioning that feedforward performance is limited by:

- the ability to derivate ω^* without noise and phase lag for inertia compensation
- the accuracy of energy losses model for friction compensation.

Next paragraph shows a comparison between these types of controller implemented in a EHM velocity closed-loop.

3.3.4 Advantages and Limitations of Feedforward Compensator

A numerical comparison is then carried out on velocity closed-loop time response when three different types of controller were implemented:

- a) P proportional controller
- b) P proportional controller plus inertia feedforward (FF) compensation
- c) P proportional controller plus full FF compensation

The command consists of a speed step $\omega^*(t) = \omega_0 \cdot u(t)$, with $u(t) = 0$ for $t < 1$ s and $u(t) = 1$ for $t \geq 1$ s, $\omega_0 = 1000$ rpm. Figure 3.6 shows the reference speed step $\omega^*(t)$ and the speed response $\omega(t)$ in the three cases a), b) and c).

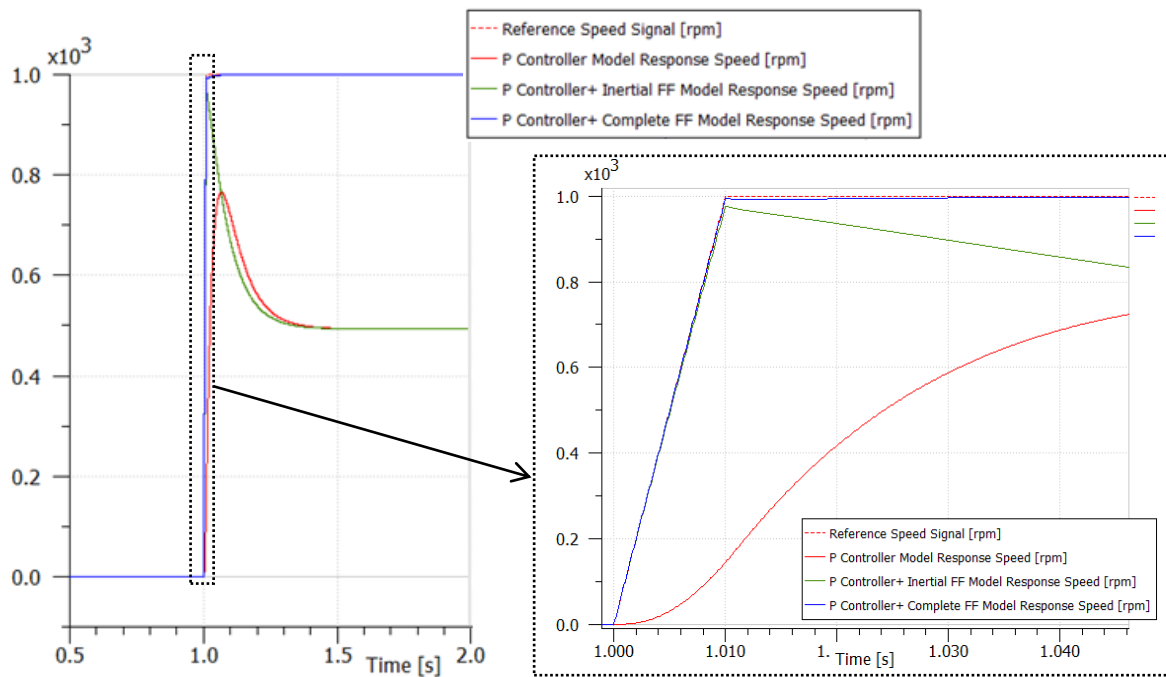


Figure 3.6 Simulation of the speed time response $\omega(t)$ obtained by analytical model for three different cases. The torque limit is fixed to C_{max}

The FF compensator with inertial anticipation improves the acceleration phase without modifying the steady-state value obtained with a simple P controller. It demonstrates that the inertial effect is the major contributor to dynamic error during transient and that the acceleration requirement is nearly met by adding only inertial feedforward.

The full FF compensator produces double improvement: in acceleration and steady-state conditions. It reduces nearly to zero the velocity error. The advantages of a full FF are so evident when compared to P controller.

If the full FF is compared to PID controller, some considerations can be made about. In general the use of a PID controller requires the interaction study between functional and parasitic effects depending on integral and derivative actions.

The derivative action improves the closed-loop stability. It also produces a feedforward action on the set point derivative that cannot be separated from the derivative feedback. The result is a simultaneous action on performance where two actions work together: a stabilizing action due to a derivation feedback of actual output signal and a feedforward action due to a derivation of command signal. However the gains of these actions are identical that does not make it possible to dissociate the actions. It also suffers from other limitations as noise generated by derivative action and incapacity to stabilize modes which are very badly damped [6].

The integral action improves accuracy and eliminates the static error. If integral action takes benefits to system accuracy and rapidity, on the other hand it generates also phenomena which can degrade practical stability. They are about overshoot in transient condition, a low frequency oscillation of linear origin and a low frequency oscillation related to system non-linearities [6].

However system frequency responses in magnitude and phase are related each other: in fact integral action brings also a phase reduction of 90° and derivative action brings also a magnitude increase, both profitless for stability. PID controlled system final synthesis has so to take into account the practical limitations just exposed.

The feedforward structure is faster and more effective than a closed-loop structure because it is in open-loop [7]. The advantage in the use of feedforward compensator is that it does not affect the closed-loop system stability because the action of anticipation is robust (as far as the model is sufficient accurate).

Some attention has to be paid concerning the hydrostatic contribution because Δp is a function of ω through the eq.s (3.3) - (3.4): it means that finally the dependence on Δp builds a loop on feedback speed ω that could modify the dynamical stability of the system operating in speed closed-loop. The quality of feedforward compensators design so depends on good knowledge of the system parameters J_m , β_{fm} , β_{fp} , α_{fm} , α_{fp} and V_0 . The J_m , β_{fm} , α_{fm} and V_0 are parameters from catalogue and so well-known, while, the β_{fp} and α_{fp} , are determined through the parametric model based on experimental data exposed in Chap. 2, and so having a certain level of uncertainty.

In conclusion, the analytical linear approach previously conducted, permits to:

- 1) analyse the contribution of functional and parasitic parameters in acceleration transient by means of system open loop dynamics and to identify the more important effects,
- 2) analyse the system dynamics when the velocity closed loop control is implemented by means of its transfer function properties and the time response characteristics,
- 3) implement a full feedforward compensator in the EHM velocity closed loop control and to demonstrate the advantages compared with P controller.

The model also shows some limitations due to uncertainty of parasitic effects when modelled in a linear way. It is the case of the pump internal leakages and frictional torques

and of fluid Bulk Modulus. In practice, the pump energy losses depend non-linearly on line pressure, speed and temperature and they affect especially the steady-state condition. The Bulk Modulus that is assumed invariant in the model, hardly affects the acceleration and so a more advanced modelling has to be developed to make the predicted response more realistic.

3.4 Detail Model through a Full Virtual Prototype

A full virtual prototype is developed in AMESim in order to improve the analysis developed in 3.3 by adding all the non-linearities neglected in the former modelling phase. The virtual prototype reproduces the full test bench built in Parker laboratory and described in Chap. 1. It consists of EHM (electric motor, vane pump and shaft coupling), hydraulic circuit, inverter and velocity closed-loop control developed into Simulink Real-Time Workshop (Fig. 3.7).

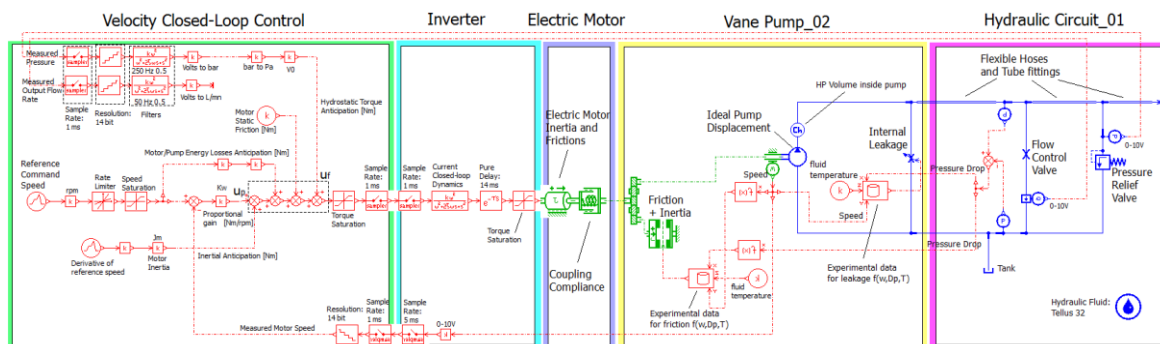


Figure 3.7 Full Virtual Prototype

3.4.1 Velocity Closed-Loop Control and Inverter

The velocity closed-loop control, modelled in AMESim, reproduces the control structure implemented in Simulink environment where a full feedforward compensator is also inserted (fig. 3.8). A rate limiter and speed saturation are added to prevent that the command speed ω exceeds the allowed values. The command torque signal C_m^* , obtained by the sum of signals u_p and u_f in accordance to eq. (3.22), is outputted and sampled at 1

ms. The feedback analogical signals, provided by the measurement box, are also represented. They correspond to measured pressure, output flow rate and actual speed. Each feedback analogical signal is firstly sampled and quantized by the Simulink acquisition system with resolution grade of 14 bit. After that each signal is filtered, with typical second order filters, in order to reduce noise (damping ratio of 0.5 and frequency of 250/50 Hz depending on treated signal dynamics) and finally transformed from Volts into the correspondent measurement unit. We have been obliged to introduce filters for reducing the measurement noise that hardly affected the signals.

The inverter receives the command torque C_m^* , sent by Simulink, and samples it at 1 ms. The motor currents closed-loop dynamics is also represented by a second order transfer function, as described in section 3.2.1. The demand torque C_m is finally generated after having been delayed and saturated (upper limit equal to C_{max}). In the bottom of inverter block the feedback speed signal ω is firstly sampled at 5 ms and after sent by the inverter to Simulink model through the measurement box.

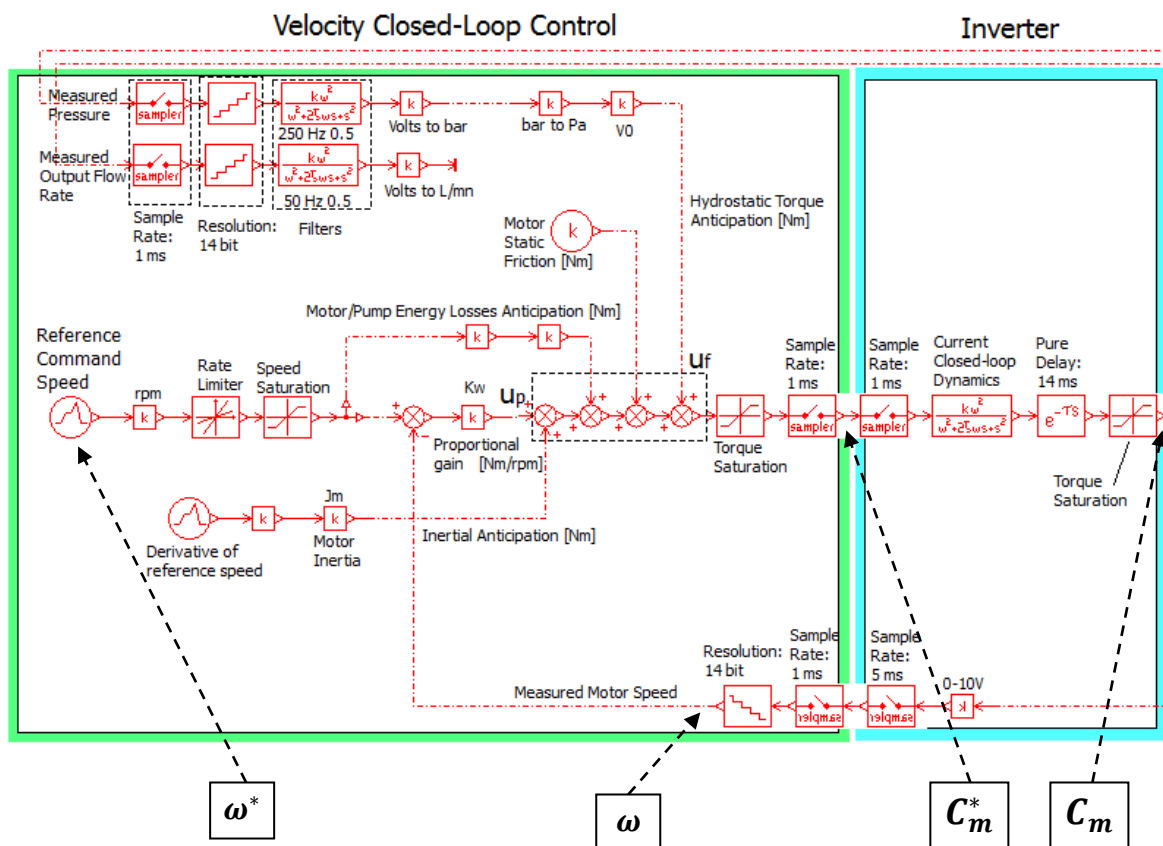


Figure 3.8 Virtual prototype of velocity closed-loop control and inverter

3.4.2 Electric Motor and Motor/Pump Coupling

The electric motor is just modelled by means of a sub-model that reproduces its inertia and the effects of viscous and Coulomb frictions, in accordance to eq. (3.14), figure 3.9. The motor/pump coupling is instead modelled through a spring-damper. Since motor and pump are connected by a single shaft, the high stiffness is simulated by a high spring stiffness (equal to continuous motor torque \bar{C}_m per rotation degree) and null damping coefficient.

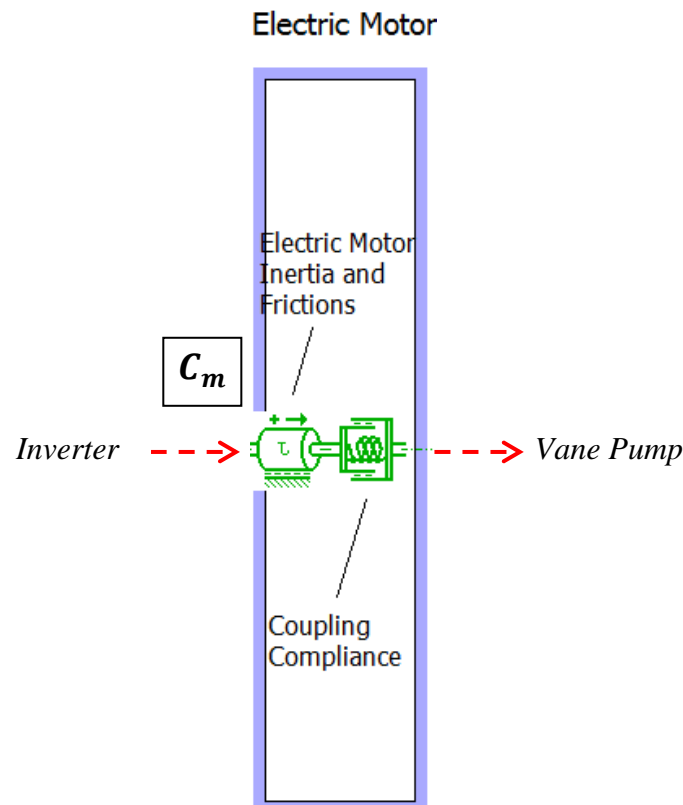


Figure 3.9 Virtual prototype of electric motor

3.4.3 Vane Pump_02 Prototype

The virtual prototype of the vane pump (fig. 3.10), corresponds to an improved version of the pump prototype described in Chap. 2 where the followings modifications are made:

- 1) Addition of a volume chamber that simulates the HP pump volume
- 2) Internal leakages and frictions are evaluated by look-up tables which also depend on fluid temperature

The reason of point 1) is due to interest in evaluating the variation of the fluid hydraulic capacity C_h that plays a fundamental role during the acceleration, as exposed in section 3.3.

Concerning the point 2), the look-up tables are now more complete because constituted by all the experimental data obtained at the three fluid temperatures 45, 60 and 75 °C described in Chap. 2. In this case the temperature represents a constant input to be fixed at the beginning of simulation and that remains invariant during all running time.

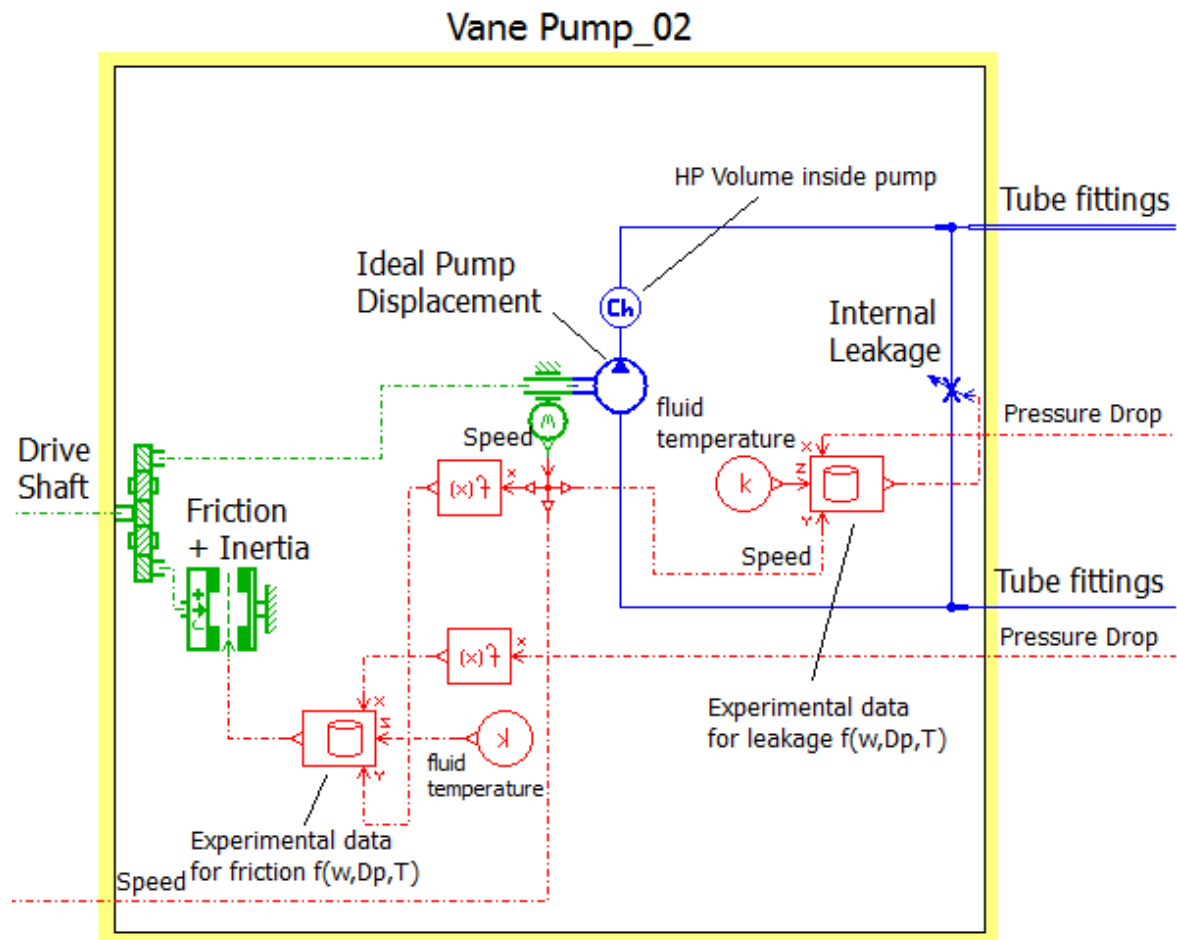


Figure 3.10 Vane pump_02 virtual prototype

3.4.4 Hydraulic Circuit_01

The virtual prototype of the hydraulic circuit consists of flow control valve, pressure relief valve, flexible hose, tube fittings and tank, in accordance with the test bench described in Chap. 1. The pressure and flow rate sensors are also modelled by simple transducers which send analogical signals in volts towards the measurement box. The sensors

dynamics are not taken into account. It is interesting to remark that both the flexible hose and tube fittings are modelled by complex lumped elements in which resistive R , capacitive C and inertial I effects are considered. The sequence of these effects depends on the order of connection between the hydraulic components, as showed in figure 3.11. In detail, the two hydraulic components modelling the tube fittings on the top of figure, are respectively represented by a sequence (from left to right-side): $IR-C-IR$, $C-IR$. The flexible hose is instead modelled by means of a lumped distributive sub-model in which all the variables, as pressure and flow rate, are calculated at a number of selected nodes (from 0 to 100). In this case the sequence of parasitic effects is the following: $C-IR-***-IR-C$ depending on number of nodes. It has the advantages of providing a homogenous implementation of all the 1-D Navier-Stokes equations, associated to each node, which are reduced to a set of ordinary differential equations. The drawback is that the computational time hardly increases due to the introduction of extra state variables [8].

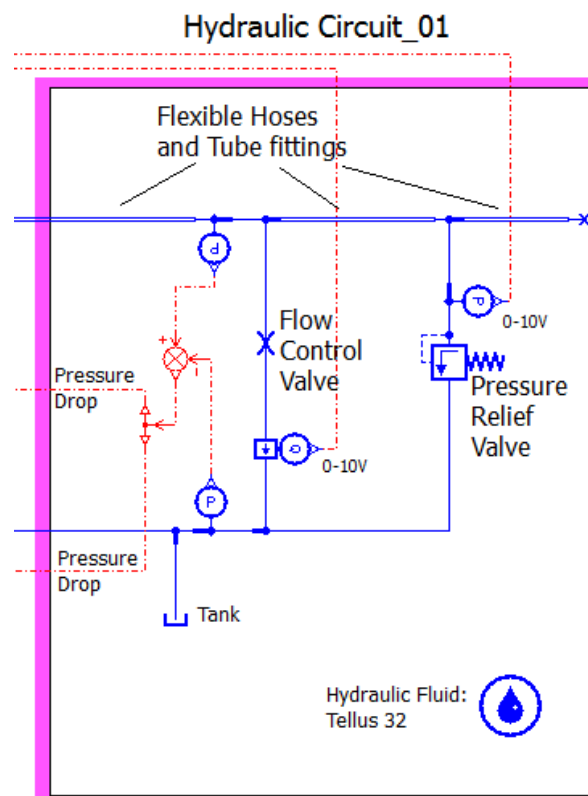


Figure 3.11 Virtual prototype of the hydraulic circuit

The steady state friction is taken into account by using a friction factor. This is calculated for each component as function of flow conditions which depend on pipe roughness and Reynolds number, the latter calculated as internal variable of sub-model.

The frequency dependent friction is also evaluated through a dynamic number of state variables used to correct the flow rate derivatives in the lumped inertia elements.

The compressibility of the fluid is calculated in an advanced manner by using an Effective Bulk Modulus β_e . This is based on evaluation of contribution relative to wall compliance and to air content in the hydraulic fluid.

3.4.5 Advantages of Virtual Prototyping: Energy Losses and Bulk Modulus

The full virtual prototype potentially improves the linear analytical modelling exposed in 3.3, in the simulation of EHM acceleration and of steady-state condition.

It indeed enables to evaluate the pump energy losses in a more complete form by means of look-up tables including all the experimental data obtained in laboratory.

In addition it determines the fluid hydraulic capacity C_h through the calculation of a variable Effective Bulk Modulus β_e that makes the C_h more realistic. The β_e is expressed by the following relation [9]:

$$\frac{1}{\beta_e} = \frac{(1 - \varepsilon)}{\beta_f(p, T)} + \frac{\varepsilon}{\Gamma p} + \frac{D_{in}}{E t} \quad (3.25)$$

where

ε = volumetric content of air/vapour in the liquid

Γ = polytropic index of the transformation of air/gas content

D_{in} = inner diameter of the pipe

t = pipe wall thickness

E = Young's modulus of the pipe material

Equation (3.25) shows the β_e dependence on parasitic effects and on operating conditions (pressure and temperature). The difficulty is to determine all these dependences because they are not known a priori. In order to quantify preliminarily the contribution of each parasitic effect, a calculation is firstly carried out and based on literature and manufacturer's data, [9] to [20] (more details are inserted in Appendix B). The result of this preliminary evaluation establishes the acceptable range for the following parameters:

- $\Gamma \in [1; 1.4]$
- $\varepsilon \in [1; 10]\%$
- $E \in [9076.8; 90706.8] \text{ bar}$

The saturation pressure P_{sat} of the fluid represents another fundamental parameter to be identified because it influences the aeration. For pressure lower than P_{sat} , the aeration process is in fact induced and the air dissolved in the fluid starts to come out of the solution as free gas.

After that, the comparison with real tests permits to vary these parameters inside range in order to obtain more accurate values and finally to make the virtual results close to real ones.

3.5 Laboratory Tests for Acceleration

Laboratory tests are performed in order to compare the results obtained by means of linear analysis and virtual prototype. During tests, the motor speed is closed-loop controlled three different type of controller as just described in 3.3.4: P proportional controller, P proportional controller plus inertia FF compensation and P proportional controller plus full FF compensation. The controller is implemented into Simulink that directly drives the inverter by torque demand signal C_m^* .

A command speed step $\omega^*(t) = \omega \cdot u(t)$, with $u(t) = 0$ for $t \leq 1 \text{ s}$ and $u(t) = 1$ for $t \geq 1.01 \text{ s}$, $\omega = 1000 \text{ rpm}$, is applied. An acceleration transient of 10 ms is thus commanded. The output flow at operating point is fixed by setting opening of the hydraulic load valve, prior the test running, in order to produce the following five values of pressure difference Δp : 0, 25, 50, 75 and 100 *bar*. 15 tests are so finally performed by varying line pressure value and control type.

During tests the following variables are measured: command speed ω^* , measured speed ω , line pressure Δp , output flow rate Q_{out} , command motor torque C_m^* , estimated motor torque C_{est} , tank temperature T_{tank} .

In order to compare measured and simulated speeds, characteristics of the time response

of speed are considered, as showed in figure 3.12:

- Δt_{drive} : time delay between command and measured speed
- Δt_{ω} : rise time necessary to speed increase from 0 to 1000 rpm
- ω_{max} : maximum measured speed
- ω_{∞} : steady-state speed (ω_{∞})

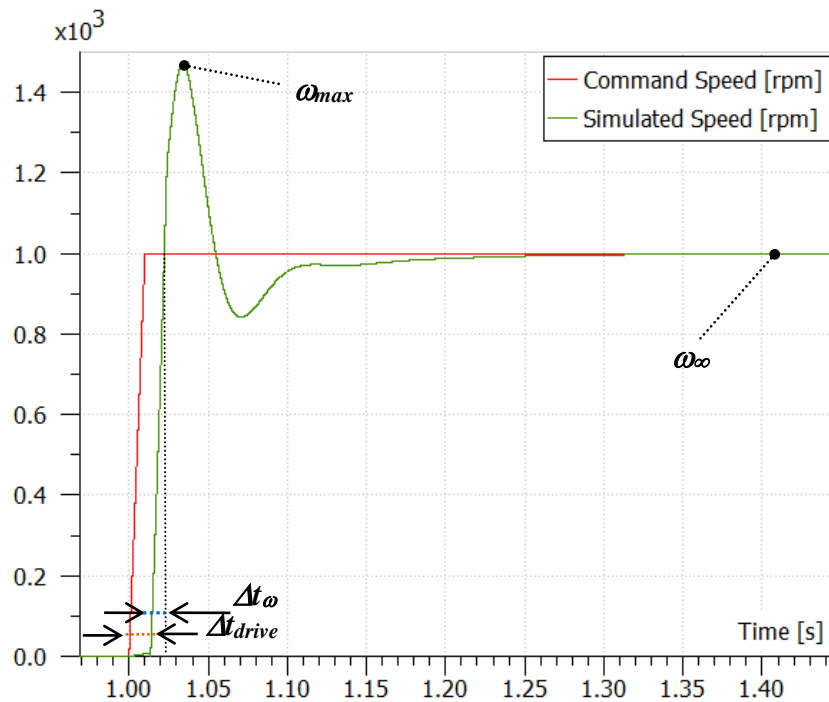


Figure 3.12 Characteristics of the measured speed time response

3.5.1 Simulation Procedure of Prototype

The procedure used to simulate the full virtual prototype is constituted by three simulation steps. The objective is to make the simulated curves close to experimental ones by varying the parameters described in 3.4.5 concerning the evaluation of β_e . With reference to scheme in the figure 3.13, the sequence of steps is as follows:

- **First Step.** It concerns the simulation of the partial AMESim model constituted by the *hydraulic circuit + pump* (block A in the fig. 3.13). In this case the input signal of the model is represented by the measured motor speed $\tilde{\omega}$. This simulation permits to neglect the mechanical contributions and command chain. The

parameters are varied in accordance to calculated ranges. The outputs of the model are: $\Delta p'$ and Q_{out}' .

- **Second Step.** The *mechanical components* are added: electric motor and pump inertia and frictions (**block B**). In this case the input signal of the model is represented by the estimated torque C^{\wedge} . This simulation permits to neglect the command chain. The three parameters are varied in accordance to ranges. The outputs of the model are: $\Delta p'$, Q_{out}' and ω' .
- **Third Step.** The *velocity closed-loop control and the inverter* are added in order to build the complete AMESim model (**block C**). In this case the input signal to model is represented by the command speed ω^* . The parameters are varied in accordance to ranges. The outputs of the model are: $\Delta p'$, Q_{out}' , ω' and C' .

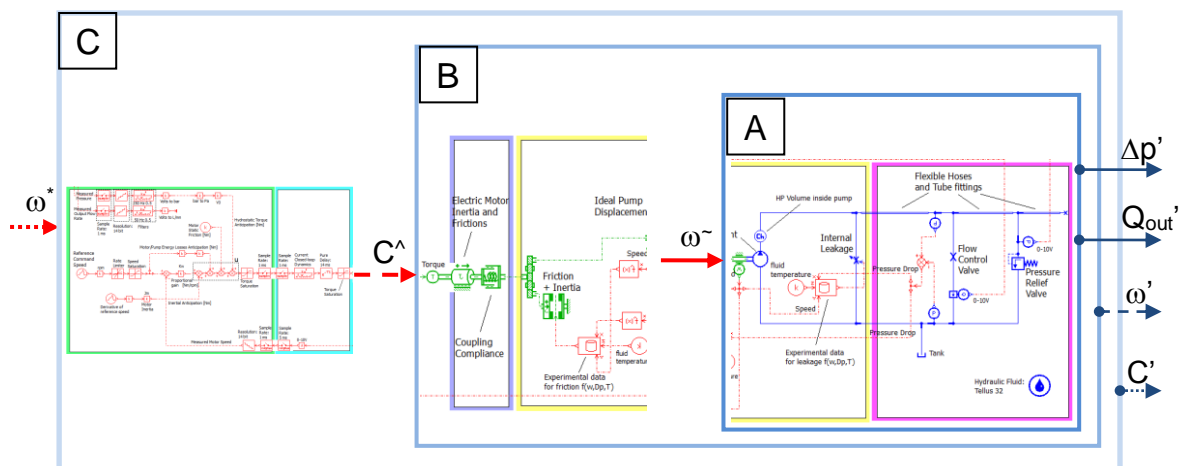


Figure 3.13 Scheme of simulation steps sequence

This type of simulation, based on partial AMESim model, enables to vary the three parameters in a more gradual way by observing their influence on system's variables. It also enables to obtain a compromise solution that is close to real performance of line pressure, output flow rate and motor speed.

Next chapter shows the comparison between experimental curves and simulated ones provided by the complete AMESim virtual prototype.

3.6 Comparison between Analytical Model, Real and Virtual Tests

Figure 3.14 shows an example of comparison between experimental, analytically and virtually simulated time response of motor speed and line pressure drop. It refers to case of full FF compensator implemented in the velocity closed-loop control and a hydraulic load produced by pressure difference of $\Delta p = 100 \text{ bar}$.

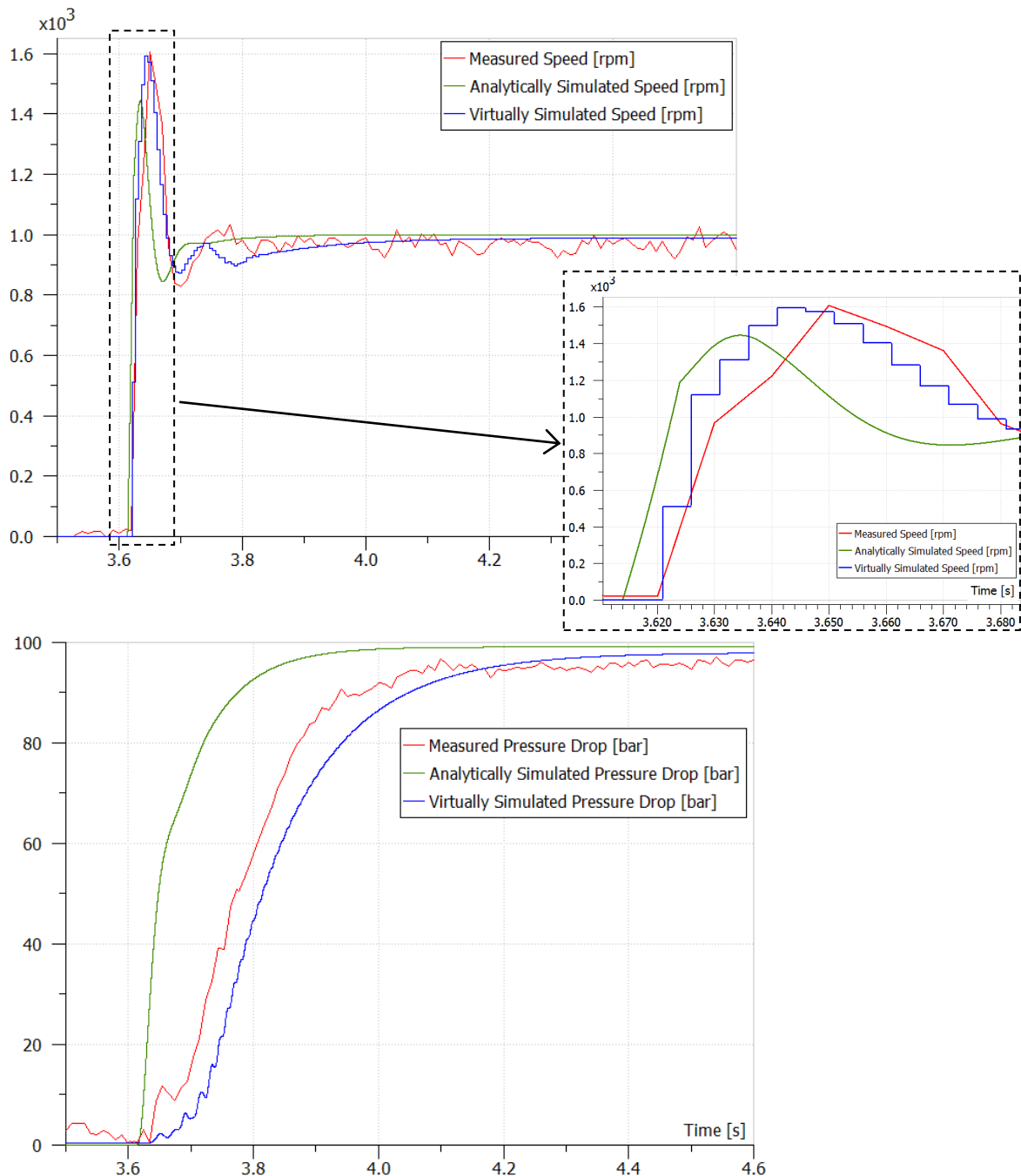


Figure 3.14 Comparison between measured, analytical and simulated speeds (top) and pressures

The time response of the measured speed ω is composed by an initial extent of acceleration in which the maximum overshoot ω_{max} is reached in about 30 ms. After that an intermediary region is characterized by speed reduction due to increase of hydrostatic torque $V_0\Delta p$. The fluid compressibility in fact slows down the increase of Δp in the hydraulic circuit that needs about 0.5 s to reach the steady-state of 96 bar. The speed thus oscillates for about 0.2 s before to reach its regime value ω_∞ in the next region.

The simulated speed by means of the analytical model, evolves in a similar way than the experimental one but ω_{max} results lower of about 13 % and in advance of about 15 ms compared to experiments. The analytically simulated Δp is much more reactive (about 0.1 s in advance) and reaches the value of 99 bar.

The simulated speed through the virtual prototype, enables to reach the same experimental ω_{max} in advance of just 5 ms. Although it has a light different oscillation of speed in the intermediary region, ω_∞ is then achieved in the same experimental times. The virtually simulated Δp has the same evolution trend of experiments but only delayed of 40 ms. In the initial region it shows a pressure ripple due to modelling of flexible hose through a distributive hydraulic line with lumped elements, as described in section 3.4.4 (5 internal nodes are selected to simulate the natural modes of line up to fifth order). The final value is about 98 bar.

Thanks to simulation accuracy provided by the full virtual prototype compared to analytical approach, the virtual prototype is so selected to reproduce the acceleration transient and the steady-state phase. This is then validated by means of comparison with experimental results.

3.6.1 Validation of Full Virtual Prototype

Table 3.5 summarises all the data acquired during the 15 experiments and simulations by means of the full virtual prototype. The speed is compared through the characteristics of its time response: Δt_{drive} , Δt_ω , ω_{max} and ω_∞ . The relative errors ε_i are evaluated by means the following expression:

$$\varepsilon_i = \frac{|var^{experimental} - var^{simulated}|}{var^{experimental}} * 100 \quad (3.26)$$

where the variables are respectively represented by the four characteristics mentioned above.

Tests	Δt_{drive}		ε_{dr}	Δt_{ω}		$\varepsilon_{t\omega}$	ω_{max}		ε_m	ω_{∞}		ε_{∞}
	[ms]			[ms]			[rpm]			[rpm]		
0 bar	<i>26</i>	<u>19</u>	<i>27</i>	<i>30</i>	<u>35</u>	<i>16</i>	<i>1134</i>	<u>1114,2</u>	<i>1,7</i>	<i>912</i>	<u>918,7</u>	<i><1</i>
	<i>14</i>	<u>14</u>	<i>0</i>	<i>10</i>	<u>10</u>	<i>0</i>	<i>1650</i>	<u>1645</u>	<i><1</i>	<i>912</i>	<u>918,7</u>	<i><1</i>
	<i>15</i>	<u>14</u>	<i>6</i>	<i>10</i>	<u>10</u>	<i>0</i>	<i>1698</i>	<u>1666,8</u>	<i>1,8</i>	<i>1002</i>	<u>994,9</u>	<i><1</i>
25 bar	<i>26</i>	<u>19</u>	<i>27</i>	<i>30</i>	<u>35</u>	<i>16</i>	<i>1134</i>	<u>1112,4</u>	<i>1,9</i>	<i>756</i>	<u>789,4</u>	<i>4</i>
	<i>16</i>	<u>14</u>	<i>0</i>	<i>10</i>	<u>10</u>	<i>0</i>	<i>1650</i>	<u>1644,3</u>	<i><1</i>	<i>780</i>	<u>789,4</u>	<i>1,1</i>
	<i>16</i>	<u>14</u>	<i>12</i>	<i>10</i>	<u>10</u>	<i>0</i>	<i>1668</i>	<u>1666,3</u>	<i><1</i>	<i>1002</i>	<u>993,3</u>	<i><1</i>
50 bar	<i>26</i>	<u>19</u>	<i>27</i>	<i>30</i>	<u>35</u>	<i>16</i>	<i>1134</i>	<u>1112,4</u>	<i>1,9</i>	<i>684</i>	<u>705,2</u>	<i>3</i>
	<i>16</i>	<u>14</u>	<i>12</i>	<i>12</i>	<u>10</u>	<i>16</i>	<i>1638</i>	<u>1644,2</u>	<i><1</i>	<i>684</i>	<u>705,2</u>	<i>3</i>
	<i>15</i>	<u>14</u>	<i>6</i>	<i>10</i>	<u>10</u>	<i>0</i>	<i>1662</i>	<u>1666,2</u>	<i><1</i>	<i>1002</i>	<u>992,7</u>	<i><1</i>
75 bar	<i>26</i>	<u>19</u>	<i>27</i>	<i>32</i>	<u>35</u>	<i>9</i>	<i>1098</i>	<u>1112,3</u>	<i>1,3</i>	<i>588</i>	<u>644,8</u>	<i>9,5</i>
	<i>16</i>	<u>14</u>	<i>12</i>	<i>14</i>	<u>10</u>	<i>28</i>	<i>1632</i>	<u>1644,2</u>	<i><1</i>	<i>588</i>	<u>644,8</u>	<i>9,5</i>
	<i>16</i>	<u>14</u>	<i>12</i>	<i>13</i>	<u>10</u>	<i>23</i>	<i>1680</i>	<u>1666,2</u>	<i><1</i>	<i>978</i>	<u>990,8</u>	<i>1,2</i>
100 bar	<i>26</i>	<u>19</u>	<i>27</i>	<i>32</i>	<u>35</u>	<i>9</i>	<i>1110</i>	<u>1112,3</u>	<i><1</i>	<i>542</i>	<u>598,7</u>	<i>10</i>
	<i>16</i>	<u>14</u>	<i>12</i>	<i>15</i>	<u>10</u>	<i>33</i>	<i>1624</i>	<u>1644,2</u>	<i>1,2</i>	<i>543</i>	<u>598,7</u>	<i>10</i>
	<i>16</i>	<u>14</u>	<i>12</i>	<i>13</i>	<u>10</u>	<i>23</i>	<i>1662</i>	<u>1666,2</u>	<i><1</i>	<i>978</i>	<u>989,5</u>	<i>1,2</i>

Table 3.5 Comparison between measured data and **simulated data by virtual prototype** when the following controller is implemented: *P controller*, *P controller + feedforward compensator of inertial contributions* and *P controller + complete feedforward compensator*

In order to interpret the table, it is necessary to observe that the *measured data* are in italic font while the **simulated data** are in bold and underlined. The colours represent the type of controller implemented in the system control: P controller (blue), P controller + feedforward compensator of inertial contributions (green) and P controller + full feedforward compensator (red). The results can be resumed in the following way:

- 1) Δt_{drive} is simulated with relative errors dependent on type of used controller: maximum ε_{dr} of 27 % are obtained when a P controller is implemented but they are then reduced to 6/12 % by using the feedforward compensators
- 2) Δt_{ω} is better simulated generally in tests at low pressure drop with errors ε_{ω} which are also reduced to zero up to 50 bar with full FF compensator. For pressure higher than 50 bar ε_{ω} increased up to 33%

- 3) If the total time delay is considered, constituted by sum of Δt_{drive} and Δt_{ω} , the full virtual prototype enables to reproduce it with relative errors lower than 22% correspondent to about 5 ms. It could be justified by the fact that the total time delay depends on all the sample rates of the input/output signal port of Simulink model and inverter which could not be in synchronisation
- 4) ω_{max} is simulated with high accuracy being ε_m lower than 2 %
- 5) ω_{∞} is generally simulated with ε_{∞} lower than 1 % (except that for Δp higher than 50 bar where ε_{∞} increases but never overcome the 10 %)
- 6) The full virtual prototype in general appears independent from operative conditions of Δp in terms of all time response characteristics, in contrast to experimental data which show an increase of total time delay and a reduction of ω_{max} with Δp increase
- 7) Even if not listed in table, the Δp is also compared in steady-state (Δp_{∞}) and in transient conditions. The increase of Δp during acceleration is simulated with time delays lower than 50 ms while the steady-state values are simulated with errors lower than 2 %

The simulations carried out through the full AMESim model have also been permitted to determine the values of the unknown parameters that influence the β_e (paragraph 3.4.5). The following table lists the final selected values of these parameters.

Parameters dependent β_e	Value
Young's modulus for flexible hoses : E	$9 \cdot 10^4 \text{ bar}$
Air Content ε	2.7 %
Air/Vapour Polytropic Index: Γ	1.4
Fluid Saturation Pressure: P_{sat}	1000 bar

Table 3.6 Value of the parameters influencing β_e selected by means of comparison between experiments and virtual results

In conclusion, it is possible to assert that the virtual prototype enables to reproduce the measured speed and pressure during the acceleration and in steady-state conditions, with good accuracy. The relative errors are lower than 22 % for the total time delay, 2 % for ω_{max} , 1 % for ω_{∞} and 2 % for Δp_{∞} .

3.7 Depressurisation Transient

In the introduction of this chapter some considerations are made about the depressurisation transient requirements. During depressurisation, the line pressure has to be reduced from a steady-state value to null through a reduction of motor speed. In practice this transient can be controlled in closed-loop by acting on motor speed or on line pressure. Customers generally prefer to control the motor speed because, by commanding an inversion of positive rotation of pump, it is possible to minimize the time for reducing the line pressure to zero. The drawback is that the negative speeds are limited by pump technology, as just described in Chap. 2, and this type of control can finally cause pump failure. Consequently a control of line pressure is favourable because it permits to limit the minimum speed but it is also less performing.

In this context the objective is just to reproduce depressurisations by controlling the motor speed or line pressure within the pump technological limits. The full virtual prototype previously described is validated for depressurisation too.

3.8 Laboratory Tests for Depressurisation

Laboratory tests are performed in order to compare the experimental and simulated results. During tests, the motor speed or the line pressure is closed-loop controlled by action on the motor torque using respectively: a P controller plus hydrostatic torque and frictions feedforward compensator.

Table below summarises all the performed tests. Firstly two tests are performed by controlling pressure in closed-loop. In this case a pressure step $\Delta p^*(t)$ is commanded that imposes a reduction from steady-state value to zero in a specific delta time Δt . The step is given by: $\Delta p^*(t) = \Delta p_0 \cdot u(t)$, with $u(t) = 1$ for $t \leq 5$ s and $u(t) = 0$ for $t > 5 + \Delta t$ s, $\Delta p_0 = 125$ bar @ 240 rpm. In *test-01* $\Delta t = 10$ ms while in *test-02* $\Delta t = 50$ ms. The speed is instead closed-loop controlled in the two other tests in which a step $\omega^*(t)$ is commanded for reducing the speed from steady-state value to zero in a specific delta time Δt . The speed step corresponds to: $\omega^*(t) = \omega \cdot u(t)$, with $u(t) = 1$ for $t \leq 5$ s and $u(t) = 0$ for $t > 5 + \Delta t$ s, $\omega = 240$ rpm @ 125 bar. In *test-03* $\Delta t = 10$ ms while in *test-04* $\Delta t = 50$ ms.

During tests the following variables are measured: command speed ω^* , measured speed ω ,

line pressure Δp , output flow rate Q_{out} , command motor torque C_m^* , estimated motor torque C_{est} and tank temperature T_{tank} .

<i>N. Test</i>	<i>Controlled Variable</i>	<i>Initial Conditions - Command Ramp Time</i>
01	Line Pressure	125bar@240rpm-10 ms
02	Line Pressure	125bar@240rpm-50 ms
03	Motor Speed	240rpm@125bar-10ms
04	Motor Speed	240rpm@125bar-50ms

Table 3.7 Tests performed for depressurisation

In order to compare measured and simulated speeds, characteristics of the time response of speed are evaluated, as showed in figure 3.15:

- ω_{min} : minimum motor speed
- $t_{\omega_{min}}$: time duration with negative motor speed
- $t_{\Delta p}$: time duration to reach the 95% of pressure drop

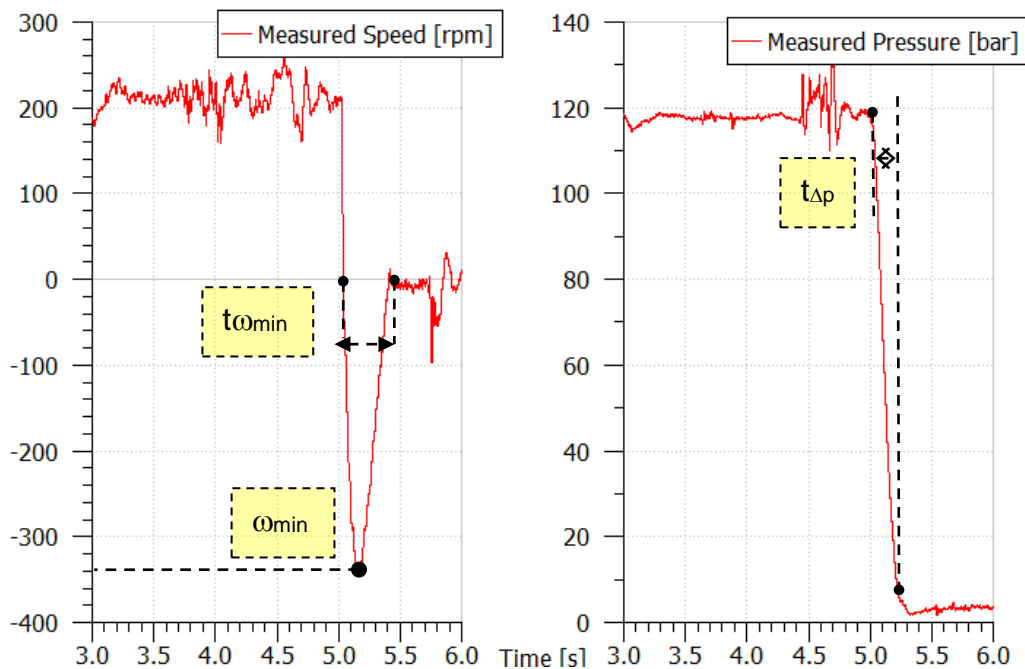


Figure 3.15 Characteristics of speed and pressure time response

3.8.1 Simulation Procedure for Virtual Prototype: Determination of Optimum Young's Modulus of the Flexible Hose

The validation procedure exposed in 3.5.1 has permitted to identify the values of the unknown system parameters: air content, saturation fluid pressure, polytropic index of air/gas and the Young's Modulus E of the flexible hose. These parameters are now maintained invariant unless the Young's Modulus E of the flexible hose. In fact it could assume different values as function of operating pressure conditions. Instead a study conducted for the determination of the hydraulic capacity of rubber hoses shows this dependence [19]: E varies as function of increase or reduction of the pressure inside the pipe.

E is so determined through an optimization process based on the experimental results of *Test-01* in tab. 3.7. It consists of varying the E inside a fixed values range in order to reduce the gaps between measurements and simulated: $\min(\omega_{min-measured} - \omega_{min-simulated})^2$. The optimization is run through AMESim tool (more details are inserted in next section 4.7.1.1) and the final value of E is calculated after eight iterations. Figure 3.16 shows the values of E determined in each process step.

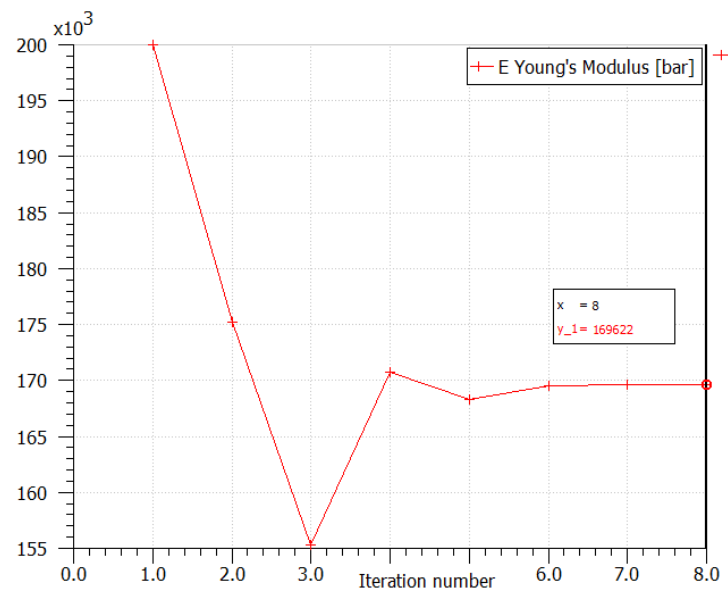


Figure 3.16 Iterations of the optimization process for the E determination

The value of E that permits to obtain the same ω_{min} measured in the *Test-01* is thus determined. It corresponds to $1.696 \cdot 10^5$ bar. This value is then tested for all the other simulations to verify its robustness and it is finally selected.

AMESim permits to insert a value of the Young's Modulus in the pipe models characteristics. Unfortunately it is not possible to vary this value during the simulation and so we have just evaluated an equivalent value. In this case of simulation of depressurization phases, an optimum value is identified that takes into account the presence of a pressure drop equal to 125 bar. Consequently we have calculated a value $E(p = 125\text{bar}) = E_0 + k_E 125 = 169600 \text{ bar}$.

By means of the calculations carried out for the acceleration phase, we have calculated a different value of E that can be considered correspondent to $p = 0\text{bar}$. So $E(p=0\text{bar}) = E_0 = 90000 \text{ bar}$. These two results permit to obtain more information about the E of pipe.

3.9 Comparison between Experimental and Simulated Results

Figures 3.17 show the comparison of experimental and simulated measured speed and pressure for *Test-01*.

Table below shows the comparison between the experimental and simulated characteristics of speed and pressure time response.

The relative errors are calculated by means of the (3.26) with exception of $\varepsilon_{\omega_{min}}$ that is evaluated as follows:

$$\varepsilon_{\omega_{min}} = \frac{|\omega_{min}^{experimental} - \omega_{min}^{simulated}|}{(\omega_{steady-state} + |\omega_{min}^{experimental}|)} * 100 \quad (3.1)$$

In order to interpret the table, it is necessary to observe that the *measured data* are in italic font.

N. Test	ω_{min}		$\varepsilon_{\omega_{min}}$	$t\omega_{min}$		$\varepsilon_{t\omega_{min}}$	$t\Delta p$		$\varepsilon_{t\Delta p}$
	<i>[rpm]</i>	<i>[rpm]</i>		<i>[s]</i>	<i>[s]</i>		<i>[s]</i>	<i>[s]</i>	
01	-335	-326	1,6	<i>0,38</i>	0,40	5	<i>0,22</i>	0,19	14
02	-320	-319	0,2	<i>0,36</i>	0,39	8	<i>0,22</i>	0,20	9
03	-83	-95	3,6	<i>0,03</i>	0,026	13	<i>0,65</i>	0,75	15
04	-7	-9	0,8	<i>0,02</i>	0,017	15	<i>0,89</i>	0,90	1

Table 3.8 Comparison between experimental and simulated data

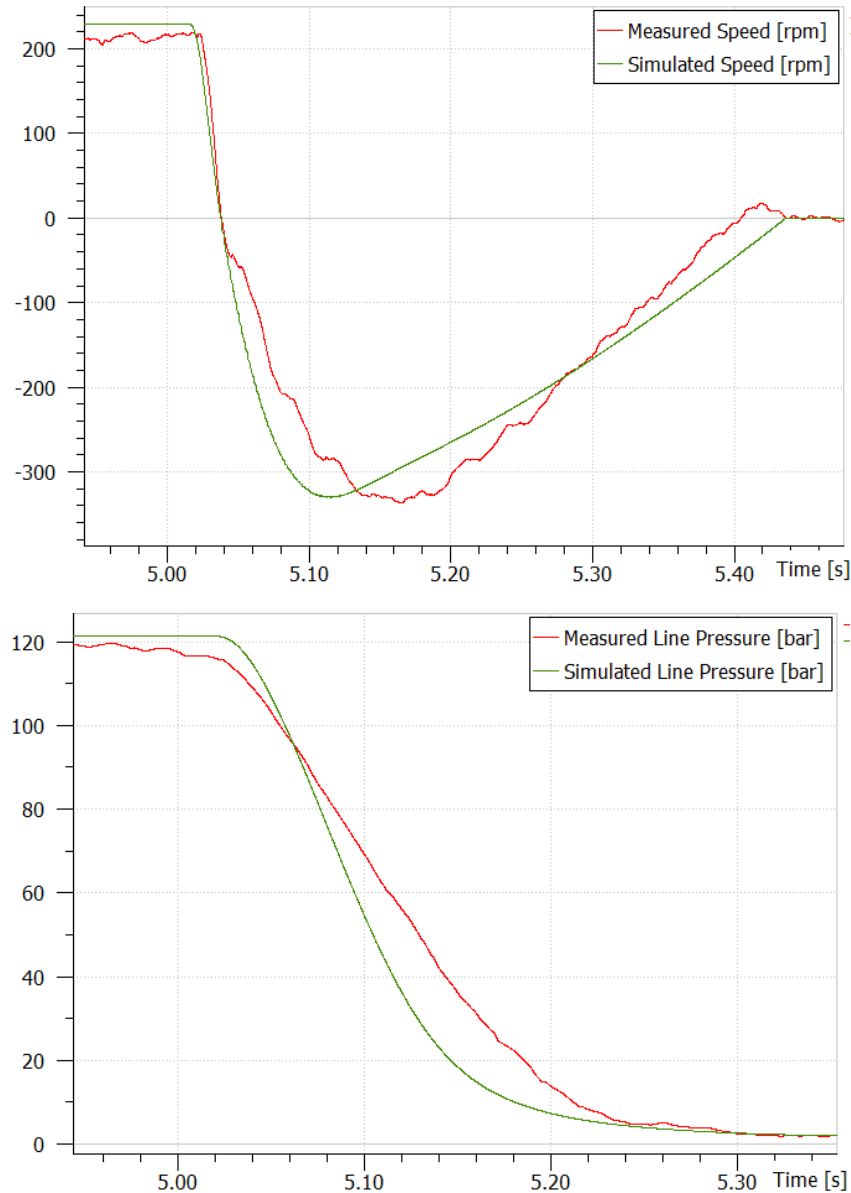


Figure 3.17 Experimental and simulated speed and pressure in Test01

On the basis of the results provided in the table 3.8, it is possible to assert that:

- 1) ω_{min} is simulated with relative errors $\varepsilon_{\omega_{min}}$ lower than 4 %,
- 2) $t_{\omega_{min}}$ is simulated with $\varepsilon_{t_{\omega_{min}}}$ lower than 15 %,
- 3) $t_{\Delta p}$ is simulated with $\varepsilon_{t_{\Delta p}}$ lower than 15 %.

The full virtual prototype thus enables to reproduce the depressurisation with good accuracy especially in the minimum reached speed ω_{min} .

3.10 Conclusion

In this chapter the acceleration and depressurisation transients of a typical cycle of an IMM have been analysed. The reference architecture relative to test bench has firstly been defined and the principal equations describing its dynamics have been described. After that the contributions of system parameters which can limit the module performance during acceleration have been evaluated separately by means a progressive approach based on open-loop analysis. Numerical values have also been provided.

The importance of adding a pump speed closed-loop, for module control in acceleration, has then been showed by means of linearized model. The study was based on assumptions obtained thanks to conclusions about the parameters contribution in first part of chapter. An improvement of control architecture has then been achieved by implementation of a feedforward compensator. The advantages in better acceleration capability and null static error of the complete closed-loop controlled system have been analytically simulated.

A detail model of full test bench has been created in AMESim by consisting of velocity closed-loop controller, inverter, electric motor, shaft coupling, vane pump and hydraulic circuit. The vane pump prototype is an improved version of the model described in Chapter 2, thanks to representation of HP pump volume. The advantages of the full virtual prototype concern the simulation of the non-linearities effects as the pump energy losses and the fluid compressibility. In particular the fluid compressibility has been made more realistic by evaluating the dependences of the Effective Bulk Modulus from line pressure, fluid temperature, saturation pressure of fluid, gas polytropic index, air/vapour content and hydraulic hoses compliance. Laboratory tests have then been performed and the full virtual prototype has finally been validated for the acceleration transient and steady-state condition.

After that the depressurisation transient has been simulated through the same full virtual prototype and laboratory tests have permitted to validate this prototype. Line pressure or pump speed have been closed-loop controlled during the laboratory tests by the use of feedforward compensation. The prototype validation procedure has also permitted to determine an optimum Young's modulus that was suitable for simulating the dependences of hoses deformability from pressure drop during depressurisation.

References

- [1] F. G. Franklin, J. D. Powell, A. Emami-Naeini. Feedback Control of Dynamic Systems. 4th edition, Prentice Hall, 2002.
- [2] Parker Catalogue. NX Servomotors NX Series. *Technical Manual PVD 3663*, July 2014.
- [3] T. Van den Elshout. Obtaining Time Reduction in the Movement of a Clamp Mechanism. *University of Twente, Netherlands, March 2006*.
- [4] H. Zhang, L. Quan. The Kinetic Characteristics of the Clamping Unit in Injection Molding Machine Driven by New Pump Control System. *Advances in Information Sciences and Service Sciences (AISS), Volume 4, Number 21, November 2012*.
- [5] D. Zheng. Iterative Learning Control of an Electro-hydraulic Injection Molding Machine with Smoothed Fill-to-pack Transition and Adaptive Filtering. *PhD Thesis, Department of Mechanical Engineering, University of Illinois at Urban-Champaign, 2002*.
- [6] J-C. Maré. Considerations pratiques sur les correcteurs PID dans le domaine de l'énergie fluide. *Revue Fluides, pp 8-17, Numéro Spécial Matériels, Septembre 2000*
- [7] P. Tatjewski. Advanced Control of Industrial Processes. *Structures and Algorithms. Springer-Verlag London, 2007*.
- [8] LMS-AMESim, *Hydraulic Library Rev 11 – User's guide*
- [9] H. E. Merritt. Hydraulic Control Systems. *John Wileys and Sons, Cincinnati, Ohio, 1967*.
- [10] F. J. Hanly. Fluids for High-Pressure Industrial Hydraulic Systems, *SAE Technical Paper 670697, 1967*.
- [11] G. E. Totten. Handbook of Hydraulic Fluid Technology. *Marcel Dekker, 2000*.
- [12] P. K. B. Hodges. *Hydraulic Fluids*. Petroleum Consultant Norway, Elsevier, 1996.
- [13] G. V. Fracastoro. Fondamenti e Applicazioni di Termodinamica. *Department of Energy, Politecnico di Torino, December 2000*.
- [14] C. E. Brennen. Cavitation and Bubble Dynamics. *Oxford University Press 1995*.
- [15] R. T. Fenner, J. N. Reddy. Mechanics of solids. *CRC Press LLC 1999*.
- [16] S. P. Timoshenko. Strength of Materials. *Dunod 1930*.
- [17] <http://www.semperflex.com/en/hydraulic-hoses/products/hydraulic-hose/>
- [18] M. Vasina, L. Hruzik. Experimental Determination of Hydraulic Capacity of Pressure Hoses. *Journal of applied science in the thermodynamics and fluid mechanics. Vol. 3 No. 2/2009*.
- [19] www.contitech.de/pages/produkte/.../fluid_tech-info_en.pdf
- [20] P. J. Chapple. Turbo Machinery – Hydraulic Stiffness, Tep4195. *Department of Energy and Process Engineering, NTNU (Norwegian University of Science and Technology), April 2004*.

Cavitation

Dans ce chapitre les phénomènes de cavitation et d'aération sont décrits et les dommages mécaniques principaux sur la pompe à palettes sont montrés. Un modèle analytique fonctionnel est développé qui prend aussi en compte la ligne hydraulique entre la pompe et le réservoir. Les effets résistifs, inertiels et capacitifs sont considérés dans les équations. Ce modèle a permis d'évaluer les relations principales entre les paramètres fondamentaux du système et la pression du fluide à l'entrée de la pompe. Les limitations de ce modèle sont remarquées quand une comparaison est effectuée avec des prototypes virtuels développés dans l'environnement AMESim.

Deux prototypes virtuels sont donc créés qui améliorent la modélisation de la ligne d'aspiration et de l'intérieur de la pompe à travers des sous-modèles inclus dans la bibliothèque d'AMESim. Les effets liés aux conditions de flux (laminaire or turbulent), la présence de delta de pression concentrée et la variation de Bulk Modulus avec les conditions de fonctionnement, la déformabilité des parois et le contenu d'air, sont simulés par les prototypes. Le prototype virtuel complet est finalement validé en démontrant qu'il est capable de prévoir, avec exactitude, l'évolution de la pression du fluide à l'entrée de la pompe.

4 Identification of Operating Conditions Favourable for Cavitation Development

In this chapter the phenomena of cavitation and aeration is analysed in order to identify the operating conditions which can favour the inception process during typical acceleration phases of vane pump. First section describes the phenomenon in terms of nucleation, growth and implosion of cavities, intensity influencing factors, and mechanical degradations. Possible methods to detect cavitation are listed. Analytical approach is then developed to point out the key relationships between fundamental parameters and performance of test bench. An advanced modelling is finally developed based on virtual prototyping in order to simulate the pressure time variation at pump inlet during acceleration transients.

4.1 Introduction

Cavitation affects fluid power systems and components like valves, orifices and hydraulic pumps. It produces undesirable effects which can reduce the efficiency and the working life of system until to final failure. Erosions are typically produced which locally degrade the solid surface and which can cause fluid contamination, leakage, reduction of flow rate and blockages. High frequent vibrations and noise represent other consequences of cavitation which generate acoustic levels much higher than during usual operation [1].

Aeration is a phenomenon that occurs when air is brought into the fluid by producing a foamed substance. The initial properties of the standard fluid are so lost and it can generate mechanical degradations like wear between parts, high noise level and finally components destruction [2]. A correlation exists between the two phenomena just mentioned and it will be described in next paragraph.

In order to prevent the phenomena and to guarantee accurate system performance, it is firstly fundamental to verify their existence and to identify the inception points of cavitation inside components. A method to detect cavitation is developed in this context and described below.

4.2 Cavitation

Cavitation is a physical phenomenon which leads to nucleation, growth and collapse of cavities filled with vapour or gas inside a hydraulic fluid at constant current temperature. In normal atmospheric pressure conditions, the hydraulic fluid also contains dissolved air in a certain volumetric percentage. The solubility of air is generally high in the mineral oils compared to other hydraulic media like water and phosphate ester: typically 8-9 % volume of dissolved air for mineral oil (ISO type HM) and only 2 % for water at 0 °C and normal atmospheric pressure [3].

Let's consider the fluid in the conditions of high pressure inside a hydraulic circuit represented by the point A in fig. 4.1, with all dissolved air. If the pressure reduces, the value of *saturation pressure* is reached. It generally corresponds to atmospheric value if the tank is not pressurized. If the pressure shuts down again the point B is reached: in these conditions the aeration process is induced and the dissolved air starts to come out of the solution as free gas. Air bubbles are so produced. By reducing again the fluid pressure, the aeration process continues until to all the dissolved air is free.

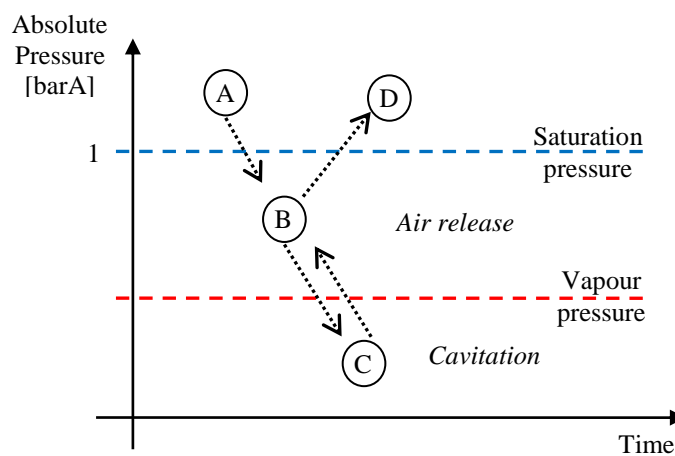


Figure 4.1 Variation of the fluid pressure versus time: aeration and cavitation processes

When the fluid pressure is further reduced, the *vapour pressure* is achieved (point C). Below the vapour pressure, the fluid starts to vaporize and cavities start to fill with vapour. In these conditions, cavities can be filled with vapour, gas or both. The growth of cavities depends on gas and vapour content and it can be derived from static equilibrium conditions analysis for a spherical nucleus [4]. Figure 4.2 shows the variation of cavities radius as function of the fluid pressure adjacent to cavity (ambient pressure in figure) and

gas content. When the fluid pressure is reduced below the vapour value, the cavity grows in a stable way and it tends to reach an equilibrium radius. If the pressure drops below a critical value, the cavity becomes unstable and it grows explosively. In this region unstable nuclei cannot exist unless some external mechanism stabilise them but it is not yet fully understood. Smaller is the gas content in the cavities and lower pressures are required to increase their dimensions. Diffusion of gas is also possible from cavities into the surrounding fluid that makes the cavities to disappear [4].

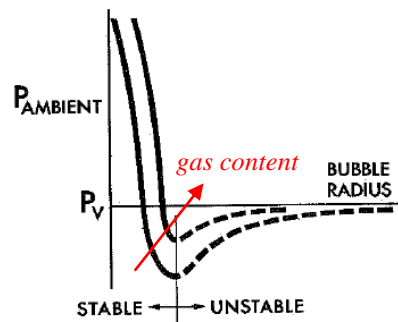


Figure 4.2 Plots of the conditions for static equilibrium of cavitation nuclei. Variation of pressure adjacent to cavity as function of cavities radius and gas content, from [4]

When the cavities are subjected to a very rapid increase of pressure, their growth is stopped and they finally implode: they disappear due to air dissolution and vapour condensation. This can produce an impact pressure which causes mechanical damages. Implosion is more violent, by generating high pressure peaks, if the gas content is smaller because lower pressures are reached during the cavities growth (fig. 4.2).

The *vapour pressure* depends on hydraulic fluid type. It rapidly increases with temperature [5]. Table 4.1 shows the vapour pressure of typical mobile hydraulic oil as function of temperature [6]. For the Tellus 32, it corresponds to 10^{-4} mbar at $40\text{ }^{\circ}\text{C}$ (datasheet provided by supplier). In practice a lower value of vapour pressure is considered at which the cavities reach such a dimension that their implosion produces visible and not negligible mechanical damages. It typically corresponds to -0.2 bar (0.8 bar_A).

T [$^{\circ}\text{C}$]	20	40	60	80	100	120	140
p [mbar]	$9 \cdot 10^{-5}$	$6 \cdot 10^{-4}$	$4 \cdot 10^{-3}$	$2 \cdot 10^{-2}$	$8 \cdot 10^{-2}$	$3 \cdot 10^{-1}$	$8 \cdot 10^{-1}$

Table 4.1 Vapour pressure of a typical hydraulic oil as function of temperature, from [6]

By increasing pressure above saturation value up to initial condition, the process of re-absorption of air bubbles is instead achieved. It has generally different dynamics and consequently the final resulting air content can be or not the same than in starting conditions before aeration [7].

4.2.1 Effects on Vane Pump

Cavitation erosion is the mechanical consequence of the collapse of the cavities when they come into a region at high pressure. The erosion mechanism is still not fully understood. Nevertheless two possible mechanisms seem to be at the origin [5]:

- Symmetrical collapse

It acts when the cavity implodes within the fluid, far from solid boundaries. A shock wave is emitted to the surrounding fluid (Fig. 4.3)

- Asymmetrical collapse

It develops itself when the cavity is in contact or close to solid boundary and the cavity is perturbed in an asymmetrical way. After cavity deformation, the fluid penetrates through cavity and a micro-jet is formed (Fig. 4.3)

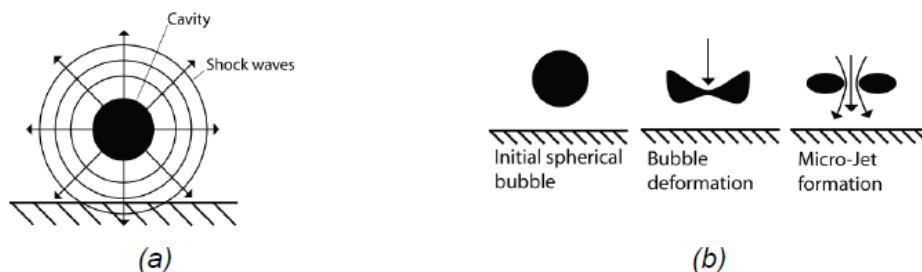


Figure 4.3 Cavitation erosion: symmetrical collapse (a) and asymmetrical collapse (b), from [8]

However these mechanisms do not permit to fully explain the mechanical degradation produced by cavities implosion. To justify the effect of erosion, it is necessary to consider the simultaneous collapse of several cavities, “a cloud”, which act through a mutual interaction.

The intensity of cavitation depends on some factors: geometry of flow path, pressure distribution and fluid properties. The degree of erosion is a function of the surface material properties, like hardness, work hardening capability, grain size, stress state and also corrosion [1].

In the case of vane pump, craters are sometimes observed which come from cavitation erosion, fig. 4.4: they are created in the port plates, in the area between the suction port and pressure port, around the pressure bleeds slots. Craters can be also observed on the pins which push the vane against the cam profile (Fig. 4.5).

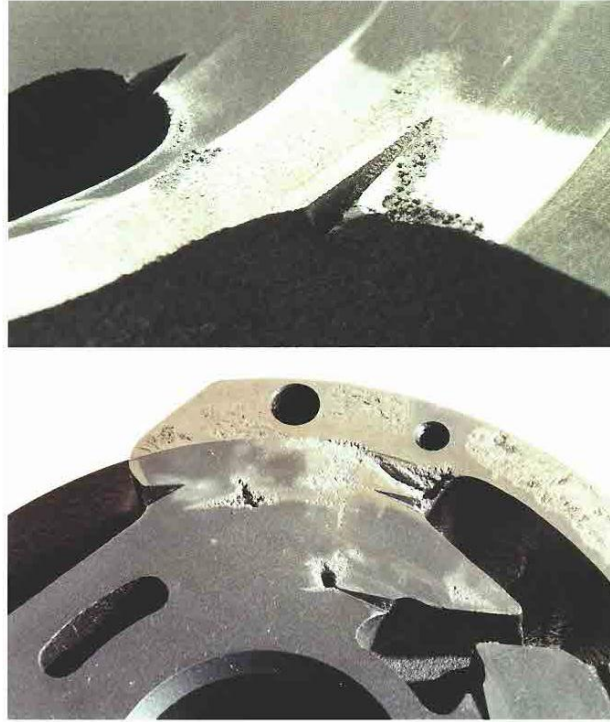


Figure 4.4 Cavitation erosion: craters on port plate, from [2]



Figure 4.5 Cavitation erosion: craters on pins, from [2]

It is important to remark that generally the erosion is not formed in the place where the cavitation incepts but downstream, being the cavities transported by stream flows [1]. Wrong conclusions are sometimes made concerning the cavitation nucleation locations and consequently wrong preventive actions are developed.

High-frequently noise is produced when the cavities implode and high pressure peaks are generated. High vibrations levels are also generated by the shock waves emitted during

cavities collapse: high pressure peaks and high flow acceleration can be so measured in order to identify both the inception and the implosion phase.

Another effect of cavitation is to reduce the flow rate that outputs from pump. In order to understand this effect, it is necessary to consider the flow through an orifice (Fig. 4.6). Assuming quasi-stationary flow conditions and incompressible fluid, the Bernoulli's equation permits to correlate the velocities of the fluid to the static pressure in upstream and downstream section across the orifice: constant sum of dynamic and static pressure is so assured. When the fluid velocity increases locally in downstream, a reduction of static pressure is induced that can achieve the vapour pressure. The cavities are so created and transported along the flow. Then, they implode as long as they come into a high pressure region. When the pressure shuts down below the vapour pressure, the quasi-stationary and incompressibility conditions are not more valid and physical processes like evaporation, re-condensation and outgasing of dissolved air occur. If the cavitation is further intensive, the exit flow rate does not more increase even if the downstream pressure continues to decrease. The flow outputting from orifice deviates from its theoretical value: it refers to “saturation” or “choking” phenomenon (Fig. 4.6) [1].

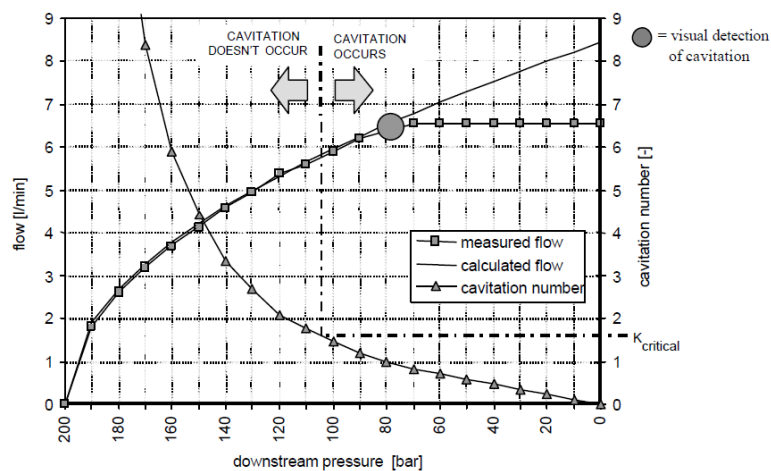


Figure 4.6 Saturation of the flow rate through an orifice produced by cavitation, from [1]

Figure shows also the evolution of the cavitation number that was introduced by Thoma and Leroux in 1923-1925 to identify the cavitation conditions for orifices. It is a non-dimensional parameter defined as the ratio between the static pressure and the dynamic pressure. Its critical value $K_{critical}$ corresponds to cavitation inception (fig. 4.6).

On the basis of these considerations, the vane pump behaves in the same way of orifice: when it rotates at constant speed and cavitation occurs with choking phenomenon

generation, the final result is a reduction of output flow rate compared to theoretical value. Orifices are situated in several places inside pump like: pump inlet and outlet, in the suction side to bring into contact the volume chambers with the suction channel, between the vane tips and the cam ring, in the discharge side etc. There are also orifices installed along the hydraulic connection between pump and tank which are to be taken into account. In fact they can reduce locally the pressure below the vapour value, facilitate the nucleation of cavities which, travelling along the stream flow, finally implode inside pump in high pressure area.

It is also important to underline that cavitation and aeration conditions can develop both in steady-state and transient regime. Especially high acceleration imposed to pump, produces locally increase of fluid velocity that promotes pressure drop, and thus in certain occasions air release and cavitation too.

4.2.2 Methods to Detect and Prevent Cavitation

Several methods exist to determine the presence of cavitation inside pump. Direct methods are based on visual observation to identify location points where cavities collapse. This method is obviously useful to detect cavitation but not to prevent it. Indirect methods permit also to prevent cavitation by means of comparison of measured data before and after cavitation. It is the case of monitoring of steady-state flow behaviour that compares the pump experimental output flow rate to theoretical value. Other methods are based on measurements of frequency spectrum of acoustic pressure and vibrations to detect the generation of the shock waves induced by cavities collapse [1].

Moreover alternative qualitative approach to prevent cavitation is constituted by numerical simulations using Computational Fluid Dynamic (CFD). Studies are exposed concerning the simulation of cavitation flow in vane pumps, [8] to [10]. 1-D, 2-D and 3-D averaged Navier-Stokes equations and Rayleigh cavitation model, taking into account the liquid-vapour mass transfer, were solved. By evaluating the spatial variation of fluid density [10], or the pressure and volume fraction profile inside pump [8] and [9], the nucleation of cavitation were investigated in steady-state conditions. Specific erosion points were identified, as in the rotor outlet interface, and the influence that the vane radius can have on cavitation area was analysed [9]. Nevertheless the high time expense makes these

simulations not very practical. In addition, geometrical simplifications were made to avoid numerical convergence problems which reduce the accuracy of leakages and cavitation simulation. The tested operating conditions at constant rotational speed, limit the results given that only steady-state performance were run without evaluating dynamic phases. Effective Bulk Modulus did not consider the deformability of components.

In this context an innovative approach is proposed based on virtual prototype of EHM able to identify the operating conditions that can promote the cavitation. In particular it simulates locally the time variation of the static pressure for determining whether or not the vapour pressure is reached under specific conditions. A detailed model is built for pump and for the hydraulic connection between pump and tank. It will be described in next paragraphs.

4.3 Aeration

Aeration is a phenomenon that occurs when air is brought into the fluid. As it was previously described in last paragraph, the reduction of the fluid pressure below the saturation value generates release of the air dissolved in the fluid. Other external causes can promote aeration as [3], [2]: a suction pipe under vacuum that is not sealed, a deteriorated shaft seal, a return line coming back to tank above the oil level, low fluid level in tank and insufficient residence time, etc.

The effects of aeration are both on fluid properties and on components surfaces. The variation of the Effective Bulk Modulus due to air content was already exposed in Chap. 3. Also the fluid density reduces as function of the amount of free air volume fraction. Free air can slightly modify the viscosity of the hydraulic fluid too [3]. High noise level is noted and possible damage to components can be observed.

In particular wear between parts can be produced. It is the case of the vanes: usually hydrostatically balanced, they are subjected to imbalance due to variation of fluid compressibility caused by free air. They so move sideways with erratic movements that destroy the lubricant oil film between them and the port plate. The result is severe grooves which mark deeply the port plate and sometimes break the vane too, fig. 4.7.

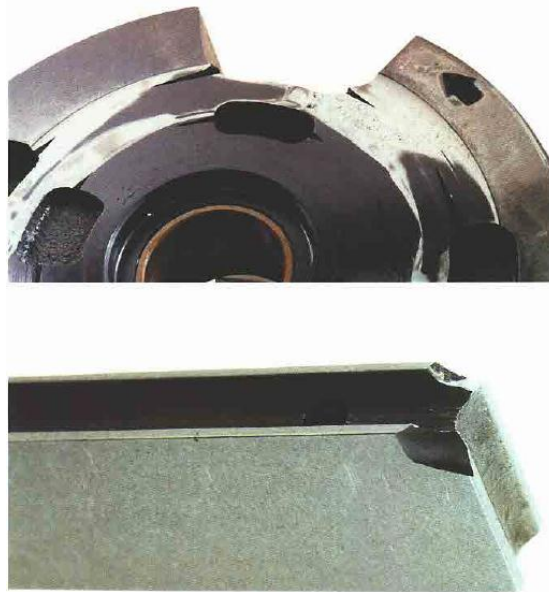


Figure 4.7 Aeration damage: grooves on port plate (up) and vane break (down), from [2]

Sometimes the free air bubbles can implode when a sudden compression under adiabatic conditions acts without previously reaching the vapour pressure. The pressure creates the ignition and the gas combusts at very high temperature as high as 1300 °C [2]. The film of fluid near bubbles undergoes a thermal degradation and it can assume a black colour and a burnt odour. Figure 4.8 shows a black mark on cam ring due to air bubbles implosion that can be transformed in craters.



Figure 4.8 Aeration damage: black mark on cam ring due to air bubble implosion, from [2]

4.4 Analytical Model for Inlet Pipe and Pump

At preliminary level of modelling, an analytical functional model is developed to evaluate the time variation of local pressure and the key relationships with the fundamental system parameters. The objective is to prevent the development of cavitation and aeration phenomena by means of analysis of static pressure reduction in pump inlet when accelerations are imposed. As just discussed in last paragraphs, the aeration and cavitation originate in regions where the pressure locally shuts down respectively below the saturation and vapour value. The section reduction in pump inlet can be the cause of local reduction of pressure in vena contracta due to increase of fluid velocity. So at this level, the analysis focuses only on pump inlet and the pump is not modelled in internal details but just as a volume that varies as function of rotational speed. For that, the analogy is made with a linear hydraulic jack where the volumetric variation of the jack chamber, due to piston motion, corresponds to quantity of fluid suck by the pump during its rotation. The complete model refers to test bench described in Chap. 1 and it consists of (fig. 4.9): tank, inlet pipe, including tube fittings, and pump.

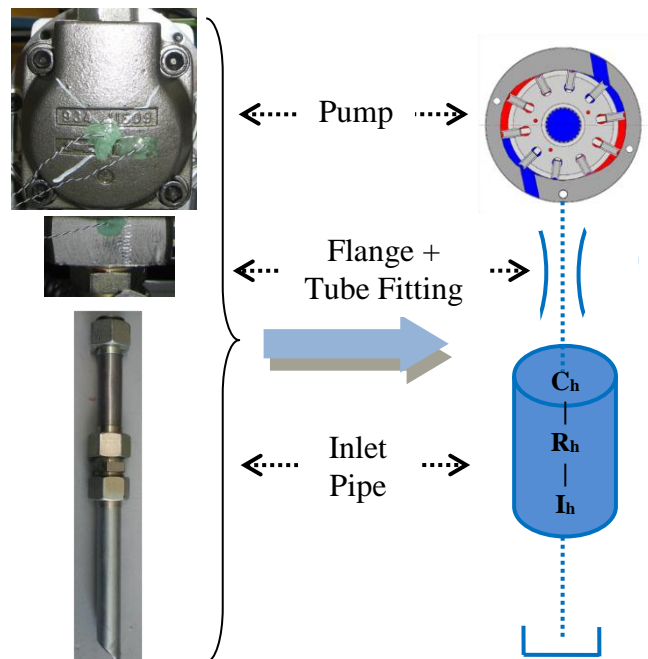


Figure 4.9 Schematic of the complete analytical model

By evaluating the time variation of pressure, when acceleration is imposed to pump, the parasitic inertial and capacitive contributions become important, as well as resistive effects, and so they are taken into account. They are listed below:

- Inertial (I_h)
- Capacitive (C_h)
- Resistive (R_h)

A lumped modelling is carried out in this analytical approach and the I_h - R_h - C_h sequence is selected for dealing the three effects (fig. 4.9). It is useful to remark that the type of chosen sequence plays a fundamental role in the resolution of the equations' system. An analogy can be made with electrical circuits. In these circuits, the voltage and current respectively correspond to flow rate and line pressure of hydraulic circuits and the arrangement of inductors, resistors and capacitors determines the flow of current through the circuit. In next paragraphs the system's equations are developed for the hydraulic connection between pump and tank, constituted by pipe and the tube fittings, and for vane pump.

4.4.1 Pipe and Tube Fitting: Inertial and Resistive Effects

The inertial and resistive effects of the hydraulic line depend respectively on fluid inertia I_h and on viscous frictional losses distributed along the pipe. The correlation between them can be expressed through the Second Newton's Law to fluid applied on fluid inside pipe.

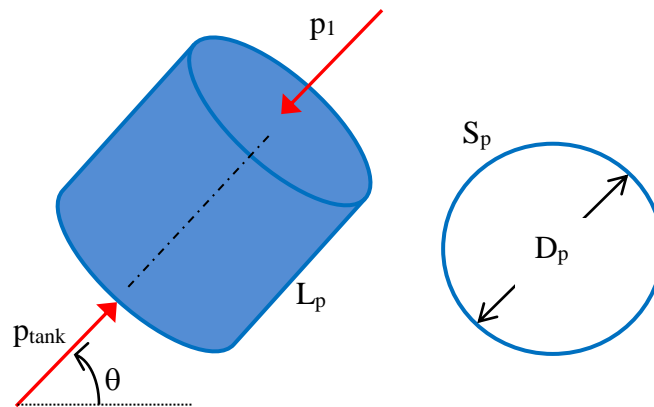


Figure 4.10 Schematic of the Pipe and of the inside contained fluid

The pipe is schematized as a cylinder, fig. 4.10, where its geometrical characteristics are inserted: D_p is the inside pipe diameter, L_p is the pipe length, S_p the cross section area and θ is the angle formed between ground and the cylinder axis direction (positive rotation values if the pump is above tank). The tube fitting has the following geometrical characteristics: D_t is the inside throttle diameter, L_t is the throttle length and S_t the cross

section area.

By applying the Second Newton's Law to fluid, it results:

$$p_{tank} - p_1 - \rho L_p g \sin(\theta) - \Delta p_{loss}^{tot} = I_h \frac{dQ_1}{dt} \quad (4.1)$$

where

p_{tank} = tank pressure

p_1 = pipe output pressure towards pump

ρ = fluid density

g = gravity acceleration

Δp_{loss}^{tot} = total pressure losses due to viscous frictional forces

$I_h = \rho(L_p/S_p + L_t/S_t)$ = fluid inertia

Q_1 = flow rate

In order to get the eq. 4.1, the following assumptions were made:

- The pipe is considered straight (tube bends generate pressure losses), with length greater than the transition length [11], and with constant cross section area
- The total pressure losses Δp_{loss}^{tot} , due to viscous frictional forces, consists of the distributed contribution along all pipe length Δp_{loss}^{pipe} and the concentrated contribution in tube fitting $\Delta p_{loss}^{throttle}$:

$$\Delta p_{loss}^{tot} = (p_{tank} - p_1) = (p_{tank} - p_0) + (p_0 - p_1) = \Delta p_{loss}^{pipe} + \Delta p_{loss}^{throttle} \quad (4.2)$$

- The Hagen-Poiseuille law is used to describe the pressure loss Δp_{loss}^{pipe} , due to viscous frictional forces, under the flow conditions hypothesis of fully laminar [11]:

$$\Delta p_{loss}^{pipe} = (p_{tank} - p_0) = f_p \frac{L_p \rho}{D_p} \frac{v_p^2}{2} \quad (4.3)$$

where

$f_p = \frac{64}{R_e^{pipe}}$ is the friction factor for laminar conditions

$R_e^{pipe} = \frac{\rho Q_1 D_p}{\mu S_p}$ Reynolds Number

$v_p = \frac{Q_1}{S_p}$ average fluid velocity

- The losses concentrated in tube fitting $\Delta p_{loss}^{throttle}$ are described by means of a

throttle modelling [11]. Its geometrical characteristics are defined: D_t is the inside throttle diameter, L_t is the throttle length, S_t the cross section area. Under the assumption of laminar flow conditions, the relation between average fluid velocity v_t and pressure drop $\Delta p_{loss}^{throttle}$ is the same of (4.3):

$$\Delta p_{loss}^{throttle} = (p_0 - p_1) = f_t \frac{L_t \rho}{D_t} \frac{v_t^2}{2} \quad (4.4)$$

where

$f_t = \frac{64}{Re^{throttle}}$ is the friction factor for laminar conditions

$Re^{throttle} = \frac{\rho Q_1 D_t}{\mu S_t}$ Reynolds Number

$v_t = \frac{Q_1}{S_t}$ average fluid velocity

- The fluid density is supposed constant temporally and spatially
- The fluid temperature is supposed constant (the laminar flow is temperature sensitive as it depends on viscosity)
- Entrance and exit losses due to edge form (sharp-edged, square-edged...) are neglected

The assumption of laminar flow conditions is based on preliminary calculation of Reynolds number Re in the inlet pipe, as function of data inserted in the pump catalogue. In that, a velocity between 0.5 and 1.9 m/s is permitted in pump inlet. By fixing the velocity to maximum permissible value and the diameter of inlet pipe at 25 mm , Re is finally calculated $Re = 2000$. The laminar conditions are so assumed for this first modelling step.

4.4.2 Pump and Inlet Pipe: Hydraulic Capacity

In order to evaluate the capacitive effects in the acceleration pump phase, it is necessary to apply the Flow Conservation Equation to Control Volume given by the total volume of the circuit V_{tot} (fig. 4.11).

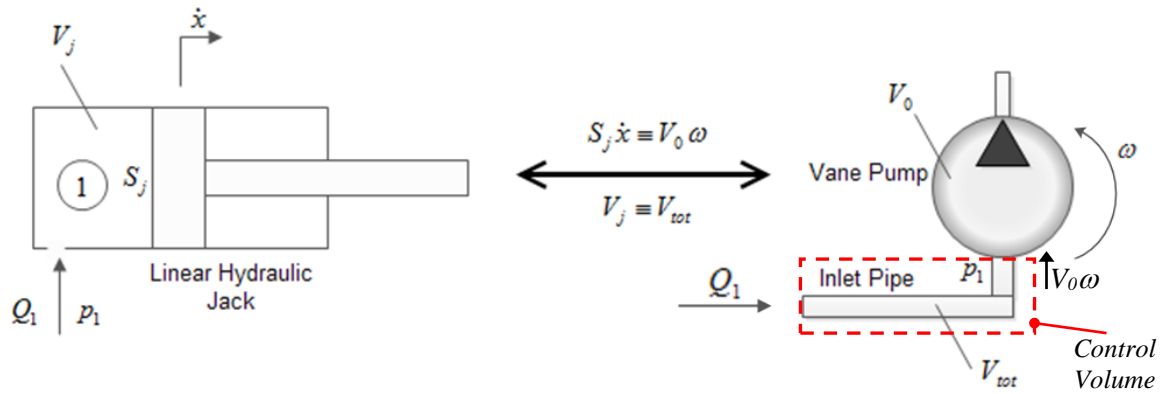


Figure 4.11 Equivalence between pump and linear hydraulic cylinder

As mentioned in the introduction of 4.4, the pump is modelled as a volume that varies as function of rotational speed. For that, the analogy is made with a linear hydraulic jack where the volumetric variation of the jack chamber, due to piston motion, corresponds to quantity of fluid suck by the pump during its rotation, fig. 4.11. As observed in the figure, the input pump flow rate $V_0\omega$ corresponds to the temporal variation of cylinder chamber I volume $S_j dx/dt$. The chamber volume V_j corresponds to V_{tot} .

The Flow Conservation Equation, written with reference to control volume of the inlet pipe shown in figure 4.11, is as follows:

$$Q_1 - V_0\omega = \frac{V_{tot}}{\beta_e} \frac{dp_1}{dt} \quad (4.5)$$

where

V_0 = pump displacement

V_{tot} = total volume of fluid filling the inlet pipe

β_e = Effective Bulk Modulus of the fluid

In order to get the (4.5), the following assumptions have been added:

- The internal pump leakages are neglected
- The fluid density is spatially supposed constant

- The pressure inside pump is supposed equal to inlet pressure p_I : in reality the pressure inside pump, suction side, is lower than pressure in pump inlet to achieve the pressure drop necessary to suck up the fluid towards the volume chambers

By observing the (4.5), first term Q_I of first member represents the flow rate that enters into the inlet pipe while second term is the pump input flow rate. The term of second member is the parasitic contribution of capacitive type.

4.4.3 Resolution of Model

The equations, describing the complete functional model useful to describe the time variation of pressure in pump inlet and exposed in last paragraphs, are listed in Table 4.2.

Complete model for inlet pressure simulation: Pump + Inlet Pipe	
Pipe and Tube Fitting	
<i>Second Newton's Law</i>	
$p_{tank} - p_0 - \rho L_p g \sin(\theta) - \Delta p_{loss}^{tot} = I_h \frac{dQ_1}{dt} \quad (4.a)$	
$\Delta p_{loss}^{tot} = \Delta p_{loss}^{pipe} + \Delta p_{loss}^{throttle}$	
<i>Hagen-Poiseuille Law</i>	
$\Delta p_{loss}^{pipe} = (p_{tank} - p_0) = f_p \frac{L_p \rho}{D_p^2} v_p^2 \quad ; \quad \left(v_p = \frac{Q_1}{S_p} \right) \quad (4.b)$	
$\Delta p_{loss}^{throttle} = (p_0 - p_1) = f_t \frac{L_t \rho}{D_t^2} v_t^2 \quad ; \quad \left(v_t = \frac{Q_1}{S_t} \right) \quad (4.c)$	
Pump	
<i>Flow Conservation Equations</i>	
$Q_1 - V_0 \omega = \frac{V_{tot}}{\beta_e} \frac{dp_1}{dt} \quad (4.d)$	

Table 4.2 Summary of System's Equations

By re-elaborating the equations of table, it is possible to obtain only an equation in the variable \tilde{p}_1 defined as the difference between p_I and p_{tank} : $\tilde{p}_1 = p_1 - p_{tank}$.

In detail, the expressions of the pressure losses (4.b) and (4.c) and of Q_I obtained from (4.d) are substituted respectively in the Δp_{loss}^{tot} and in the Q_I of (4.a). The expression of p_0

got by (4.c) is also inserted in (4.a). By neglecting the constant contribution of gravitational forces (Hp: $\theta = 0$ in eq. 4.1), the equation in the complex domain s is finally given by:

$$\tilde{p}_1(s) = -H_p(s) \omega(s) \quad (4.6)$$

where

$$H_p(s) = \frac{K_a(1+\tau_p s)}{\left(\frac{s^2}{\omega_p^2} + 2\frac{\xi_p}{\omega_p}s + 1\right)}$$

$$K_a = R_h^{tot} V_0 \quad \text{Transfer function gain}$$

$$\tau_p = \frac{I_h}{R_h^{tot}} \quad \text{Time constant}$$

$$\xi_p = \frac{R_h^{tot}}{2} \sqrt{\frac{C_h}{I_h}} \quad \text{Damping ratio}$$

$$\omega_p = \sqrt{\frac{1}{C_h I_h}} \quad \text{Natural pulsation}$$

$$I_h = \rho \left(\frac{L_p}{S_p} + \frac{L_t}{S_t} \right) \quad \text{Hydraulic Inertia}$$

$$R_h^{tot} = 32\mu \left(\frac{L_p}{D_p^2 S_p} + \frac{L_t}{D_t^2 S_t} \right) \quad \text{Total hydraulic resistance}$$

Equation (4.6) is the representation in the complex domain of the second order differential equation in the variable \tilde{p}_1 and function of 10 parameters: ρ , μ , β_e , V_{tot} , L_p , S_p , D_p , L_t , S_t , and D_t . The input signal corresponds to pump speed ω .

Table 4.3 lists the numerical value of the parameters constituting the transfer function $H_p(s)$ of (4.6). $H_p(s)$ consists of a zero and a pair of conjugate complex poles placed in the half-plane of Real negative axis side in the (Real,Imm) complex domain.

The geometrical characteristics of the test bench, described in Appendix A are used in the calculation and the fluid density ρ and the dynamic viscosity μ are instead maintained constant and equal to values provided by literature for Tellus 32 at 45 °C and atmospheric pressure. The effective Bulk Modulus β_e is also maintained constant and assumed equal to

1000 bar (this represents an actual medium value that was obtained through the simulations of full virtual prototype described in chapter 3).

<i>Transfer Function</i>	$H_p(s) = \frac{K_a(1 + \tau_p s)}{\left(\frac{s^2}{\omega_p^2} + 2\frac{\xi_p}{\omega_p}s + 1\right)}$		
<i>Gain</i>	$K_a =$	[Pa s/rad]	5.04
<i>Natural Pulsation</i>	$\omega_p =$	[rad/s]	740.17
<i>Damping Ratio</i>	$\xi_p =$	[-]	0.0013
<i>Zero</i>	$-1/\tau_p = -\frac{R_h^{tot}}{I_h}$	[1/s]	-1.88
<i>Poles</i>	$p_{1p} = -\xi_p \omega_p + j\omega_p \sqrt{1 - \xi_p^2}$	[1/s]	-0.94+j740.16
	$p_{2p} = -\xi_p \omega_p - j\omega_p \sqrt{1 - \xi_p^2}$	[1/s]	-0.94-j740.16

Table 4.3 Characteristics of the transfer function in \tilde{p}_1

The expression in time domain of \tilde{p}_1 , when an input speed step of constant value ω is imposed, is finally obtained as follows:

$$\tilde{p}_1(t) = \left[1 - \sqrt{\frac{1 - 2\xi_p \omega_p \tau_p + \omega_p^2 \tau_p^2}{1 - \xi_p^2}} e^{-\xi_p \omega_p t} \sin\left(\omega_p \sqrt{1 - \xi_p^2} t + \varphi_p\right) \right] K_a \omega_0 \quad (4.7)$$

where

$$\varphi_p = \arg\left(1 - \xi_p \omega_p \tau_p + j\omega_p \tau_p \sqrt{1 - \xi_p^2}\right) + \arg\left(\xi_p + j\sqrt{1 - \xi_p^2}\right)$$

In next paragraph a different modelling based on virtual prototyping is proposed and later compared to analytical model exposed in this section.

4.5 Virtual Prototypes: Inlet Line and Pump Modelling

In this section two different prototypes are described that enable to simulate the time evolution of the fluid pressure in pump inlet during the acceleration phase. A comparison is firstly carried out between the two prototypes in order to identify the similarities and differences. After that, the analytical model response is compared to best virtual prototype obtained by the previous comparison.

The building of the virtual prototypes consists in detailed modelling of the inlet hydraulic line between pump and tank, with particular attention to representation of:

- variations of the inside diameters in pipe and tube fittings that potentially cause charge losses (resistive effects)
- volumes (capacitive effects)
- lengths and cross-section areas (inertial effects)

A more advanced model of the pump is also provided, compared to preceding models described in Chap. 2 and 3, that reproduces its interior orifices and volumes in suction and discharge sides.

The advantage of the virtual prototyping in AMESim environment is represented by the ability to simulate non-linear phenomena at an advanced accuracy level, not evaluated in the functional model in 4.4. In particular the following phenomena are modelled:

- Variations of flow conditions (laminar and turbulent)
- Variation of Bulk Modulus as function of fluid pressure, fluid air content and pipe compliance
- Presence of edge forms (sharp-edged, square-edged...) that contribute to concentrated pressure losses

Next paragraph describes a first basic prototype of pump and inlet hydraulic line.

4.5.1 Basic Prototype: Characterisation of Inlet Line

Figure 4.12 shows the *Vane Pump_03* and the *Hydraulic Circuit_02* virtual prototypes developed in AMESim for simulation of operating conditions favourable to cavitation.

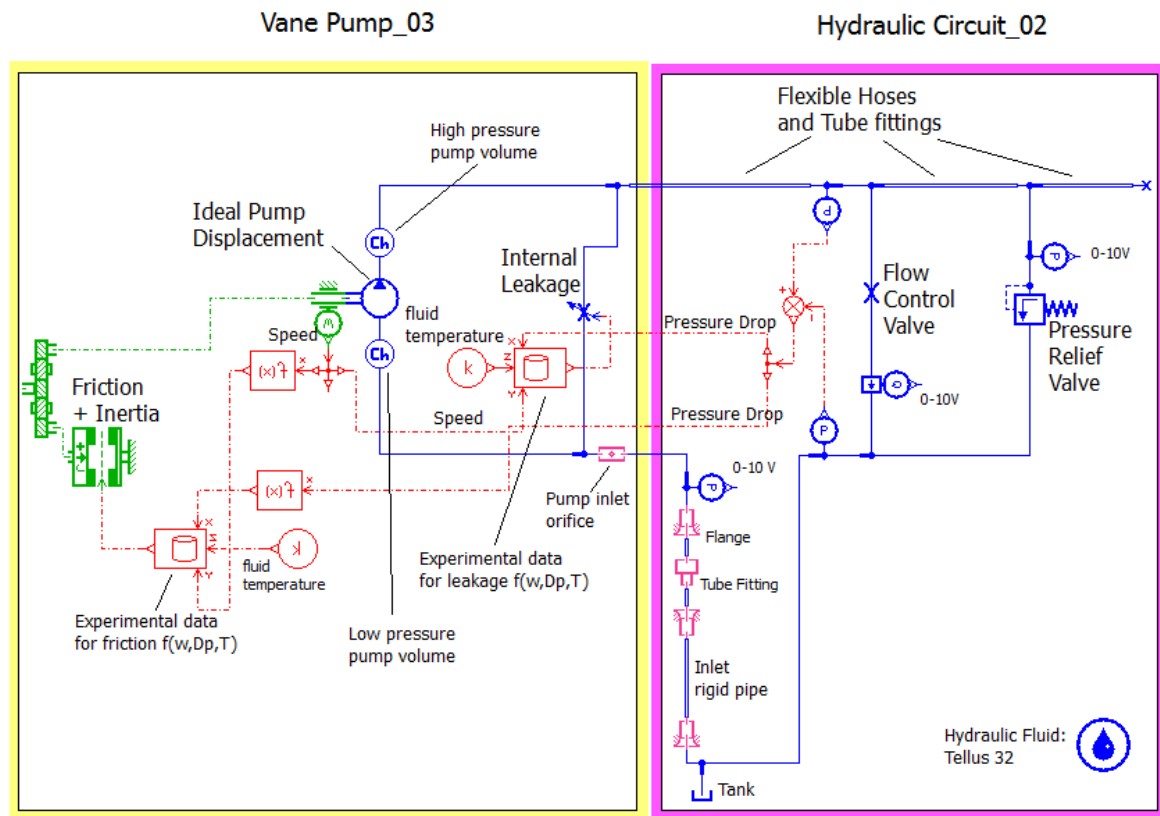


Figure 4.12 Virtual prototypes of vane pump and hydraulic circuit for cavitation evaluation

The prototypes are obtained by modifying the models previously developed in Chap.3. The differences with last prototype concern an improved modelling of inlet line and pump.

At this modelling level, the pump model corresponds to *Vane Pump_02* (showed in fig. 4.13) with the following additions:

- Pump inlet orifice
- Low pressure volume

Vane Pump_03

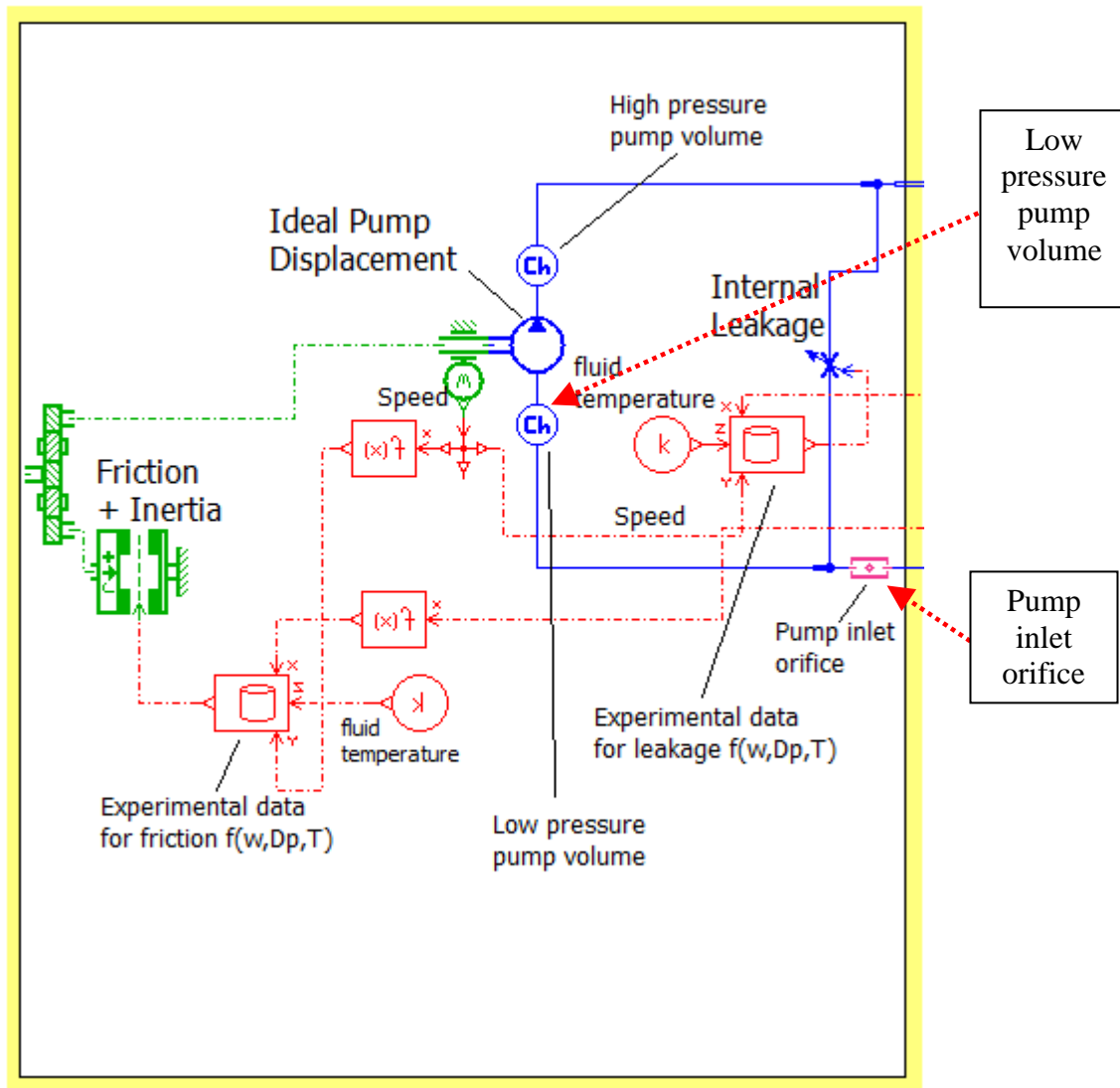


Figure 4.13 Vane Pump virtual prototype: Vane_Pump_03

The inlet line is constituted by following components, in reference to test bench described in chapter 1 whose characteristics are inserted in Appendix A (fig. 4.14):

- Straight rigid pipe, included inlet probe
- Tube fitting
- Flange
- Connection pipe/tube fitting, tube fitting/flange and flange/pump inlet

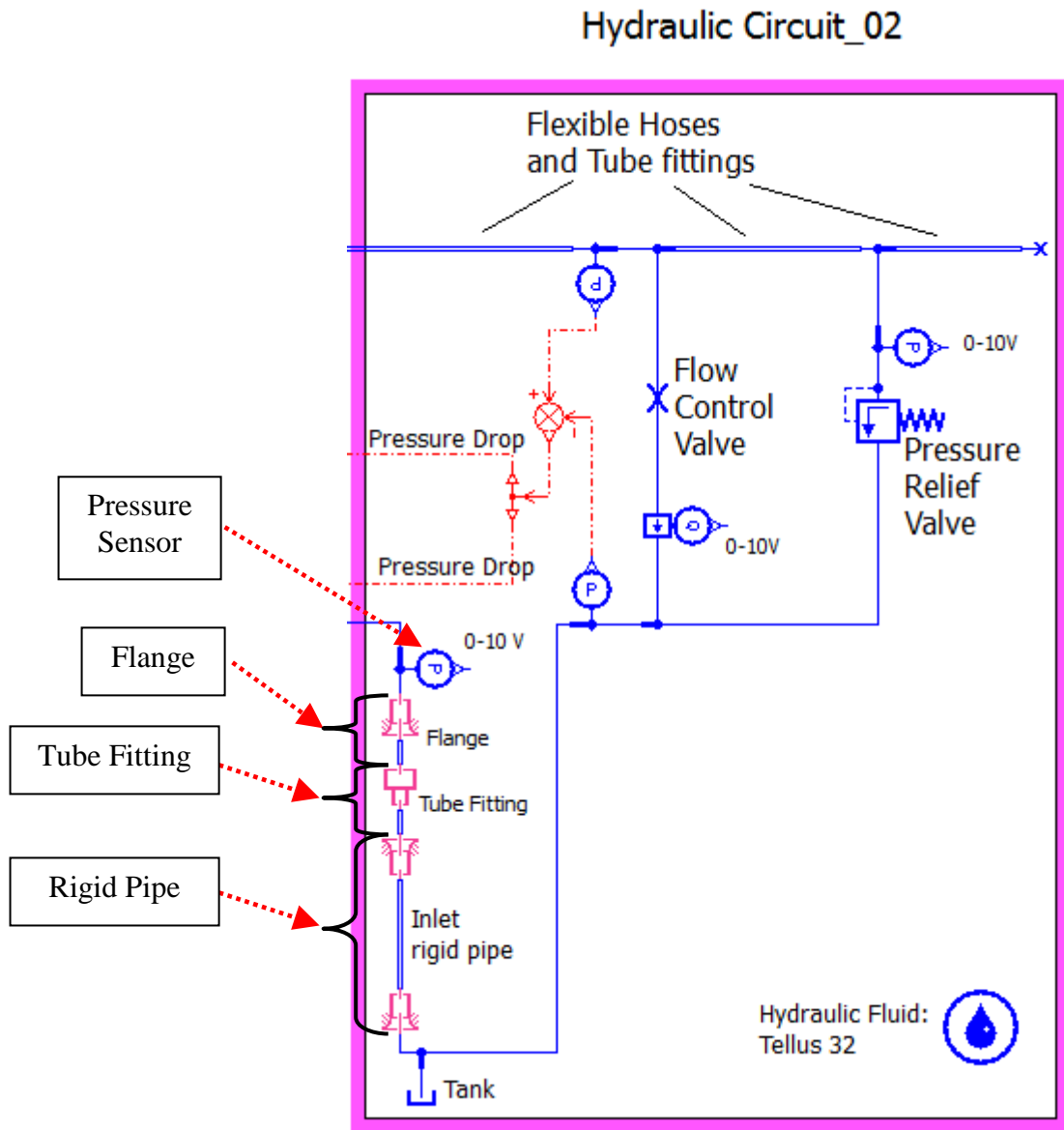


Figure 4.14 Hydraulic circuit virtual prototype with inlet line modelling: Hydraulic_Circuit_02

4.5.2 Advanced Prototype: Characterisation of Pump Interiors

The advanced prototype differs from the basic prototype for a more accurate modelling of the pump interiors, in particular of the connections between parts in low pressure volume. Figure 4.15 shows the total volume inside pump filled with hydraulic fluid at low pressure, with some simplifications. It is represented by:

- 1- drain volume inside cap
- 2- volume delimited by the external surface of cam ring and the housing
- 3- volume inside housing
- 4- volume in the low pressure chambers including the volume of the bulbs placed at the bottom of the vanes

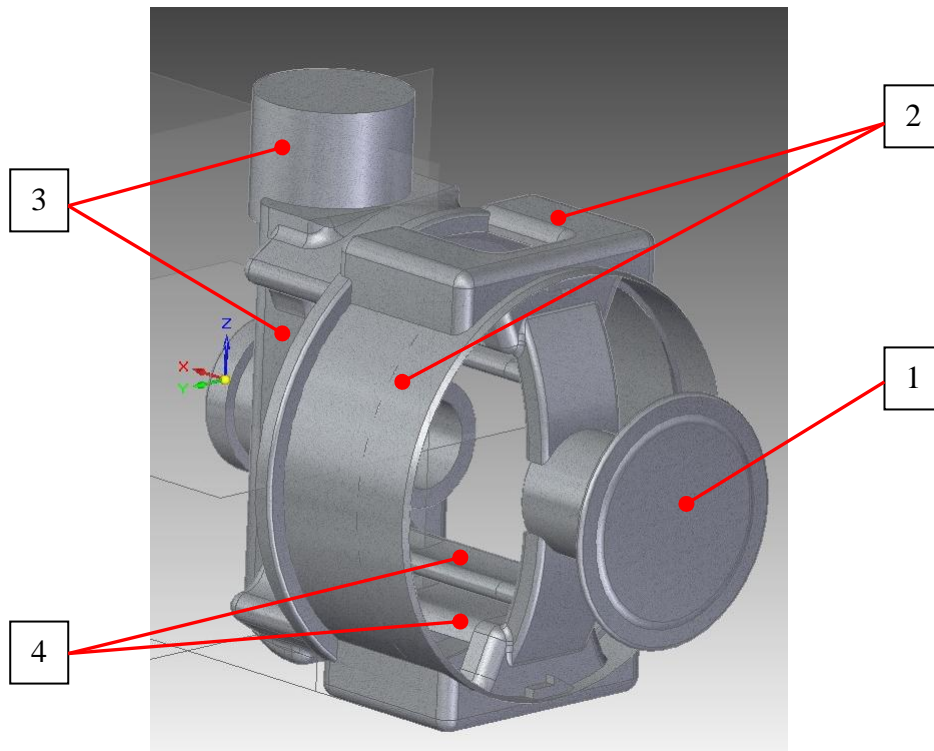


Figure 4.15 Representation of total volume at low pressure inside pump

Figures 4.16 show two sections of the total volume: on the left there is the section obtained through a vertical plane containing the shaft axis while on the right there is the section perpendicular to first section passing through the symmetry plane of the cam ring.

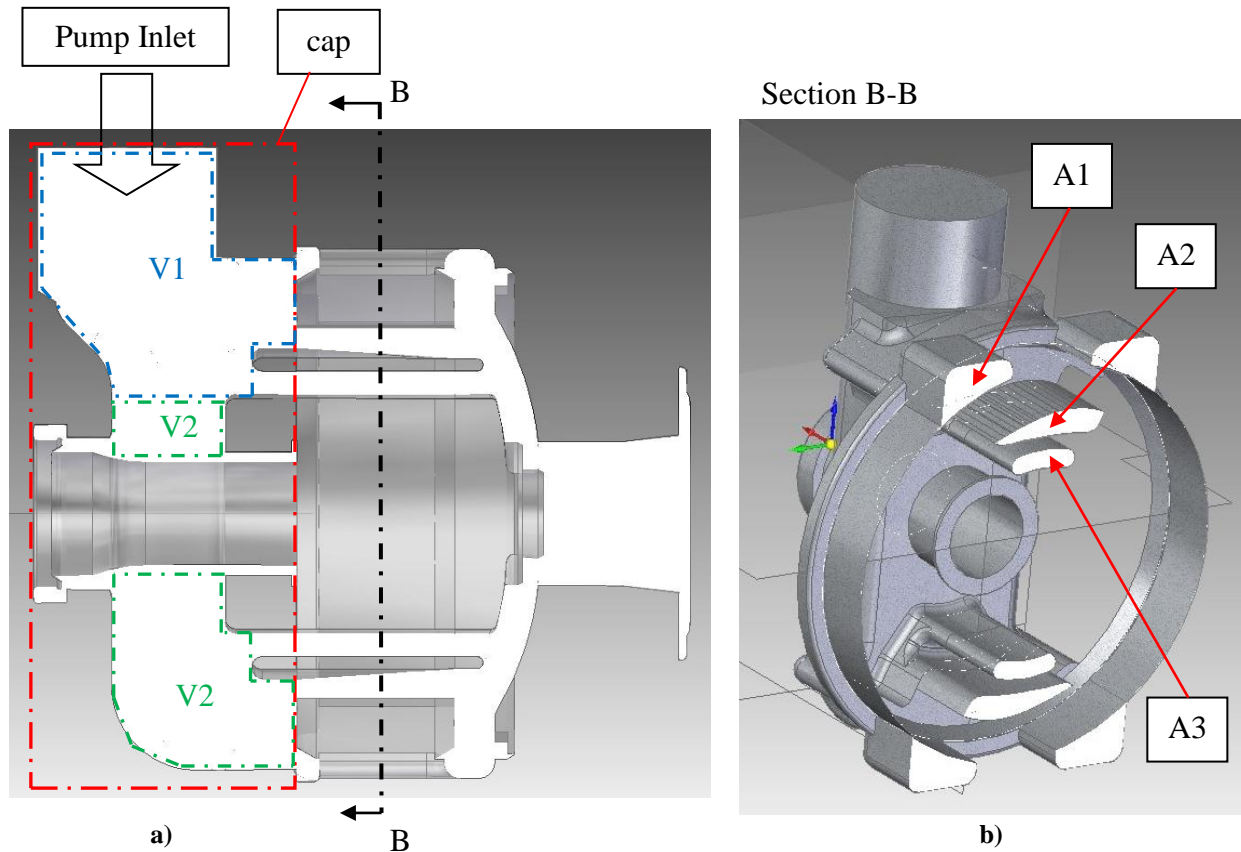


Figure 4.16 Representation of total volume section: a) longitudinal section, b) transversal section

By observing the figures 4.16 it is possible to note three types of orifice identified with the areas: A1, A2 and A3. They respectively correspond to:

- A1 = area of the orifices that permit the passage of hydraulic fluid at the external of the cam ring in order to facilitate the filling of the displacement chambers from two opposite directions. This orifice is generated in the cap but it changes its dimensions by crossing the zone between the cam ring and the housing (fig. 4.16b). In order to simplify the analysis, it is supposed that A1 has constant cross-sectional area along all orifice length.
- A2 = area of the orifice the sends the hydraulic fluid inside the chambers. It is defined by the cam ring profile and the rotor. In reality this orifice is smaller because of the presence of the vanes but they are neglected. The orifice is extended with constant cross-sectional area up to the end of cam ring.

- A3 = area of the orifice that sends the hydraulic flow inside the bulbs at the bottom of the vanes. This orifice is generated in the cap (fig. 4.16a) having the section showed A3 but it is not equivalent to bulbs sections (they are smaller). In order to simplify the analysis, it is supposed that the bulbs have the same section of the cap orifice and so this orifice is extended with constant cross-sectional area up to the end of cam ring.

The characteristics of the three orifices inside pump, are inserted in the Appendix A.

The building of the virtual prototype consists in modelling of the orifices by characterising them in terms of diameter, cross-sectional area and length in order to take into account the associated resistive effects. Figure 4.17 shows the advanced prototype. In this prototype the pump total volume at low pressure is divided into three parts as showed in figure 4.16a: V1 corresponds to volume included between the pump inlet orifice and the four orifices that are placed in the top of the pump, V2 represents the rest of the volume of the housing reduced of V1, V3 is the total volume at low pressure reduced of V2+V1. It represents an improved model of pump where the resistive, inertial and capacitive effects are again evaluated through lumped model but it is now constituted by a series of I, R and C elements and not more by a single element as in last prototype. It can thus be dealt as an intermediary modelling between a lumped and a full distributed.

Orifices inside pump

All the orifices inside pump are modelled through a sub-model that represents a short tube where the discharge coefficient C_q is calculated as function of the flow number λ and the ratio between orifice length and diameter, in accordance to graphs provided by literature [12] (sub-model OR004). The flow number λ determines the flow conditions, laminar or turbulent. Being non circular the orifice section, an equivalent diameter D_{eq} has to be calculated as function of the cross-sectional *Area* and orifice section *perimeter*, given by:

$$D_{eq} = \frac{4 \text{ Area}}{\text{perimeter}} \quad (4.8)$$

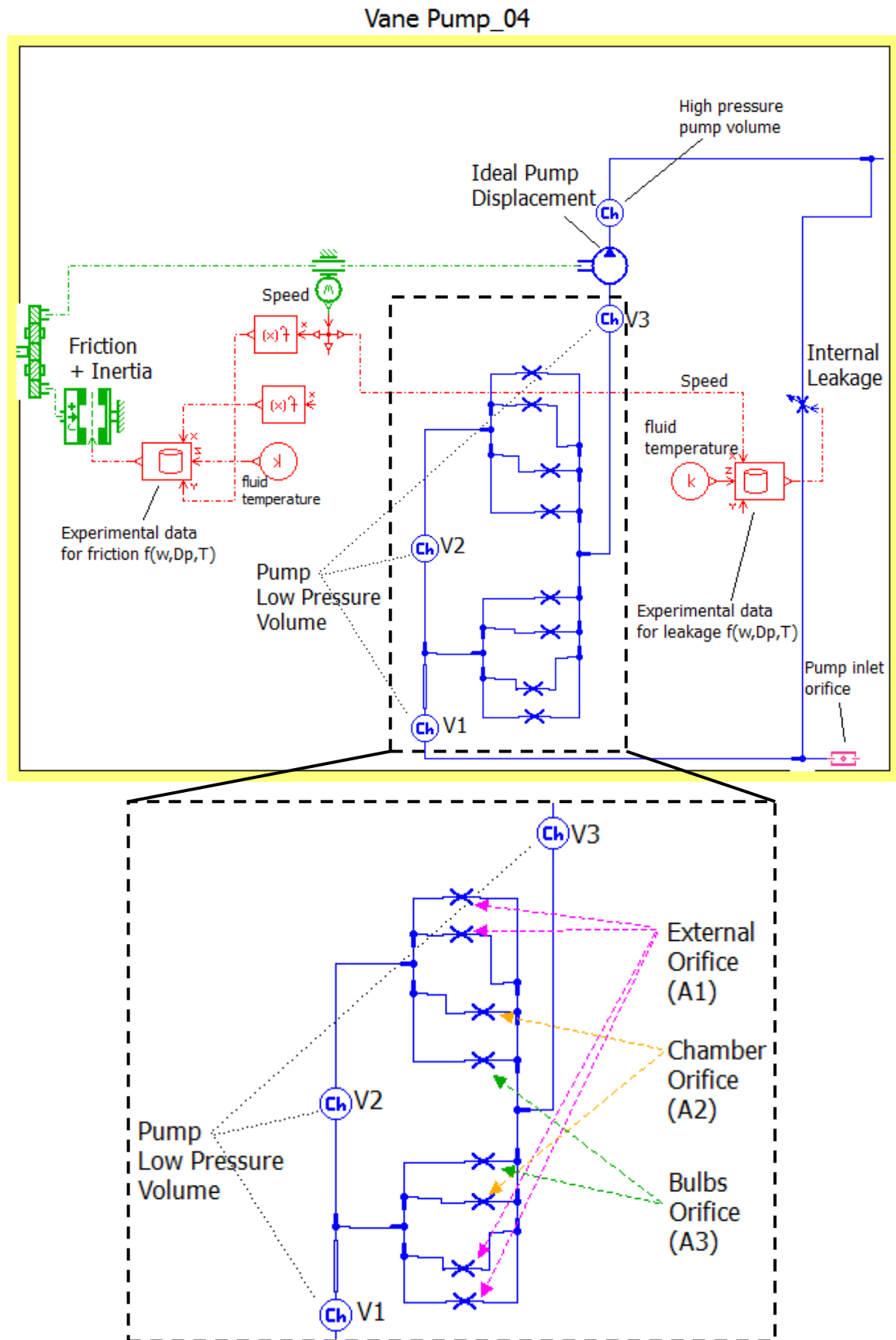


Figure 4.17 Advanced Prototype: Pump interior and inlet pipe

4.5.3 Comparison between Prototypes

The two prototypes are now performed and compared by means of the same simulation test. An input step of speed is imposed from 0 to 3000 *rpm*, starting at 7 *s*, achieved in 10 *ms* and stopping at 12 *s*. The virtual prototype also needs the input signal of pressure produced in pump outlet, discharge side: a pressure step is imposed from 0 to 150 *bar*, achieved in 10 *ms*.

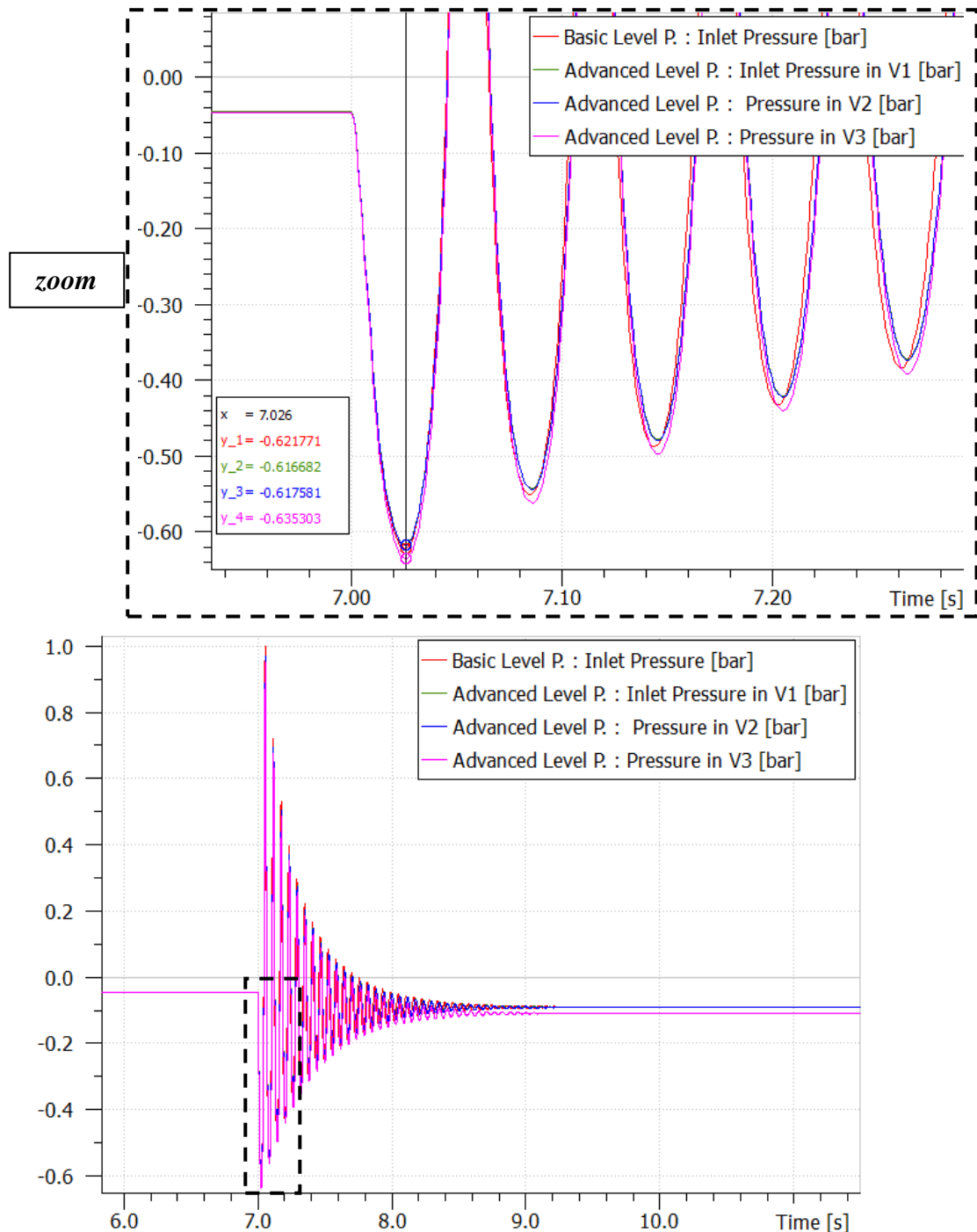


Figure 4.18 Inlet Pressure and inside pump with the two different prototypes

The results of pressure in pump inlet are showed in figure 4.18 where in the legend, basic level P. refers to result obtained by the prototype described in paragraph 4.5.1 while the advanced level P. refers to prototype in 4.5.2. In both of them, the pressure before the step of speed started at 7 s, has negative value (about -0.04 bar relative) due to effects produced by the gravity, given that the inlet pipe is vertically installed. After that, there is not an appreciable difference between the responses of the two prototypes: in fact they provide a minimum value of pressure that differs less of 3 %: -0.622 bar for the basic prototype and -0.635 bar for the advanced one.

The minimum reached pressure is much higher of the vapour pressure of the fluid, set to -0.2 bar in the model. The phenomenon of air release is so active and the phenomenon of cavitation too.

The advanced prototype is able to provide three different values of pressure: in V1 it represents the inlet pressure (as the pressure provided by the basic prototype), in V2 it is the pressure inside the cap while the pressure in V3 it is the pressure obtained in the housing.

The CPU time (Central Processing Unit) of the advanced prototype is higher than the basic one. Table 4.4 shows a comparison in terms of integration type, solver, tolerance and ratio between the execution T_{exec} and simulation T_{sim} time. The integration type, the solver and the tolerance are the same in both of them. The tolerance is set at 10^{-5} that is a typical suitable value for simulating models which include the use of hydraulic fluid properties. The observation of ratio T_{exec}/T_{sim} permits to conclude that the advanced prototype takes more time (about 33 %) than the basic prototype to run simulation. However the CPU time can be lowered for both of them by reducing the total number of saved variables during simulation. Just thinking that the advanced prototype saves up to 145 variables versus 45 of the basic one.

<i>Prototype</i>	<i>Integration Type</i>	<i>Integration Solver</i>	<i>Tolerance</i>	T_{exec}/T_{sim}
Basic (paragraph 4.5.1)	Variable	DASSL	10^{-5}	1,33
Advanced (paragraph 4.5.2)	Variable	DASSL	10^{-5}	2

Table 4.4 Comparison between advanced and basic prototype in terms of integration option and CPU time

In conclusions, even if the advanced prototype characterises in a more accurate way the inside of the pump by means of orifices and partial volumes modelling, it provides results nearly equivalent to results obtained by the basic prototype with a gap less of 3 %. It

means that the modelling of the inlet line plays a dominant role when compared to orifice effects inside pump. As consequence, the basic prototype is selected to simulate the time variation of pressure in pump inlet, thanks to its lower expense time. It is then compared to analytical model in next section.

4.6 Comparison between Analytical and Virtual Model

The comparison carried out in 4.5.3 between the two virtual prototypes performance, has permitted to select the basic prototype for simulation of cavitation/aeration phenomena thanks to its lower computational time compared to advanced model.

In this paragraph the simulated results provided by the basic prototype are compared to analytical results provided by the functional model exposed in 4.4.

In detail, the time evolution of pressure in pump inlet is evaluated when an input step of speed 0-1000 *rpm*, achieved in 10 *ms*, is commanded. The line pressure is imposed to be equal to 0 *bar* relative, equivalent to no hydraulic load (flow control valve in open position).

In addition, the following simplifications are made to better compare the analytical and virtual model:

- 1) the inlet hydraulic line is supposed in horizontal position (pump and tank at the same level) to neglect the gravitational effects
- 2) the inlet hydraulic line is assumed constituted by only the straight rigid pipe and the orifice in pump inlet. The flange and tube fitting are so not taken into account

These simplifications are justified on the grounds that: the point 1) permits to remove a constant contribution reproduced in the same way by the two models and so not fundamental to comparison. The point 2) permits especially to neglect the resistive effects due to edge forms of connections. The presence of tube fitting and flange is in reality not negligible but the interest is just to compare the two models by highlighting the capacitive effects and effects due to flow conditions.

Figure 4.19 shows the comparison of pressure in pump inlet produced by the analytical model, exposed in 4.4 and the virtual prototype exposed in 4.5.1.

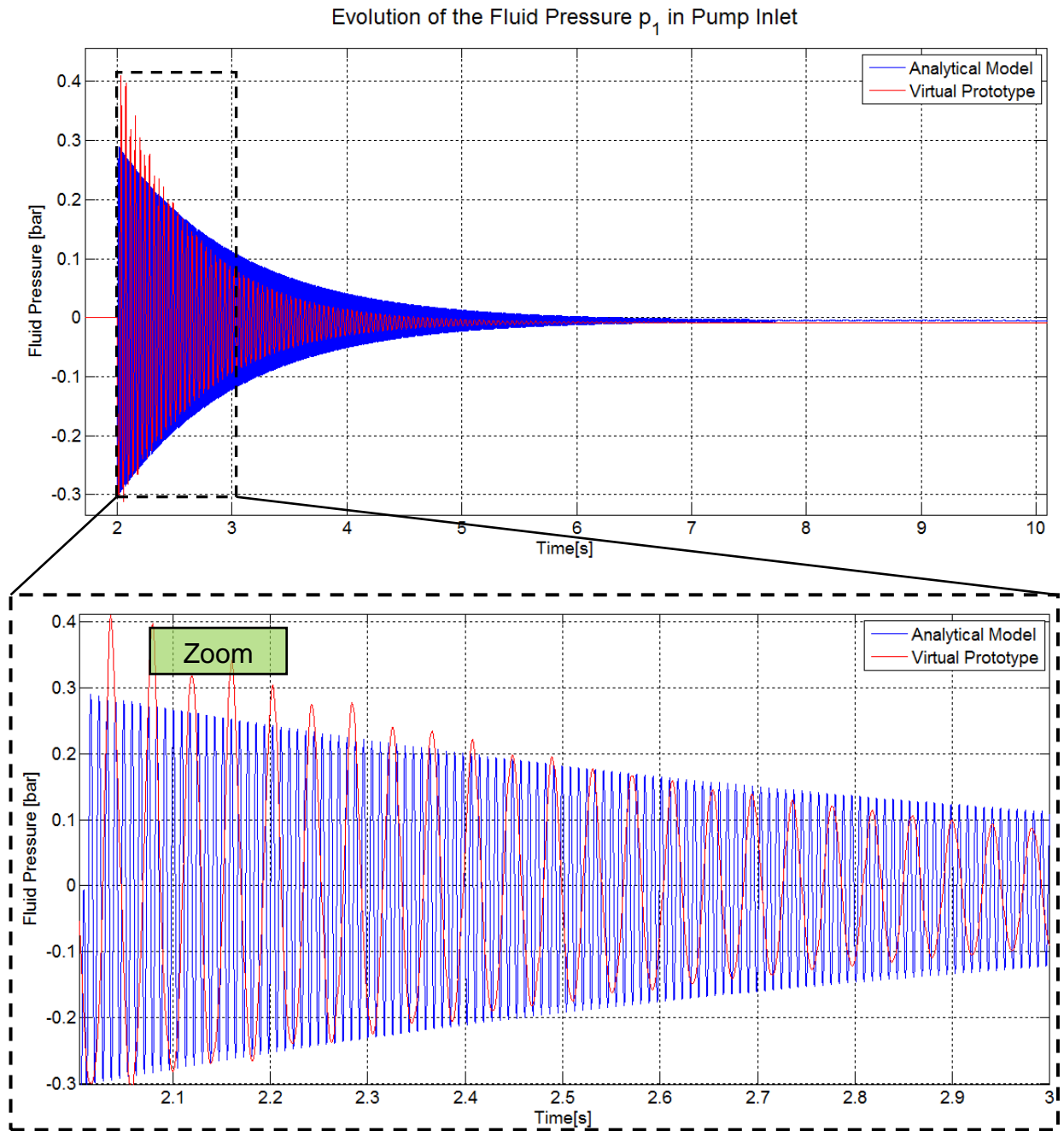


Figure 4.19 Comparison between analytical model and virtual basic level prototype results: temporal evolution of pressure in pump inlet

In reference to results showed in figure 4.19, it is possible to summarise the main difference in this way:

- 1) The **natural frequency** f_h in the AMESim model is lower than in analytical model.

It varies and it depends on **effective Bulk Modulus** β_e and fluid density ρ : $f_h =$

$$\frac{1}{2\pi L} \sqrt{\frac{\beta_e}{\rho}}. \text{ The Bulk Modulus used by AMESim is a function of: air content, wall}$$

compliance and fluid pressure and temperature. It results lower than β_e used in the analytical model. The **density** is a function of fluid pressure and temperature. In the analytical model both β_e and ρ are maintained constant for all simulation.

- 2) The **oscillation range** and p_{1min} depend on hydraulic capacity C_h and on flow conditions through the damping ratio ξ_p (tab. 4.3).

In the AMESim model, the system **hydraulic capacity** C_h results higher (because β_e is lower) and it increases the damping ratio ξ_p by facilitating the reduction of oscillations.

The introduction of the orifice in the virtual prototype adds pressure losses that depend on flow conditions: if the **turbulent conditions** are established, the resistive effects increase and also the damping ratio ξ_p

- 3) The **final value** is lower in the AMESim model (about of 30 %) because it depends on resistive contribution (through the gain K_a of the transfer function in tab. 4.3) that results higher in the virtual prototype
- 4) The **settling time** in the virtual prototype reduces because the increase of ξ_p dominates compared to reduction of natural pulsation ω_p

The principal difference between the two approaches is that the analytical model uses a constant value of effective Bulk Modulus (fixed at 5000 bar) while the virtual prototype uses a value of β_e that varies during simulation because it is dependent on: air content (fixed at 2 % volumetric percentage), pipe deformability ($E=2*10^6$ bar, rigid straight pipe) and operating conditions (pressure and temperature). We could modify the value of β_e in the analytical model in order to be closer to the result provided by AMESim, but the objective of this comparison is that of showing: 1) the effect produced by a variable fluid compressibility on the oscillation damping; 2) that, even if the two different approaches provide a comparable minimum pressure value p_{1min} , wrong results interpretation can be made when the hydraulic capacity of the fluid is maintained constant and when the turbulent conditions of flow are not taken into account.

In conclusion, the comparison between analytical and virtual models has permitted to show that:

- The dynamics of pressure at pump inlet is hardly influenced by the hydraulic capacity and the flow conditions

- A simplified modelling of these two effects can deal with limitations in the simulation especially of oscillation frequency and damping and also of final value
- The higher realism of virtual prototyping is confirmed as just demonstrated in chapter 3

The virtual prototype is thus selected as best tool for simulating the pressure at pump inlet. In next section, it is compared to experimental results obtained in laboratory for its validation.

4.7 Laboratory Tests

The performances obtained through the basic virtual prototype are then compared to the real performances achieved in laboratory. The final objective is to validate the virtual prototype that enables to predict the time evolution of pressure at pump inlet.

In order to acquire sufficient data and to carry out the comparison, tests are performed in laboratory by using the test bench in Chap.1. During tests, the motor speed is closed-loop controlled by action on the motor torque using a P controller plus a full FF compensator, as described in Chap. 3. The controller is then implemented into in the SpeedGoat host controller that drives directly the motor inverter as a torque demand signal.

Table 4.5 summarises the operating conditions for each test.

Each test is characterised by:

- An input step of speed commanded from 0 to maximum speed by imposing the rise time,
- The pressure in the hydraulic circuit is determined before starting test by setting the opening of the flow control valve,
- The fluid temperature in tank is maintained constant for all tests time duration: it corresponds to environment conditions of 30 °C.

<i>Command Speed Step</i>	<i>Rise Time of Step</i>	<i>Line Pressure</i>	<i>Tank Temperature</i>
[rpm]	[ms]	[bar]	[°C]
0-1000	[10, 20, 30, 50, 100, 200]	[0, 100]	30
0-2000			
0-2400			

Table 4.5 Operating conditions for laboratory tests

It is observable that the maximum command speed is varied in the range between 1000 and 2400 rpm with rise time from 10 to 200 ms.

The line pressure conditions of 0 bar, equivalent to flow control valve in fully opened position, and 100 bar. In total 36 tests are so performed.

During tests the following variables are measured: command speed ω^* , measured speed ω , line pressure Δp , pump inlet pressure Δp_{in} , output flow rate Q_{out} , command motor torque C_m , estimated motor torque C_{est} , tank temperature T_{tank} .

In order to compare measured and simulated Δp_{in} , some characteristic of the time response of pump inlet pressure is evaluated, as showed in figure 4.20:

- **p₁** : minimum pressure in first peak
- **p₂** : maximum pressure in second peak
- **p₃** : minimum pressure in third peak
- **t_{Δp1}** : time delay between measured and simulated p₁
- **f_p** : time frequency of Δp_{in} evaluated between the peaks p₁ and p₃

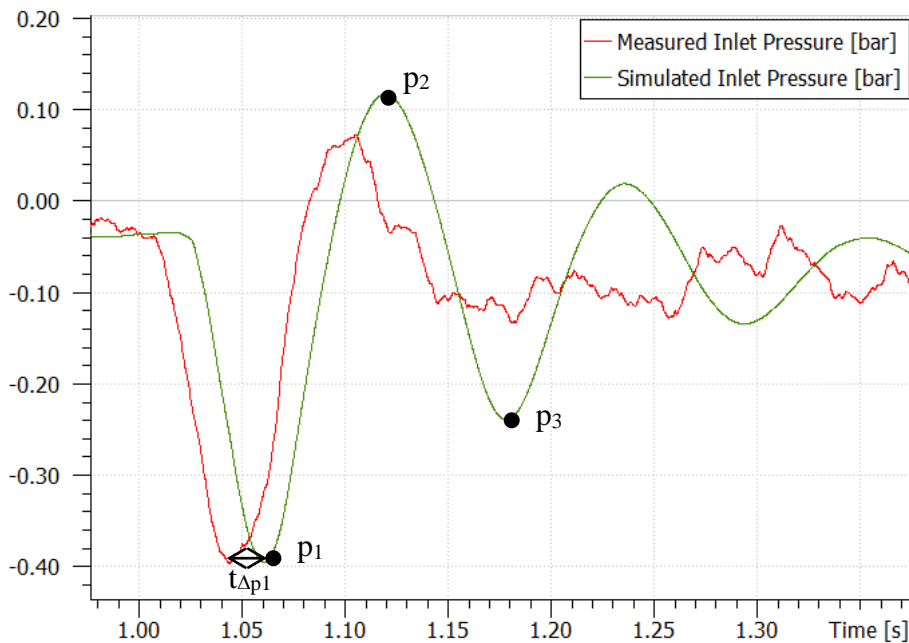


Figure 4.20 Comparison of inlet pressure between measured and simulated results for command step of 2000 rpm imposed for 10 ms

4.7.1 Simulation Procedure

The procedure used to run the virtual prototype is exposed in this paragraph. The objective is to validate the complete virtual prototype constituted by the closed-loop speed control, the frequency drive, the mechanical components, the hydraulic circuit and the virtual prototype of inlet line and pump just described in 4.5.1. The virtual prototypes of closed-loop speed control, the frequency drive and the electric motor with shaft compliance have been validated in Chap. 3. So the virtual prototype of inlet line and pump is now to be validated. With reference to scheme in the figure 4.21, the sequence of steps is as follows:

- **First Step.** It concerns the simulation of the partial virtual prototype constituted by the *inlet line + pump* (block A in the fig. 4.21). In this case, the input signals of the model are represented by the measured motor speed $\tilde{\omega}$ and the measured line pressure Δp^{\sim} . This simulation permits to neglect the mechanical contributions, the command chain, the frequency drive and the rest of hydraulic circuit. The output of the model is the pressure in pump inlet $\Delta p_{in}'$.
- **Second Step.** The *electric motor*, the *shaft compliance*, the *frequency drive*, the *closed-loop speed control* and the rest of *hydraulic circuit* are added (block B) in order to obtain the complete virtual prototype of the test bench. In this case the input signal of the model is represented by the command speed ω^* . The outputs of the model are the pressure in pump inlet $\Delta p_{in}'$, $\Delta p'$, Q_{out}' , $\tilde{\omega}'$ and C' .

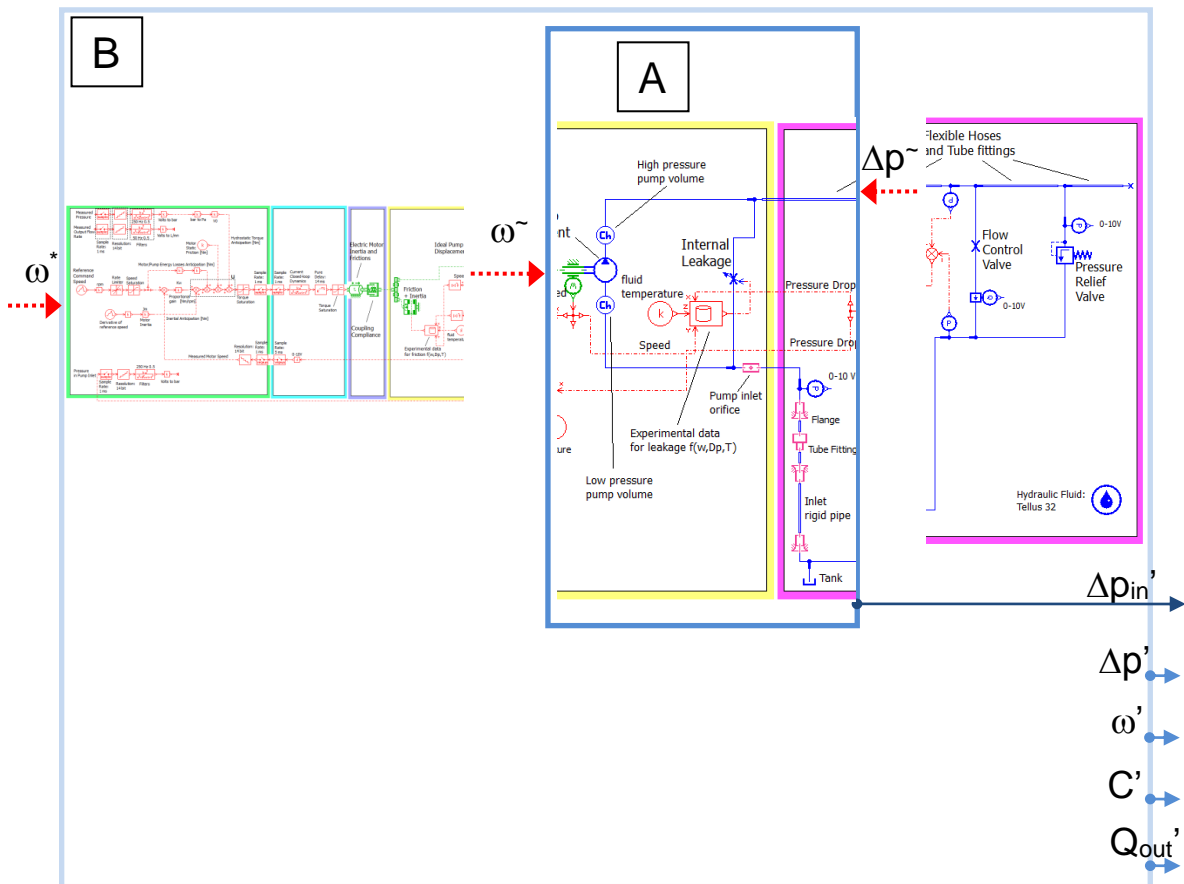


Figure 4.21 Scheme of simulation steps sequence

This type of simulation based on partial AMESim model, enables some parameters to be varied in a more gradual way by observing their influence on system's variables. It enables to obtain a compromise solution that is close to real performance of pressure in pump inlet.

4.7.1.1 Determination of Optimum Fluid and Friction Factors Characteristics

During the first step of simulation described in last paragraph, an optimisation procedure is carried out in order to identify the best value of the unknown parameters of the system. They concern both fluid properties and characteristics of inlet line. In detail:

- Saturation pressure of the fluid P_{sat}
- Fluid air content ε

- Friction factor k_f of connection flange/pump inlet and of the inlet probe of rigid pipe
- Critical Reynolds number Re_{cr} in the connection flange/pump inlet and of the inlet probe of rigid pipe
- Number of state variables for frequency dependent friction (f_{dp}) in the rigid pipe
- Relative roughness of rigid pipe and of pump inlet orifice

In total 9 parameters are unknown.

The applied procedure consists of three points:

- 1) Identification of a numerical range (min, max) for each parameter through data acquired from literature and through assumptions. In particular the range of the friction factors are obtained by means a preliminary calculation based on geometrical characteristics measured in test bench and the formulas extracted by [14].
- 2) Performing a *Design of Experiments* (DOE), tool in the design exploration module of AMESim: it permits to determine the relationship between the parameters and $\Delta p_{in}(t)$. The two extreme values, previously defined in 1) for each parameter, are set as *levels*. Runs are then performed by combining the parameters *levels*: 2^N runs are so necessary, where N is the total number of *levels* (Technique of Full factorial). The aim is so to establish the influential parameters which play a fundamental role on the time evolution of Δp_{in} , in particular on value of p_1 showed in fig. 4.20

The final result of DOE shows that the relative roughness of components and the number of state variables for f_{dp} have a less important contribution on p_1 compared to others. Consequently their values are fixed and maintained constant for all runs

- 3) An *Optimization process* is then applied, by using a tool in the design exploration module of AMESim. The best set of parameters has to be found to make the measured and simulated p_1 close each other. The chosen criteria is in fact to minimise the square of pressure difference: $\min (p_{1measured} - p_{1simulated})^2$. A laboratory test is taken as reference for the measured p_1 and correspondent to: speed step 0-

1000 rpm in 10 ms, 0 bar (refers to Tab. 4.5). A genetic algorithm is selected that randomly generates a population of “individuals” which represent sets of parameters. The best individuals are kept and the others are removed from population and replaced. In addition, individuals also mutate through perturbations added to their values. After several generations, individuals converge to one best solution [13]. 20 iterations are finally carried out.

Table 4.6 summarises all the final values of parameters.

Saturation pressure	[bar]	0.69
Air content	[%]	5.6
k_f of flange/pump inlet	[-]	0.24
k_f of inlet probe of rigid pipe	[-]	0.84
Re_{cr} of flange/pump inlet	[-]	997
Re_{cr} of the inlet probe of rigid pipe	[-]	535
N. of state variables for fdp in rigid pipe	[-]	3
Relative roughness of pipe	[-]	10^{-5}
Relative roughness of pump inlet orifice	[-]	10^{-5}

Table 4.6 Final values of the system parameters obtained by means of optimisation process

4.7.1.2 Free Air Propagation inside Model: Limitations of AMESim

It is remarkable in the table 4.6 that the properties selected for the fluid in the inlet hydraulic line differ from the fluid properties previously chosen for the high pressure hydraulic circuit, Chap. 3.

There, the achieved simulation procedure has permitted to determine the following fluid properties: $P_{sat} = 1000 \text{ bar}$ and $\varepsilon = 2.7 \%$. The complete virtual prototype has been validated for acceleration, steady-state and depressurisation phases by evaluating speed, line pressure, output flow rate and motor torque. That prototype does not simulate the time variation of pressure in pump inlet, being the inlet hydraulic line represented only through a basic sub-model without parasitic contributions. The pressure at pump inlet so corresponds to atmospheric pressure in tank.

Now a distinction is made about properties of the fluid filling the low pressure (inlet line between pump and tank) and the high pressure hydraulic circuit: in the hydraulic circuit at

high pressure the fluid properties correspond to values obtained in Chap. 3, whereas in the inlet line the properties are listed in the table 4.6. In order to justify this choice, it is necessary to make some observations about the potentiality of AMESim.

It is important to underline that AMESim Rev11 has some limitations about the way to simulate the dynamic processes, like cavitation and aeration. AMESim software creates lumped parameters models based on control volumes (CVs) in which the fluid properties are assumed uniform. The mass conservation is so satisfied, for each CV, by the flow continuity equation where the density variations are neglected: the flow rates represent the input ports of each CV and are calculated through laminar or turbulent orifices equations at a reference pressure p_r and density $\rho_r = \rho(p_r)$. For each CV, the pressure p , obtained by the flow conservation equation resolution, is then used to calculate the density ratio $\rho(p)/\rho_r$. This ratio, multiplied by the flow rate, determines the mass time derivative [7], [15].

The fluid air mixture density ρ is a function of the pressure p and of the instantaneous gas content included in the CV. The instantaneous gas content is evaluated in each CV by means of the Henry's Law: the mass fraction of undissolved gas varies linearly with the fluid absolute pressure, obtained as just mentioned. It represents a steady-state equation that permits to calculate an instantaneous value of gas content in the fluid. The rapid rate of density of the fluid air mixture is hence considered to ensure the consistency between density and Effective Bulk Modulus β_e , through the following expression [7]:

$$\rho = \rho_r e^{\int_{p_r}^p \frac{dp}{\beta_e}} \quad (4.9)$$

where β_e that takes into account the presence of undissolved gas and pipe wall compliance.

Therefore AMESim Rev11 does not propagate the free gas content between adjacent control volumes. It makes majors assumptions that can be listed as follows:

- 1) the fractional air content and the saturation pressure do not vary with time or position
- 2) the volume of the free air varies only with pressure (and not with temperature) through the constant polytropic index Γ
- 3) for fluid pressure higher than P_{sat} all air is considered dissolved in the liquid
- 4) aeration, air absorption and cavitation are dealt as instantaneous processes
- 5) below P_{sat} the undissolved air fraction is obtained by the Henry's Law in such a

way that the sum of undissolved and dissolved air remains invariant and equal to initial air content

In reality the aeration and air absorption are not instantaneous processes but they can involve a time constant of order of minutes: the nature of fluid and flow conditions play a fundamental role [16]. And again, if a hydraulic system operates below the saturation pressure and the pressure suddenly rises above the saturation pressure, the air bubbles collapse and the air dissolves in the liquid: it represents a faster process than previous one but not instantaneous. It is so possible to have undissolved air above the saturation pressure during transients [7].

A separate mass balance for free air would be useful to provide an expression of gas fraction time derivative: it would also include the external transport of free air between adjacent CVs, as proposed in [16] (this feature is considered for addition in the software subsequent version 12).

In conclusion, in order to improve the simulation of cavitation and aeration phenomena, it is supposed that the fluid properties vary between low pressure and high pressure hydraulic circuit. Figure 4.22 shows qualitatively the variation of fraction of undissolved air/gas content as function of the fluid absolute pressure, in accordance to Henry's Law, implemented in the complete virtual prototype.

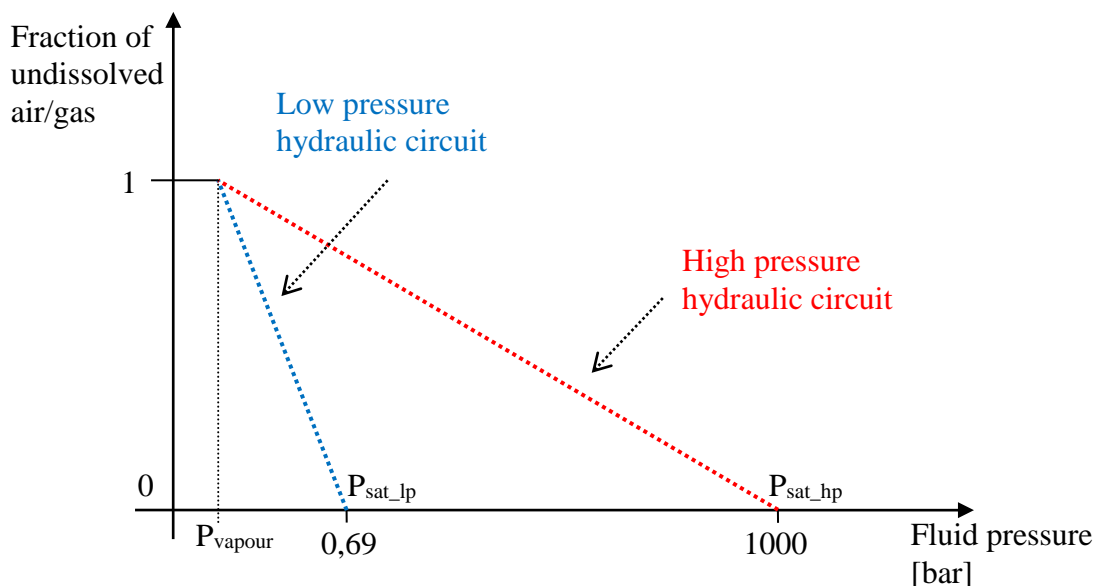


Figure 4.22 Henry's law in AMESim: fraction of undissolved air/gas versus fluid pressure in high and low pressure hydraulic circuit

It is assumed that:

- 1) In high pressure circuit, at pressure higher than P_{sat} , all air is not fully dissolved but a certain fraction of free air remains
- 2) The fraction of free air is less sensitive to pressure variation in the high pressure circuit than in low pressure circuit
- 3) The fraction of air content in low pressure circuit is chosen higher than the air content in high pressure circuit in order to increase the sensitivity of the fluid compressibility to free air in low pressure domain

4.8 Comparison between Measured and Simulated Pressure

The measured and simulated pressures at pump inlet are finally compared. The simulated pressure is obtained through the complete virtual prototype described in 4.7.1. Figure 4.23 shows a typical example of result. It refers to the conditions of command step of speed equal to 2400 *rpm* achieved in 10 *ms* and no hydraulic load. It is notable that before imposing the speed step (starting at 1 *s*) the pressure is negative due to gravitational contribution. After that the capacitive and inertial effects excite the line that begins to oscillate with a frequency dependent on them. Typically damped in 0.5 *s*, the pressure then stabilizes on a value that is function of all the lumped and distributed pressure losses in the hydraulic circuit. The simulated pressure damps more slowly than measurement due to a lack of modelled resistive effects.

It is important to highlight that, the presence of the time delay in the frequency drive adds to the samplers of all the inputs/outputs signal ports and produces an increase of the speed error ε_{ω} in the closed-loop speed control. An important overshoot of the measured motor speed is so generated during the acceleration phase. Just thinking that the figure 4.23 shows in reality the reduction of inlet pressure when the measured speed reaches the maximum value of 2850 *rpm* in 30 *ms* and not the desired speed of 2400 *rpm* in 10 *ms*!

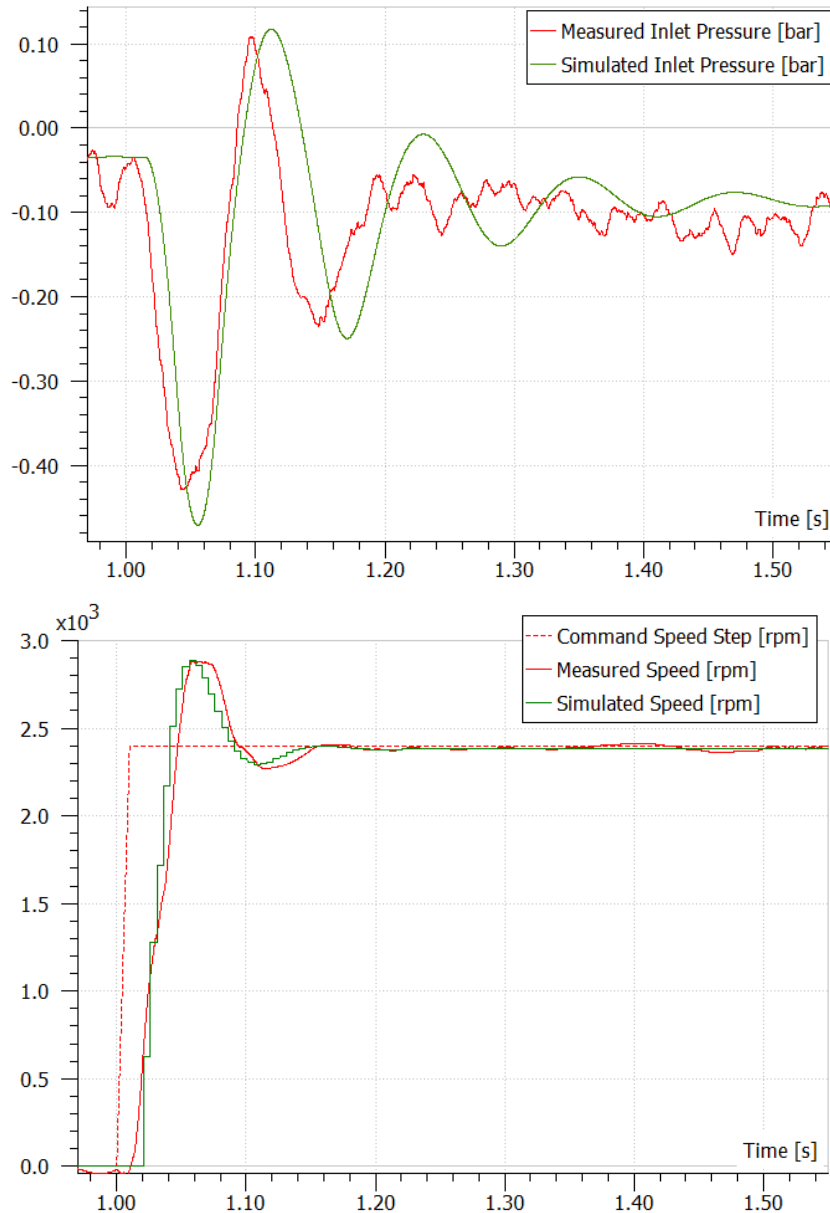


Figure 4.23 Comparison of inlet pressure between measured and simulated results for command step of 2400 rpm imposed for 10 ms and 0bar

Table 4.7 lists the comparison in terms of: minimum pressure in first peak p_1 , maximum pressure in second peak p_2 , minimum pressure in third peak p_3 , time delay between measured and simulated p_1 $t_{\Delta p_1}$ and time frequency of Δp_{in} evaluated between the peaks p_1 and p_3 f_p . The relative errors are also evaluated as just described through the equation 3.26 in the Chap. 3.

Operating Conditions [rpm,ms,bar]	p_1 [bar]			p_2 [bar]			p_3 [bar]			Delay [ms]	f [Hz]		
	ε_1	ε_2	ε_3	ε_1	ε_2	ε_3	ε_1	ε_2	ε_3		ε_f		
1000,10,0	-0,29	-0,29	0	0,09	0,12	33	-0,15	-0,20	33	19	8,6	8,3	3
1000,20,0	-0,3	-0,27	10	0,08	0,11	38	-0,11	-0,15	36	10	9,2	8,4	9
1000,30,0	-0,29	-0,26	10	0,07	0,09	29	-0,16	-0,18	13	8	9,3	8,6	7
1000,50,0	-0,19	-0,20	5	0,05	0,05	0	-0,12	-0,15	25	6	9,2	8,4	9
1000,100,0	-0,13	-0,12	7	-0,01	-0,01	0	-0,08	-0,08	0	10	8,8	8,4	4
1000,200,0	-0,08	-0,08	0	-0,04	-0,04	0	-0,08	-0,08	0	8	8,4	8,4	0
1000,10,100	-0,32	-0,29	9	0,26	0,16	38	-0,16	-0,22	38	18	11,7	9,1	22
1000,20,100	-0,3	-0,27	10	0,2	0,13	35	-0,18	-0,21	16	20	10,5	9,1	13
1000,30,100	-0,29	-0,27	7	0,19	0,12	36	-0,17	-0,2	17	16	12,5	9,8	21
1000,50,100	-0,24	0,22	8	0,13	0,08	38	-0,12	-0,16	33	14	10,1	8,4	16
1000,100,100	-0,13	-0,12	8	-0,01	-0,01	0	-0,09	-0,09	0	20	7,3	6,7	8
1000,200,100	-0,08	-0,08	0	-0,04	-0,04	0	-0,07	-0,07	0	10	10	8,3	17
2000,10,0	-0,40	-0,43	7	0,08	0,11	38	-0,13	-0,18	38	9	8,4	8,4	0
2000,20,0	-0,48	-0,48	0	0,14	0,19	35	-0,16	-0,2	25	9	8,8	8,2	7
2000,30,0	-0,48	-0,48	0	0,19	0,19	0	-0,28	-0,3	7	9	9,5	8,8	7
2000,50,0	-0,39	-0,38	3	0,14	0,11	21	-0,2	-0,23	15	11	9	8,5	5
2000,100,0	-0,24	-0,21	12	-	-0,03	-	-	-0,11	-	14	8,6	8,6	0
2000,200,0	-0,15	-0,14	7	-	-0,06	-	-	-0,12	-	8	-	8,2	-
2000,10,100	-0,45	-0,43	4	0,22	0,13	40	-0,19	-0,25	32	12	11,3	9,1	19
2000,20,100	-0,46	-0,45	2	0,21	0,18	14	-0,28	-0,29	4	12	10,7	9,1	15
2000,30,100	-0,44	-0,44	0	0,2	0,18	10	-0,26	-0,29	11	11	10	9,1	9
2000,50,100	-0,41	-0,39	5	0,18	0,15	17	-0,24	-0,27	12	10	11,3	9,1	19
2000,100,100	-0,21	-0,23	10	-0,02	-0,02	0	-0,12	-0,12	0	11	8,3	7,4	10
2000,200,100	-0,13	-0,12	8	-0,04	-0,05	25	-0,12	-0,12	0	12	10	9,1	9
2400,10,0	-0,45	-0,47	4	0,13	0,12	8	-0,21	-0,25	19	9	9,4	8,7	7
2400,20,0	-0,46	-0,48	4	0,14	0,13	7	-0,20	-0,27	33	8	10	9,1	9
2400,30,0	-0,47	-0,49	4	0,14	0,14	0	-0,22	-0,27	23	12	8,5	8,5	0
2400,50,0	-0,43	-0,43	0	0,06	0,08	33	-0,23	-0,23	0	10	9,1	8,3	9
2400,100,0	-0,28	-0,26	7	-0,04	-0,05	25	-0,14	-0,12	14	13	8,2	7,1	10
2400,200,0	-0,14	-0,14	0	-0,04	-0,05	25	-0,14	-0,15	7	11	9,1	9,1	0
2400,50,100	-0,43	-0,39	9	0,23	0,17	26	-0,23	-0,23	0	7	11,4	9,4	18
2400,100,100	-0,27	-0,25	7	-0,04	-0,05	25	-0,13	-0,12	8	18	11,2	9,4	16
2400,200,100	-0,15	-0,14	7	-0,04	-0,04	0	-0,13	-0,13	0	10	11,2	9,4	16

Table 4.7 Comparison between measured and simulated data

By observing the table 4.7 it is possible to assert that:

- The virtual prototype enables the minimum pressure reached in pump inlet p_1 to be simulated with a relative error inferior at 10 %
- The maximum pressure in second peak p_2 and the minimum pressure in third peak p_3 are simulated with variable relative errors from 0 up to 40 %
- The time delay between measured and simulated p_1 $t_{\Delta p_1}$ remains below the 20 ms
- The relative errors concerning the time frequency of Δp_{in} f_p , evaluated between the peaks p_1 and p_3 , is below the 10 % in tests with no load while it is below the 20 % for the tests with line pressure equal to 100 bar.

In conclusion, the virtual prototype is a useful tool to predict the time evolution of the pressure in pump inlet, in terms of minimum reached peak p_1 , with relative errors lower than 10 %. It so permits to determine the limit conditions of operation which avoid the reduction of pressure below the -0.2 bar, such a value being considered critical for cavitation development.

4.9 Conclusions

In this chapter the phenomena of cavitation and aeration have been described and the principal mechanical damages on vane pump have been showed. An analytical model at functional level has been developed that takes into account the inlet hydraulic line between pump and tank. The resistive, inertial and capacitive effects have been considered in the equations. It has permitted to point out the principal relationships between the fundamental parameters of system and the fluid pressure in pump inlet. The limitations of this model have been remarked when a comparison is carried out with virtual prototypes developed in AMESim environment. In fact two virtual prototypes have been created which improve the modelling of the inlet line and of the pump interior by means of sub-models of AMESim libraries. In particular the effects of flow conditions, the presence of concentrated pressure losses in edge forms and the variation of Effective Bulk Modulus as function of operating conditions, wall compliance and air content are dealt in the prototypes. It so makes the simulations more realistic, as verified through comparison with experimental data. The complete virtual prototype has finally been validated by demonstrating its accuracy to predict the time evolution of fluid pressure in pump inlet.

References

- [1] T. Koivula. On Cavitation in Fluid Power. *Proceeding of 1st FPNI-PhD Symposium. September 20-22, 2000. Hamburg, Germany. ISBN 3-00-006510-5, pp. 371-382.*
- [2] Parker Catalogue HY29-0022/UK. Hydraulic Pumps & Motors Vane Troubleshooting Guide. *August, 2013.*
- [3] P. K. B. Hodges. *Hydraulic Fluids.* Petroleum Consultant Norway, Elsevier, 1996.
- [4] P. Eisenberg. Cavitation Damage. *Hydronautics Incorporated. December 1963, pp. 121-128.*
- [5] W. S. Lamb. Cavitation and Aeration in Hydraulic Systems. *Bedfordshire, UK. BHRGroup, 1987.*
- [6] J. U. Thoma. Modern Oilhydraulic Engineering. *Trade & Technical Press LTD, 1970.*
- [7] LMS IMAGINE. HYD Advanced Fluid Properties. *Technical Bulletin N. 17, 2011.*
- [8] F. Brusiani, G. M. Bianchi, M. Costa. Evaluation of Air/Cavitation Interaction Inside a Vane Pump. *4th European Automotive Simulation Conference. July 6-7 2009. Munich, Germany.*
- [9] Q. Zhang, X. Y. Xu. Numerical Simulation on Cavitation in a Vane Pump with Moving Mesh. *ICCM 2014, July 28-30, Cambridge, England.*
- [10] S. Hain-Wurtenberger. Simulation of Cavitating Flow in Vane Pumps. *3rd European Automotive CFD Conference, July 5-6 2007. Frankfurt, Germany. Pp. 285-293.*
- [11] H. E. Merritt. *Hydraulic Control Systems. John Wileys and Sons, Cincinnati, Ohio, 1967.*
- [12] D. McCloy, H. Martin. Control of Fluid Power : Analysis and Design. *2nd edition, Ellis Horwood Limited 1980.*
- [13] LMS IMAGINE. *Help AMESim: Optimization, Robustness, Design of Experiments*
- [14] I. E. Idelcik. Handbook of Hydraulic Resistance. *Begell House 1980.*
- [15] J-C. Maré, N. Van Laethem. Contribution to the Modeling, the Simulation and the Control Synthesis of an Aerospace Electro-Hydrostatic Actuator. *5th International Fluid Power Conference, March 20-22 2006. Aachen, Germany. Pp. 201-212.*
- [16] J. Zhou, A. Vacca, P. Casoli, A. Lettini. Investigation of the Impact of Oil Aeration on Outlet Flow Oscillations in External Gear Pumps. *IFPE 2014, Int. Fluid Power Expo, March 4-8 2014. Las Vegas, USA.*

Divergence Thermique

Dans ce chapitre le phénomène de la divergence thermique est tout d'abord décrit. Quelques solutions sont ensuite proposées pour améliorer la performance de la pompe pendant la phase d'injection statique d'un cycle typique de la machine à injecter. Un modèle thermique fonctionnel, puis un modèle thermique avancé, basé sur le prototypage virtuel, représentent la clé pour évaluer la performance de la pompe à travers la prévision de la température du fluide.

L'approche analytique fournit une vue préliminaire sur les sources principales de pertes de puissance, permet d'effectuer une étude sur l'importance de chaque terme sur la dynamique du système, permet de vérifier les limitations liées à l'hypothèse de coefficients de transfert thermique constants, justifie le développement d'un modèle avancé qui permet de faire toutes les améliorations que le modèle fonctionnel ne peut pas garantir.

Le modèle avancé est basé sur le prototypage virtuel et il fournit l'évolution de la température respectivement du fluide, de corps de la pompe, de corps du moteur et du support. Une distribution uniforme de température à l'intérieur de chaque corps est assumée. La pompe, le moteur et le support sont modelés à travers une masse globale sans modeler les sous-composants comme le rotor, la came, les palettes dans la pompe. Le modèle ne simule donc pas les gradients de température et une erreur de température peut être produite entre les résultats simulés et mesurés, les derniers obtenus par des thermocouples situés dans des points spécifiques sur la surface des corps. Le prototype virtuel thermique complet permet d'évaluer avec une bonne fiabilité les transferts thermiques entre le fluide, la pompe, le moteur, le support et l'environnement externe en prenant aussi en considération la variation des coefficients de convection avec les conditions de fonctionnement. Ce modèle montre également l'influence significative de l'échange de chaleur entre la pompe et le moteur et montre le manque de connaissance des modèles pour le calcul des facteurs de convection dépendants des géométries et des conditions opérationnelles.

5 Thermal Divergence²

In this chapter the phenomenon of the thermal divergence is firstly described. Then some solutions are proposed to improve the pump performance affected by thermal issues under typical cycle's phases of injection moulding machine. An analytical functional thermal model and an advanced thermal model, based on virtual prototyping, represent the key to evaluate the pump performance through the prediction of the operative fluid temperature.

5.1 Phenomenon Description

Today the demands on drive systems and control in typical stationery machineries, like presses, die castings and injection moulding machines, are pressing to increase service pressure, velocities and repeatability over a long period of time [1]. Specific requested operating conditions so stimulate the pump to operate up to its thermal limit and to facilitate the development of the thermal divergence phenomenon. The energy pump losses are at the origin of this phenomenon. The most critical phase in a typical cycle of an injection moulding machine is constituted by the static injection where high pressure has to be hold (from seconds for plastic, to minutes for rubber) in the injection ram that remains quite steady. In this situation, the pump operates at very low outlet flow (e.g. 1 *l/mn* for 60 *l/mn* rated flow) that only evacuates a minor fraction of the energy generated by the pump internal energy losses (friction and leakage). As pump temperature rises, the internal leakage increases, and again contributes to increase the pump temperature (fig. 5.1).

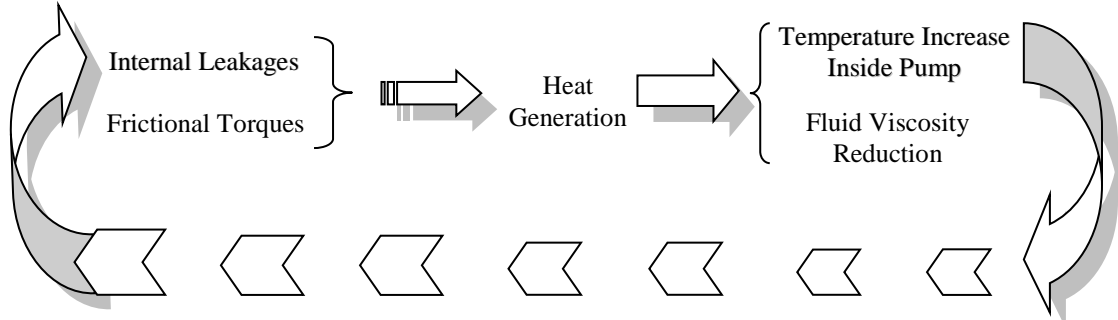


Figure 5.1 Schematic of the thermal cycle at the origin of the thermal divergence phenomenon

² It is not a divergence strictly speaking

Therefore, during the static injection phase, the pump temperature may reach excessive values that directly impact its service life. The fluid temperature should not exceed 90 °C in order to avoid pump failures due to parts wearing or jamming.

For this reason, it is of particular importance to manage properly the operation of the pump during the injection phase, e.g. by adequate definition of the pump efficiency at extremely low speed or by increasing the outlet flow to evacuate the heat generated inside pump.

As consequence of this research work on EHM energy efficiency, the energy consumption and the production rate of a moulding machine will be also quantifiable and the advantage of the proposed electro-hydrostatic solution will be highlighted.

Studies on energy efficiency were already proposed in last years, thanks to the developments of electrically driven modules, to demonstrate the competitiveness of EHMs, as demonstrated in [2] and [3]. Energy saving requirement becomes fundamental for selecting between the electromechanical and electrohydraulic solutions, and also inside the electrohydraulic solutions range, between speed-controlled variable-displacement and fixed-displacement pumps. [4] addressed the advantages of speed-controlled fixed-displacement pumps involving piston and internal gear pumps in terms of energy potential and low noise level too when compared to variable-displacement solutions. The thermo energetic behaviour became then a new important step in research when new energy-efficient electrohydraulic compact drives were developed in last decades [5]. In comparison with conventional servo-controlled drives, they are equipped with a small oil volume and so their high sensitivity to heat flow has now to be investigated, as led in [6].

Concerning the aeronautical sector, thermal aspects have been continuously addressed since the early 2000s for flight control actuators, e.g. [7], with the rise of more electrical commercial aircrafts. In these applications, the axial-piston type pumps are drained and the thermal balance is considered for long time operation (a flight mission): the scope of the thermal hydraulic simulation is far from the need related to static injection in moulding machines. Thermal analysis was again carried out for A380 hydraulic system in order to simulate and predict the thermal behaviour of the new flight control architecture that relied on hydraulic and electric power [8]: in this application the temperature limitations are to be guaranteed for the seals service life and for avoiding chemical composition changes of the hydraulic fluid. Nabtesco developed a thermal design tool based on simultaneous Bondgraph and FEM analysis to simulate the temperature distribution in EHAs and to

demonstrate their superiority to conventional hydraulic actuators: by using Bondgraph for fluid temperature determination and FEM for temperature distribution of EHA structure, an interactive data transfer process was achieved but with high computational times (about 6 hours [9]).

Today, the use of the fixed-displacement vane pump in an EHM for stationery machinery represents an innovative solution. Indeed, it generates low noise and low flow ripple compared to other technologies (gear or piston pump) [10]. Recent fixed-displacement Parker vane pumps are well-known for their high performances, high efficiency, low noise levels, low pressure ripple, good compactness, mounting flexibility and good reliability. In order to provide fast proposals in response to call for tender, it is necessary to develop an accurate thermal hydraulic analysis that defines properly the operation of pump and finally of EHM.

5.2 Proposed Solutions

There is a growing interest in EHM for applications which involve several actuators used in sequence, as it is the case of cyclical machines. However, the thermal divergence becomes an issue when the pump is not externally drained and operates at high pressure and extremely low flow simultaneously. This issue can be attenuated, as done by Parker, by installing an external hydraulic bypass at fixed section (fig. 5.2). The bypass, linked to HP volume of the pump, increases the pump output flow by creating an external leakage that spills into the tank. It results particularly suitable when a constant pressure has to be maintained on cylinders (i.e. static injection in IMM). When the reference pressure is established, the pump continues to run for maintaining the pressure but it does no more deliver output flow to cylinder. In this condition, a permanent volume turns inside pump by collecting heat produced by the energy losses. The function of the external bypass is thus to generate a continuous output flow that enables to recirculate fluid for pump cooling. It represents a cheap solution but not very efficient because it permanently provides an external leakage flow of about 0.7 l/min at 200 bar (equivalent to about 233 W of released power and 5.87 GJ of consumed energy over 1 year). It however remains competitive given that the external leakage flow only corresponds to about the 1 % of the

rated flow.

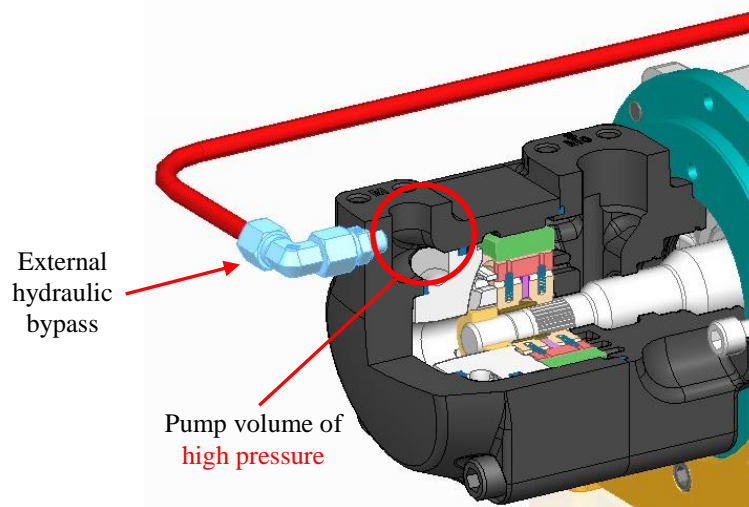


Figure 5.2 External hydraulic bypass linked to high pressure pump volume for maintaining constant the line pressure and for fluid recirculation

Another solution still under study to reduce temperature inside pump, consists in evacuating the internal leakages, principal source of heat generation, out of pump by means of an external drain linked to pump LP drain volume (fig. 5.3). This volume indeed collects a significant quantity of leakages produced inside pump.

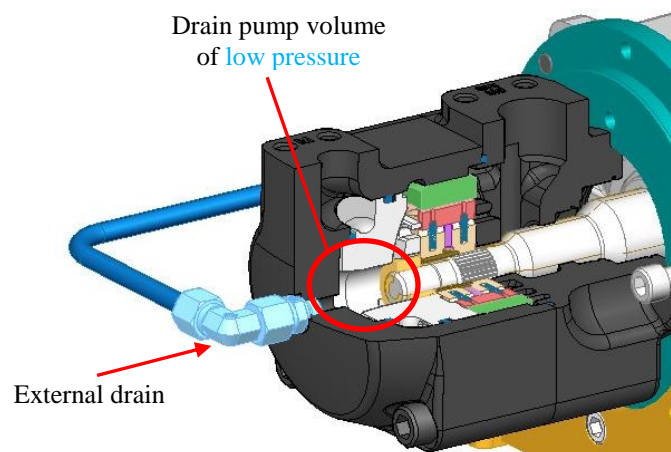


Figure 5.3 External drain linked to drain pump volume of low pressure to evacuate the internal leakages and to reduce the temperature inside pump

These solutions are able to reduce the maximum temperature reached inside pump by increasing the time duration of holding pressure phase, consistently with the pump service life. The disadvantage is constituted by the consumed energy level that makes them a bit less competitive for application where the energy saving requirement is hardly strict.

By using conventional configurations of vane pump without external drains or hydraulic bypass, a possible solution is to manage properly the pump operation by: firstly identifying the energy pump losses as function of all operating conditions (line pressure, pump speed and fluid temperature), and finally by predicting with accuracy its thermal hydraulic behaviour. In such a way pump failures are avoided and in the same time machine's cycle requirements are met. On the way to full simulation-based design, developing a realistic thermal-hydraulic model of the EHM at a system level can so significantly contribute to this purpose and also to shorten preliminary studies in response to stationery machinery designers' call for tender.

In next paragraph a functional analytical model describing the pump thermal balance will be developed for a preliminary design in order to determine the key relationships between pump performance and fundamental parameters. Successfully the analysis concerns with an advanced model, based on virtual prototyping, that permits to evaluate all the non-linearities contributions neglected in the functional analysis.

5.3 Functional Thermal Model of Pump

In this paragraph a functional model, that analyses linearly the thermal hydraulic behaviour of the vane pump, is described. A lumped-parameters method and one-dimensional flow, based on conservation of energy, is applied to develop a linear model for modelling and simulating the fluid temperature inside pump and the temperature of pump body. Other studies were already proposed for pumps thermal-hydraulic modelling, as it is the case of a fixed displacement axial piston pump [11]. In this thesis, the intention is to improve the analysis in [11] by evaluating in detail the contributions of pump energy losses as function of operating conditions and also by considering the heat exchanges between pump and other parts (shaft and motor).

The scope is thus to identify preliminarily the parasitic effects that play a major role in the temperatures and in the heat transfer mechanisms between parts.

The full equations' system is provided and it applies to hydraulic fluid and pump body. The equations are the following:

- Flow Conservation Equation (see eq. 3.3 in Chap. 3) + assumptions of incompressible fluid
- Parametric model of pump energy losses (see eq. 2.2-2.3 in Chap. 2)
- Model of fluid properties versus temperature
- Momentum Balance (see eq. 3.1 in Chap 3) and Work Rate Equilibrium
- Energy Conservation Balance
- Heat Transfer Equations

5.3.1 Fluid Properties versus Temperature: Viscosity Model

The energy pump losses are expressed by means of the parametric model described in Chapter 2 as function of: line pressure drop, pump speed and dynamic viscosity dependent on fluid temperature. In practice, the fluid dynamic viscosity varies with pressure and temperature. However the dependence from pressure is neglected [12] as just mentioned in section 2.2.2. Now, to develop a functional thermal hydraulic model of the pump in a linear form, it was assumed that:

- 1) The dynamic viscosity of the fluid is a linear function of temperature

By using the Taylor's series expansion until first order for the exponential, the expression $\mu_o = \mu_i e^{-\sigma(T_o - T_i)}$, inserted in (2.2), is reduced to:

$$\mu_o = \mu_i [1 - \sigma (T_o^f - T_i^f)] \quad (5.1)$$

where

T_o^f = output fluid temperature

T_i^f = input fluid temperature

In the case where it is necessary to linearize the ratio $1/\mu_o$, e.g. in the internal leakage parametric relation, the following equation is used by neglecting the second order effects:

$$\frac{1}{\mu_o} = \frac{1}{\mu_i} [1 + \sigma (T_o^f - T_i^f)] \quad (5.2)$$

5.3.2 Work Rate Equilibrium

The Momentum Balance (eq. 3.1) correlates the torques applied on motor/pump shaft. It also permits to determine the associated power losses by simple manipulation, as described below. The assumptions are here made of acceleration and motor frictions contributions negligible compared to other terms.

Each term of (3.1) is multiplied for the pump speed ω and the contribution of acceleration ($J_{tot}\dot{\omega}$) is neglected compared to other terms. By using then the expression (3.3) for describing the output flow rate Q_o as function of pump displacement V_o and the internal leakages Q_{lp} , the (3.1) is finally reduced to eq. 5.3:

$$C_m \omega = Q_o \Delta p + Q_{lp} \Delta p + C_{fp} \omega \quad (5.3)$$

Equation 5.3 describes the equilibrium of pump input (term on left-side of equal sign) and output powers (on right-side). The second and third terms on right-side of equal sign represent the power losses respectively due to pump leakages and frictions. The work rate losses \dot{W}_{loss} can thus be defined by the following expression:

$$\dot{W}_{loss} = \dot{W}_i - \dot{W}_o = Q_{lp} \Delta p + C_{fp} \omega \quad (5.4)$$

5.3.3 Energy Conservation Balance

The First Law of Thermodynamics is applied to evaluate the time variation of fluid temperature T_{f-in-p} over the pump through the Energy Conservation Balance [13]. Having relevant importance the thermal exchange of the fluid with the pump body, the energetic equilibrium is also applied to pump wall by quantifying the change in time of its temperature T_{p-body} .

At this modelling level, the system, constituted by the pump body and the hydraulic fluid, is studied. Figure 5.4 shows the sketch map of the full system that is considered for energy balance: it consists of two distinct control volumes (nodes), the fluid and the pump body. The thermal exchanges are evaluated between fluid, pump body, electric motor and environment air. At this modelling level, the following effects are considered:

- 1) Internal forced convection between fluid and pump wall, \dot{Q}_{fp}
- 2) Natural convection from pump towards the environment, \dot{Q}_{pe}

3) Thermal conduction between pump and motor body, \dot{Q}_{pm}

By observing the figure 5.4, the fluid node receives an enthalpy flow rate associated to input and output fluid mass (blue arrows). The power pump loss is then represented by dashed orange arrow of the internal leakages and frictions which flow in the fluid node.

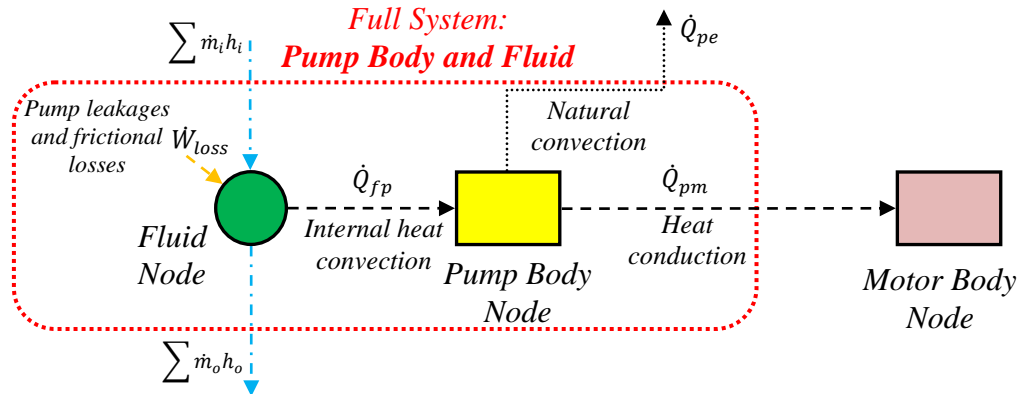


Figure 5.4 Sketch map of the Control Volumes of the full analysed system and thermal exchanges between: hydraulic fluid, pump body, motor body and environment air

The total system energy rate \dot{E}_{tot} , is composed by:

$$\dot{E}_{tot} = \dot{U} + \dot{E}_{cin} + \dot{E}_p \quad (5.5)$$

where

U = internal energy

E_{cin} = kinetic energy

E_p = potential energy

E_{cin} and E_p can be normally neglected³ compared to U .

The **Energy Conservation Balance** for a generic Control Volume can be thus written:

$$\dot{U} + \sum \dot{m}_o h_o - \sum \dot{m}_i h_i = \dot{Q}_{tot}^{heat} - \dot{W}_{tot} \quad (5.6)$$

where

\dot{m}_o = output fluid mass rate

\dot{m}_i = input fluid mass rate

h_o = output enthalpy associated to output fluid mass

³ Example of calculation for evaluating the magnitude orders of U , E_{cin} and E_p

$p = 200 \text{ bar}$	$\rho_{\text{Tellus-32}} = 872 \text{ kg/m}^3 @ 15 \text{ }^\circ\text{C}$	$v = 10 \text{ m/s}$	$z = 1 \text{ m}$
$U = p/\rho = 2,3 \cdot 10^4 \text{ J/kg}$		$E_{cin} = v^2/2 = 50 \text{ J/kg}$	$E_p = g z = 9,8 \text{ J/kg}$

h_i = input enthalpy associated to input fluid mass

\dot{Q}_{tot}^{heat} = total heat rate exchanged with exterior

\dot{W}_{tot} = rate of total work

\dot{W}_{tot} is reduced by the work required to push the mass into and out the control volume that is included in enthalpies terms. In the equation 5.6 it is assumed that:

- 1) the kinetic and potential energy of incoming and outgoing fluid are negligible compared with internal energy
- 2) the specific enthalpy depends only on temperature and pressure because the fluid phase does not change [13]

The time derivative of enthalpy, \dot{h} , is given by [14]:

$$\dot{h} = c_p \dot{T} + (1 - \alpha_p T) \nu \dot{p} \quad (5.7)$$

where

c_p = specific heat of the fluid at constant pressure

α_p = thermal expansion coefficient

ν = kinematic viscosity of the fluid

The final rearranged form of the equation 5.6 is obtained by inserting the eq. 5.7 and by adding the following hypotheses:

- 3) Dependence of h from pressure neglected in comparison to dependence from temperature
- 4) c_p supposed to be constant and independent from temperature range (25 ÷ 75 °C)

The (5.6) is now rewritten for fluid and pump wall. For the fluid node (fig. 5.4), being the mass rate equal to: $\dot{m} = \rho Q$, it is given by:

$$C_f \dot{T}_f + \rho_o Q_o c_{pf} T_o^f - \rho_i Q_i c_{pf} T_i^f = -\dot{Q}_{fp} + \dot{W}_{loss} \quad (5.8)$$

where:

$$C_f \dot{T}_f = \dot{U}$$

\dot{T}_f = time derivative of fluid temperature T_f

$C_f = m_f c_{pf}$ thermal capacity of the fluid

m_f = fluid mass

c_{pf} = specific heat of fluid at constant pressure

ρ_o = output fluid density

ρ_i = input fluid density

\dot{Q}_{fp} = heat flow rate between fluid and pump body

For the pump body node, the (5.6) becomes:

$$C_p \dot{T}_p = \dot{Q}_{fp} - \dot{Q}_{pm} - \dot{Q}_{pe} \quad (5.9)$$

where

$$C_p \dot{T}_p = \dot{U}$$

\dot{T}_p = time derivative of pump body T_p

$C_p = M_p c_{pp}$ thermal capacity of the pump body material

M_p = pump mass

c_{pp} = specific heat at constant pressure of pump material

\dot{Q}_{pm} = heat flow rate between pump and motor

\dot{Q}_{pe} = heat flow rate between pump and environment

5.3.4 Heat Transfer Equations

The heat can be transferred through convection, conduction and radiation. The equations, used for describing the heat transfer mechanisms, apply to generic simplified geometries like spheres, cylinders, parallelepipeds and wall. The convection, whether natural or forced, between a solid surface and a fluid, can be expressed by the Newton's law of cooling [13] as follows:

$$\dot{Q}_{conv} = h_{conv} A \Delta T \quad (5.10)$$

where

\dot{Q}_{conv} = convection heat flow rate

h_{conv} = convection heat transfer coefficient

A = contact surface

ΔT = difference of temperature between surface and fluid sufficiently far from surface

When the conduction occurs through a wall, the Fourier's law is used to express the heat transfer rate in steady conditions [13]:

$$\dot{Q}_{cond} = \frac{\lambda_t}{L} A \Delta T \quad (5.11)$$

where

\dot{Q}_{cond} = conduction heat flow rate

λ_t = thermal conductivity of the wall

L = thickness of the wall

A = wall area

ΔT = difference of temperature between the two wall surfaces

If the conduction takes place between two solids in contact each other, another parameter is generally used, defined as thermal contact conductance h_{cond} , for reducing the (5.11) in an analogous form of Newton's law of (5.10). The (5.11) is so substituted by:

$$\dot{Q}_{cond} = h_{cond} A \Delta T \quad (5.12)$$

where

$h_{cond} = \lambda_t/L$ = thermal contact conductance

A = interface area

ΔT = effective temperature difference at the interface

The thermal radiation that can be emitted from a surface towards air is described by the Stefan-Boltzmann law [13] in the following manner:

$$\dot{Q}_r = \sigma_s \varepsilon_s A \Delta T^4 \quad (5.13)$$

where

\dot{Q}_r = radiation heat flow rate

σ_s = Stefan-Boltzmann constant

ε_s = emissivity of the surface

A = surface area

ΔT = temperature difference between solid surface and environment

The heat transfer coefficients h_{conv} and h_{cond} evaluate the dependences from a lot of variables as: bodies geometry, contact area, flow conditions, material and fluid characteristic properties. These coefficients are known for simplified geometries but their identification results very difficult for more complex geometries and in specific operating conditions, like in this research context.

The objective is thus to evaluate all these coefficients as function of the geometry of each component composing the EHM and of flow conditions (laminar or turbulent).

In order to get a first estimation of the heat transfer coefficients at this modelling level, the values are obtained from existing models associated with generic heat transfer schemes [5], [13], [15] and [16], and **maintained invariant** for any time during simulation.

With reference to eq.s (5.10) to (5.13), the following equations are used for the functional thermal model. The heat flow rate due to internal forced convection between fluid and pump body \dot{Q}_{fp} , is expressed by means of:

$$\dot{Q}_{fp} = h_{int_conv} A_{in}^p (T_o^f - T_o^p) \quad (5.14)$$

where

h_{int_conv} = internal forced convection heat transfer coefficient

A_{in}^p = internal pump area in contact with fluid, obtained from CAD simulation

T_o^f = output temperature of the fluid

T_o^p = output temperature of the pump body

The heat flow rate due to natural convection between pump and environment \dot{Q}_{pe} , is given by:

$$\dot{Q}_{pe} = h_{conv}^p A_{ext}^p (T_o^p - T_e) \quad (5.15)$$

where

h_{conv}^p = natural convection heat transfer coefficient

A_{ext}^p = external pump surface in contact with air, obtained through CAD simulation

T_e = temperature of environment

The heat flow rate associated to conduction between pump and motor body \dot{Q}_{pm} , is obtained by:

$$\dot{Q}_{pm} = h_{cond}^{pm} A_{cont}^{pm} (T_o^p - T_o^m) \quad (5.16)$$

where

h_{cond}^{pm} = thermal contact conductance through the common shaft and the coupling

A_{cont}^{pm} = contact area between pump and motor body

T_o^m = output temperature of motor body

The radiation is not taken into account at this modelling level because considered of second order compared to other contributions.

5.3.5 Resolution of Functional Model

The equations describing the complete thermal hydraulic model of the pump exposed in last paragraphs, are summarised in Table 5.1. They involve two state variables (T_f and T_p) and 18 parameters.

Complete Thermal Hydraulic Model of Pump: Equations	
<i>Flow Conservation Equation</i>	
$Q_o = Q_i$	<i>(see in Chapter 3) (5.a)</i>
$Q_i = V_o \omega - Q_{lp}$	<i>(see in Chapter 3) (5.b)</i>
<i>Energy Pump Losses and Viscosity Linear Model</i>	
$Q_{lp} = \beta_{lp} \omega^A + \gamma_{lp} \frac{\Delta p^B}{\mu_o}$	<i>(see in Chapter 2) (5.c)</i>
$C_{fp} = \alpha_{fp} + \beta_{fp} \mu_o \omega^C + \gamma_{fp} \Delta p^D$	<i>(see in Chapter 2) (5.d)</i>
$\mu_o = \mu_i [1 - \sigma (T_o^f - T_i^f)]$	<i>(5.e)</i>
$\frac{1}{\mu_o} = \frac{1}{\mu_i} [1 + \sigma (T_o^f - T_i^f)]$	<i>(5.f)</i>
<i>Momentum Balance and Work Rate Equilibrium</i>	
$\dot{W}_{loss} = Q_{lp} \Delta p + C_{fp} \omega$	<i>(5.g)</i>
<i>Energy Conservation Balance</i>	
$C_f \dot{T}_f + \rho_o Q_o c_{pf} T_o^f - \rho_i Q_i c_{pf} T_i^f = -\dot{Q}_{fp} + \dot{W}_{loss}$	<i>(5.h)</i>
$C_p \dot{T}_p = \dot{Q}_{fp} - \dot{Q}_{pm} - \dot{Q}_{pe}$	<i>(5.i)</i>
<i>Heat Transfer Equations</i>	
$\dot{Q}_{fp} = h_{int_conv} A_{in}^p (T_o^f - T_o^p)$	<i>(5.l)</i>
$\dot{Q}_{pe} = h_{conv}^p A_{ext}^p (T_o^p - T_e)$	<i>(5.m)</i>
$\dot{Q}_{pm} = h_{cond}^{pm} A_{cont}^{pm} (T_o^p - T_o^m)$	<i>(5.n)</i>

Table 5.1 System of equations of the thermal hydraulic model of pump at functional level

Some substitutions were carried out in order to obtain the time variation of the temperatures T_f and T_p through the Energy Conservation Equations 5.h and 5.i. In detail: the (5.e) in (5.d) and the (5.f) in (5.c), the (5.c) in (5.b), the (5.b), (5.a), (5.l) and (5.g) all in (5.h) and finally the (5.l) to (5.n) all in (5.i).

Table 5.2 summarises the full analytical system, for the determination of the time variation of T_f and T_p : it is composed by two second order linear coupled differential equations with variable coefficients.

Differential Equation for T_f	
$m_f c_{pf} \dot{T}_f + T_f \left[\rho c_{pf} Q_o - \frac{\gamma_{lp}}{\mu_i} \sigma \Delta p^2 + \mu_i \beta_{fp} \sigma \omega^{3.6} + h_{int_conv} A_{in}^p \right] =$ $= \frac{\gamma_{lp}}{\mu_i} \Delta p^2 + \mu_i \beta_{fp} \omega^{3.6} + \beta_{lp} \omega^{0.19} \Delta p + \gamma_{fp} \omega \Delta p^{3.1} + \alpha_{fp} \omega + h_{int_conv} A_{in}^p T_p$	(5.17)
Differential Equation for T_p	
$M_p c_{pp} \dot{T}_p + T_p (h_{int_conv} A_{in}^p + h_{cond}^{pm} A_{cont}^{pm} + h_{conv}^p A_{ext}^p) =$ $= h_{int_conv} A_{in}^p T_f + h_{cond}^{pm} A_{cont}^{pm} T_m - h_{conv}^p A_{ext}^p (T_i - T_e)$	(5.18)

Table 5.2 Differential equations in T_f and T_p

The input signals to system consist of: operating conditions (line pressure drop Δp , pump speed ω and output flow rate Q_o), motor body temperature T_m , initial and environment temperatures T_i and T_e (figure 5.5). The equations in table 5.2 and the figure 5.5 represent a generic form for evaluating the time evolution of T_f and T_p when variations of speed ω , pressure drop Δp , motor temperature T_m and environment temperature T_e occur. In the specific case analysed (holding pressure phase), ω , Δp and T_e are assumed invariant during simulation. So they rightly contribute at the determination of the equilibrium condition while only the value of T_m corresponds to perturbation.

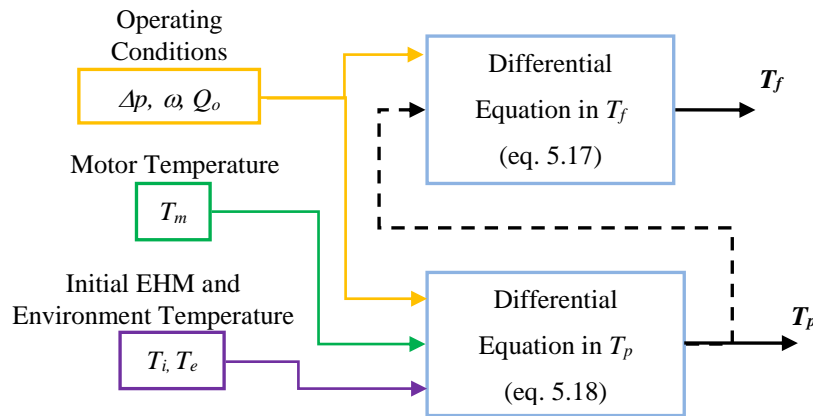


Figure 5.5 Schematic of the input ports to differential equations in T_f and T_p

There is no analytical solution of eq. (5.17) and (5.18). Consequently, some hypotheses are thus made to get a formal solution. Based on idea of **simulating the temperatures**

evolution during a typical holding pressure phase, characterized by constant line pressure, the following assumption is added:

- 1) All the coefficients of the differential equations are maintained constant for any simulation time and equal to values at the starting point of simulation

In addition, to reduce the number of system inputs:

- 2) The output flow Q_o is linked to line pressure Δp by adding a further equation describing the load hydraulic characteristic generated by the flow control valve installed in the hydraulic circuit. It derives from eq. 3.4 where the dependence on dynamic viscosity is now taken into account. It is as follows:

$$Q_o = A_{f_{cv}} \frac{\Delta p}{\mu_i} \quad (5.19)$$

Equation (5.19) describes the linear dependence of the output flow rate by the opening position of the valve ($A_{f_{cv}}$) and the dependence by the fluid viscosity through the coefficient μ_i , evaluated at the initial operating conditions. This expression is in accordance with the experimental curves obtained in laboratory. The output flow Q_o is so reduced to a constant input, while Δp is maintained constant during the simulation of static injection phase.

Thanks to assumptions 1) and 2), the system is transformed into two second order linear differential equations with constant coefficients in the variable T_f and T_p and in function of the following input signals: Δp , ω , T_m , T_i and T_e .

The hypothesis of constant coefficients could be too sweeping for the calculation of the equations' system solution in holding pressure phases because in particular Δp , ω and Q_o vary. In this phase, Δp is generally maintained constant thanks to closed-loop control, while the speed ω increases in order to compensate the effects of reduction of output flow rate Q_o that is produced by fluid temperature rise. Consequently a study is conducted to evaluate the contribution of each term constituting the two equations and their possible variation as function of operating conditions. The result is that:

- The coefficients of the equations dependent on ω have a negligible contribution compared to other terms, and so they are not taken into account hereinafter⁴

The simplified transfer functions of temperature T_f are obtained by inserting in (5.17) the expression of T_p given by (5.18). T_f is thus a function of the inputs Δp , ω , T_m , T_i and T_e in the complex domain of the variable s :

$$T_f(s) = \mathbf{H}_{f0}(s) \frac{1}{m_f c_{pf}} \left[\frac{\gamma_{lp}}{\mu_i} \quad \mu_i \beta_{fp} \quad \beta_{lp} \quad \gamma_{fp} \quad \alpha_{fp} \right] \begin{bmatrix} \Delta p^2 \\ \omega^{3.6} \\ \omega^{0.19} \Delta p \\ \omega \Delta p^{3.1} \\ \omega \end{bmatrix} + \quad (5.20)$$

$$\mathbf{H}_{f1}(s) T_m + \mathbf{H}_{f2}(s) (T_i - T_e)$$

The transfer functions, H_{f0} , H_{f1} and H_{f2} , included the damping ratio ξ_{f0} and the undamped natural pulsation ω_{f0} of the common denominator D_{f0} , are summarised in table 5.3. Two constant coefficients ΣHA and $HAha$ are also defined and used to simplify the expressions. The D_{f0} is characterised by a poles pair placed in the quadrants of (Re, Imm) plane with Real negative axis. The numerator of H_{f0} , N_{f0} , is constituted by a zero of real negative part defined by τ_{f0} . The made simplification of neglecting the contribution dependent on ω in the (5.17) and (5.18), generates precision errors just lower than 7 %.

In order to evaluate the level of accuracy of this analysis conducted until now, a comparison is carried out with measured results obtained in laboratory tests. Next paragraph describes the performed laboratory tests and the comparison.

⁴ The terms dependent on ω are four orders of magnitude smaller than the other comparable contributions

$\Sigma HA =$	$h_{int_{conv}} A_{in}^p + h_{cond}^{pm} A_{cont}^{pm} + h_{conv}^p A_{ext}^p$	
$HAha =$	$(h_{cond}^{pm} A_{cont}^{pm} + h_{conv}^p A_{ext}^p) h_{int_{conv}} A_{in}^p$	
$H_{f0}(s) =$ $= K_{f0} \frac{N_{f0}(s)}{D_{f0}(s)}$	$K_{f0} =$	$1/(\tau_{f0} \omega_{f0}^2)$
	$N_{f0}(s) =$	$1 + \tau_{f0} s$
	$D_{f0}(s) =$	$\frac{s^2}{\omega_{f0}^2} + 2 \frac{\xi_{f0}}{\omega_{f0}} s + 1$
$\tau_{f0} =$	$\frac{M_p c_{pp}}{\Sigma HA}$	
$\xi_{f0} =$	$\frac{1}{2 \frac{HAha (h_{cond}^{pm} A_{cont}^{pm} + h_{conv}^p A_{ext}^p)}{m_f c_{pf} (M_p c_{pp})^2} \sqrt{[1 + (\rho c_{pf} A_{fcv} \frac{\Delta p}{\mu_i} - \frac{\gamma_{lp}}{\mu_i} \sigma \Delta p^2) (\frac{\Sigma HA}{HAha})]}}$	
$\omega_{f0} =$	$\sqrt{\frac{HAha}{m_f c_{pf} M_p c_{pp}} [1 + (\rho c_{pf} A_{fcv} \frac{\Delta p}{\mu_i} - \frac{\gamma_{lp}}{\mu_i} \sigma \Delta p^2) (\frac{\Sigma HA}{HAha})]}$	
$H_{f1}(s) =$	$\frac{1}{\omega_{f0}^2 D_{f0}(s)} \frac{h_{cond}^{pm} A_{cont}^{pm} h_{int_{conv}} A_{in}^p}{m_f c_{pf} M_p c_{pp}}$	
$H_{f2}(s) =$	$-\frac{1}{\omega_{f0}^2 D_{f0}(s)} \frac{h_{conv}^p A_{ext}^p h_{int_{conv}} A_{in}^p}{m_f c_{pf} M_p c_{pp}}$	

Table 5.3 Expression of transfer functions of T_f and properties of H_{f0}

5.4 Laboratory Tests

During the tests, the pump outlet pressure is closed-loop controlled in accordance with the controller schematic proposed in fig. 1.16. In this case the closed-loops are achieved only on pressure and on motor currents while the speed closed-loop is not added for simplifying the interaction between controllers. The external pressure closed-loop control, conceived and implemented in the control station, thus provides the input command for the motor current control, the latter operated by the inverter. The pressure controller consists of a proportional control plus feedforward action to compensate for friction, inertia and hydrostatic torque, as just described for the case of speed closed-loop in Cap. 3. As mentioned in section 1.3, the static injection phase is characterised by high constant

pressure at low delivery flow rate. In order to simulate this operating condition, the output flow is so fixed by setting the opening of the hydraulic load valve prior the test running. This set value corresponds to starting point of static injection. In order to facilitate discussions at pump factory level, the pump starting point of static injection is defined by the effective volumetric efficiency η_{vol} at which the pump is driven to generate a constant output pressure of 160 *bar*. Two values of η_{vol} are thus selected:

- $\eta_{vol} = 10\%$ that requires the pump to start static injection at 124 *rpm* (4.1% rated speed) of shaft velocity at 45°C (**Test-01**)
- $\eta_{vol} = 30\%$ that requires the pump to start static injection at 146 *rpm* (4.9% rated speed) of shaft velocity at 45°C (**Test-02**)

Five temperatures sensors are installed, as showed in fig. 1.22 and 1.23 of Chapter 1 and are⁵: at pump outlet T_o , in drain pump volume T_{f-in-p} , into the pressure plate T_{pp} , at pump housing surface T_{p-body} and at motor housing surface T_{m-body} . In addition the temperature of the fluid inside tank is recorded, T_{tank} , and ω , Δp , Q_{out} and C_{est} are also recorded.

5.4.1 Experimental Results

During the tests, the fluid temperature increases, due to heat produced inside the pump by the energy losses, and continue to increase the energy losses, as described in the thermal divergence process at the beginning of this chapter. In order to compensate the effects of increase of internal leakages which reduce the pump output flow, the motor speed ω is automatically increased by action of pressure closed-loop control.

Figures 5.6 show the experimental results concerning the time evolution of the three temperatures: T_{f-in-p} , T_{p-body} and T_{m-body} .

The laboratory *Test-01* is stopped when the fluid temperature T_{f-in-p} reached the limit of 90 °C (308 *s*) while *Test-02* is stopped when the T_{f-in-p} was close to steady-state conditions (453 *s*).

As expected, both experimental results highlight that the measured fluid temperature inside pump T_{f-in-p} increases more rapidly than the pump body T_{p-body} and the motor body

⁵ In this chapter T_{f-in-p} corresponds to T_{asp} and T_{pp} corresponds to T_{plate} defined in Chapter 1

T_{m-body} temperatures. T_{f-in-p} is characterized by two different thermal time constants: the first one of about $3/4$ s while the second one is much higher, over 7 min. The pump body has a thermal constant time of at least 16 min while the motor body thermal time constant is about 27 min from catalogue.

In *Test-02*, it is also observed that, the pump transfers heat to motor for all test duration while in *Test-01* the motor firstly transfers heat to pump body. This is due to different initial conditions of T_{m-body} that underlines as the motor can also work as a heat source for the pump.

5.4.2 Comparison between Measured and Analytically Simulated Results

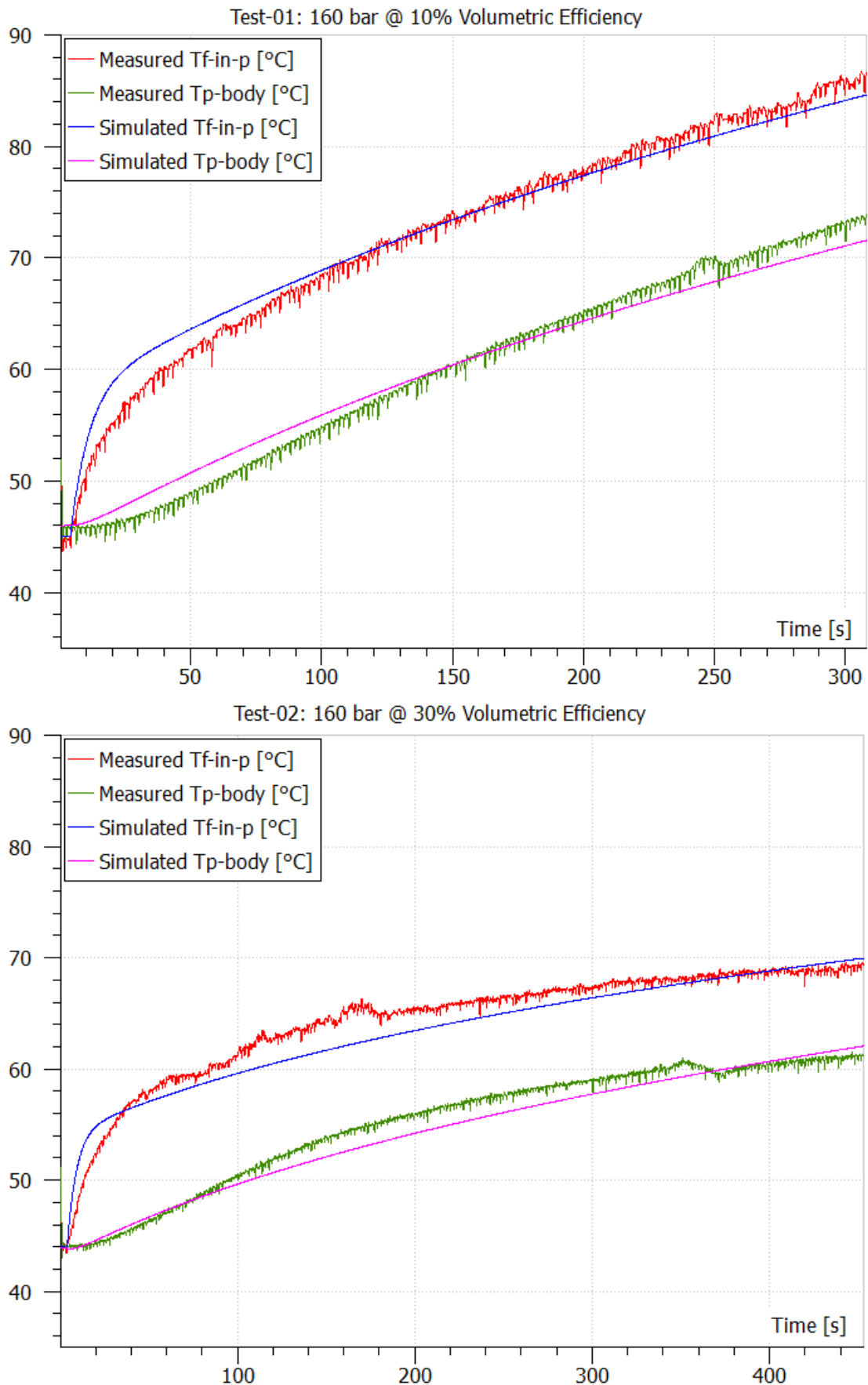
The measured results are then compared to simulated results obtained through the functional model described in 5.3. Concerning the input signals to functional model:

- T_i and T_e are selected in accordance to starting point of each experiments
- The measured T_{m-body} is used as T_m input
- Δp is modeled as a step signal of value of 160 bar
- ω is modeled as a step signal of value equivalent to initial condition speed

Figures 5.6 show the comparison between measured and simulated temperatures in terms of: T_{f-in-p} and T_{p-body} .

It is interest to remark that the selection of the measured T_{m-body} as functional model input: reduces the order of the differential equations of full system, reduces the numbers of unknown parameters to be identified and finally reduces the modeling errors accumulation. On the basis of this important simplification, the simulated temperatures remain close to the measured ones.

The maximum temperature gaps between simulated and measured T_{f-in-p} are lower than 3.5 °C while for T_{p-body} the gaps are lower than 2.2 °C. The simulated and measured temperatures differ principally in the initial and middle regions while in the final regions the errors reduce themselves.



Although the simulated results are close to measured one in the final extent, it is also notable a little divergence in the simulated trend that makes the simulation gradually away from measurements, with a risk of gap increase out of tests range.

Table 5.4 lists all the parameters, initially unknown, which are identified after comparison. They are obtained by varying manually one-by-one inside the numerical range determined by literature.

Heat Transfer Coefficient [W/m ² /K]	Test-01: 160bar @ 10% Vol. Eff.	Test-02: 160bar @ 30% Vol. Eff.
Internal forced convection	600	700
Natural convection for pump body	25	25
Pump/motor thermal conductance	3000	3000

Table 5.4 Value of heat transfer coefficients selected in the functional model

It is interesting to note that the values of the internal forced convection are different for the two tests: it is due to fact that the convection depends also on flow conditions which are dependent on pump rotational speed. So in *Test-01* the convection coefficient is deliberately set lower than in *Test-02*, given that ω_i was of 122 rpm compared to 146 rpm in *Test-02*. The final values are in accordance to values of literature, [15]. Natural convection coefficients are initially determined by the empirical relations and then scaled by an incremental factor that takes into account the realistic convection in laboratory where drafts could occur [6]. These final values are coherent to values proposed in [16]. Although the simulated responses are close to the measured ones, the thermal hydraulic functional model has some limitations as described hereinafter.

- 1) In reality, the heat transfer coefficients change with time because they depend on several time function variables as flow conditions and fluid properties. Consequently, fixing their value prevents the changes in heat transfer to be evaluated as function of the operating conditions characterizing the specific test.
- 2) The input signals, to differential equation in T_f , dependent on Δp and ω describing the power losses flow (eq. 5.17) are supposed constant and invariant with the fluid

viscosity time variation because the initial viscosity μ_i is maintained constant during all time simulation. In reality the reduction of fluid viscosity produced by temperature increase, increases the power losses linked to the internal leakages. Also the effective increase of pump speed ω during test increases the mechanical losses of pump, even if it has a minor effect compared to internal leakage. Consequently the time variation of power losses absorbed by the fluid represents a non negligible factor that impacts the results. Just a thinking that the volumetric losses due to internal leakages increases from about 290 to 1160 W (factor 4) by reducing the viscosity from 45 to 90 °C of fluid temperature. The mechanical losses evolve from 243 to 310 W due to increase of ω (results provided by the analytical model for *Test-01*). Based on the above in order to obtain results more realistic, the viscosity μ_i in the input signals to system is not calculated to initial point but at $i=60$ °C to increase enough the power losses. The results showed in figures 5.6 are obtained with this modification.

- 3) The hypothesis of constant coefficients of the differential equations places limits to system's solution. In particular the terms in Q_o varies in reality because of function of viscosity (eq. 5.19). Table 5.5 shows the values of poles pair and zero characterizing the transfer function H_{f0} of T_f . The values correspond to initial starting point at 45 °C, 160 bar and 122 rpm (*Test-01*). It is also observable the two calculated time constants τ_1 and τ_2 : τ_2 results more in agreement with experiments while τ_1 is higher due to an under estimated value of ω_{f0} that depends on heat transfer coefficients and on fluid viscosity, as showed in Tab 5.3. In fact the reduction of viscosity has as consequence an increase of ω_f that moves the poles towards the value more negative along the Real axis in the (*Re,Imm*) plane, with consequent increase of system rapidity response (lower time constants).

In conclusion, the analytical model appears useful for rapid estimation of thermal balance through simple design sheets (e.g. Excel). However advanced modelling results necessary to be developed in order to establish all the relationships between temperature variations and operating conditions. The contributions of all parasitic effects, neglected in this first modelling step, also have to be evaluated because they can play an important role in the thermal hydraulic coupling of the EHM.

K_{f0}	s	60.49
ω_{f0}	1/s	0.0195
ξ_{f0}	-	3.43
τ_{f0}	s	42.84
$p_1 = -\xi_{f0}\omega_{f0} + \sqrt{\xi_{f0}^2 - 1}$	1/s	-0.0029
τ_1	s	344
$p_2 = -\xi_{f0}\omega_{f0} - \sqrt{\xi_{f0}^2 - 1}$	1/s	-0.131
τ_2	s	7.6

Table 5.5 Values of characteristics of H_f for Test-01

5.5 Advanced Model: Virtual Prototyping

In this paragraph an advanced modelling is proposed in order to take into account all the effects neglected in the functional model. Firstly a vane pump thermal model is described while after a full thermal model. The experimental and analytical results are compared to underline the advantages of virtual prototyping versus the analytical approach.

5.5.1 Vane Pump Thermal Virtual Prototype

A thermal pump model is developed in LMS-AMESim environment [17] in order to simulate the heat exchanges between hydraulic fluid, pump body and external environment and finally to evaluate the time history of the fluid temperature inside pump [18].

The model is built from AMESim libraries, as far as possible, in order to take benefit of well established, numerically robust and documented sub-models. In this model look-up tables are preferred to parametric model exposed in Cap. 2, to evaluate the energy losses of the vane pump: they enable frictions and leakages to be reproduced within the range of experimental data acquired in laboratory. Unfortunately, the rapid temperature increase does not allow taking measurements at extremely low shaft velocities for feeding the

model tables. It is important to note that out of the experimental range, data have to be extrapolated that introduces modelling uncertainties.

Figure 5.7 displays the thermal-hydraulic virtual prototype of the vane pump created in AMESim. The virtual prototype principally consists of two parts. The bottom of figure reproduces the pump energy losses.

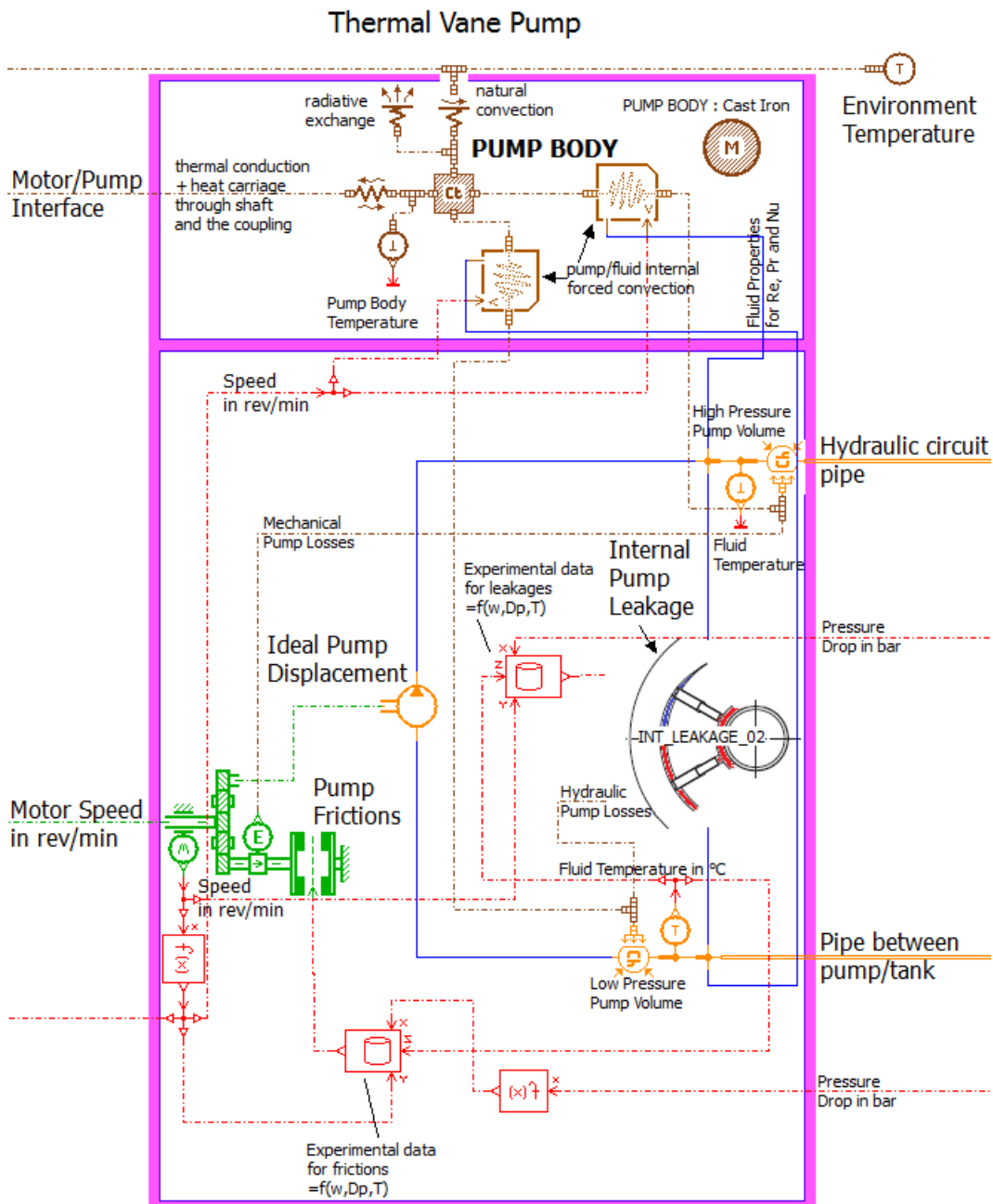


Figure 5.7 Vane pump thermal-hydraulic virtual prototype

The model interface are: pump/circuit thermal-hydraulic (right-hand side) and the

pump/motor mechanical (left-hand side). The second part, in the top of figure, represents the pump body and its thermal interaction with electric motor (left-hand side) and environment (upper side).

In the first part, the vane pump is modelled according to the Bond-Graph of Chap.2. The internal leakages and the frictional torques are calculated as function of pump speed, line pressure and temperature of the fluid inside pump. In reality, these energy losses depend on hydraulic pressure produced inside the pump but, in this work, they are made dependent on line pressure measured out of the pump, in the high pressure hydraulic circuit. Two thermal-hydraulic volumes are added at suction and delivery sides where mass and energy balances are simultaneously applied. Fluid temperature is measured in the suction volume (LP drain volume) and in the discharge volume at high pressure, in accordance with the effective placement of the thermocouples in the real pump of the test bench. From a causal point of view, the thermal-hydraulic model computes torque, flow and heat flow from shaft/body angular velocity, pressure at pump ports and ambient temperature. One important choice is related to the location where heat is injected in the pump model. The heat generated by the pump leakages is transferred directly to hydraulic fluid filling the suction pump volume because it is mainly carried by the fluid that recirculates internally from the high pressure to the low pressure domain. A “super-component”, constituted by basic sub-models, is built to calculate the heat due to internal leakages (Appendix C).

The heat due to pump friction is transferred to hydraulic fluid filling the discharge volume. This choice is driven by considering that the pump friction is mainly produced in the regions where the back pressure increases the contact loads between sliding and mating parts.

In the top part of the model, the pump body is considered as a single solid made of cast iron that exchanges heat with motor, fluid and ambient: internal forced convection between body and fluid, thermal conduction and heat carriage between pump and motor through shaft and coupling, natural convection and radiation with environment. The internal forced convection is achieved by means a tailor-made “super-component” that is built by starting from basic sub-models of AMESim library (fig. 5.8). It permits to take into account the flow conditions and fluid properties in the evaluation of heat transfer. In particular, the Nusselt number is calculated as function of Prandtl and Reynolds numbers. The Reynolds number determines the condition of laminar or turbulent flow and the

friction factor is consequently identified too. More details are inserted in paragraph 5.5.3.1.

In practice, the main issues encountered during the development of the thermal-hydraulic pump model are related to the modelling and parameterisation of heat exchange between components, as just exposed for the analytical model.

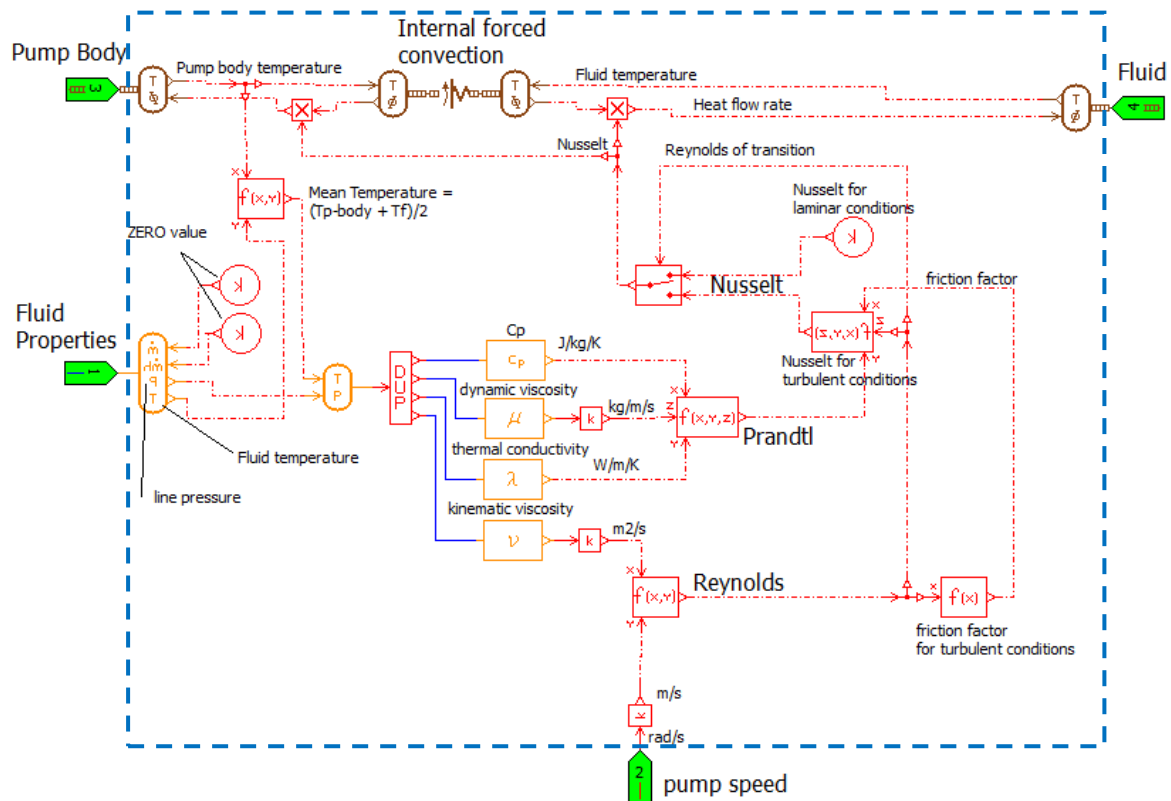


Figure 5.8 “Supercomponent” for internal forced convection evaluation

5.5.2 Full Thermal Model

In order to evaluate correctly the time evolution of the fluid temperature inside pump, it is necessary to connect the thermal-hydraulic pump virtual prototype, described in 5.5.1, to the model of electric motor, base support and hydraulic circuit. In this way, it is possible to simulate the complete heat transfers between hydraulic fluid, pump, electric motor, base support, hydraulic circuit and external environment. The full modelled system is represented schematically through the sketch map in Figure 5.9. The complete virtual

prototype is composed by a thermal-mechanical modelling of the electric motor, a thermal-hydraulic modelling of the hydraulic circuit and a thermal modelling of the base support where the module is installed. The following temperatures are calculable by model: fluid T_{f-in-p} , pump body T_{p-body} , motor body T_{m-body} and base support T_{s-body} .

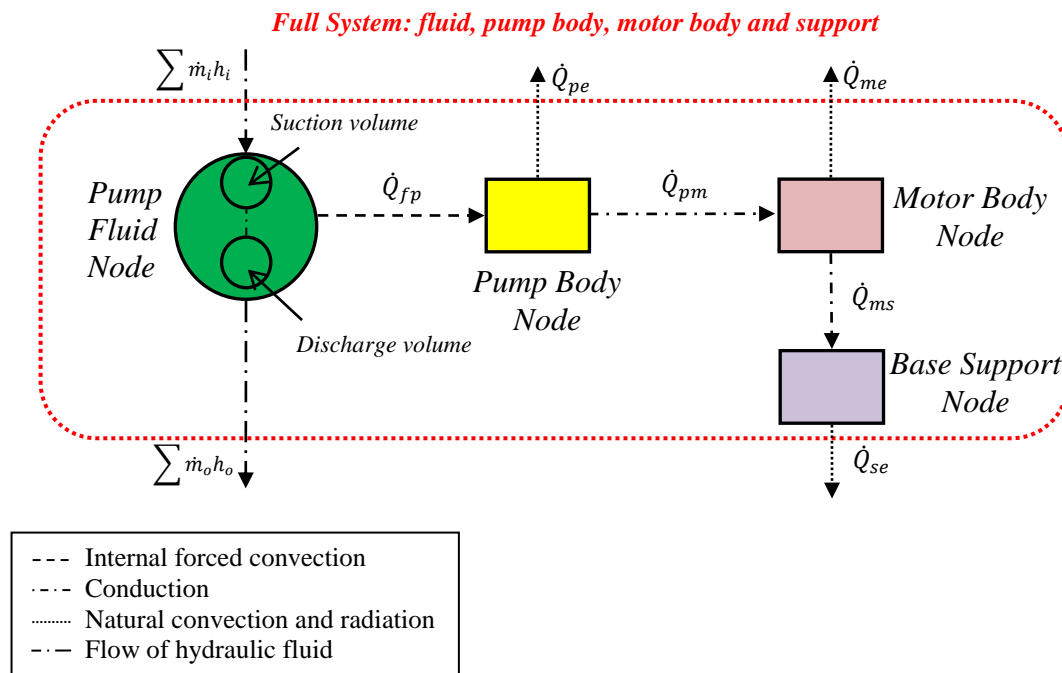


Figure 5.9 Sketch map of full system modelled in the advanced analysis through virtual prototyping

As the inverter can output a signal image of the electromagnetic torque, it is decided to avoid modelling the inverter, the motor electromagnetics and the control loops in order to keep the model simple at preliminary design stage. Therefore the electric motor is modelled as a perfect power transformer plus copper losses, friction and rotor inertia.

Such a decision sets up a high challenge for the validation of the EHM model. Indeed, when the inverter and the control loops are modelled, as generally done, any modelling error impacting the fastest states (e.g. electromagnetic torque - or current) has a low influence on slower state variables (e.g. velocity). In the present case, as no loop is modelled, the model is forced to operate in full open loop where modelling errors sum: impact of friction on speed for a given drive torque, impact of leakage on output flow for a given shaft velocity, impact of output flow on output pressure for a given hydraulic load...and in addition impact of temperature on every effect.

Figure 5.10 shows the full thermal-hydraulic model of EHM in AMESim environment

used to emulate the real test bench performance.

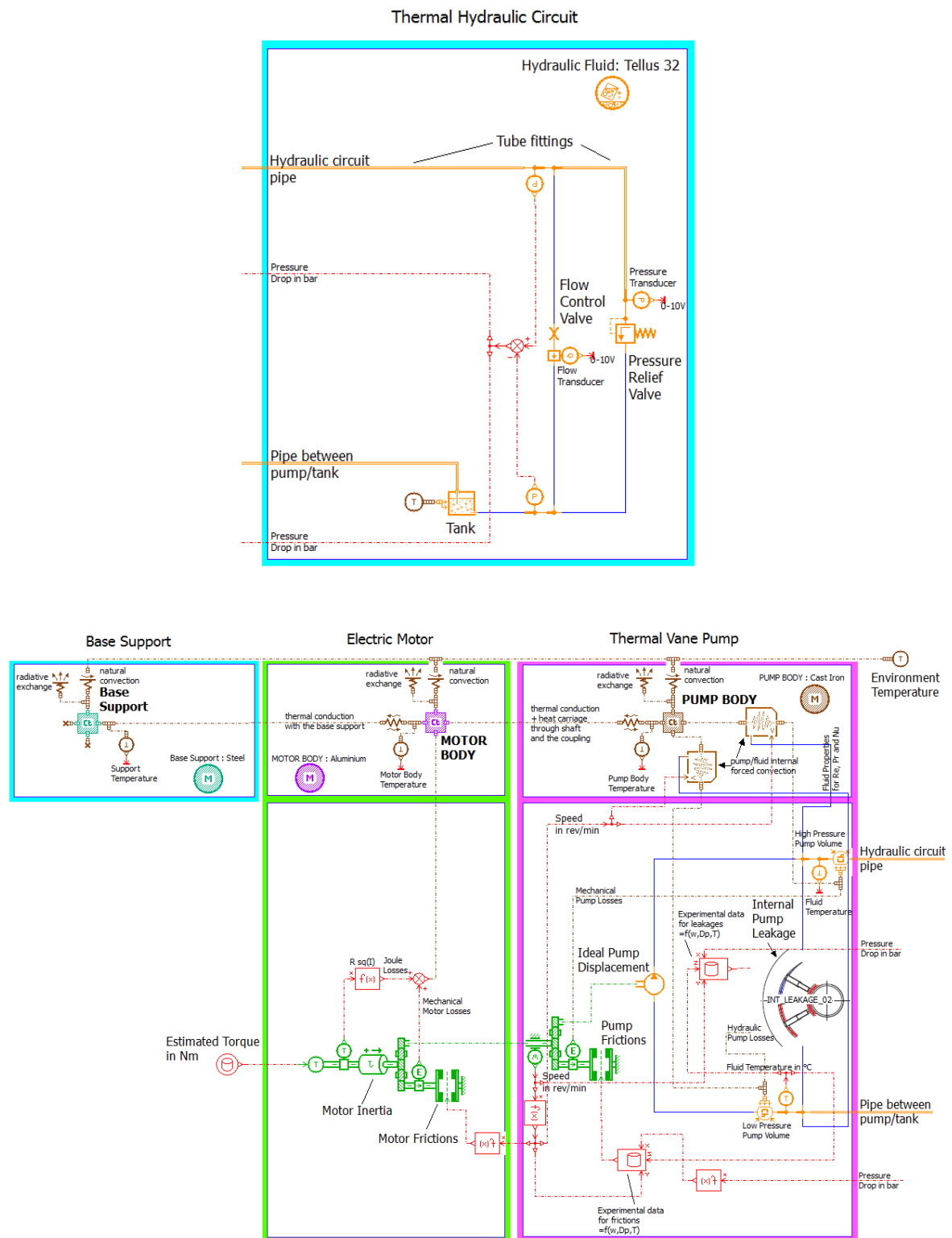


Figure 5.10 Complete thermal virtual prototype of EHM (top: hydraulic load and test bench, bottom; electrohydraulic module)

Motor copper losses P_{copper} are calculated from the motor electromagnetic constant K_m , the windings resistance R_m and the estimated torque C_{est} by the following expression:

$$P_{copper} = R_m \left(\frac{C_{est}}{K_m} \right)^2 \quad (5.21)$$

The mechanical power losses due to friction are also introduced from motor supplier data. The motor body exchanges heat with pump body and with its base support through thermal conduction. At the same way of the pump body, it interacts with the ambient air by means of natural convection and radiation with environment walls.

The model of the hydraulic circuit consists of thermal-hydraulic pipes with simulated compressibility and friction effects, load control valve, pressure relief valve, tank and sensors.

5.5.3 Heat Transfer Parameters Identification

By starting from the first estimation of the heat transfer coefficients from the functional model where they are assumed constant for all time duration, 5.3.5, an improvement of heat transfer models is now driven by variable coefficients determined through traditional equations based on number of Nusselt evaluation.

5.5.3.1 Internal Forced Convection

Internal forced convection coefficients h_{int_conv} are usually extracted from the calculation of the Nusselt number Nu according to equation (5.22):

$$h_{int_conv} = \frac{Nu k_f}{L_c} \quad (5.22)$$

where

k_f = fluid thermal conductivity

L_c = characteristic length of pump correspondent to cam inner diameter, maximum rayon

There are a lot of models for calculation of the Nusselt number versus flow conditions (Reynolds number Re) and fluid temperature condition (Prandl number Pr). However, any

model applies to very specific geometries or flow that do not match with the real operation of a hydraulic pump. In the present work, when the flow is in turbulent conditions, Nusselt correlation for internal forced convection between pump body and hydraulic fluid is estimated with the Dittus-Boelter equation associated to turbulent flow in tubes. This is obtained by modification of the Colburn equation (5.23) where $n = 0.4$ for heating of the fluid flowing in the tube [13]:

$$Nu = 0.125 f Re Pr^n \quad (5.23)$$

The (5.23) is valid for Reynolds numbers higher than 1×10^4 and for Prandtl numbers in the range $0.7 \leq Pr \leq 160$. The friction factor f is determined through the McAdams power law relation (5.24) that applies to fully developed turbulent flow in smooth tubes [13]:

$$f = 0.184 Re^{-0.2} \quad (5.24)$$

When the laminar conditions occur, the friction factor is equal to $64/Re$ and the Nusselt number is taken equal to the constant value of 4.36. This corresponds to fully developed laminar flow in a circular tube subjected to constant surface heat flow [13].

The properties of the fluid are calculated at the bulk mean fluid temperature given by:

$$T_{mean} = \frac{T_{f-in-p} + T_{p-body}}{2} \quad (5.25)$$

This approach enabled the effect of flow and temperature to be considered in the calculation of the convective coefficient but required the friction factor f and the characteristic length L_c to be set as model parameters.

5.5.3.2 Natural Convection and Radiation

The natural convection over surface mechanics is taken into account to evaluate the heat transfer between the external environment and respectively pump body, motor body and base support. The heat transfer coefficients h_{conv} are calculated by the same expression for the h_{int_conv} (5.22) where k_f is now the thermal air conductivity and L_c is the pump length. The Nu is determined by means of empirical correlations dependent on the Rayleigh number R_a which is the product of the Grashof number G_r and the Prandtl number Pr [13]:

$$Ra = GrPr = \frac{g\beta(T_s - T_\infty)L_c^3}{\nu^2} Pr \quad (5.26)$$

where

g = gravitational acceleration

β = coefficient of air volume expansion

T_s = surface temperature

T_∞ = fluid temperature far from the surface

ν = kinematic viscosity of air

Table 5.6 summarises all the empirical relations for the calculation of N_u applied for each system component. The pump body is assimilated to a sphere having the same external surface area, the motor body was compared to a horizontal cylinder having the same side area and finally, the base support was compared to a horizontal plane having the same surface area and perimeter.

System Component	Shape	Nusselt number
Pump body	Sphere	$N_u = 2 + \frac{0.589R_a^{1/4}}{[1 + (0.469/P_r)^{9/16}]^{4/9}}$
Motor body	Horizontal cylinder	$N_u = \left\{ 0.6 + \frac{0.387R_a^{1/6}}{[1 + (0.559/P_r)^{9/16}]^{8/27}} \right\}^2$
Base support	Horizontal plane	$N_u = 0.15 R_a^{1/3}$

Table 5.6 Nusselt numbers calculation for natural convection over the surface of: pump and motor body and base support

The heat radiation is now considered because, even if it usually represents the smallest contribution to total heat exchanges, it cannot be negligible when the released and absorbed powers are evaluated in a temperature prediction approach [16]. The expression (5.13) is used for the heat radiation transfer \dot{Q}_r , where the emissivity is taken equal to $\varepsilon_s = 0.18$ for pre-polished aluminium of motor body [6], $\varepsilon_s = 0.6$ for cast iron of pump body and $\varepsilon_s = 0.56$ for rolled steel sheets of base support, from literature.

5.5.3.3 Thermal Conduction

Heat transfer at the interface between the EHM components (pump and motor) is evaluated by means of the thermal conduction and contact resistance [13]. It is assumed to be heat conduction between pump and motor body through the coupling and the common shaft. Now a thermal contact conductance is considered dependent on several parameters as: the surface roughness, material properties, temperature and pressure at the interface. The difficulty in determining the heat transfer in this case is solved by assuming an overall constant thermal contact conductance, based on typical values for dissimilar metal surfaces pressed at high pressure each other ($10^3 \div 10^4 \text{ W/m}^2/\text{K}$ of order of magnitude) [13]. Concerning the thermal conduction between motor body and base support, the thermal resistance network for heat transfer through a two-layer plane wall is applied. In this way, it is firstly possible to estimate the total thermal resistance as the arithmetic sum of the individual thermal resistances of motor body and support.

5.6 Comparison between Analytical model, Real and Virtual Tests

The experimental results are finally compared to simulated results obtained by means of the full thermal virtual prototype of EHM and to simulated results obtained analytically through the functional model.

Figures 5.11 compare the measured and simulated temperatures of: T_{f-in-p} , T_{p-body} and T_{m-body} . The T_{m-body} of the analytical model is not plotted because it is not calculated but it represents simply a system input, taken equal to measured signal, as already explained in 5.4.2. In the virtual prototype the initial conditions of temperatures are set according to the measurements. The flow control valve static hydraulic characteristic is modelled using look-up tables providing the mass flow rate as function of Δp and T_o that are acquired from the experimental data.

Although the virtual model is run under a very constraining (open-loop) approach, the virtually simulated T_{f-in-p} remain close to the measured ones. The maximum relative errors are lower than 5 % in *Test-01* (3 °C of temperature gap) and lower than 2 % in *Test-02*

(1.4 °C of temperature gap). The virtually simulated and measured T_{f-in-p} differ principally in the initial extent due to an overestimation of heat absorbed by fluid, while the final values result are very accurate: the temperature gap is lower than 0.4 °C.

For the analytical model the maximum temperature gaps between simulated and measured T_{f-in-p} are generally lower than 6 % (correspondent to 3.5 °C).

Concerning the pump body T_{p-body} , obtained by virtual prototype, differ from the measured ones, due to the higher simulated absorbed powers, of about 5 °C for *Test-01* and 2.3 °C for *Test-02*. The maximum temperature gaps between analytically simulated and measured T_{p-body} are instead about 2.2 °C for *Test-01* and 1.5 °C for *Test-02*.

The T_{m-body} of virtual prototype are instead very close to measured ones with temperature gaps that remain lower than 1.3 °C.

Table 5.7 shows the values of the heat transfer coefficients selected in the complete EHM virtual prototype. It is possible to observe that the internal forced convection coefficients h_{int_conv} varied during each simulation because the equation (5.23) for calculation of N_u , as function of Re and Pr , is implemented in the prototype by means of the “supercomponent” showed in figure 5.8. In *Test-01* the initial h_{int_conv} is lower than in *Test-02* due to lower starting ω that makes the initial Reynolds number Re lower. After that the increases of both ω and T_{f-in-p} increase greatly the h_{int_conv} in both *Test-01* and in *Test-02*: it is remarkable that the increase of 100% of ω and T_{f-in-p} with reference to starting point conditions for *Test-01*, made the h_{int_conv} to be increased of 146%. The natural convection coefficients also vary, in accordance to expressions of Nusselt number listed in tab. 5.6, but their variation (lower than 8 %) does not exert a significant influence on results. They can be thus considered invariant and equal to initial values showed in table.

<i>Heat Transfer Coefficient [W/m²/K]</i>	<i>Test-01: 160bar @ 10% Vol. Eff.</i>	<i>Test-02: 160bar @ 30% Vol. Eff.</i>
Internal forced convection	from 1202 to 2964	from 1211 to 2208
Natural convection for pump body	from 25 to 27	from 25 to 27
Natural convection for motor body	from 20 to 21.6	from 20 to 21.6
Natural convection for base support	from 25 to 27	from 25 to 27
Pump/motor thermal contact conductance	8600	8600
Motor/support thermal contact conductance	15400	15400

Table 5.7 Values of heat transfer coefficients selected for EHM virtual simulations

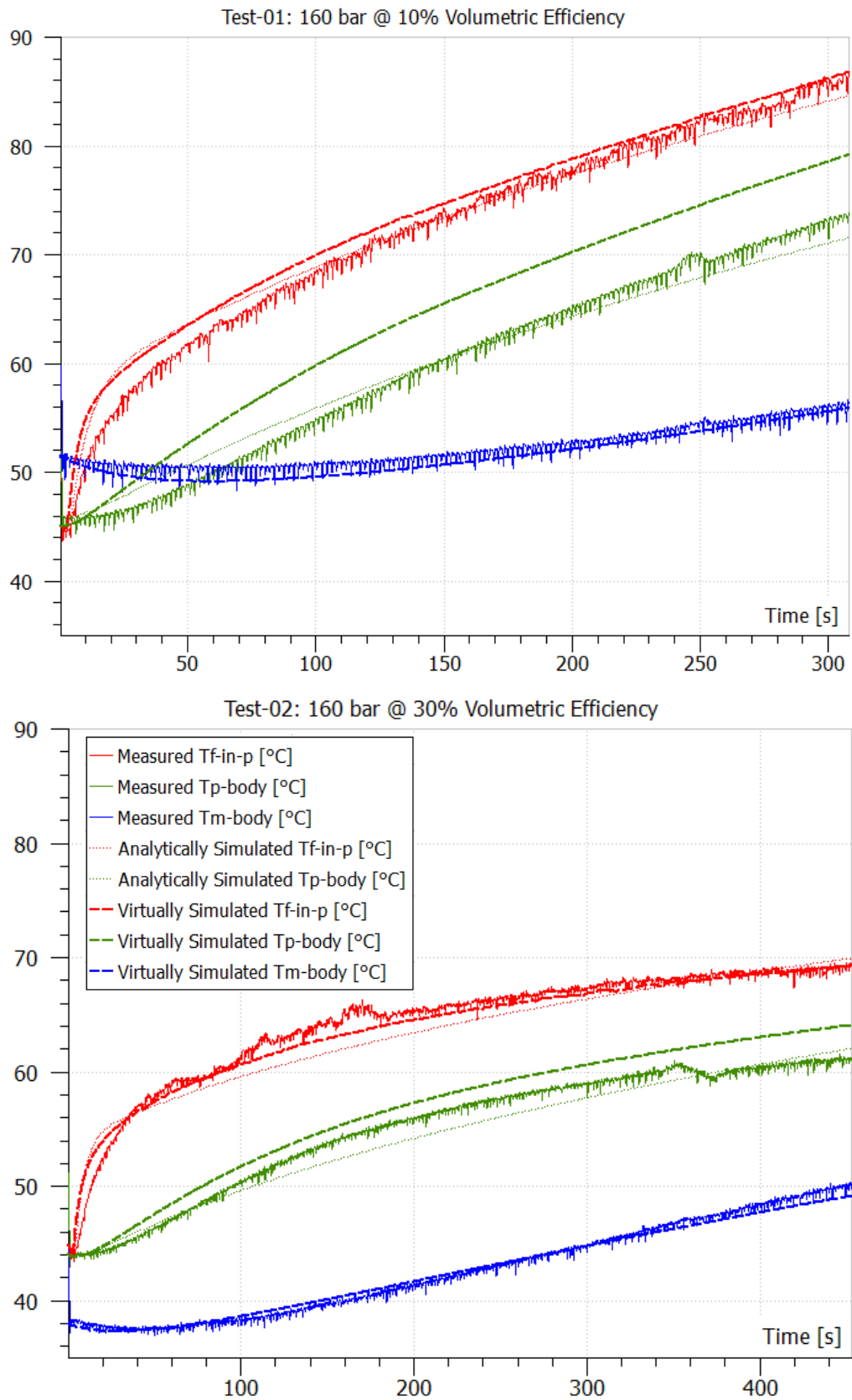


Figure 5.11 Comparison between measured, analytically and virtually simulated temperatures: Test-01 (top) and Test-02 (bottom)

Comparing the heat transfer coefficients for forced convection and for thermal contact conductance used in the analytical functional model, they now result much higher, more than double of previous ones (Tab. 5.4). It means that the analytical approach, although able to reproduce the temperatures simulation with good accuracy in the considered time simulation, has limitations in the prediction of the right heat transfer between EHM parts and fluid.

In this attempt, it is also interesting to use the results of virtual prototype for quantifying the different power flows. Figure 5.12 shows the percentage of simulated absorbed and released power contributions at the end test times (in the top), and the overall absorbed and released energies during all time duration (in the bottom) for respectively pump body, motor body and fluid. Figures relative to *Test-01* are on the left while relative to *Test-02* are on the right.

Concerning the pump body, it is notable that the percentages of each absorbed/released power are similar for the two tests and that the volumetric losses, associated to pump internal leakages, represent the major contribution of absorbed power. The increase of internal energy of the fluid produces an enthalpy flow rate towards the pump body that represents the second contribution, more important than the mechanical losses due to pump frictions. Another fundamental observation is the importance of pump/motor thermal conduction that contributes with a percentage over the 80 % of total pump released powers. The major source of heat absorbed by the motor body is instead provided by the pump while the electrical power of the motor represents a minor contribution. The thermal conduction with the base support finally permits to transfer the most of quantity of heat previously stored.

The figures relative to absorbed and released powers of the fluid show that the volumetric and mechanical losses, assumed initially stored in the fluid by the model, are completely released to pump body at the end of simulation. Only in the *Test-02* it remains about 200 W of volumetric losses again stored in the fluid. The major percentage of released power is the enthalpy flow rate transported by the fluid flowing out of pump. Concerning the overall net energies, it is calculated 12 kJ and 4 kJ for the fluid at the end of each simulation to increase its temperature respectively of 41 °C and 24 °C: it corresponds to an average energy value of 0.29 kJ/°C and 0.17 kJ/°C.

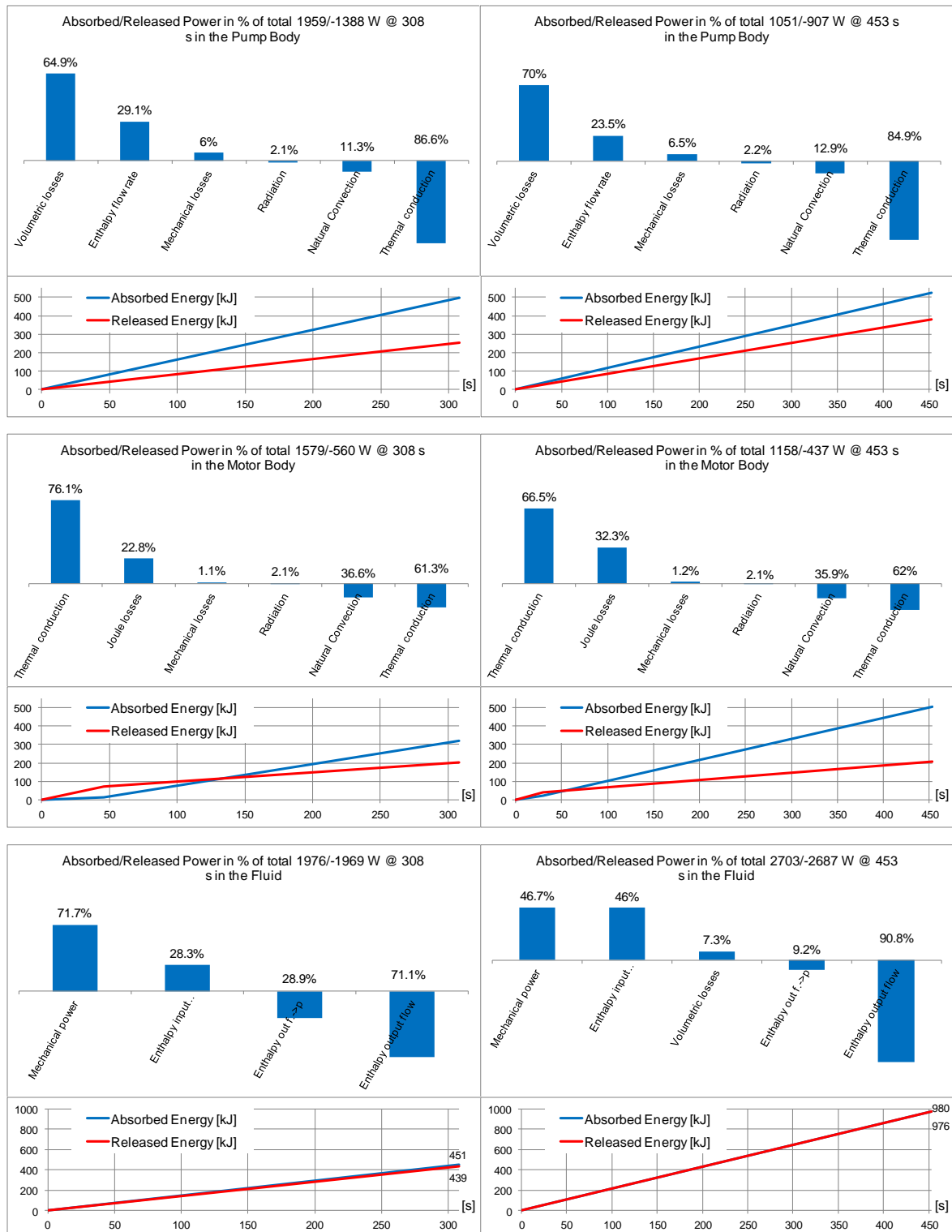


Figure 5.12 Contributions of absorbed and released powers at the end simulation time (top of each figure) and absorbed and released energies (bottom of each figure) for pump body, motor body and fluid. Data of Test-01 in left column and data of Test-02 in right column.

This difference is due to different value of h_{int_conv} that governs the heat flow between pump and fluid (Tab. 5.7): in fact h_{int_conv} firstly lower in *Test-01* than in *Test-02*, becomes

higher at the end of simulation by increasing the released power and by increasing finally the total net absorbed energy.

The analytical model is not able to provide adequately the power losses during all simulation because they are only calculated at the running starting point and after they are maintained constant until the simulation end.

5.7 Conclusions

At a final overview on the thermal hydraulic modelling and simulation of the complete EHM, it is possible to assert that the analytical approach:

- 1) Provides a preliminary view on the principal sources of power losses
- 2) Permits to have a study carried out about the importance of each term on system dynamics, by neglecting certain terms dependent on pump speed
- 3) Permits to raise awareness of the limitations due to the supposed constant heat transfer coefficients
- 4) Shows the limits of modelling based on assumptions which could mislead by its apparent good results in temperature simulation
- 5) Justifies the development of an advanced model that enables to make all those improvements that the functional model is not able to guarantee

The advanced model based on virtual prototyping:

- 1) Provides the time evolution of temperature respectively of fluid, pump body, motor body and base support by assuming a uniform temperature distribution inside each of them. In fact pump, motor and support are modelled through an overall mass without modelling the sub-components like the rotor, cam-ring, vanes, cap and housing for pump. Consequently the model does not simulate the temperature gradients and so a temperature error can be produced between simulated and measured results, last ones obtained through thermocouples located in specific points on bodies' surface. It is the case of pump body.

- 2) Another observation can be made about the sensitivity of the virtual model to extrapolation of energy pump losses out of the range of experimental data: the pump experimental internal leakages and frictional torques are implemented in the model by means of look-up tables whose range of operating conditions is showed in Cap. 2. The model so extrapolates linearly the energy pump losses out of this range but it could produce not negligible errors that could modify significantly the final results. Just thinking to the internal leakages that represent the major contribution to power absorbed by pump body, and a little error of leakage flow evaluation, it would generate big errors on volumetric losses
- 3) Nevertheless enables to predict correctly the time evolution of temperatures, especially of the fluid inside pump, although the full model is validated in a very constraining way that made all modelling errors cumulated
- 4) Permits to evaluate with good reliability the heat transfers between fluid, pump and motor body, base support and external environment by taking also into account the variation of the convection coefficients as function of operating conditions
- 5) Shows the significant influence of the heat exchange between the pump and the motor on the fluid temperature and the lack of knowledge models for calculation of convection factors that can apply to the geometry and the operative conditions associated with the application's need

References

- [1] S. Helduser. Development trends in electrohydraulic drives and controls. *6th International Fluid Power Conference, March 31-April 2, 2008. Dresden, Germany. Pp. 29-64.*
- [2] K. Muller, and U. Dorn. Variable speed drives – customer benefits in injection molding machines and presses. *7th International Fluid Power Conference, March 22-24, 2010. Aachen, Germany.*
- [3] A. Feuser. Modern electrohydraulic drive technology for stationary machinery in industrial automation. *7th International Fluid Power Conference, March 22-24, 2010. Aachen, Germany.*
- [4] S. Helduser. Improved energy efficiency in plastic injection moulding machines. *8th Scandinavian International Conference of Fluid Power, May 7-9, 2003. Tampere, Finland.*
- [5] A. Helbig, C. Boes. EHA – A New Approach for Motion Control Actuators. *The 13th Mechatronics Forum International Conference, 2012. Linz, Austria. Pp. 165-179.*
- [6] S. Michel, T. Schulze, J. Weber. Energy-Efficiency and Thermo Energetic Behaviour of Electrohydraulic Compact Drives. *9th International Fluid Power Conference, March 24-26, 2014. Aachen, Germany. Pp. 163-177.*
- [7] B. Johansson, J. Andersson, P. Krus. Thermal Modelling of an Electro Hydrostatic Actuator system. *Proceedings of the International Conference on Recent Advances in Aerospace Actuation Systems and Components, June 13-15, 2001. Insa Toulouse, France. Pp 49-54.*
- [8] S. Lauckner. Thermal Analysis and Simulation of the A380 Hydraulic System. *Proceedings of the International Conference on Recent Advances in Aerospace Actuation Systems and Components, November 24-26, 2004. Insa Toulouse, France.*
- [9] W. Takebayashi, Y. Hara. Thermal Design Tool for EHA. *Proceedings of the International Conference on Recent Advances in Aerospace Actuation Systems and Components, November 24-26, 2004. Insa Toulouse, France.*
- [10] S. Habibi, and A. Goldenburg. Design of a new high performance electrohydraulic actuator. *IEEE/ASME Transactions on Mechatronics, Vol.5, 2000.*
- [11] C. Li, Z. Jiao. Thermal-Hydraulic Modeling and Simulation of Piston Pumps. *Chinese Journal of Aeronautics, November 2006. Proceedings vol. 19, n. 4, pp. 354-358.*

- [12] H. Rahnejat. Tribology and Dynamics of Engine and Powertrain: Fundamentals, Applications and Future Trends. *Woodhead Publishing Limited, 2010.*
- [13] Y. A. Cengel. Heat and Mass Transfer, *McGraw-Hill, 2006.*
- [14] F. W. Sears, G. L. Salinger. Thermodynamics, Kinetic Theory and Statistical Thermodynamics. *Third Edition, Addison-Wesley, 1975.*
- [15] K. Li, Z. Lv, K. Lu, P. Lu. Thermal-hydraulic Modeling and Simulation of the Hydraulic System Based on the Electro-Hydrostatic Actuator. *The Third International Symposium on Aircraft Airworthiness, ISAA 2013. Procedia Engineering 80 (2014), pp. 272-281.*
- [16] M. Zecchi, A. Mehdizadeh, M. Ivantysynova. A Novel Approach to Predict the Steady State Temperature in Ports and Case of Swash Plate Type Axial Piston Machines. *The Thirteenth Scandinavian International Conference on Fluid Power, June 3-5, 2013. Linköping, Sweden. Pp. 177-187.*
- [17] LMS-AMESim:
http://www.plm.automation.siemens.com/en_gb/products/lms/imagine-lab/amesim/
- [18] E. Gnesi, J-C. Maré, J. L. Bordet. Modeling and Simulation of Thermal Hydraulic Coupling in Electro Hydrostatic Modules Involving Fixed-Displacement Vane Pumps. *14th Scandinavian International Conference of Fluid Power, May 20-22 2015. Tampere, Finland.*

Conclusion

Dans cette dissertation, un nouveau module électro-hydrostatique (EHM) est proposé et étudié en détail avec l'accent spécial sur des questions induites par son utilisation dans les machines à injecter. Ce module associe, dans une unité intégrée, un servomoteur brushless Parvex NX860 et une pompe à palettes Parker, série T7. La pompe à palettes a été préférée pour son haut rendement, basse pulsation de pression et basse émission acoustique. Cependant ce choix incite des contraintes sévères car la pompe n'a pas de drain externe et son domaine de fonctionnement est impérieusement limité à delta positif de pression et vitesses supérieures à -66 % de la valeur nominale.

Aujourd'hui, la demande de modules, dans les machines à injecter, concerne principalement : haut rendement énergétique, hautes pression de service et vitesse et grande fiabilité de contrôle. Ceux-ci permettent respectivement de réduire la consommation d'énergie de la machine et le temps du cycle en améliorant aussi la qualité de parties produites.

Ce travail de recherche a pour but de fournir une approche, basée sur modèles virtuels, qui est capable de déterminer rapidement et efficacement la performance du module en fonction des besoins du client et d'identifier les avantages et les limitations des composants constituant le module même. Les questions spécifiques qui se posent et qui concernent les exigences les plus sévères dans un cycle typique d'injection, sont : la performance dynamique de l'EHM pendant les phases d'accélération et de décompression afin de réduire le temps du cycle et augmenter la productivité, les phénomènes de cavitation et d'aération qui peuvent significativement réduire la durée de vie de la pompe l'augmentation de la température, pendant les phases à faible vitesse et haute pression, qui peut rapidement mener au grippage de la pompe.

Conclusion

In this dissertation, an innovative electro-hydrostatic module was proposed and studied in details with special focus on issues induced by its use in injection moulding machines. This module combines, in an integrated unit, a Parvex NX860 series brushless servo motor and a Parker T7 series vane pump. Vane pump was preferred for its high efficiency, low ripple and low acoustic emission. However this choice induces severe constraints because the pump is not externally drained and its domain of operation is imperatively limited to positive pressure difference and velocity no lower than -66 % of the rated value.

Today the demand for drives, in typical injection moulding applications, mainly concerns: high energy efficiency, high outputs (pressure and velocity) and great control accuracy. These respectively permit to reduce the machine energy consumption and cycle time while improving the part quality.

This research work aimed at providing fast and efficient model-based approaches to determine the performance limits versus the customer's needs and the advantages and drawbacks of the module's components. Specific issues were addressed and dealt which concern the most severe requirements of injection moulding machines' cycle, which are:

- Dynamic performance of the EHM during acceleration and depressurisation phases to reduce moulding cycle and to increase productivity,
- Cavitation/aeration phenomena in transient phases that may significantly reduce the pump lifetime,
- Rapid temperature increase during low speed / high pressure that may rapidly lead to pump jamming.

According the above issues, analytical functional approach was initially followed in order to identify the key relationships between the fundamental system parameters and drive performance. After a linear approach, progressive modelling was introduced, with resort to non-linear virtual prototypes, to increase realism and accuracy of the simulated responses.

The first chapter was dedicated to the review of the units, composing the injection moulding machines, and the functional process for manufacturing moulded parts. The evolution of drive technology through the years was addressed by highlighting the recent maturity of electro-hydrostatic modules versus electro-mechanical and servo-hydraulic ones. Typical cycles of rubber and of plastic IMMs were described to show the machine's requirements that the drive system has to fulfil. In Chapter 2, the state of art of the vane pump was presented with particular focus on its advantages and limitations compared with the other principal competitors. The operation principle and the basic components of vane pump Denison technology were also described. The modelling at vane pump level was then proposed by evaluating with attention its energy losses coming from internal leakages and frictional torques. The knowledge in modelling frictions and leakages is a mandatory step because they influence module static and dynamic operation as well as thermal behaviour. In parallel to the modelling activity, we conceived, assembled and operated a test bench at Parker laboratory to enable the models to be experimentally validated. Several tests were specified and carried out to collect data on energy losses in a larger operating domain than commonly covered prior our work. During tests, the operating conditions were varied in terms of output pressure, pump speed and temperature of the fluid. The operating range, in which the laboratory tests were performed in this work, was however limited by thermal issues. In fact it resulted very difficult to keep the temperature constant during tests at low speed due to a lack of sufficient recirculation of fluid inside pump.

After that, a parametric model was developed with the main target to balance the model complexity and realism. A nine 9-parameters model was found suitable for supporting the control design and the preliminary functional models of dynamical and thermal module performance. Unfortunately it was not consistent with accurate and advanced simulations requirements because it introduced non-negligible modelling errors. In order to solve this drawback, a hydraulic virtual prototype was thus created, in the Siemens-AMESim environment, to simulate the pump energy losses. It was based on look-up tables constituted by all the experimental data recorded in laboratory. The energy losses was so calculated, as function of pressure and speed at selected temperature, by means of interpolation inside the operating range and of extrapolation out of the range. A specific sub-model, of the AMESim mechanical library, was selected for dealing the numerical implementation of transition between sticking and sliding conditions in the region around

the condition of zero speed.

Once the pump energy losses were calculated and reproducible by means a virtual prototype, in Chapter 3 the acceleration and depressurisation transients of a typical injection moulding machine's cycle were analysed. The contributions of system parameters on module performance were firstly identified through a progressive approach based on open-loop qualitative and quantitative analysis. It permitted to point out how the motor peak maximum torque, the hydrostatic torque and the fluid compliance may significantly affect the acceleration phase.

After that the importance of adding a pump speed closed-loop, for module control in acceleration, was showed by means of linearized functional model. This study was based on assumptions determined through the previous analysis which allowed modelling simplifications. An added hypothesis concerned the fluid compliance that was considered time-invariant. An improvement of control architecture was then achieved by implementation of a feedforward compensator in parallel to feedback controller. The advantages in better acceleration capability and null static error of the complete closed-loop controlled system were analytically simulated by exciting it through a command step of speed.

In order to increase the modelling level accuracy, a detail model of full test bench was then created in AMESim. It consisted in modelling the velocity closed-loop controller, the inverter, the electric motor, the motor/pump coupling, the vane pump and the hydraulic circuit. The vane pump prototype was an improved version of that described in Chapter 2, thanks to representation of pump high pressure volume through a hydraulic capacity chamber. In this model all the non-linearities effects relative to EHM and hydraulic circuit were simulated. In particular the fluid compressibility was made more realistic by evaluating the dependences of Effective Bulk Modulus from line pressure, fluid temperature, saturation fluid pressure, gas polytropic index, air/vapour content and deformability of hydraulic hoses. Fifteen laboratory tests were then performed by imposing command speed steps of 1000 *rpm* and by varying the charge load. They permitted to compare the measurements to analytical and simulated results. The full virtual prototype was finally validated for the acceleration transient simulation and, compared to analytical model, it was showed that:

- The full virtual prototype enabled simulating realistically the acceleration transients of machine's cycle by considering the functional and parasitic effects,

especially the influence of variable compliance of the fluid

- The model permitted to identify unknown-parameters or parameters difficult to preset which affect the dynamic performance: free air content and equivalent Young's modulus of flexible hoses

The full virtual prototype was also validated in steady-state conditions by demonstrating its high accuracy.

In last part of Chapter 3, the depressurisation transient was also simulated through the same full virtual prototype and 4 laboratory tests were performed to validate it. Output pressure or pump speed were closed-loop controlled, with addition of feedforward compensation, and pump negative speed rotations was also achieved. The prototype validation procedure permitted to determine an optimum Young's modulus that was suitable for simulating the dependences of hoses deformability from pressure drop during depressurisation. It was finally shown that:

- The full virtual prototype enabled simulating the depressurisation phase by taking into account the variation of hoses deformability produced by pressure drop

Cavitation and aeration phenomena could limit the performance in acceleration and cause severe mechanical damages on components. In Chapter 4 these phenomena were initially dealt by focusing on most common effects on vane pumps and by proposing methods for detection and prevention.

An analytical approach was then developed in order to simulate the local reduction of hydraulic pressure in pump inlet associated to cavitation inception. The pump and the hydraulic line between pump and tank were thus modelled by means of resistive, inertial and capacitive effects. To simplify the modelling, these effects were treated through lumped parameters and assumptions were also added concerning constant fluid compliance and laminar flow conditions everywhere. At the end of this preliminary analysis, the principal hydraulic and geometrical parameters of the laboratory test bench, which influence the time variation of pressure, were so identified.

After that it was decided to increase the simulation realism. Virtual prototypes were built to model the vane pump and the hydraulic line at high accuracy level. Two prototypes were in particular created for the vane pump by starting from the pump prototype described in Chapter 3: first one improved the previous by adding the modelling of pump

low pressure volume and the inlet orifice. Second one proposed a more detailed modelling of pump internal orifices and volumes. To determine the pump characteristics necessary for this last model, calculations were carried out by means of 3-D CAD software. The hydraulic line modelling was also accurately improved by representing rigid pipe, tube fitting and flange. The advantages of virtual prototyping in this case concerned the evaluation of: variations of flow condition, of fluid compliance, concentrated pressure losses in correspondence of edge forms and frequency dependent friction. Some considerations were also made to underline the prototype limits, in the simulation of dynamic processes, due to lack of information propagation between adjacent control volumes. A solution was so proposed to solve it by imposing different fluid properties in the suction and discharge line of circuit.

A comparison between the two pump prototypes was carried out by showing no significant differences in the simulation of pressure in pump inlet and inside pump. A comparison with the analytical model then permitted to verify the higher superiority of the virtual prototype and 36 laboratory tests were finally performed to validate it. It was shown that the full virtual prototype enabled simulating accurately the minimum pressure reachable in pump inlet during typical acceleration phases

The rapid increase of temperature that may degrade the module performance during low speed and high pressure phases was analysed in the last Chapter 5. A preliminary thermal hydraulic modelling of the vane pump was firstly proposed in linear form. The heat transfer coefficients between pump, ambiance and electric motor were supposed to be time invariant. The system resolution provided the time variation of the temperature of pump body and fluid inside pump. Compared to tests performed in laboratory, the analytical results exhibited good general trends but with unacceptable final temperature divergence that took away from experiments.

The potentiality of virtual prototyping was so employed thanks to development of a complete thermal prototype of module. The vane pump energy losses were here simulated also as function of fluid temperature. The heat transfer coefficients were made dependent from operating and flow conditions. The absorbed and released powers of pump, motor and module base support were simulated too. Laboratory tests were performed to identify all the unknown heat coefficients of prototype and finally to validate it. It was showed that the module thermal virtual prototype enabled simulating with realism the time evolution

of the temperature of: fluid inside pump, pump and motor body, base support.

Further improvements and investigations can take appropriate action in ongoing works.

They can be listed as follows:

- The acceleration, depressurisation and steady-state phases were simulated in accordance to experimental results obtained by the laboratory test bench. The virtual prototype could be used to test other hydraulic circuit configurations in order to predict the effects generated by: long hydraulic lines between module and load, complex load impedances coming from the presence of valves, different types of control, etc.
- The simulation of the pressure in pump inlet permitted the identification of critical operating conditions for cavitation inception during accelerations. The virtual prototype could be used to optimise the pump/tank/inlet pipe assembly for best acceleration capability without cavitation.
- The thermal virtual prototype was validated for a limited operating range. It should be extended in order to generalise the validation domain.
- The thermal virtual prototype could be useful to demonstrate the benefits of the proposal characterised by the module immersed inside tank, compared to conventional modules installed outside tank.
- The injection moulding machine's cycle repeatability may affect the heat exchanges and the temperatures rise in the module. The simulation of an entire machine's cycle would permit to evaluate if and how it affects the thermal behaviour of the module.
- The virtual prototyping could be interfaced with CFD models of module components and co-simulation could be performed to take into account other parameters not considered in this work like: components deformation, 3D detail models, pressure gradients, etc.

Today Parker needs are pressing to demonstrate the thermal benefits of an immersed solution of EHM especially during typical static injection phase. Simulations of the module thermal virtual prototype inside tank will be thus a priority for quantifying the heat exchange between module and hydraulic fluid inside tank. In the same time, the

extension of the validation range of the thermal virtual prototype has to be carried out in order to have a more global vision for the whole module behaviour. Other laboratory tests have to be performed for acquiring data useful to validate the model. Another fundamental aspect to be soon dealt, concerns the evaluation of the non-linearities, as pump components deformation and pressure gradients inside the cartridge, which were not taken into account. CFD models will be thus developed and interfaced with virtual prototypes in order to simulate the contribution of these parasitic effects and finally to optimise cam profile and components design where necessary.

Appendix A-Characteristics of Components constituting the Test Bench

The characteristics of the vane pump and electric motor integrated in the Parker module are inserted in this appendix. The characteristics of the hydraulic circuit composing the test bench built in laboratory and the information about the inverter and the Speedgoat are also added.



Vane Pump T7ASW E22

<i>Displacement</i>		22.5	cc/rev
<i>Weight</i>		11.3	kg
<i>Inertia</i>		0.00032	kgm ²
<i>External convective area</i>		91022	mm ²
<i>Internal convective area</i>		27290	mm ²
<i>Maximum inner cam diameter</i>		34	mm
<i>A1 Orifice</i>	Cross-Sectional Area	130	mm ²
	Perimeter	50.7	mm
	Length	21.1	mm
<i>A2 Orifice</i>	Cross-Sectional Area	103	mm ²
	Perimeter	57.7	mm
	Length	28.1	mm
<i>A3 Orifice</i>	Cross-Sectional Area	60	mm ²
	Perimeter	36.2	mm
	Length	38.3	mm
<i>V1 volume</i>		50	cm ³
<i>V2 volume</i>		60	cm ³
<i>V3 volume</i>		65	cm ³
<i>HP volume</i>		80	cm ³

Electric Motor NX860WAF

Weight	27	kg
Inertia	0.0092	kgm ²
Viscous friction	0.0002322	Nm/rpm
Coulomb friction	0.57	Nm
External convective area	268600	mm ²

SERVOMOTEURS SANS BALAIS
NX860WAF
ELECTRONIQUE DE COMMANDE
AC890SD-43 2730 E
(400V)

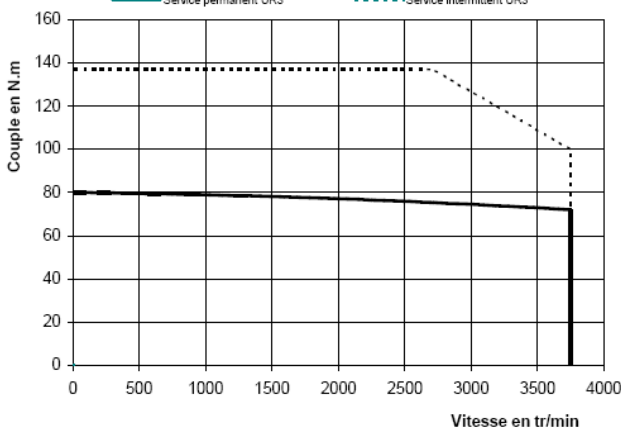



Caractéristiques moteur refroidi par eau: débit 5 l/min, température < 25°C

Couple en rotation lente	M ₀	Nm	83	
Courant permanent en rotation lente	I ₀	A _{rms}	56,9	
Couple pic	M _p	Nm	137	--
Courant pour obtenir le couple pic	I _p	A _{rms}	108	--
FEM par 1000 t/min (25°C)*	K _e	V _{rms}	96,1	
Coefficient de couple électromagnétique	K _t	Nm/A _{rms}	1,46	
Résistance du bobinage (25°C)*	R _b	Ω	0,238	
Inductance du bobinage*	L	mH	3,04	
Inertie du rotor	J	kgm ² ×10 ⁻⁵	920	
Constante de temps thermique	T _{th}	min	2	
Masse du moteur	M	kg	27	
Tension du réseau d'alimentation	UR1 UR2 UR3	V _{rms}	400	- - -
Vitesse nominale	Nn1 Nn2 Nn3	t/min	3750	- - -
Couple nominal	Mn1 Mn2 Mn3	Nm	72,03	- - -
Courant nominal	In1 In2 In3	A _{rms}	49,22	- - -
Puissance nominale	Pn1 Pn2 Pn3	W	28290	- - -

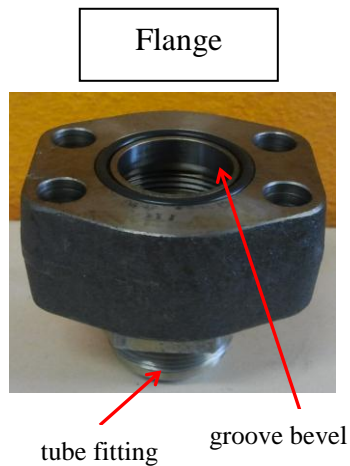
Toutes les données sont en valeurs typiques pour des conditions d'utilisation standard
* Entre deux phases
Tensions et courants sont donnés en valeurs efficaces

— Service permanent UR1 - - - Service intermittent UR1
— Service permanent UR2 - - - Service intermittent UR2
— Service permanent UR3 - - - Service intermittent UR3



Hydraulic Circuit

▪ Inlet Pipe: Flange + Straight Rigid Pipe



<i>Flange + Tube Fitting</i>		
<i>Flange Groove</i>		
Inside Groove Diameter	31.8	mm
Groove thickness	3.2	mm
Groove Depth	10	mm
Groove Bevel Depth	5	mm
<i>Flange</i>		
Flange Length	40	mm
Total Flange+Tube Fitting Assembly length	80	mm
<i>Tube Fitting</i>		
Tube Fitting Length	57	mm
Tube Fitting Inside Diameter	27.2	mm
Tube Fitting Thickness	5.5	mm
<i>Calculated Characteristics</i>		
Flange Inside Diameter	38.2	mm
Flange Inside Length (between groove/tube fitting)	13	mm
Volume TOT	0.056	l

<i>Rigid Pipe</i>		
Inside Diameter	25.3	mm
Length	430	mm
Exit hook length	30	mm
Total Volume	0.216	l

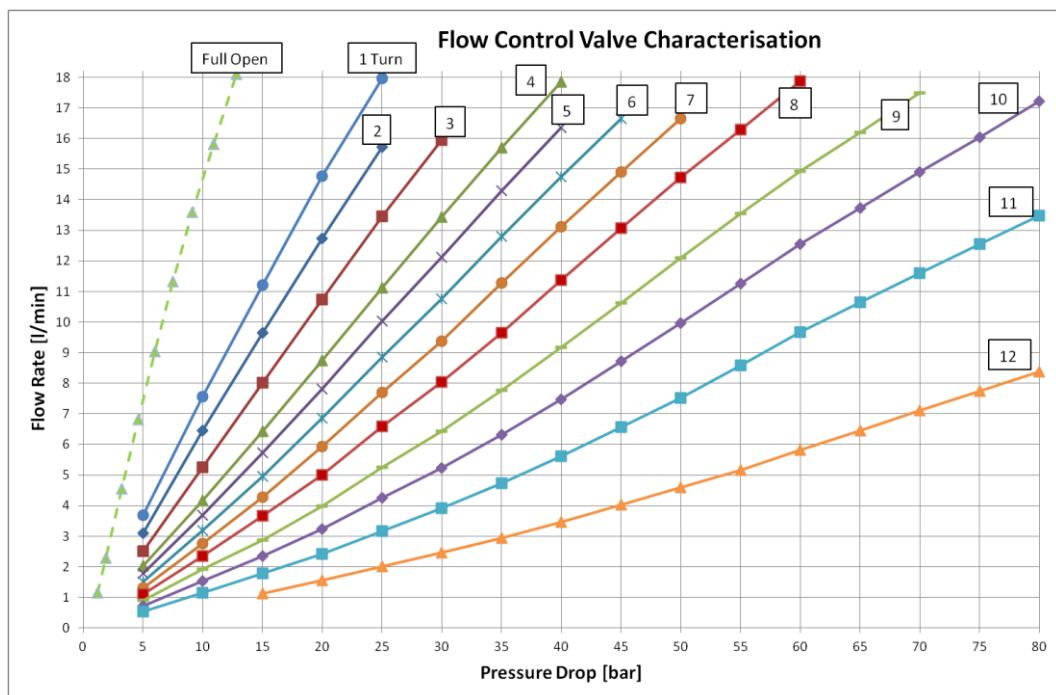
- **Flexible hose + Total volume of HP Hydraulic Circuit**

<i>Length</i>	2.38	m
<i>Inner diameter</i>	26	mm
<i>Thickness</i>	6.35	mm
<i>Total volume of pipe</i>	1.26	l
<i>Total volume of HP hydraulic circuit</i>	1.8	l

Main Signals in the Test Bench

<i>Description</i>	Sensor Model	Electrical Range	Physical Range
Pressure in HP hydraulic circuit	Lucas Schaevitz P901-0002	-10 V ~ + 10 V	0 ~ 200 bar
<i>Pressure in pump inlet</i>	Jumo dTrans p30	-10 V ~ + 10 V	-1 ~ 1.5 bar
<i>Output flow rate</i>	VSE.flow VS 0.2	-10 V ~ + 10 V	0.02 ~ 18 l/min

The figure concerns laboratory data, acquired in the frame of this thesis, in order to characterise the flow control valve. The output flow rate is recorded by varying pressure drop and the opening positions of the valve. The curves are relative to fluid constant temperature equal to 20 °C. It is interesting to remark that the valve behaviour is almost laminar in the all operating conditions.



Appendix B - Preliminary Calculation of Effective Bulk Modulus through the Evaluation of Parasitic Contributions

It was discussed in the Chapter 3 about the difficulty of evaluating the Effective Bulk Modulus β_e as function of parasitic parameters. A preliminary calculation is thus carried out for quantifying it. It is described as follows (all the references in this appendix are inserted at the end of Chap. 3).

By considering a finite volume of liquid subjected to a change in pressure Δp , its volume decreases by an amount $\Delta V=(V-V_{in})$ proportional to pressure increase, the fluid Bulk Modulus β_f can be so expressed by [10]:

$$\beta_f = \frac{1}{X} = -\frac{V_{in} \Delta p}{\Delta V} \quad (\text{B.1})$$

where the negative sign denotes a volume reduction and V_{in} is the initial volume of fluid.

β_f can be then described in four different ways depending on working conditions and on compression speed, in accordance to definition in [11]:

- Secant or tangent
- Isothermal or adiabatic

In this research work, an adiabatic secant bulk modulus is selected. β_f of the pure hydraulic mineral oil is typically in the range 17500-21000 *bar* [11] but it is not constant because it varies as function of operating conditions: pressure and temperature. In addition it depends on several parasitic effects as [9]:

- free air content
- vapour content
- deformability of containers (hydraulic hoses)

Consequently, an Effective Bulk Modulus β_e , that takes into account all the parasitic contributions, has to be defined.

Let me consider a flexible container having a total inside volume V_{tot} composed by (Fig. B.1) hydraulic fluid V_f and air and/or vapour V_g . The air is present in two forms: free

(bubbles) and dissolved but the dissolved air has not effects on the β_f [12].

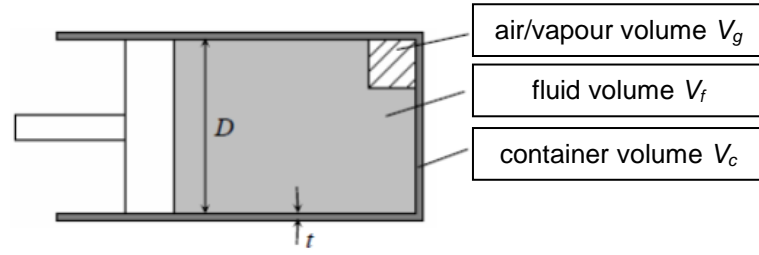


Figure B.1 Evaluation of Effective Bulk Modulus: flexible container filled with liquid and air/gas

The total volume V_{tot} can be written as (fig. B.1):

$$V_{tot} = V_f + V_g \quad (B.2)$$

If a compression is applied, Δp (e.g. moving a piston), V_{tot} is reduced by a quantity ΔV_{tot} given by:

$$\Delta V_{tot} = -\Delta V_f - \Delta V_g + \Delta V_c \quad (B.3)$$

where

ΔV_c = variation of gas volume

ΔV_c = the variation of container structure volume

By defining the following bulk moduli for each contribution by using the form of (B.1):

$$\left\{ \begin{array}{l} \beta_e = V_{tot} \frac{\Delta p}{\Delta V_{tot}} \\ \beta_f = -V_l \frac{\Delta p}{\Delta V_f} \\ \beta_g = -V_g \frac{\Delta p}{\Delta V_g} \\ \beta_c = V_{tot} \frac{\Delta p}{\Delta V_c} \end{array} \right. \quad (B.4)$$

where

β_g = Bulk Modulus of the gas

β_c = Bulk Modulus of the container

By inserting the values of ΔV_i (B.3) into the eq. (B.4), it finally results:

$$\frac{1}{\beta_e} = \frac{V_l}{V_{tot}} \frac{1}{\beta_l} + \frac{V_g}{V_{tot}} \frac{1}{\beta_g} + \frac{1}{\beta_c} \quad (B.5)$$

The eq. (B.5) expresses the dependence between the effective bulk modulus β_e and the other bulk moduli as function of percentage of the each volume. The β_e is obtained from the reciprocals of the term of this equation.

In this applications context the value of V_{tot} is known thanks to geometrical calculations of total volume of pump and hydraulic lines and the β_f is obtained from manufacturers' data. So the difficulty to determine a good value of β_e concerns the correct evaluation of the terms: β_g , β_c , and V_g .

The presence of free air and vapour can significantly reduce the Bulk Modulus of the fluid β_f : it is sufficient to think that the air is more than 10000 times as compressible as oil [11]. The effects of undissolved air on β_f are showed in figure B.2 where the β_e is plotted versus pressure and air content: this dependence is more emphasized at low pressure value when little increase of pressure produces high variation of bulk modulus in the case of small air content.

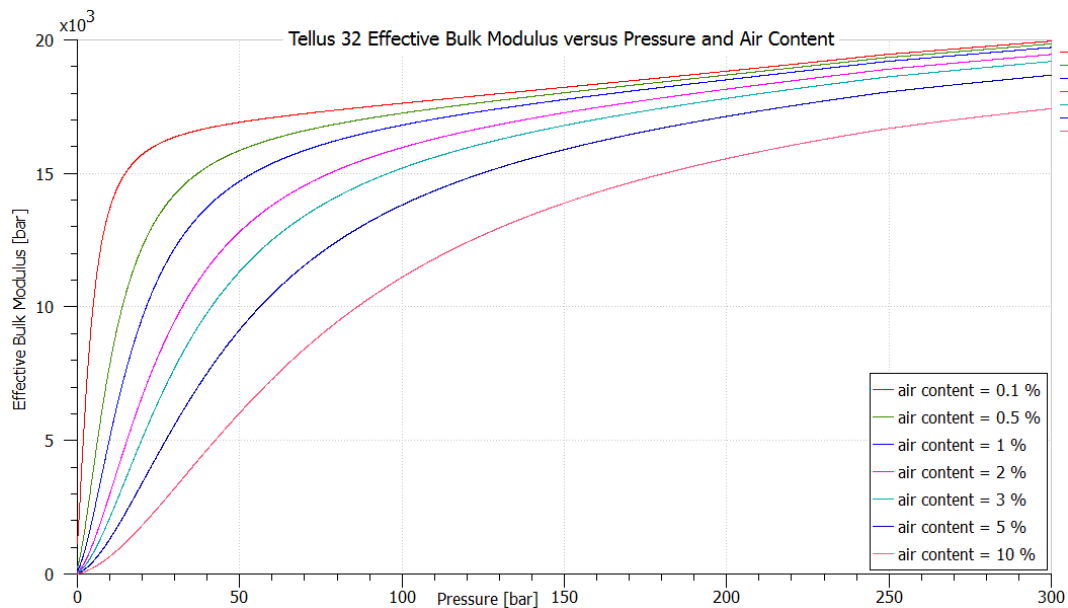


Figure B.2 Variation of Effective Bulk Modulus as function of Pressure and Air Content obtained in AMESim

In order to evaluate the parameter β_g , the air/vapor content subjected to a polytropic transformation has to be considered. By applying the First Law of Thermodynamics [13] and by using the definition of gas bulk modulus (eq. B.4), it results:

$$\beta_g = \Gamma p \quad (\text{B.6})$$

where

Γ = polytropic index of the transformation of air/vapour content

Several studies analyse the air/vapour bubbles dynamics as function of an oscillating pressure field in order to determine the effective polytropic index [14]. It is so possible to assert that the Γ can vary between:

- the isothermal conditions, equivalent to $\Gamma = 1$
- the isentropic conditions, equivalent to $\Gamma = \gamma = 1,4$ (γ is the air specific heats ratio)

To evaluating the V_g , typical realistic values of volumetric content of air/vapour in the liquid $\varepsilon = V_g/V_{tot}$ are $\varepsilon \in [1; 10]\%$.

The contribution of containers elasticity to fluid Bulk Modulus reduction, can be appreciable, even if the air content remains the principal parasitic effect. The hydraulic lines represent the major source of mechanical compliance. In order to calculate the β_c due to the flexible hoses present in the test bench, the theory of pressurized thin-walled cylinder is applied [15]. By starting from the analysis of thick-walled cylinders with constant length and no axial forces, the stress-strain equations in the form of Hooke's Law without thermal dilatation and mass forces are used [16]. Under the assumptions of radial stress component negligible compared to tangential stresses σ_r , the latter σ_r are given by [15]:

$$\sigma_t = \frac{\Delta p D_{in}}{2 t} \quad (\text{B.7})$$

where

D_{in} = the inner diameter of pipe

t = pipe thickness

The tangential strain ε_t is provided by means of the (B.8) where the expression of σ_t of (B.7) is used:

$$\varepsilon_t = \frac{\sigma_t}{E} = \frac{\Delta p D_{in}}{2 E t} \quad (\text{B.8})$$

where

E = Young's modulus of the pipe material

The tangential strain ε_t can be also written as function of change of diameter ΔD by:

$$\frac{\Delta D}{D_{in}} = \varepsilon_t \quad (\text{B.9})$$

In order to evaluate the total change of volume per unit of volume $\Delta V_c/V_{tot}$ that has to be inserted in the expression (B.4) of β_c , the following calculation is made under the assumption of invariant length of pipe ($\Delta L=0$). It results:

$$V_{tot} + \Delta V_c = \frac{\pi}{4} L (D_{in} + \Delta D)^2 \quad (\text{B.10})$$

By developing the square in (B.9) and by neglecting the term of second order (ΔD_{in}^2), the ΔV_c can be write as follows ($V_{tot} = \frac{\pi}{4} L D_{in}^2$):

$$\Delta V_c = \frac{\pi}{2} L D_{in} \Delta D \quad (\text{B.11})$$

The expression of $\Delta V_c/V_{tot}$ is finally obtained through the (B.10) and (B.8):

$$\frac{\Delta V_c}{V_{tot}} = 2 \frac{\Delta D}{D_{in}} = 2\varepsilon_t \quad (\text{B.12})$$

In conclusion the container bulk modulus β_c is given by:

$$\beta_c = V_{tot} \frac{\Delta p}{\Delta V_c} = \frac{\Delta p}{2\varepsilon_t} = \frac{E t}{D_{in}} \quad (\text{B.13})$$

The difficulty is now to evaluate the Elastic Modulus of the wall E , being D_{in} and t known. The flexible hose used in the test bench is of multispiral hydraulic type.



Figure B.3 Flexible Hoses: Semperit DIN 31 EN 856 4SH, from [17]

It consists of four spiral layers of high tensile steel wire, used as reinforcement, while the tube is in synthetic rubber (fig. B.3) (Semperit DIN 31 EN 856 4SH [17]). It means that the value of E is given by contributions of steel wires and rubber. In addition E is not constant but it varies as function of operating pressure in a non-linear way: a study conducted for the determination of hydraulic capacity of rubber hoses shows this dependence [18].

In order to estimate E , some references are used to define the range of possible values, in particular the minimum E_{min} and the maximum E_{max} .

The E_{min} is so obtained from [19] that provides the volume increases of hose assemblies when hoses with two braids of high tensile steel wire are used (type 2SN). The figure B.4 represents the different volume increases $\Delta V_c/L$ as function of nominal diameter DN. Clearly the 4SH hose types results more resistant than 2SN types.

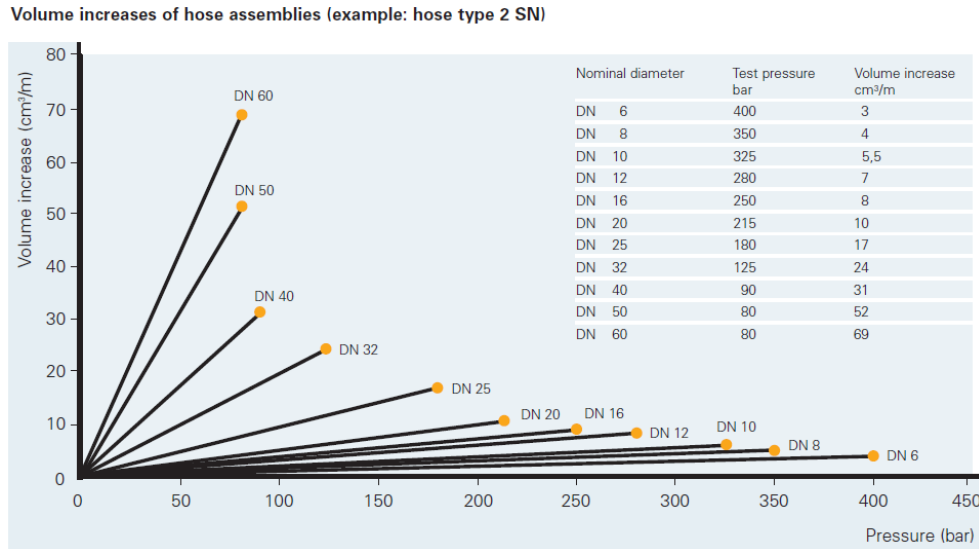


Figure B.4 Volume increases of hose assemblies: hose type 2SN, from [19]

Let take the DN 32. The $\Delta V_c/L$ as function of operating pressure results (table in fig. B.4):

$$\frac{\Delta V_c}{L} = \frac{24}{125} \Delta p \tag{B.14}$$

where
 L = pipe length

By using the expression of β_c by means of the eq. (A.13), the E_{min} is thus obtained:

$$E_{min} = \beta_c \frac{D_{in}}{t} = \frac{\Delta p}{\frac{\Delta V_c}{V_{tot}}} \frac{D_{in}}{t} = 11346 \text{ bar} \tag{B.15}$$

where the value of parameters are relative to test bench and listed in the table below.

D_{in}	t	L	V_{tot}	Δp	ΔV_c	β_c
[mm]	[mm]	[m]	[cm ³]	[bar]	[cm ³]	[bar]
26	6.35	2.38	1263.6	50	22.8	2771

Table B.1 Parameters used for determining the minimum of Elastic Modulus of pipe E_{min}

In order to evaluate E_{max} , the reference [20] is indeed used that provides empirical results showed in table B.2. In the table the ratio between β_e and β_f are listed. The air content is not considered in this calculation.

Hose Type	β_e/β_f
4 wire, spiral, 25 mm bore	0.48
2 wire, braid, 25 mm bore	0.27
2 wire, braid, 38 mm bore	0.26
1 wire, braid, 25 mm bore	0.23

Table B.2 Effective tangent bulk modulus at 30 °C and 170 bar (expressed as a ratio of the bulk modulus of mineral oil), from [20]

If $\beta_f = 20000$ bar is chosen the β_e thus results (hose with 4 wire selected in the table):

$$\beta_e = 9600 \text{ bar} \quad (\text{B.16})$$

The value of β_c is so obtained from (B.5) when the air content is not taken into account:

$$\beta_c = \frac{\beta_e \beta_f}{\beta_f - \beta_e} = 18461 \text{ bar} \quad (\text{B.17})$$

E_{max} is finally calculated by the eq.s (B.15), β_c given by (B.17) and the parameters of table B.1:

$$E_{max} = 75589 \text{ bar} \quad (\text{B.18})$$

In conclusion, by rewriting the (B.5) by using the (B.6) and (B.13), β_e is given by

$$\frac{1}{\beta_e} = \frac{(1 - \varepsilon)}{\beta_l(p, T)} + \frac{\varepsilon}{\Gamma p} + \frac{D_{in}}{E t} \quad (\text{B.19})$$

where the following range of values are calculated

- $\Gamma \in [1; 1,4]$
- $\varepsilon \in [1; 10]\%$
- $E \in [11346; 75589] \cdot (1 \pm k) \text{ bar} = [9076.8; 90706.8] \text{ bar}$

The range of E is then extended of 20 % ($k = 0.2$) in order to consider a certain level of calculation uncertainty.

Appendix C - Thermal Supercomponent for Calculation of Released Powers associated to Pump Internal Leakages

